Investigation of relativistic shock waves and Mach cones in a partonic cascade

Dissertation
zur Erlangung des Doktorgrades
der Naturwissenschaften

vorgelegt beim Fachbereich Physik
der Johann Wolfgang Goethe-Universität
in Frankfurt am Main

von

Ioannis Bouras
aus Offenbach am Main

Frankfurt am Main 2013
(D 30)

Vom Fachbereich Physik (13) der Johann Wolfgang Goethe-Universität
als Dissertation angenommen.

Dekan: Prof. Dr. Joachim Stroth

Gutachter: Prof. Dr. Carsten Greiner, Prof. Dr. Dirk H. Rischke

Datum der Disputation:

Contents

List of Figures

Deutschsprachige Zusammenfassung

Übersicht

Die Entstehung des Universums, die Entstehung des Lebens und die Entstehung eines Bewusstseins sind die wohl drei interessantesten Gebiete heutiger Forschung, welche mit unterschiedlichen Methoden angegangen werden können. Die Entstehung des Bewusstseins ist heute ein großes Teilgebiet der Hirnforschung, wobei die Entstehung des Lebens und die davon ausgehende Entwicklung verschiedener Spezies ein Gebiet der Evolutionsbiologie sind [1, 2, 3]. Die Frage nach der Entstehung des Universums, welches vor 13.7 Milliarden Jahren mit dem Urknall entstanden sein soll, und seiner Beschaffenheit sind ein Gebiet der heutigen modernen Physik. Soweit wir heute wissen existieren vier Grundkräfte in unserem Universum. Es handelt sich dabei um die starke, die schwache, die elektromagnetische und die gravitative Wechselwirkung. Die ersten drei Kräfte bilden das sogenannte Standardmodell der Physik [4, 5, 6].

Um die Grundbausteine der Materie unseres Universums zu erforschen, werden in großen Beschleunigern wie am *Relativistic Heavy Ion Collider* (RHIC) am *Brookhaven National Laboratory* (BNL) und am *Large Hadron Collider* (LHC) am *Conseil Europeén pour la Recherche Nucléaire* (CERN) schwere Ionen bei hohe Energien zur Kollision gebracht. In einer kontrollierten experimentellen Umgebung wird die nukleare Materie dabei sehr stark komprimiert und erreicht auf diese Art und Weise sehr hohe Energiedichten und Temperaturen. In diesem Fall wird ein neuer Zustand der Materie erreicht, welcher als Quark-Gluon-Plasma (QGP) bezeichnet wird [7, 8, 9] und in der sehr frühen Phase des Universums existiert haben soll. In diesem Stadium sind die Elementarteilchen, Quarks und Gluonen, nicht mehr in Hadronen gefangen, was als *Farbeinschluss* bezeichnet wird, sondern ungebunden, was als *asymptotische Freiheit* bezeichnet wird. Dieser Zustand hat eine sehr kurze Lebensdauer in der Größenordnung um $\Delta t \simeq 5 - 10$ fm/c, da das System schnell expandiert und abkühlt, wobei wiederum ein (Phasen-)Übergang eintritt, wenn eine pseudo-kritische Temperatur, T_c, erreicht wird. Dieser Übergang zeichnet sich dadurch aus, dass die Elementarteilchen Quarks und Gluonen wieder zu Hadronen rekombiniert werden, welche später in den jeweiligen Detektoren gemessen werden.

Der Farbeinschluß, welcher es nicht erlaubt, freie Quarks und Gluonen zu beobachten, macht eine direkte Untersuchung des in Schwerionenkollisionen erzeugten Quark-Gluon-Plasmas unmöglich. Deshalb müssen die Eigenschaften der final gemessenen Hadronen genau erfasst werden, um eine genügend große Menge an experimentellen Daten zu erhalten. Mithilfe von verschiedenen theoretischen Modellen, bei denen davon ausgegangen wird, dass eine Quark-Gluonische Phase generiert wird, können durch Vergleich mit den experimentellen Daten Rückschlüsse auf dessen Eigenschaften gezogen werden.

Eine Eigenschaft, welche dabei anfangs nicht erwartet wurde, war das starke kollektive Verhalten und die damit eingehende rasche Thermalisierung der ungebundenen

Quarks und Gluonen. Die Messung des elliptischen Flusses in nicht-zentralen Kollisionen impliziert, dass sich das QGP wie eine nahezu perfekte Flüssigkeit verhält. Die Annahme einer perfekten Flüssigkeit wurde in späteren Jahren jedoch relativiert, da die Viskosität des QGP einen endlichen Wert hat. Eine mit der Entropiedichte reskalierte Viskosität, η/s, welche ein Maß für die Stärke der Dissipation des Systems ist und welche über den direkten Vergleich mittels viskoser hydrodynamischer Rechnungen extrahiert werden kann [10, 11, 12, 13, 14, 15, 16, 17], liegt sehr nahe an den vorhergesagten unteren universellen Grenzen [18, 19, 20]. Dies deutet darauf hin, dass das QGP die wohl perfekteste Flüssigkeit unseres Universums ist.

Ein weiterer Hinweis für die Existenz einer solchen Phase von ungebundenen Quarks und Gluonen ist die Unterdrückung von hoch-energetischen Teilchen, welche man als Jets bezeichnet. Diese Unterdrückung von Jets wird in der Fachsprache auch als *Jet-Quenching* bezeichnet [21, 22, 23, 24]. Die sehr kleine Viskosität des Mediums führt dazu, dass Jets in der frühen Phase der Schwerionenkollisionen unterdrückt werden, insofern sie das erzeugte heiße und dichte Medium durchqueren sollten. Sogenannte Zwei-Teilchen-Korrelationen weisen darauf hin [25, 26, 27, 28], dass die Energie der Jets sich auf die weiteren weichen Teilchen des Mediums verteilt und unter bestimmten Umständen eine Doppel-Peak-Struktur in den Zwei-Teilchen Korrelationen erscheint. Ursprünglich wurde angenommen, dass dieses Signal ausschließlich durch die Wechselwirkung der Jets mit dem Medium hervorgerufen wird. Eine über Jahre viel versprechender Erklärungsversuch für diese Struktur waren Stoßwellen in Form von Mach´schen Kegeln, welche durch mit Überschallgeschwindigkeit propagierende Jets induziert werden [29, 30]. Mit der Annahme eines Mediums, welches sich wie eine fast perfekte Flüssigkeit verhält, werden durch die Energie- und Impulsdeposition des Jets Schallwellen erzeugt, welche interferieren und auf einem Kegel mit einem Öffnungswinkel liegen, welcher von der Geschwindigkeit des Jets und der Geschwindigkeit der emittierten Schallwellen abhängt. Auf dieser Kegelfront, welche auch als Stoßfront bezeichnet wird, werden Teilchen mit einem bestimmten Emissionswinkel in Bezug zur Richtung des Jets emittiert, was in einem vereinfachten Bild zu einer im Experiment beobachteten Doppel-Peak-Struktur führen soll. Dennoch existieren auch andere mögliche Beiträge, welche zu solch einer Struktur führen können. Das ist zum Beispiel der trianguläre Fluss, welcher aus fluktuierenden Anfangsbedingungen in Schwerionenkollisionen resultiert [15, 31, 32].

Die Tatsache, dass sich das in Schwerionenkollisionen erzeugte Medium wie eine fast perfekte Flüssigkeit verhält und hochenergetische Jets unterdrückt werden, ist ein starkes Indiz für die Bildung von Stoßwellen in Form von Mach´schen Kegeln. In dieser Arbeit wird die Frage untersucht, wie sich solche Stoßwellen und Mach´sche Kegel in einem idealen und stark viskosen Medium ausbreiten, welche Einflüsse verschiedene Formen der Energiedeposition haben und ob ein solcher Mach´scher Kegel in der Tat einen Beitrag zu der Doppel-Peak-Struktur liefert. Für diese Untersuchungen benutzen wir ein mikroskopisches Transportmodell, welches die relativistische Boltzmann-Gleichung (rBE) löst. Der Vorteil im Vergleich zu viskosen hydrodynamischen Modellen ist, dass Zeitentwicklung von Jet und Medium innerhalb eines gemeinsamen Modells beschrieben werden können. Ein weiterer Vorteil dieses Modells ist, dass man damit Nichtgleichgewichtsphänomene und Systeme mit starken Gradienten verlässlich beschreiben kann, was bei viskosen hydrodynamischen Modellen nicht der Fall ist. Die genaue Lösung der

rBE dient im weiteren auch dazu, entsprechende dissipative hydrodynamische Formalismen auf die Grenzen ihrer Anwendbarkeit zu überprüfen. Dies erreichen wir, indem wir Stoßwellenphänomene in einem kontrollierten eindimensionalen Szenario untersuchen, was für die kinetische und viskose hydrodynamische Theorie ein harter Testfall ist. Die folgende Arbeit basiert auf den Publikationen [33, 34, 35, 36, 37, 38].

Relativistische kinetische Theorie und Hydrodynamik

Die relativistische Hydrodynamik ist eine klassische Feldtheorie, welche makroskopische Objekte wie Flüssigkeiten beschreiben kann. Hierbei muss angenommen werden, das jedes Flüssigkeitselement nahe am thermodynamischen Gleichgewicht und die mikroskopischen Längenskalen, wie die mittlere freie Weglänge, λ_{mfp}, klein gegenüber den makroskopischen Längenskalen wie die Ausdehnung des untersuchten Systems, L, sind. Die kinetische Theorie dagegen beschreibt die Dynamik von einfachen Gasen auf einer mikroskopischen Ebene. Ihr Vorteil gegenüber der hydrodynamischen Theorie ist, dass ihre Anwendbarkeit nicht auf Systeme nahe am thermodynamischen Gleichgewicht beschränkt ist. Das bedeutet, dass sie auch Systeme beschreiben kann, in welchen die mikroskopischen Längenskalen viel größer als die makroskopischen Längenskalen ist. Eine bekannte Größe, welche das Verhältnis der mikroskopischen gegenüber der makroskopischen Längenskala beschreibt, ist die Knudsen-Zahl,

$$Kn = \frac{\lambda_{\mathrm{mfp}}}{L} \,.$$
(0.1)

Von einer nahezu idealen Flüssigkeit spricht man, wenn $Kn \ll 1$, dagegen spricht man von viskosen Flüssigkeiten, wenn $Kn \lesssim 1$. Im Bereich $Kn \approx 1$ gilt die Theorie der Hydrodynamik nicht mehr als anwendbar und im Bereich $Kn \gg 1$ wird von einem nicht interagierenden, freien Gas gesprochen.

Die einfachste Form einer kinetischen Theorie ist die relativistische Boltzmann-Gleichung (rBE) [39, 40, 41],

$$p^\mu \partial_\mu f(x,p) = C_{22} + C_{23} + \cdots \,,$$
(0.2)

welche die Raumzeitevolution der Einteilchenverteilungsfunktion, $f(x,p)$, unter Berücksichtigung von Wechselwirkungsprozessen beschreibt. Die vollständige Information über das System ist jederzeit durch die Einteilchenverteilungsfunktion, $f(x,p)$, gegeben. Die makroskopischen Größen des Systems können aus der Verteilungsfunktion extrahiert werden. Solche Größen sind unter Umständen der Energie-Impuls-Tensor, $T^{\mu\nu}$, und der Teilchenfluß-Vektor, N^μ. Die Lösung der rBE ist ein schwieriges Unterfangen und nur nur numerisch möglich, was in dieser Arbeit mittels des in **Kapitel** 6 vorgestellten kinetischen Transportmodell BAMPS (**B**oltzmann **A**pproach To **M**ulti-**P**arton **S**cattering) [41] gelöst wird. Mittels einer stochastischen Beschreibung der Kollisionen ist es dem Modell möglich, die rBE in einer sehr effizienten Weise zu lösen, was in dieser Arbeit am Beispiel der Simulation von relativistischen Stoßwellen demonstriert wird.

Die Gleichungen für die ideale Hydrodynamik folgen direkt aus der Energie-, Impuls-

und Teilchenerhaltung,

$$\partial_\mu T^{\mu\nu} = 0 \,, \tag{0.3}$$
$$\partial_\mu N^\mu = 0 \,. \tag{0.4}$$

Die wesentlichen Größen hierbei sind der Druck, p, die Energiedichte, e, die Teilchendichte, n, und die Vierer-Geschwindigkeit, u^μ. Zusammen mit einer Zustandsgleichung, $p(n, e)$, hat man ein geschlossenes System von Gleichungen. Möchte man jedoch dissipative Effekte mit berücksichtigen, was zum Beispiel notwendig ist, wenn man das QGP beschreiben möchte, werden weitere Gleichungen benötigt. Hierbei wird $T^{\mu\nu}$ und N^μ in einen Gleichgewichtsanteil und dissipativen Anteil zerlegt,

$$N^\mu = N_{\mathrm{eq}}^\mu + \delta N^\mu = n u^\mu + V^\mu \,, \tag{0.5}$$
$$T^{\mu\nu} = T_{\mathrm{eq}}^{\mu\nu} + \delta T^{\mu\nu} = e u^\mu u^\nu - (p + \Pi)\, \Delta^{\mu\nu} + W^\mu u^\nu + W^\nu u^\mu + \pi^{\mu\nu} \,. \tag{0.6}$$

wobei hiermit die Volumenviskosität, Π, der Wärmefluß, q^μ, und der Scherspannungstensor, $\pi^{\mu\nu}$, eingeführt werden.

Mithilfe der Grad´schen Methode [42] oder der Expansion in der Knudsen-Zahl [40] kann ein Zusammenhang zwischen den makroskopischen Größen und der Verteilungsfunktion, $f(x, p)$, hergestellt werden, wobei die Koeffizienten wie die Scherviskosität, η, der Wärmeleitkoeffizient, κ, oder die Volumenviskosität, ζ, von der ihr zu Grunde liegenden mikroskopischen Theorie abgeleitet werden können. In **Abschnitt** 3.4 wird diese Vorgehensweise kurz skizziert und die wichtigsten viskosen hydrodynamischen Formalismen vorgestellt. Das sind zum einen die relativistischen relaxationsbasierten Gleichungen zweiter Ordnung von Israel und Stewart (IS) [43, 44, 45], welche kausal sind und standardmäßig genutzt werden, um die Evolution des QGP in Schwerionenkollisionen zu beschreiben. Zusätzlich zeigen wir die erst kürzlich in [35, 46, 47] vorgestellte Theorie RTRFD (Resummed Transient Relativistic Fluid Dynamics), welche unter Benutzung der Momentenmethode hergeleitet wurde. Beide Theorien werden im Laufe der Arbeit mit den numerischen Lösungen der rBE auf ihre Anwendbarkeit untersucht. Zur numerischen Realisierung wird das viskose hydrodynamische Modell vSHASTA genutzt, welches im **Appendix** D kurz vorgestellt wird[1].

Stoßwellen und Mach´sche Kegel in idealer Hydrodynamik

In der idealen Hydrodynamik ist die Entropie eine Erhaltungsgröße. Dies trifft nicht mehr zu, wenn Lösungen mit einer Diskontinuität auftreten, welche als Stoßwellen bezeichnet werden. Stoßwellen zeichnen sich durch abrupte Änderungen von Druck, Energiedichte oder Geschwindigkeit aus und propagieren schneller als die Schallgeschwindigkeit durch ein Medium. Stoßwellen sind keine seltenen Phänomene in der Natur und treten in einer imposanten Form bei Sternenexplosionen auf, was auch als Supernovae bezeichnet wird. Weiterhin spielen interstellare Stoßwellen, welche durch das Eindringen von Gas- und Staubwolken in eine gasreiche Galaxie erzeugt werden, eine nicht unbedeutende Rolle bei Sternentstehungsprozessen.

---

[1]Wir danken H. Niemi und E. Molnar für die numerischen Berechnungen mittels vSHASTA und für die gelieferten Resultate.

Die Ausbreitung von Stoßwellen in solchen Systemen ist ein komplexer Prozess, dessen Simulation numerisch aufwendige Modelle erfordert. Dennoch ist es möglich, Konfigurationen zu finden, in welchen man die Ausbreitung von Stoßwellen in stark vereinfachten Systemen untersuchen kann. Ein sehr bekanntes Problem aus der Mathematik ist das relativistische Riemann-Problem (rRP). Es behandelt die Ausbreitung einer Stoßwelle in einer idealen Flüssigkeit welche aus einer anfänglichen Diskontinuität von thermodynamischen Größen und/oder Geschwindigkeit folgt. Im speziellen Fall, in welcher das Medium links und rechts von der Diskontinuität in Ruhe ist, breitet sich eine Stoßwelle in den Bereich mit kleinerem Druck aus, wobei gleichzeitig in die entgegengesetzte Richtung eine Verdünnungswelle mit Schallgeschwindigkeit in den Bereich höheren Druckes propagiert. Beide Wellen sind miteinander über eine Kontaktunstetigkeit verbunden. Eine analytische Lösung für das rRP wird in **Kapitel** 5 für eine einfache Zustandsgleichung diskutiert. Im Allgemeinen dient diese analytische Lösung zur Überprüfung von numerischen Modellen im Hinblick auf ihre Genauigkeit, was zum Teil auch in dieser Arbeit erfolgt.

Ein weiteres bekanntes Phänomen, in welchem Stoßwellen auftreten können, sind Mach´sche Kegel. Wenn eine sehr schwache Störung mit einer Geschwindigkeit schneller als der Schall durch ein Medium propagiert, emittiert die Störung Schallwellen, welche interferieren und einen Mach´schen Kegel bilden. Diese Kegelfront besitzt einen Öffnungswinkel, welcher von der Geschwindigkeit der Störung und der Schallgeschwindigkeit abhängt. Die Ausbreitung von Mach´schen Kegeln ist im Allgemeinen sehr kompliziert, wenn nicht von einer schwachen und gleichmäßig propagierenden Störung ausgegangen werden kann. Im Falle einer nicht schwachen Störung werden anstatt Schallwellen Stoßwellen emittiert, wobei die Kegelfront auch als Stoßwellenfront bezeichnet werden kann[2]. Der Öffnungswinkel des Mach´schen Kegels hängt in diesem Fall von der Geschwindigkeit der Störung und der Stoßwellengeschwindigkeit ab. Zusätzlich treten nicht-lineare Effekte wie *Diffusion Wake* und *Head Shock* auf, welche von der Form der Energiedeposition abhängen. Im Weiteren ist der Einfluss von Viskosität und anderen Faktoren auf die Entwicklung von Stoßwellen auch in Form von Mach´schen Kegeln aktuell noch eine weitgehend offene Frage und wird in dieser Arbeit mittels des kinetischen Transport-Modells BAMPS untersucht.

Diskussion und Ergebnisse

Die numerischen Ergebnisse der Arbeit werden in zwei Kapiteln dargestellt. In **Kapitel** 7 behandeln wir die Untersuchung von Stoßwellen in einem $(1+1)$-dimensionalen System, wobei in **Kapitel** 8 die Untersuchung von Stoßwellenphänomenen in Form von Mach´schen Kegeln durchgeführt wird.

---

[2]Solche Mach´schen Kegel werden in der Natur zum Beispiel durch Überschallflugzeuge erzeugt. An der Front des Mach-Kegels werden Stoßwellen erzeugt, welche von einem Beobachter als lauter Knall wahrgenommen werden.

Untersuchung von Stoßwellenphänomenen in kinetischer Theorie und dissipativer Hydrodynamik

Das Hauptanliegen in **Kapitel** 7 liegt darin, Stoßwellen mit dem kinetischen Transportmodell BAMPS in einem statischen System zu untersuchen, welches im Weiteren auch als Referenzlösung für die dissipativen hydrodynamischen Formalismen dienen soll. Um die Performanz und Genauigkeit von BAMPS zu überprüfen, vergleichen wir deren Resultate mit der analytischen Lösung des rRP für eine ideale Flüssigkeit im masselosen Limit. Es zeigt sich, dass durch einen sehr großen Wirkungsquerschnitt, σ, oder äquivalent dazu durch einen sehr kleinen Wert für η/s mittels isotroper binärer Kollisionen das nahezu ideale Flüssigkeitslimit erreicht wird und die Lösungen dieses Modells damit in diesen Regionen vertrauenswürdig sind. Nun ist es möglich, den kompletten Übergang von idealen zu viskosen Stoßwellen mittels BAMPS zu untersuchen, indem wir systematisch die mittlere freie Weglänge des Systems erhöhen. Es zeigt sich, dass die diskontinuierliche Stoßfront, Kontaktunstetigkeit und Verdünnungswelle mit erhöhter Viskosität ausschmieren und die genannten Bereiche für sehr große Viskositäten nicht mehr voneinander zu unterscheiden sind. Weiterhin beobachten wir auch, dass Stoßwellen eine gewisse Zeit benötigen, um sich zu entwickeln, was in **Abschnitt** 7.1.4 im Detail diskutiert wird. Für einen festen Wert für η/s ist die Lösung bei frühen Zeiten stark viskos, wohingegen sich bei späteren Zeiten die Charakteristiken des Stoßwellenprofiles entwickeln. Eine Größe, welche diese Entwicklung am besten beschreiben kann, ist die Knudsen-Zahl, Kn. Aufgrund der anfänglichen Unstetigkeit können wir hier ein Skalierungsverhalten erkennen. Mithilfe dieses Skalierungsverhaltens können wir in einer weiteren Studie in **Abschnitt** 7.1.5 abschätzen, dass Stoßwellenphänomene in einem gluonischen Medium in Schwerionenkollisionen und bei endlicher Lebenszeit des QGP nur dann entwickeln können, wenn der Wert für η/s nicht wesentlich größer als 0.2 ist.

Die Stärke der Stoßwelle hängt im wesentlichen vom Druckunterschied links und rechts von der anfänglichen Diskontinuität ab. Mithilfe von BAMPS ist es möglich, verschiedene Szenarien von Druckunterschieden zu untersuchen, was in **Abschnitt** 7.1.3 demonstriert wird. Weitere Lösungen des rRP werden in **Abschnitt** 7.2 im Detail untersucht. Hier diskutieren wir den Effekt von inelastischen Prozessen, den Effekt einer nicht-verschwindenden Masse, sowie die Entwicklung von Stoßwellen mit zwei verschiedenen Teilchensorten, welche über unterschiedliche Wirkungsquerschnitte untereinander und miteinander wechselwirken. Inelastische Prozesse führen zu einer chemischen Äquilibrierung, wohingegen eine endliche Masse die Untersuchung der Volumenviskosität erlaubt, da diese nicht wie im masselosen Limit verschwindet. Ein System von mehr als einer Teilchensorte zeigt dagegen den hohen Grad an Komplexität, welcher in einer solchen Konfiguration auftreten kann.

Die numerischen Lösungen von BAMPS dienen in **Abschnitt** 7.1.2 dazu, den Gültigkeitsbereich der IS-Theorie, welche mit vSHASTA numerisch implementiert wird, zu überprüfen. Für kleine Viskositäten ist die Übereinstimmung zwischen der rBE und IS Theorie hervorragend, aber nimmt mit größerer Viskosität stark ab. Für sehr große Viskositäten erzeugt die IS-Theorie Diskontinuitäten, welche in den Lösungen der rBE nicht auftreten. Wir argumentieren, dass ein Teil dieser Diskrepanz daher kommt, dass die IS-Theorie nicht für große Knudsen-Zahlen anwendbar ist, was eine starke

Einschränkung dieser Theorie darstellt. Gleichzeitig kann man auch erkennen, dass der Formalismus von IS im Gegensatz zum Scherfluß auch bei kleinen Knudsen-Zahlen den Wärmefluss nicht richtig beschreiben kann. Die Lösung dieses Problems wird in RTRFD durch Berücksichtigung höherer Momente erreicht. In **Abschnitt 7.3** werden in einem etwas modifiziertem Szenario die Lösungen der rBE mit dem IS-Formalismus und mehreren Varianten von RTRFD verglichen. Die Untersuchung von Systemen mit großen Gradienten in Druck und Fugazität zeigen die deutlichen Verbesserungen von RTRFD gegenüber dem IS-Formalismus. Dies wird zum einen damit begründet, dass die Transportkoeffizienten wie die Scherviskosität, η, oder der Wärmeleitkoeffizient, κ, exakter berechnet werden und auch die Kopplung der beiden dissipativen Ströme richtig implementiert ist.

Der Bereich der Stoßwellenfront kann auch in deren Ruhesystem untersucht werden, was uns erlaubt, diese in einem höheren Detailgrad zu untersuchen. Dies wird in **Abschnitt** 7.4 dargestellt. Hier werden links und rechts von der statischen Box thermische Reservoire simuliert, und nach einer hinreichend langen Zeit erreicht das System eine stationäre Lösung. Zum einen bestätigen wir hiermit, dass die Stoßwellenfront proportional zur mikroskopischen Längenskala ist, und zum anderen zeigt ein Vergleich mit RTRFD die Einschränkung relaxationsbasierter dissipativer Formalismen, zu denen auch der IS-Formalismus gehört. Bei sehr hohen Geschwindigkeiten der Stoßwellenfront erscheint in allen dissipativen Formalismen eine Diskontinuität, welche nicht in den Lösungen der rBE enthalten ist, was eine starke Einschränkung der Anwendbarkeit solcher Formalismen impliziert. Wir vermuten, dass die systematische Einbeziehung von Momenten aus Tensoren höheren Ranges[3] in RTRFD dieses Problem lösen kann, was jedoch noch einer eingehenden Studie bedarf.

Untersuchung von Mach´schen Kegeln in einem kinetischen Transportmodell

In **Kapitel** 8 wenden wir uns der Untersuchung von Mach´schen Kegeln in dem kinetischen Transportmodell BAMPS zu.

Da Mach´sche Kegel oft mit einer Doppel-Peak-Struktur in Verbindung gebrachte werden, möchten wir mit Hilfe eines einfachen Modells den Ursprung einer solchen Doppel-Peak-Struktur verstehen, was in **Abschnitt** 8.1 im Detail dargestellt wird. Dieses Modell beschreibt einen idealisierten Mach´schen Kegel in einer zweidimensionalen Ebene und zeigt, dass eine Doppel-Peak-Struktur nicht immer auftaucht und sehr stark von der Stärke der Stoßwelle abhängt. Darüber hinaus zeigt dieses vereinfachte Modell, dass unter Benutzung von Cuts im Impulsraum eine Doppel-Peak-Struktur von Teilchen aus dem höher-energetischen Bereich stammt.

Anschließend untersuchen wir in **Abschnitt** 8.2 die Struktur der relativistischen Mach´schen Kegeln mithilfe des mikroskopische Transportmodells BAMPS in einem statischen $(2+1)$-dimensionalen System. Dies erlaubt die Untersuchung eines Mach´schen Kegels ohne den Einfluss von externen Faktoren wie einer Expansion. Die Simulationen werden mit zwei verschiedenen Arten von Projektilen realisiert, das PED- und JET-Szenario. Das PED-Szenario zeichnet sich durch eine reine Energiedeposition aus,

---

[3]größer als 2.

wohingegen beim JET-Szenario Energie und Impuls in das Medium deponiert werden. Wir variieren die Energiedeposition in das Medium und untersuchen im Weiteren auch den Einfluss einer endlichen Viskosität auf die Struktur des Mach´schen Kegels.

Wir beobachten die Entwicklung von Mach´schen Kegeln für beide Sorten von Projektilen in einer nahezu perfekten Flüssigkeit, wobei die Struktur des Mach´schen Kegels für jedes Projektil unterschiedlich ist. Das JET-Szenario zeigt die Entwicklung des Mach-Kegels, zusätzlich aber sind ein starker *Head Shock* und eine in die Richtung des Projektils propagierende *Diffusion Wake* sichtbar. Das PED-Szenario zeichnet sich dadurch aus, dass eine *Anti-Diffusion Wake* auftaucht, dagegen aber kein *Head Shock*. In allen Szenarien beobachten wir weiterhin, dass der Emissions- und Öffnungswinkel des Mach-Kegels stark von der Energiedeposition abhängen. Zusätzlich, und wie schon in den vorigen Untersuchungen mit Stoßwellen im rRP, neigt ein großer Wert für η/s dazu, die kegelartige Struktur und weitere Charakteristika jeglicher Profile zu zerstören. Je größer die Viskosität bzw. je länger die Zeit für die Entwicklung des Mach-Kegels ist, desto mehr hängt die finale Struktur des Mach´schen Kegels von den Eigenschaften des Projektils ab. Aufgrund der speziellen Implementierung der Projektile können wir ähnlich wie beim rRP ein Skalierungsverhalten finden.

Obwohl Mach-Kegel-ähnliche Strukturen in BAMPS beobachtet werden, sind diese nicht zwingend mit einer Doppel-Peak-Struktur in der extrahierten azimuthalen Teilchenverteilung, $dN/(Nd\phi)$, verbunden. Es zeigt sich, dass nur das PED-Szenario zusammen mit einer sehr hohen Energiedeposition zu einer solchen Doppel-Peak-Struktur führt. Im JET-Szenario kann diese Struktur nicht beobachtet werden, da der Beitrag von den Flügeln des Mach-Kegels von den Beiträgen des *Head Shock* und der *Diffusion Wake* überschattet wird. Das PED-Szenario besitzt in dieser Form aber keine Korrespondenz in der Schwerionenphysik. Das JET-Szenario hingegen ist ein vereinfachtes Modell, zeigt jedoch, dass eine Doppel-Peak-Struktur nicht von einem Energie und Impuls deponierenden Teilchen erzeugt werden kann. Eine endliche oder gar sehr große Viskosität zeigt hier keine Verbesserung, sondern führt stattdessen zu einer Zerstörung der Doppel-Peak-Struktur aus dem PED-Szenario.

In **Abschnitt** 8.4 untersuchen wir schlussendlich die Bildung von Mach´schen Kegeln in einer vollen $(3 + 1)$-dimensionalen zentralen Schwerionenkollision mit Glauber-Anfangsbedingungen [48, 49]. Diese Anfangsbedingungen implizieren eine radiale und longitudinale Expansion. Wir ersetzen hier das Projektil durch einen hoch-energetischen Jet mit anfangs endlicher Energie und Impuls. Für kleine Werte der Viskosität ist die Bildung von Mach´schen Kegeln sichtbar, während diese Struktur für große Viskosität verloren geht. Aufgrund des Jet-Quenching ist die Stoßwellenfront stark gekrümmt und Jet-induzierte Mach´sche Kegel, welche durch den radialen Fluss abgelenkt werden, sind stark deformiert.

Die extrahierte azimuthale Zwei-Teilchen-Korrelation zeigt eine Doppel-Peak-Struktur, wenn sich der Jet in einem einzelnen Event in entgegengesetzte Richtung zum radialen Fluss bewegt. Dies impliziert, dass der starke Beitrag des *Head Shocks* und der *Diffusion Wake* durch die radiale Expansion aufgehoben wird und der Beitrag ausgehend von den Flügeln des Mach-Kegels wieder zum Vorschein kommt. Betrachtet man hingegen die Überlagerung von vielen verschiedenen möglichen Wegen eines Jets, erscheint auch hier eine Doppel-Peak-Struktur. Dieser Beitrag stammt von abgelenkten deformierten Mach´schen Kegeln, deren *Head Shock* und *Diffusion Wake* diese Doppel-

Peak-Struktur induzieren. Für beide möglichen Szenarien ist die Beobachtung einer Doppel-Peak-Struktur für $\eta/s = 0.08$ am stärksten ausgeprägt. Ein größerer Wert für η/s neigt dazu, diese Struktur zu zerstören.

Die Resultate in diesen Szenarien zeigen, dass eine von Mach´schen Kegeln induzierte Doppel-Peak-Struktur nur zum Vorschein kommt, wenn eine radiale Expansion existiert. Dies wurde schon in vorigen Überlegungen und Rechnungen gezeigt [30,50,51]. Das naive Bild, dass nur die Flügel des Mach´schen Kegels eine Doppel-Peak-Struktur erzeugen, wird von unseren Rechnungen nicht unterstützt. Der Beitrag von abgelenkten und deformierten Mach´schen Kegeln zu einer Doppel-Peak-Struktur ist größer, wobei diese aus dem *Head Shock* und *Diffusion Wake* stammt. Obwohl fluktuierende Anfangsbedienungen in Schwerionenkollisionen einen sehr starken Beitrag zur Doppel-Peak-Struktur in Zwei-Teilchen Korrelationen zu liefern scheinen [15, 31, 32], ist der aus der Wechselwirkung von Jet und Medium resultierende Beitrag nicht zu vernachlässigen. Mach´sche Kegel scheinen in Schwerionenkollisionen zu existieren. Jedoch ist die Doppel-Peak-Struktur nicht die beste Observable für Mach´sche Kegel in Schwerionenkollisionen.

1. Overview

1.1. This work

In this work the main emphasis is put on the investigation of relativistic shock waves and Mach cones in hot and dense matter using the microscopic transport model BAMPS (**B**oltzmann **A**pproach To **M**ulti-**P**arton **S**cattering), based on the relativistic Boltzmann equation (rBE). Using this kinetic approach we study the complete transition from ideal-fluid behavior to free streaming. This includes shock-wave formation in a simplified $(1+1)$-dimensional setup as well as the investigation of Mach-cone formation induced by supersonic projectiles and/or jets in $(2+1)$- and $(3+1)$-dimensional static and expanding systems. We further address the question whether jet-medium interactions inducing Mach cones can contribute to a double-peak structure observed in two-particle correlations in heavy-ion collision experiments. Furthermore, BAMPS is used as a benchmark to compare kinetic theory to several relativistic hydrodynamic theories in order to verify their accuracy and to find their limitations. This work is based on the publications $[33, 34, 35, 36, 37, 38]$.

1.2. Abstract

We solve numerically the relativistic Riemann problem (rRP) in viscous matter employing the microscopic transport model BAMPS. We demonstrate the transition from ideal to viscous shock waves by varying the shear viscosity over entropy density ratio, η/s, from zero to infinity. With increasing viscosity the sharp and discontinuous characteristic structures are smoothened out. The shock waves need a certain time to develop and a scaling behavior is found, which can be expressed in terms of the Knudsen number, Kn. We show that an η/s ratio larger than 0.2 prevents the development of well-defined shock waves on timescales typical for ultrarelativistic heavy-ion collisions. In addition, we solve the rRP by including inelastic processes in BAMPS. Furthermore, we extend our discussion by solving the rRP for a gas of massive particles and to a system of more than one component.

We compare the numerical solutions of the rBE solved by the microscopic transport model BAMPS to the solutions of the Israel-Stewart (IS) theory. Comparisons between these two approaches clarify and point out the regime of validity of second-order hydrodynamics to describe relativistic shock phenomena. We find that a good agreement for several observables between these two approaches requires a Knudsen number of $Kn_e < 1/2$. However, it is shown that the IS theory cannot reproduce phenomena associated with heat flow. This failure is resolved by the recently derived theory RTRFD (Resummed Transient Relativistic Fluid Dynamics) by comparing the numerical solutions to the rBE in scenarios with large pressure and fugacity gradients.

The microscopic transport model BAMPS is also employed to investigate the shock-front region in its rest frame. A detailed study indicates that the shock-front width is proportional to a microscopic length scale. We use the numerical solutions of BAMPS to compare relativistic kinetic theory to the solutions of relativistic dissipative hydrodynamics. We find limitations of relativistic dissipative hydrodynamics when describing the shock-front region for large propagation speeds of the shock front.

Using BAMPS we extend the investigation on the evolution of conical structures originating from a supersonic projectile or source moving through a hot gas of ultra-relativistic particles. Using different scenarios for the interaction between source and matter and different transport properties of matter, we study the formation and the structure of Mach cones in a simplified $(2+1)$-dimensional static system. In particular, a dependence of the Mach-cone angle on the details and rate of the energy deposition from projectile to matter is investigated. Similarly to the shock waves in one dimension a scaling behavior is found. Furthermore, the two-particle correlations extracted from the numerical calculations are compared to an analytical approximation. We find that the propagation of a highly energetic particle through matter does not lead to the appearance of a double-peak structure as observed in ultrarelativistic heavy-ion collision experiments. The reason is the strongly forward-peaked energy and momentum deposition in the head-shock region, which overshadows the contribution from the Mach cone wings. In addition, we investigate the influence of the viscosity to the structure of Mach cones by adjusting the cross section. A clear and unavoidable smearing of the profile depending on a nonzero ratio of the shear viscosity to entropy density is clearly visible.

The formation of Mach cones are also studied in a full $(3+1)$-dimensional setup of ultrarelativistic heavy-ion collisions. For smooth initial conditions and central collisions the jet-medium interaction is studied using highly-energetic jets and various values of the shear viscosity over entropy density ratio, η/s, of the matter. For small viscosities, the formation of Mach cones is visible, while for large viscosities characteristic structures smear out and eventually vanish. The extracted azimuthal two-particle correlation show a double-peak structure if, in a single event, the jet propagates in the direction opposite to the radial flow. This implies that the contribution from the head shock and from the diffusion wake is superimposed by the radial flow and the contribution of the Mach-cone wings can show up. Considering the superposition of many different jet paths, a double-peak structure also appears. The double-peak structure then originates mostly from a superposition of deflected jet-induced Mach cones with the contribution originating from head shock and diffusion wake. Increasing the value of η/s tends to destroy the double-peak structure for any possible scenario.

1.3. The road map

In Chapter 2, we provide a general introduction to the field of heavy-ion collisions and discuss the observables motivating the existence of (conical) shock-wave phenomena. In Chapter 3, we introduce the general framework of kinetic theory and relativistic hydrodynamics in order to provide the framework for the discussion of the phenomena discussed in this work. We continue in Chapter 4 with the basic definitions of sound

waves, shock waves, and Mach cones. We further give a theoretical description of shock discontinuities in perfect fluids. In Chapter 5 we subsequently introduce the rRP, which deals with the formation of shock waves originating from sharp discontinuities in velocity or thermodynamic variables. An analytical solution for a perfect fluid and a simple equation of state (EoS) is derived. The kinetic transport model BAMPS is thoroughly introduced in Chapter 6. We put the main emphasis on the capability of solving the rBE in an accurate way and on the extraction of hydrodynamic quantities. Chapter 7 provides the baseline for studies of shock waves. We discuss the transition from ideal to viscous shock waves in various setups using BAMPS and vSHASTA and demonstrate the range of applicability of the IS theory and RTRFD. In Chapter 8 we discuss the evolution of shock-wave phenomena in form of Mach cones and the corresponding two-particle correlations using several implementation of the projectile-matter interaction in a static system. Finally, the influence of radial flow on the formation and evolution of highly energetic jets in ultrarelativistic heavy-ion collisions and the extracted two-particle correlations are inspected. The summary and main conclusions of this work are provided in Chapter 9.

2. Introduction

The origin of the universe, the origin of life, and the emergence of consciousness are probably the three most interesting current research areas. The emergence of consciousness is today a large part of brain research, while the emergence of life and the development of various species belong to the field of evolutionary biology [1, 2, 3]. The question of the origin of the Universe is an area of current modern physics. We believe that all the matter and radiation as well as space and time were formed during the Big Bang which is believed to have occurred 13.7 billion years ago. The search for the fundamental properties of matter created during the Big Bang is one of the greatest challenges in modern physics and in the history of mankind.

Today we assume that there are four fundamental interactions of nature. These are the strong, the weak, the electromagnetic, and the gravitational interaction. For the strong, the weak, and the electromagnetic, quantum-field theoretical descriptions have been developed. These theories constitute the Standard Model of elementary particles [4, 5, 6]. The gravitational theory is described by the theory of general relativity [52] and is actually not incorporated into the Standard Model. Up to now the Standard Model of elementary particles includes six quarks, six leptons, four gauge bosons, and the Higgs boson. The Standard model is complete, but not applicable above a certain energy scale, where a more fundamental theory is valid. In this sense, the Standard model is an effective theory.

2.1. Quantum Chromodynamics

The strong interaction is described by the non-abelian gauge theory of Quantum Chromodynamics (QCD) which is invariant under SU(3) gauge transformations [53, 54, 55]. The SU(3) group transforms the *color* charge analogously to the electric charge in Quantum Electrodynamics (QED), which is represented by the symmetry group U(1). In contrast to QED which has only one charge the color charge in QCD can take three different values, N_c, [53, 54]. These values are referred to as *red*, *blue*, and *green*. The mediator of the strong interaction are gluons which hence play a similar role as photons in QED. In contrast to photons, however, gluons can interact with each other, which makes QCD a non-abelian quantum field theory. The gluons are spin-1 vector bosons. The number of these force carriers is $N_c = 3^2 - 1 = 8$, which corresponds to the octet representation[1] of SU(3).

Quarks are particles which carry fundamental color charge. They are spin-1/2 fermions which are to the best of our knowledge particles without any substructure and therefore called elementary particles. Up to now six flavors of quarks have been identified experimentally. These flavors are called *up*, *down*, *strange*, *charm*, *bottom*,

---

[1]In general, an SU(N) gauge theory has $N^2 - 1$ gauge fields.

and *top*. The up and down quarks are also called light quarks because their masses are small $\sim 2 - 6$ MeV. In contrast, the strange, charm, bottom, and top quarks have much larger masses. The quarks also carry electric charge: the up, charm, and top have an electric charge of $+(2/3)e$, while the down, strange, and bottom quarks have an electric charge of $-(1/3)e$.

The theory of QCD allows for a strict mathematical description in terms of its Lagrangian [53,54],

$$\mathcal{L}_{QCD} = i\sum_q \bar{\psi}_q^k \gamma^\mu \left(D_\mu\right)_{kl} \psi_q^l - \frac{1}{4} F_{\mu\nu}^a F^{a,\mu\nu} - \sum_q m_q \bar{\psi}_q^k \psi_{q,k} \qquad (2.1)$$

where ψ_q^k is the color component k ($k = 1, \cdots, N_c = 3$) of the quark field of flavor q and mass m_q. We identify also the field strength tensor,

$$F_{\mu\nu}^a = \partial_\mu A_\nu^a - \partial_\nu A_\mu^a - g_s f_{abc} A_\mu^b A_\nu^c \,, \qquad (2.2)$$

which is given by the gluon fields A_μ^a ($a = 1, \cdots, N_c$) and the structure constants of SU(3), f_{abc}. The non-abelian nature of QCD is reflected by the last term in the field strength tensor. This part describes the coupling of gluons to each other. $\left(D_\mu\right)_{kl} = \delta_{kl}\partial_\mu - ig_s \sum_a T_{kl}^a A_\mu^a$ is the covariant derivative and the T^a are the eight generators of SU(3).

We now introduce the two most important features of QCD, which are *confinement* and *asymptotic freedom*.

- *confinement* reflects the experimental observation that there are no isolated quarks or gluons, i.e., color particles cannot exist in an asymptotic state. Therefore, quarks form always colorless objects which are known as hadrons. Hadrons exist in different forms, namely mesons, baryons, and antibaryons. The most familiar ones are the proton, p, and the pion, π. All hadrons are bound states of quarks and antiquarks. Thereby, (anti-)baryons consist of three valence (anti-)quarks and thus are fermions, while mesons consist of quark-anti-quark pairs and thus are bosons. However, recent measurements also indicate the existence of four-quark states [56]. Further interesting colorless objects are glueballs, which have not been manifested experimentally yet [57,58].

  The best way to illustrate confinement is considering the following simplified potential between the most simple colorless object, a quark-anti-quark pair. This potential can be parametrized as

  $$V(r) = -\frac{4}{3}\frac{\alpha_s(Q^2)}{r} + kr \,. \qquad (2.3)$$

  with $k \in \mathbb{R}^+$ and $\alpha_s(Q^2) = g_s(Q^2)/4\pi$ being the strong coupling constant of QCD at a given momentum transfer, Q, or energy scale, while $g_s(Q^2)$ denotes the coupling. The first part in Eq. (2.3) denotes the Coulomb-like potential while the second is the confining part. If we try to separate the quark-anti-quark pair, i.e., if we increase the distance r between quark and anti-quark, the potential energy grows because of the second part in Eq. (2.3) [59]. As soon as the

potential energy increases beyond twice the rest mass of the quark-anti-quark, a new quark-anti-quark pair will suddenly be created, which implies that color is always confined.

- *asymptotic freedom* is a property of QCD which affects that the interaction between quarks and gluons become very weak for large momentum transfer Q, i.e., large energy scales [60,61]. In other words, quarks behave as almost free particles at large energy scales and are thus not bound inside hadrons anymore.

The existence of confinement and asymptotic freedom as well as the energy dependence of the strong coupling constant has been explored in a large variety of experiments. Figure 2.1 illustrates the decrease in $\alpha_s(Q)$ for large Q. This figure qualitatively demonstrates the concept of confinement and asymptotic freedom.
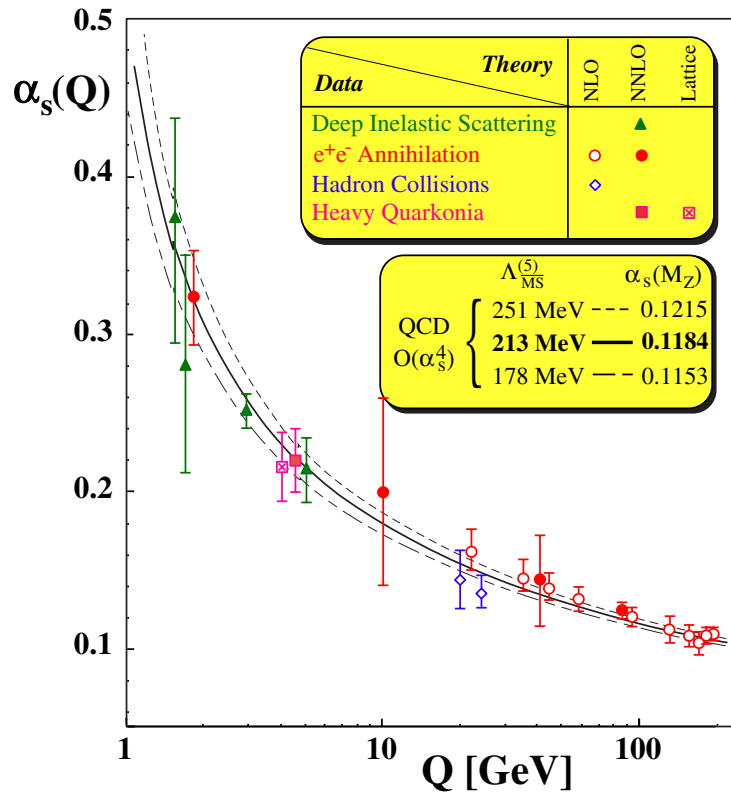
Figure 2.1.: The strong coupling constant, $\alpha_s(Q)$, at various energy scales, Q, extracted from different experimental measurements. The picture has been taken from Ref. [62].

The remarkable feature of asymptotic freedom suggests that at high energy densities and temperatures a new phase of matter, namely the Quark-Gluon Plasma (QGP), exists [7,8,9]. The QGP is believed to have existed in nature in the very early stage of the universe, a few microseconds after the Big Bang, where the energy densities and temperatures were extremely high. Such a phase of matter is further assumed to occur in the core of a neutron star where the nuclear density is several times large than for normal nuclear matter of protons and neutrons.

One of the greatest challenges in physics is to explore the QGP in a controlled experimental environment. This goal has been achieved with of ultrarelativistic heavy-ion collision (HIC) experiments which are supposed to reach conditions similar to those shortly after the Big Bang.

2.2. Ultrarelativistic heavy-ion collisions

Today the best way to explore the properties of nuclear matter is the collision of ultrarelativistic heavy ions using modern accelerators. Using sufficiently large collision energies it is possible to reach energy densities in the system, which are much larger than $e \approx 1$ GeV/fm^3. This offers the possibility to reach the state of a deconfined phase of quarks and gluons.

The era of experimental research of heavy-ion collisions has started in the mid-70s at the BEVALAC at the *Lawrence Berkeley National Laboratory* (LBNL). The BEVALAC studied excited and compressed hadronic matter at center of mass energies of 2 GeV per nucleon pair [63]. However, the energy was too small in order to reach a state of deconfined quarks and gluons as predicted by QCD. In the following years, the *Alternating Gradient Synchroton* (AGS) at the *Brookhaven National Laboratory* (BNL) and the *Super Proton Synchroton* (SPS) at the *Conseil Europeén pour la Recherche Nucléaire* (CERN) have been constructed and provided the possibility to accelerate heavy ions to ultrarelativistic energies, i.e., energies much larger than the rest mass of the constituents, for the first time. For heavy-ion experiments the AGS and the SPS have provided center of mass energies up to $\sqrt{s} = 11.5$ A GeV and $\sqrt{s} = 17.3$ A GeV, respectively.

The results obtained at fixed-target experiments at SPS signalized already the onset of a deconfined phase [64, 65]. However, clear results and the systematic investigation of the QGP became possible for the first time when the *Relativistic Heavy-Ion Collider* (RHIC) at BNL was put into operation in 2000. RHIC also was the first dedicated heavy-ion accelerator built as a collider and provided center of mass energies of up to $\sqrt{s_{NN}} = 200$ A GeV for Au + Au collisions. At RHIC, there were four experiments, BRAHMS, PHENIX, PHOBOS, and STAR, which indicated that a new phase of matter had been produced and that this phase behaves like a nearly-perfect fluid with a variety of remarkable properties [7, 10, 66, 67, 68, 69, 70, 71, 72, 73]. The major results of all experiments at RHIC have been published in so called *white papers* [25, 26, 27, 28]. Up to now, the major experiments, STAR and PHENIX, are still in operation.

Finally, the *Large Hadron Collider* (LHC) at CERN became operational in 2010. Today it is the largest and most powerful colliding facility which is also designed to find experimental evidence for the existence of the Higgs boson[2] [74]. The first heavy-ion measurements with Pb + Pb have been started in the end of 2011. Initially the LHC has reached a center of mass energy of $\sqrt{s_{NN}} = 2.76$ A TeV, but in the near future, it will reach its maximum center of mass energy of $\sqrt{s_{NN}} = 5.5$ A TeV. The experiments at the LHC are ALICE, ATLAS, CMS, and LHCb, while only ALICE is exclusively

---

[2]The Higgs boson is a spin-0 elementary particle predicted by the Standard model. The existence of the Higgs boson would confirm the existence of the Higgs field which gives an explanation why some fundamental particles have masses.

designed for heavy-ion collisions. The other experiments are almost solely used to find
the Higgs boson. So far, the results obtained at RHIC have been confirmed by the
measurements performed at the LHC [75, 76, 77, 78]. The *Facility for Antiproton and
Ion Research* (FAIR) adjacent to the *Gesellschaft für Schwerionenforschung* (GSI) is
a fixed-target experiment, which will start its HIC program in the near future[3]. The
CBM experiment at FAIR project will study the QCD phase diagram of nuclear matter
in a different regime with larger baryochemical potential.

The results at RHIC and LHC indeed imply that a hot and dense state of matter,
which is definitely not a hadronic gas of matter, is created in heavy-ion collisions.
However, the exact properties of this new phase of matter is far away from being
determined, even today, and demands a deep investigation in high-energy nuclear-
physics.

2.3. The phase diagram of QCD
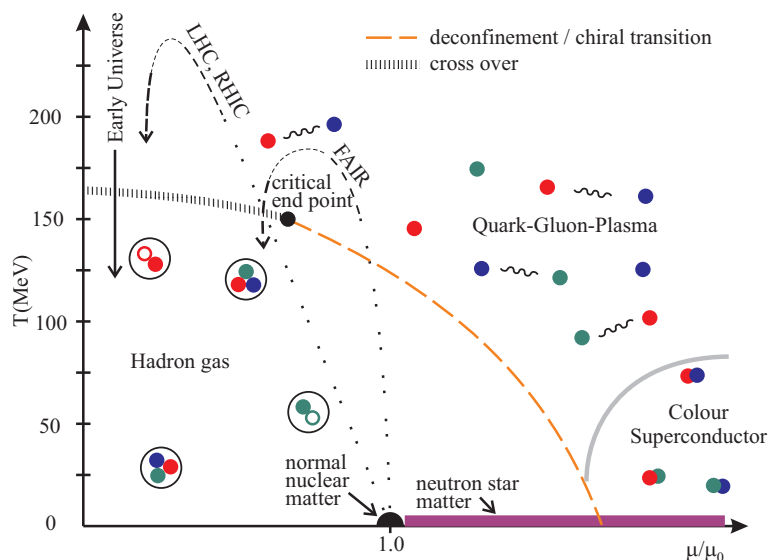
Figure 2.2.: Schematic presentation of the QCD phase diagram in terms of the temper-
ature, T, and baryochemical potential, μ. The baryochemical potential is
normalized to the one of the ground state of normal nuclear matter, μ_0.
The phase transition from the hadron gas to the QGP is assumed be of first
order at high μ and low T, which ends in a critical point of second order
and continues with a crossover afterwards. For very large baryochemical
potential a color-superconducting phase is assumed. In addition, the re-
gions assumed to be investigated by recent and future experiments are also
shown. The picture has been taken from Ref. [50].

Above we have introduced the two most important properties of QCD, which sug-
gest that nuclear matter could exist in different phases. Different phases also imply

---

[3]FAIR is planned to be operational in 2018.

that there must be a phase transition or crossover between the hadronic and deconfined phase, which may depend on several thermodynamic variables. In Fig. 2.2, we illustrate the different phases of QCD matter in terms of thermodynamic variables like the temperature, T, and the baryochemical potential, μ. The knowledge of the QCD phase diagram is rare, except for the region around $T \approx 0$ MeV and $\mu_0 \approx 924$ MeV describing the ground state of nuclear matter with a baryon density of $\rho_0 \approx 0.17$ fm^{-3} representing normal nuclear matter. The main purpose of modern physics is to obtain more information of the other different phases of QCD matter. HIC experiments are up to now the best way to explore several regions of the QCD phase diagram.

As shown in Fig. 2.2, nuclear matter forms hadrons for small temperature, T, and small baryochemical potential, μ, while for large temperatures a deconfined phase of quarks and gluons is assumed. At low T and high μ there is a phase transition, which is assumed to be of *first order* ending in a critical point of *second order* and continuing with a *crossover* [79, 80]. For very large baryochemical potential, a color-superconducting region with a various numbers of distinct phases is proposed [66,81,82].
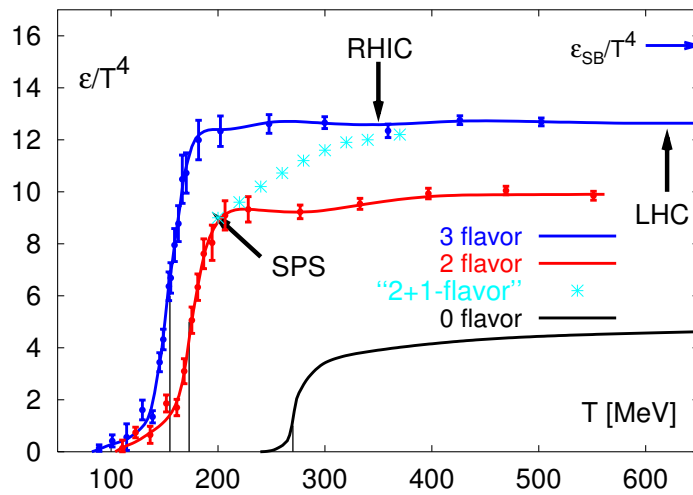
Figure 2.3.: The energy density scaled by T^{-4} as a function of temperature extracted from lattice QCD calculations. The results are shown for different numbers of flavors. In addition, the estimated temperatures reached in recent and former accelerators are shown by arrows. The figure has been taken from Ref. [72].

A derivation of the properties of nuclear matter in thermodynamic equilibrium from the QCD Lagrangian (2.1) is definitely possible, but several problems have to be taken into account. While the deconfined phase can be studied via perturbative QCD (pQCD), the confined phase and the phase transition belong to the non-perturbative region. The complexity arising from many interacting particles with different masses in different regimes of temperature and chemical potential is an almost impossible task and can only be accomplished numerically with a lot of restrictions [66]. This is realized via lattice QCD which is the most fundamental approach in order to solve non-perturbative QCD problems from first principles [83, 84]. However, solving QCD

on a lattice is technically challenging and strongly limited by computational resources.

Calculations on the lattice with vanishing baryochemical potential and including quark degrees of freedom have been performed [85, 86, 87, 88, 89, 90]. Furthermore, calculations with non-vanishing baryochemical potential, which are basically more difficult to handle due to mathematical and technical reasons, require further improvements [91, 92, 93, 94, 95].

Current lattice-QCD calculations predict a crossover for vanishing baryochemical potential around $T_c \approx 175$ MeV. Around this temperature region, the energy density and pressure increases more rapidly, but smoothly and continuously, which indicates a crossover phase transition from a gas of hadrons to a strongly coupled plasma of quarks and gluons. This is illustrated in Fig. 2.3 for different numbers of flavors. As a matter of fact, the Stefan-Boltzmann limit is not reached.

Although lattice-QCD calculations provide great insights into QCD matter in the non-perturbative regime, the application of this method is strongly limited. In order to obtain a better understanding of the phase diagram at non-zero temperature and baryochemical potentials, heavy-ion collisions and effective theoretical tools describing the QGP phase are necessary.

2.4. Signatures for the QGP
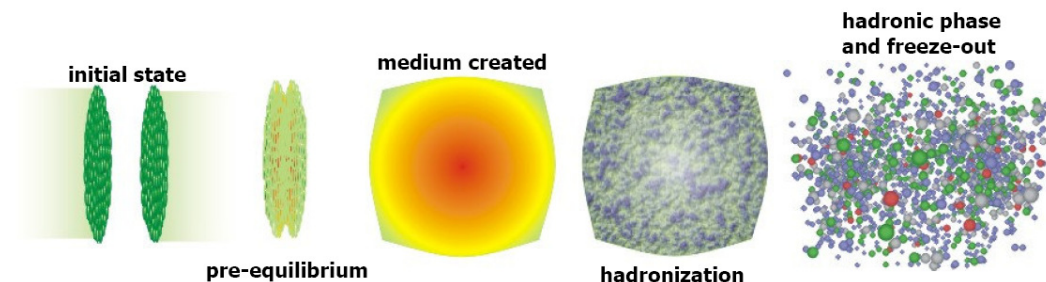
Figure 2.4.: Different stages of a heavy-ion collision. The Figure has been taken from Ref. [50].

Determining the properties of the QGP and even proving that such a state is created is a great challenge, since we have not directly access to this stage. The only stage experiments can access directly are the collision fragments in form of hadrons.

A heavy-ion collision is assumed to feature different stages shown in Fig. 2.4. First of all, heavy nuclei are accelerated to ultrarelativistic velocities of almost the speed of light. At this velocity the nuclei are Lorentz-contracted in the center of mass system of the collision. At the moment when the nuclei collide with each other, the matter gets strongly compressed indicating the *pre-equilibrium phase*. Insofar the collision energy is sufficiently large, a state of deconfined quarks and gluons is being formed. This strongly coupled QGP is possible to maintain thermal and chemical equilibrium throughout its short lifetime[4] of $\Delta t \sim 5 - 10$ fm/c. While the fireball expands and

---

[4]The lifetime depends strongly on the collision energy.

cools down, it will reach the critical temperature, T_c, at which matter locally undergoes a phase transition or crossover leading to the formation of hadrons. In this hadronic phase, matter interacts further via elastic and inelastic collisions until *chemical freeze-out* is reached. The system becomes more and more dilute and reaches finally the *kinetic freeze-out*. The outgoing hadrons and their decay products[5], respectively, reach the detectors.

From this point the identification of the final particles and their momenta has to be performed in order to reconstruct the collision process. The only possibility to prove the existence and to obtain the properties of the QGP is to analyze the particle distribution of the final hadrons and to compare them with predictions originating from theoretical models assuming the creation of the deconfined phase of matter.

An overview for the most important signatures indicating the existence of the QGP can be found in Ref. [96], the *white papers* of the experiments at RHIC [25, 26, 27, 28] and recent measurements at LHC [75, 76, 77, 78]. The most important signatures can be summarized as follows:

- early thermalization and strong collective flow, indicating an almost perfect fluid with a small shear viscosity over entropy density ratio, η/s,

- suppression of high-p_T particles indicating the creation of a hot, dense, and opaque state of matter.

We will review these signatures, since they are relevant for this work.

2.4.1. Collective flow
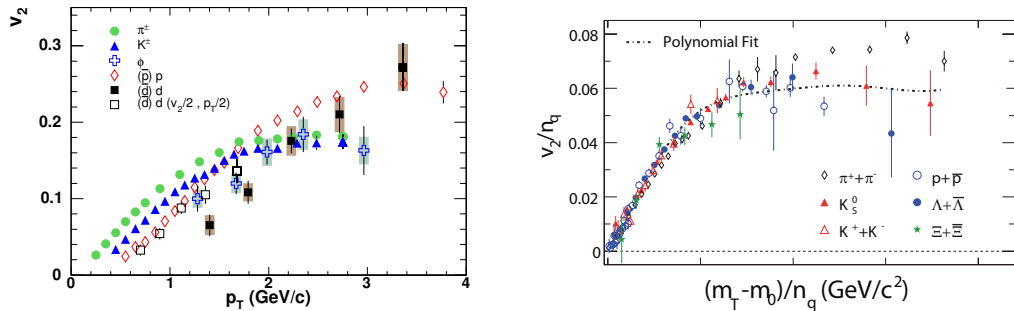
(a) Elliptic flow of identified hadrons as a function of transverse momentum, $v_2(p_T)$. Results are shown for $20 - 60\%$ central Au + Au collisions at RHIC as measured by PHENIX. The figure has been taken from Ref. [97].

(b) Elliptic flow from minimum-bias Au + Au collisions at 62.4 A GeV scaled by the number of valence quarks at RHIC as measured by STAR. The figure has been taken from Ref. [98].

Figure 2.5.: Elliptic flow of identified hadrons measured at RHIC.

The most crucial behavior of the new phase of matter created in heavy-ion collisions at RHIC and LHC is the unexpectedly strong collective flow pattern. The initial

---

[5]Some hadrons are unstable and decay after the collision.

spatial anisotropy in non-central collisions is translated into strong pressure gradients, while the strength of the translation depends on the interaction strength between the constituents of the collision. For a non-interacting gas, the spatial anisotropy would persist, while for an almost perfect fluid, a strong momentum anisotropy in the particle spectra would be observed. This momentum anisotropy can be quantified in terms of the expansion coefficients of the Fourier decomposition of the azimuthal dependence of the particle distribution [99, 100],

$$\frac{\mathrm{d}N}{p_T \mathrm{d}p_T \mathrm{d}y \mathrm{d}\phi} = \frac{1}{2\pi} \frac{\mathrm{d}N}{p_T \mathrm{d}p_T \mathrm{d}y} \left(1 + 2 \sum_{n=1}^{\infty} v_n(p_T) \cos\left[n\left(\phi - \psi_R\right)\right]\right). \qquad (2.4)$$

Here ϕ is the azimuthal angle in the transverse momentum space and v_n is referred to as the n-th order coefficient of the Fourier decomposition. The decomposition is done with respect to the reaction plane with the angle Ψ_R [25, 27].

The second coefficient of the Fourier transformation, v_2, is often referred to as the *elliptic flow*, which is the largest contribution and one of the most famous observables in the heavy-ion community. In Fig. 2.5a, we show the differential elliptic flow of identified hadrons as measured at PHENIX, which clearly demonstrates that a large elliptic flow builds up in heavy-ion collisions. The fact that most of the elliptic flow emerges during the partonic[6] phase can be inferred from Fig. 2.5b which shows the scaling of v_2 with the number of valence quarks [102, 103].

(a) Ideal and viscous hydrodynamic calculations for the differential elliptic flow, $v_2(p_T)$, compared to STAR data for charged particles.

(b) Ideal and viscous hydrodynamic calculations for the integrated elliptic flow, v_2, with respect to centrality compared to PHENIX data for charged particles. The larger the number of participants, N_{part}, the more central the collision is.

Figure 2.6.: Ideal and viscous hydrodynamic calculations compared to RHIC data for Au + Au collisions at $\sqrt{s_{NN}} = 200$ A GeV for differential and integrated elliptic flow. Both figures are taken from Ref. [10].

The large measured elliptic flow coefficient, v_2, indicates that the QGP created at RHIC and LHC could even be a perfect fluid. This was shown by comparing the ex-

---

[6]Quarks and gluons are also referred to as partons, a notation first introduced by R. P. Feynman [101].

perimental data with ideal hydrodynamic calculations in Ref. [104]. Consequently, the QGP was reported to be the most perfect fluid ever observed in nature [67]. However, a perfect fluid with full thermalization is rather unrealistic and the agreement of the calculations of v_2 with the experimental data strongly depends on the choice of the initial conditions, the hadronization process, and the equation of state (EoS), which all are uncertain. Furthermore, another uncertainty, the choice of transport coefficients such as shear viscosity, η, or bulk viscosity, ζ, comes into play. In nature the viscous transport coefficients cannot vanish but must have lower bounds [18, 19, 20], such that a perfect fluid cannot exist by definition.

It has been confirmed later that nonzero dissipation has to be taken into account in order to obtain a qualitatively better agreement with the experimental data leading to the frequent application of viscous hydrodynamics. In particular, Fig. 2.6a shows the differential elliptic flow, $v_2(p_T)$, while Fig. 2.6b shows the integrated v_2 with respect to the centrality. Both quantities have been measured at RHIC. As an overlay, hydrodynamical calculations with different values for the shear viscosity over entropy density ratio, η/s, are shown. Both figures demonstrate that ideal hydrodynamics with vanishing η/s overestimates the elliptic flow. On the other side, a nonzero value for η/s suppresses the large elliptic flow and improves the agreement with the experimental data. The value for η/s still has to be sufficiently small in order to be in reasonable agreement with the experimental data. This definitely supports the assumption of an almost perfect-fluid behavior and indicates a rapid and early thermalization. Since then, a variety of investigations about the viscosity of the QGP has been performed using dissipative hydrodynamics [10, 11, 12, 13, 14, 15] and microscopic transport theory with pQCD-based elastic and inelastic scattering processes [105, 106]. Furthermore, the extraction of the shear viscosity coefficient became very popular [16]. However, recent calculations indicate that the ratio of the shear viscosity coefficient over entropy density, η/s, is not constant but features a dependence in temperature [17].

Although the application of viscous hydrodynamics became very successful in recent HIC, there are still open questions. Besides the uncertainties in the choice of the initial conditions, hadronization, EoS, and transport coefficients, the theory of dissipative hydrodynamics is not complete yet. In heavy-ion collisions at ultrarelativistic energies the system expands very fast and gradients in matter are very large. It is still an open question to what extent hydrodynamics is applicable in describing the dynamics of such a system. Hydrodynamics is an effective theory that describes the macroscopic evolution of the system close to thermal equilibrium. Its applicability requires that either the viscosity or the gradients or both quantities are small. On the other hand, microscopic transport models can be used for systems which are also strongly out of thermal equilibrium. Therefore, a comparison between the microscopic approach and hydrodynamics can provide the limits and accuracy of the hydrodynamical description. This has been established in Ref. [45, 107] for the Bjorken scaling solution [21]. Such a comparison is also provided in this work using shock-wave scenarios and is discussed in detail in the subsequent chapters.

2.4.2. Hard probes and jet quenching

In the very early stage of the collision the constituents of the nucleons, the partons, can undergo hard collisions producing highly-energetic real partons which are back-to-back created, which simply follows from energy-momentum conservation. These partons evolve as parton showers, and are often referred to as *jets* or *hard probes*. They will finally hadronize before detected in experiments as back-to-back di-jet events. In case a hot and dense medium is created, parts of the jet will traverse this medium, interact strongly with the soft medium particles (low p_T) and loose energy. This phenomenon is known as *jet quenching* and would serve as a good probe to investigate the properties of the QGP created in heavy-ion collisions, as is has been theoretically predicted [21, 22, 23, 24]. However, the exact mechanism of the jet quenching is still to be fully understood.

A full jet reconstruction would help to get a more detailed understanding of the mechanisms taken place when jets traverse the medium. This has been done in experiments at the LHC, and methods to reconstruct jets have been developed or are still under development [108, 109, 110]. However, at the RHIC a full jet reconstruction was almost impossible due to the huge background contribution. The most promising methods in order to quantify the energy loss of jets are measurements of the nuclear modification factor and two- or three-particle correlations, which we present in the following.

Nuclear modification factor R_{AA}

As mentioned above, if a hot and dense matter like the QGP is created, jets with high transverse momentum, p_T, traversing the medium may interact strongly with the medium particles and loose energy. In heavy-ion collisions at RHIC and also recently at the LHC the suppression of jets with respect to the scaled p + p collision is found. This can be quantified in terms of the nuclear modification factor

$$R_{AA} = \frac{\mathrm{d}^2 N_{AA}/\mathrm{d}y\,\mathrm{d}p_T}{T_{AA}\,\mathrm{d}^2\sigma_{NN}/\mathrm{d}y\,\mathrm{d}p_T}\,, \tag{2.5}$$

where $T_{AA} = N_{\mathrm{coll}}/\sigma_{NN}$ is the nuclear overlap function, N_{coll} denotes the number of binary collisions in nucleus-nucleus collisions and σ_{NN} is the nucleon-nucleon cross section [48]. The nuclear modification factor, R_{AA}, is the ratio of the yield in a heavy-ion collision to the corresponding yield in a proton-proton collision, where the latter one is rescaled by the number of binary scatterings. Thus, if a jet in a heavy-ion collision undergoes jet quenching, R_{AA} will decrease indicating that in comparison to a p + p collision a hot and dense matter is created. Thus, the fact that $R_{AA} < 1$ in heavy-ion collisions is a strong signature for the creation of the QGP.

Figure 2.7 represents the nuclear modification factor for several identified hadrons in a central Au + Au collisions with $\sqrt{s_{NN}} = 200$ A GeV at RHIC as measured by PHENIX. A strong suppression is observed for most hadrons, which reflects the energy loss of the partons before fragmenting to hadrons. In contrast, $R_{AA} \sim 1$ for photons at $p_T \geq 5$ GeV, since photons do not interact strongly with the partonic medium.
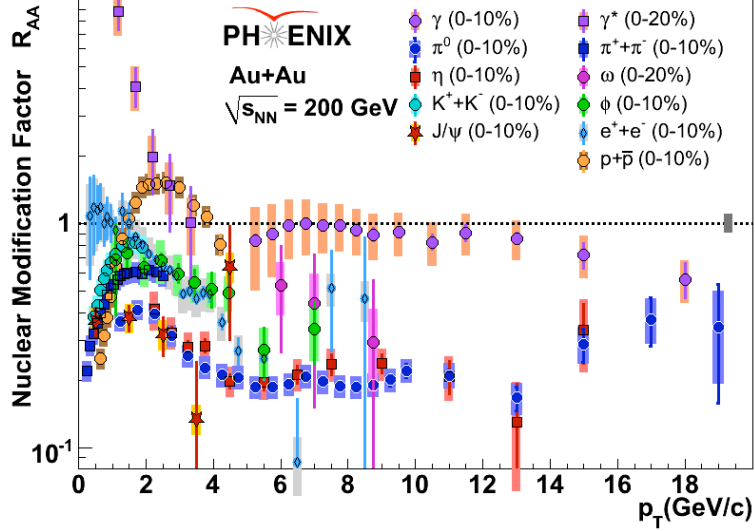
Figure 2.7.: Compilation of the nuclear modification factor R_{AA} for various identified hadrons and direct photons for central Au + Au collisions at 200 A GeV as measured by PHENIX. The figure has been taken from Ref. [111].

Two-particle correlations

As mentioned above, in the initial phase of proton-proton or heavy-ion collisions jets with high transverse momentum, p_T, are always created back-to-back as sketched in Fig. 2.8. In p + p collisions, it is expected that both jets can be measured by so called *two-particle correlations* of final hadrons, since no medium is created and accordingly no suppression occurs. This might change in heavy-ion collisions. If these jets are created at the edge of a heavy-ion collision region, one jet (*trigger particle*) propagates outside of the collision area almost without any further interaction, while the other one (*associated particle*), separated from the trigger particle by an angle of π in the azimuthal plane, traverses the hot and dense collision region and possibly is suppressed. This has been measured experimentally [25, 26, 27, 28] and indicates the existence of the QGP.

In experiment, the two-particle correlations are determined by selecting the trigger particle and measuring the azimuthal distribution of the associated particles relative to the trigger particle, i.e., $\Delta\phi = \phi - \phi_{\text{trigger}}$. For both, the trigger and associated particles a specific p_T-range has to be defined.

Figure 2.9a shows the measurements of the STAR experiment on correlations between high p_T-particles in p+p, central d+Au, and central Au+Au collisions. For the trigger particle a range of $4 < p_T^{\text{trig}} < 6$ GeV is chosen, while for the associated particles $p_T^{\text{assoc}} > 2$ GeV is used. Around $\Delta\phi \approx 0$ the enhanced correlation of a single hadron is generated in all measurements, while only in p + p and d + Au an enhanced correlation at $\Delta\phi \approx \pi$ with a broader width than the near-side peak has been found. For Au + Au collisions the correlation on the away side is missing, which demonstrates the quenching of the corresponding away-side jet.

The interaction of the jet with the medium leads to a strong energy loss of the jet.
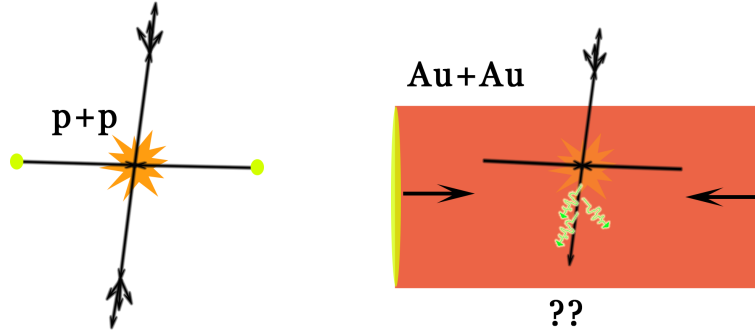
Figure 2.8.: Hard scatterings in p+p collisions produce back-to-back correlated partons, while in heavy-ion collisions at RHIC the jet is modified by the hot and dense collision region.

Since energy and momentum have to be conserved globally, the missing energy must have been distributed in the medium. This is demonstrated in Fig. 2.9b, where the range of p_T for the associated particles has been lowered to $0.15 < p_T^{\mathrm{assoc}} < 4$ GeV. As it must be, the missing fragments around $\Delta\phi \approx \pi$ appear, but surprisingly a double- or even triple-peak structure instead of only one single peak appears.

In Fig. 2.10, we show two-particle correlations from PHENIX as measured in p + p and central Au + Au collisions. Here, several p_T regions for the trigger and associated particles are considered. While for p + p collisions only a peak around $\Delta\phi \approx \pi$ is measured, this is not the case for Au + Au collisions. For $3 < p_T^{\mathrm{trig}} < 4$ GeV and $0.4 < p_T^{\mathrm{assoc}} < 1$ GeV a double-peak structure for the away-side jet is observed. With increasing p_T-range the double-peak structure is visible up to $2 < p_T^{\mathrm{assoc}} < 3$ GeV, while for $3 < p_T^{\mathrm{assoc}} < 4$ GeV, the double-peak structure disappears. For a larger p_T in trigger and associated particles the yield in Au + Au collisions vanishes and no single- or double-peak structures appears.

The appearing double-peak structure in these two-particle correlations led to a big discussion regarding its origin. Initially it was considered that such double-peak structure originated solely from the jet-medium interaction. Other explanations also included Cerenkov gluon radiation [114]. Recently, it was found that initial-state fluctuations can also play a large role in describing this observable [115].

In the following, we list the contributions currently considered to be most important for this observable:

- **Deflected Jets**
  One possible explanation is the deflection of the jet due to its interaction with the soft medium particles [116]. Due to interactions the momenta of the particles change, and its initial propagation direction accordingly changes. Furthermore, an additional possibility for a deflection of the jet might results from the strong radial flow in central and non-central collisions of heavy ions.

- **Mach Cones**
  The observation of the almost perfect-fluid behavior of the QGP also indicated the formation of shock waves in form of Mach cones [29,30]. Mach cones are assumed
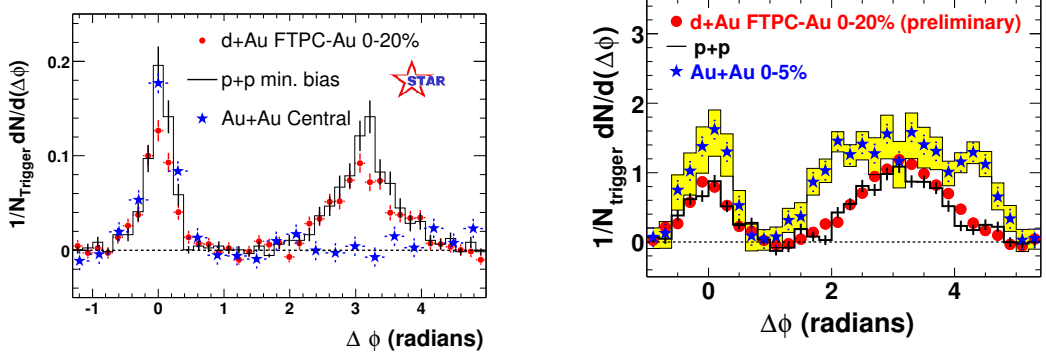
(a) Two-particle correlations for trigger particles of $4 < p_T^{\mathrm{trig}} < 6$ GeV and associated particles with $p_T^{\mathrm{assoc}} > 2$ GeV for p + p, central d + Au, and central Au + Au collisions. The figure has been taken from Ref. [25].

(b) Two-particle correlations for trigger particles of $4 < p_T^{\mathrm{trig}} < 6$ GeV and associated particles with $0.15 < p_T^{\mathrm{assoc}} < 4$ GeV for p + p, central d + Au, and central Au + Au collisions. The shading reflects systematic uncertainties. The figure has been taken from Ref. [112].

Figure 2.9.: Two-particle correlation measurements at STAR.

to be generated by supersonic jets traversing the medium and depositing energy and momentum which results in the formation and propagation of sound and shock waves. The interference of these sound and shock waves form a Mach cone, while the matter on that cone preferably propagates at a certain emission angle α with respect to the propagating jet. Mach cones have been a topic of great interest in the community of heavy-ion physics [51, 114, 117, 118, 119, 120, 121, 122, 123, 124, 125, 126, 127, 128].

The idea of shock-wave phenomena in HIC, however, is not completely new. Shock-wave phenomena such as Mach cones have been already theoretically predicted to occur in collisions of heavy nuclei in the early 1970´s [129, 130], have been experimentally investigated [131] and subsequently observed [132, 133].

The formation of shock waves and the jet-medium interaction inducing Mach cones are the main part of this thesis. This is to be discussed in the subsequent chapters.

- **Initial-state fluctuations**
  For a long time most theoretical studies of heavy-ion collisions were performed using smooth initial conditions [48]. Recently it has been shown that initial fluctuating conditions in the transverse plane, such as hot spots [134, 135], become very important when describing flow observables like triangular flow, v_3, [15, 31, 32]. It has also been argued that these initial-state fluctuations have a large contribution to the double-peak structure measured in multi-particle correlations [115, 135, 136].

Furthermore, three-particle correlations [137, 138] have been measured as an attempt
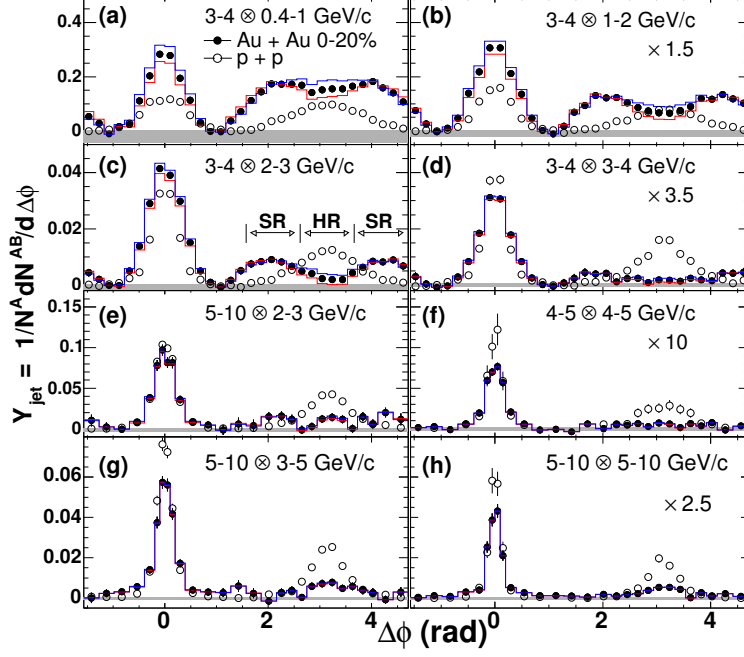
Figure 2.10.: Two-particle correlations from PHENIX in p+p and central Au+Au collisions. Several p_T-ranges for trigger and associated particles are shown. The solid histograms are shaded due to background subtraction uncertainties. The figure has been taken from Ref. [113].

to distinguish between different explanations for the appearing double-peak structure. It was for example shown that Cerenkov gluon radiation [116] could be excluded, while the scenario of the generation of shock waves in form of Mach cones or initial-state fluctuations was supported. Moreover, the measured three-particle correlations could distinguish between Mach-cone signals and random jet deflection [116].

2.5. The purpose of this work

This work is dedicated to the investigation of shock-wave phenomena in hot and dense matter using a microscopic transport model based on the relativistic Boltzmann equation (rBE). The fact that the medium created in such violent collisions of heavy nuclei behaves as an almost perfect fluid is a strong indication for the formation of shock waves. Furthermore, the strong suppression of jets indicated that shock-wave phenomena in form of Mach cones should exist.

Usually, the investigation of shock phenomena or Mach cones in HIC is realized using hydrodynamics with source terms describing the jet-medium interaction [51,119]. However, it is not clear if this modeling is able to fully describe such non-equilibrium phenomena. In the transport model employed in this work, both the jet and the medium are treated within the same formalism. Furthermore, it is able to describe systems with large gradients and in which the viscosity is very large. For both conditions hydrodynamics is expected to fail.

The first part of this work is dedicated to perform the complete transition from ideal to viscous shock waves in a simplified one-dimensional setup. The accurate solution of the rBE serves also as a benchmark to find the accuracy and limitations of different derivations of relativistic viscous hydrodynamics. Next, we continue our studies on the subject of Mach cones. We study the complete transition from ideal to viscous Mach cones in a static system using different scenarios for the jet-medium interaction. We systematically study the influence of the viscosity and energy deposition on the final profile and its two-particle correlations. Finally, we investigate the jet-medium interaction and development of Mach cones in relativistic heavy-ion collisions with nonzero dissipation, which by default includes a radial and longitudinal expansion. In a systematic study we clarify whether a Mach cone in such a scenario can contribute to the signal of a double-peak structure observed in two-particle correlations in the experiments.

2.6. Notation

As long as not indicated otherwise, we are using natural units throughout this work, i.e.,

$$\hbar = c = k_B = 1 \,. \tag{2.6}$$

Here $\hbar$ is the Planck constant divided by 2π, c is the speed of light, and k_B is the Boltzmann constant. Since $c = 1$, time and length have the same dimension. Using natural units as introduced above implies that the units GeV and fm are related to each other as

$$0.197 \,\mathrm{GeV\,fm} = 1 \,. \tag{2.7}$$

During the entire work we use a flat metric. The metric tensor hence reads

$$g^{\mu\nu} = \begin{pmatrix} 1 & 0 & 0 & 0 \\ 0 & -1 & 0 & 0 \\ 0 & 0 & -1 & 0 \\ 0 & 0 & 0 & -1 \end{pmatrix} \,. \tag{2.8}$$

Quantities featuring an arrow on top are traditional three-dimensional vectors

$$\vec{a} = \begin{pmatrix} a^1 \\ a^2 \\ a^3 \end{pmatrix} = (a^1, a^2, a^3)^T \,. \tag{2.9}$$

The superscript T indicates that the vector is to be transposed. Covariant b_μ and contravariant vectors b^μ are denoted as

$$
\begin{aligned}
b^\mu &= \begin{pmatrix} b^0 \\ \vec{b} \end{pmatrix} = (b^0, \vec{b})^T \,, \\
b_\mu &= \begin{pmatrix} b^0 \\ -\vec{b} \end{pmatrix} = (b^0, -\vec{b})^T \,,
\end{aligned}
\tag{2.10}
$$

with the greek index running from 0 to 3. Quantities with two or more greek indices we refer to as tensors. Quantities without indices are scalars. We are using the Einstein summation convention that indices appearing twice are summed over, i.e.,

$$b^\mu g_{\mu\nu} b^\mu = b_\mu b^\mu = \sum_{\mu=0}^{3} b_\mu b^\mu \, . \tag{2.11}$$

In order to improve the readability of this work, we highlight equations and expressions which require a long derivation using a box, as illustrated here,

$$\boxed{a^2 + b^2 = c^2} \, . \tag{2.12}$$

3. Relativistic hydrodynamics and kinetic theory

Relativistic hydrodynamics - also known as fluid dynamics - is a classical field theory that provides an effective long-wavelength and low-frequency description of macroscopic objects called fluids. A fluid is defined as a continuous system in which every infinitesimal volume element, dV, is assumed to be close to thermodynamic equilibrium and homogeneous in space. In this sense, in every infinitesimal fluid volume or fluid element thermodynamic quantities such as temperature, pressure, and energy/particle density are well defined.

Physically speaking, the fluid elements cannot be infinitesimal, but have to be large enough compared to microscopic distance scales to enclose a large number of particles and, at the same time, small enough compared to macroscopic distance scales in order to assure the continuum limit. Therefore, hydrodynamics, whether relativistic or not, is only applicable when there is a clear separation between microscopic and macroscopic time/spatial scales.

Kinetic theory describes the dynamics of simple gases on a microscopic level. In contrast to the theory of hydrodynamics discussed above, kinetic theory is not restricted to describe systems that are close to local equilibrium and does not require a separation between the microscopic and macroscopic scales in order to be applicable. For example, it is able to describe systems even when the microscopic or interaction length scale is of the order of the system size or even larger.

As mentioned above, hydrodynamics is only applicable occurs when there is a separation between microscopic and macroscopic scales. In kinetic theory, the microscopic scale corresponds to the average mean free path, λ_{mfp}, of the particles contained in the system. In this sense, hydrodynamics can be applied to simple gases when the mean free path, λ_{mfp}, is very small compared to gradients of thermodynamic quantities[1]. The ratio of microscopic and macroscopic length scale is referred to as the Knudsen number,

$$Kn = \frac{\lambda_{\mathrm{mfp}}}{L}\,, \tag{3.1}$$

and quantifies when hydrodynamics can be applied. When $Kn \ll 1$ is extremely small, the system is close to the ideal-fluid limit. If $Kn < 1$, the system is a viscous fluid, if $Kn \approx 1$ we are outside the validity of hydrodynamics, and $Kn \gg 1$ corresponds to free streaming.

It is important to mention that the domain of applicability of kinetic theory and hydrodynamics overlap over a big regime, as will be discussed in this work. For example, solutions of hydrodynamics and those of numerical solvers of kinetic theory are approximately the same when the mean free path, λ_{mfp}, is small. However, one should

---

[1]which provide a macroscopic distance scale.

take notice, that in this limit simulations based on kinetic theory require large computational power. On the other hand, it has been pointed out that, even when hydrodynamic solvers should be able to describe kinetic theory, they will fail if the transport coefficients are chosen incorrectly. In order to properly compare hydrodynamical simulations to those of kinetic theory, one has to implement the proper matching between the macroscopic equations of motion and the microscopic ones. For this reason, constructing a macroscopic theory that can be applied at large Knudsen numbers is very convoluted and often leads to complicated equations of motion.

In this chapter we give an overview of relativistic hydrodynamics and kinetic theory. In Sec. 3.1 we start with the basic definitions of kinetic theory, the Boltzmann[2] equation and the connection to macroscopic quantities. In the subsequent Sec. 3.2 we first provide a discussion of the description of an ideal fluid, which is then extended to viscous hydrodynamics in Sec. 3.3. We discuss the basic tensorial decompositions, the choice of reference frames and the derivation of relativistic dissipative hydrodynamics. In Sec. 3.4 we finally discuss the different derivations of viscous hydrodynamics, which are referred to in this work.

This chapter is a general summary of the knowledge from several works. For a more detailed discussion we refer to Refs. [39, 40, 139, 140, 141]. For the basic concepts of thermodynamics used in this work we refer to Ref. [142].

3.1. The Boltzmann equation in kinetic theory

In relativistic kinetic theory of simple gases the state of the system is characterized by the invariant single-particle distribution function, $f(x, p)$. The space-time evolution of $f(x, p)$ caused by particle motion and collisions among the particles is given by the relativistic Boltzmann transport equation [39, 40, 41],

$$p_1^\mu \partial_\mu f_1(x, p) = C_{22} + C_{23} + \cdots , \qquad (3.2)$$

where

$$
\begin{aligned}
C_{22} &= \frac{1}{2} \int \frac{\mathrm{d}\Gamma_2}{2} \frac{1}{\nu} \int \frac{\mathrm{d}\Gamma'_1}{2} \frac{\mathrm{d}\Gamma'_2}{2} f'_1 f'_2 \times \\
&\times |M_{1'2' \to 12}|^2 (2\pi)^4 \delta^{(4)} \left(p'_1 + p'_2 - p_1 - p_2 \right) \\
&- \frac{1}{2} \int \frac{\mathrm{d}\Gamma_2}{2} \frac{1}{\nu} \int \frac{\mathrm{d}\Gamma'_1}{2} \frac{\mathrm{d}\Gamma'_2}{2} f_1 f_2 \times \\
&\times |M_{12 \to 1'2'}|^2 (2\pi)^4 \delta^{(4)} \left(p_1 + p_2 - p'_1 - p'_2 \right) , \qquad (3.3)
\end{aligned}
$$

---

[2]Ludwig Eduard Boltzmann (1844-1906) was an Austrian physicist and philosopher, who was a professor in Graz and Wien.

denotes the collision integral for elastic $2 \to 2$ scattering processes and

$$
\begin{aligned}
C_{23} &= \frac{1}{2}\frac{1}{2!}\int \frac{\mathrm{d}\Gamma_2}{2}\frac{\mathrm{d}\Gamma_3}{2}\frac{1}{2!}\int \frac{\mathrm{d}\Gamma'_1}{2}\frac{\mathrm{d}\Gamma'_2}{2}f'_1 f'_2 \times \\
&\times |M_{1'2'\to 123}|^2 (2\pi)^4 \delta^{(4)}\left(p'_1 + p'_2 - p_1 - p_2 - p_3\right) \\
&+ \frac{1}{2}\int \frac{\mathrm{d}\Gamma_2}{2}\frac{1}{3!}\int \frac{\mathrm{d}\Gamma'_1}{2}\frac{\mathrm{d}\Gamma'_2}{2}\frac{\mathrm{d}\Gamma'_3}{2}f'_1 f'_2 f'_3 \times \\
&\times |M_{1'2'3'\to 12}|^2 (2\pi)^4 \delta^{(4)}\left(p'_1 + p'_2 + p'_3 - p_1 - p_2\right) \\
&- \frac{1}{2}\frac{1}{2!}\int \frac{\mathrm{d}\Gamma_2}{2}\frac{\mathrm{d}\Gamma_3}{2}\frac{1}{2!}\int \frac{\mathrm{d}\Gamma'_1}{2}\frac{\mathrm{d}\Gamma'_2}{2}f_1 f_2 f_3 \times \\
&\times |M_{123\to 1'2'}|^2 (2\pi)^4 \delta^{(4)}\left(p_1 + p_2 + p_3 - p'_1 - p'_2\right) \\
&- \frac{1}{2}\int \frac{\mathrm{d}\Gamma_2}{2}\frac{1}{3!}\int \frac{\mathrm{d}\Gamma'_1}{2}\frac{\mathrm{d}\Gamma'_2}{2}\frac{\mathrm{d}\Gamma'_3}{2}f_1 f_2 \times \\
&\times |M_{12\to 1'2'3'}|^2 (2\pi)^4 \delta^{(4)}\left(p_1 + p_2 - p'_1 - p'_2 - p'_3\right) ,
\end{aligned}
\tag{3.4}
$$

is the corresponding collision integral for inelastic $2 \to 3$ scattering processes. p_1, p_2, and p_3 denote the momenta of the incoming particles, p'_1, p'_2, and p'_3 the momenta of the outgoing particles. In order to avoid double counting, ν will be set to 2 if $1'$ and $2'$ are identical particles. Otherwise, ν is set to 1. We assume that there are no external forces or fields[3] and $\mathrm{d}\Gamma = \mathrm{d}^3 p/[(2\pi)^3 E]$. Above, $M_{a\to b}$ are the corresponding matrix elements which are momentum dependent and should be provided by the corresponding underlying microscopic theory. We have introduced

$$
p^\mu = \begin{pmatrix} E \\ \vec{p} \end{pmatrix},
\tag{3.5}
$$

which is the particle four-momentum with E denoting its energy. Furthermore, m is the rest mass and $\vec{p}$ is the momentum vector of a particle. The relativistic energy-momentum relation is given by $E^2 = p^2 + m^2$. We have also introduced the space-time coordinate

$$
x^\mu = \begin{pmatrix} \vec{x} \\ t \end{pmatrix}
\tag{3.6}
$$

and the partial derivative

$$
\partial_\mu \equiv \frac{\partial}{\partial x^\mu} .
\tag{3.7}
$$

The Boltzmann equation (3.2) is given by the free propagation of the distribution function on the left-hand side and the collision term on the right-hand side. In the simplified case in which no collisions occur, the solution of the Boltzmann equation becomes simple. Among other things, the solution has been determined in Ref. [143], and it is discussed for a simplified one-dimensional setup in Appendix I. This solution shall be referred to in the following as the free-streaming case. In the general case in which collisions are taken into account, solving the Boltzmann equation is rather complicated, since one has to solve equations in $(6+1)$-dimensional phase space, $(\vec{x}, \vec{p}, t)$. This demands a numerical simulation which is presented in Chapter 6.

---

[3]Such as magnetic fields.

The macroscopic quantities appearing in hydrodynamics can be shown to correspond to moments of the distribution function. The first moment is the particle four-flow,

$$N^\mu \equiv \int \mathrm{d}\tilde{p}\, p^\mu f(x, p)\,. \tag{3.8}$$

Here, $\mathrm{d}\tilde{p} \equiv g\,\mathrm{d}\Gamma = g\,\mathrm{d}^3 p/[(2\pi)^3 E]$, where g counts the internal degrees of freedom. The second moment defines the energy-momentum tensor,

$$T^{\mu\nu} \equiv \int \mathrm{d}\tilde{p}\, p^\mu p^\nu f(x, p)\,. \tag{3.9}$$

Similarly one can define higher moments of the distribution function, such as the third moment,

$$F^{\mu\nu\lambda} \equiv \int \mathrm{d}\tilde{p}\, p^\mu p^\nu p^\lambda f(x, p)\,. \tag{3.10}$$

The entropy four-current is defined as

$$S^\mu \equiv \int \mathrm{d}\tilde{p}\, p^\mu f(x, p) \left[1 - \ln f(x, p)\right]\,. \tag{3.11}$$

The Boltzmann H-theorem [39, 142] implies that the entropy production for a closed system is positive semi-definite, i.e.,

$$\partial_\mu S^\mu \geq 0\,, \tag{3.12}$$

and vanishes in thermal equilibrium. The equation above is also known as the second law of thermodynamics.

3.2. Relativistic ideal hydrodynamics

In this section we discuss the perfect-fluid limit of relativistic hydrodynamics. This limit corresponds to infinite large scattering rates, i.e., the case in which the average mean free path of the particles vanishes. This implies that there is no dissipation, i.e., the fluid is assumed to be always in local thermal equilibrium and that the entropy is conserved,

$$\partial_\mu S^\mu = 0\,. \tag{3.13}$$

One has to note, however, that the differential form above is not valid when the system features sharp discontinuities in the density or velocity profile. Hence, in the case of shock waves, entropy may be produced even for perfect fluids. We discuss this in more detail in Chapter 4.

Relativistic hydrodynamics is a classical field theory describing the time evolution of the energy-momentum tensor, $T^{\mu\nu}(x^\mu)$, particle four-flow, $N^\mu(x^\mu)$ and entropy four-current, $S^\mu(x^\mu)$. These currents describe the state of a relativistic fluid and have to be well defined locally at each space-time coordinate x^μ. From now on we explicitly leave out the position dependence (x^μ) of every hydrodynamic field.

We define an arbitrary timelike four-vector

$$u^\mu = \gamma v^\mu = \gamma \begin{pmatrix} 1 \\ \vec{v} \end{pmatrix} \tag{3.14}$$

which we normalize to unity, i.e., $u^\mu u_\mu = 1$. It shall be chosen in such a way so that it can be interpreted as the collective four-velocity of the fluid. We identify

$$\gamma = \frac{1}{\sqrt{1 - |\vec{v}|^2}} \tag{3.15}$$

as the Lorentz gamma factor and $\vec{v}$ as the velocity vector defined in the laboratory frame. The frame where

$$u^\mu_{\text{LRF}} = \begin{pmatrix} 1 \\ 0 \\ 0 \\ 0 \end{pmatrix}, \tag{3.16}$$

is called the local rest frame (LRF). An ideal fluid is defined such that the energy-momentum tensor in the local rest frame of the fluid reads

$$T^{\mu\nu}_{\text{LRF}} = \begin{pmatrix} e & 0 & 0 & 0 \\ 0 & p & 0 & 0 \\ 0 & 0 & p & 0 \\ 0 & 0 & 0 & p \end{pmatrix}. \tag{3.17}$$

This is nothing but the static equilibrium energy-momentum tensor, in which no flow of energy exists and the pressure is isotropic. We denote here e as the LRF energy density and p as the LRF equilibrium pressure. In the LRF of an ideal fluid there is no flow of particles, hence we obtain

$$N^\mu_{\text{LRF}} = \begin{pmatrix} n \\ 0 \\ 0 \\ 0 \end{pmatrix} \tag{3.18}$$

for the particle four-flow. Here n is the LRF particle density. For completeness we introduce also the LRF entropy four-current,

$$S^\mu_{\text{LRF}} = \begin{pmatrix} s \\ 0 \\ 0 \\ 0 \end{pmatrix}. \tag{3.19}$$

The conserved currents of a fluid in local equilibrium, i.e., of a perfect fluid, can be expressed as

$$T^{\mu\nu}_{\text{eq}} = e u^\mu u^\nu - p \Delta^{\mu\nu} = \int d\tilde{p}\, p^\mu p^\nu f_{\text{eq}}(x, p), \tag{3.20}$$

$$N^\mu_{\text{eq}} = n u^\mu = \int d\tilde{p}\, p^\mu f_{\text{eq}}(x, p), \tag{3.21}$$

$$S^\mu_{\text{eq}} = s u^\mu = \int d\tilde{p}\, p^\mu f_{\text{eq}}(x, p) \left[1 - \ln f_{\text{eq}}(x, p)\right]. \tag{3.22}$$

Here, the subindex "eq" denotes that the quantity is in local equilibrium. We introduced the spacelike transverse projection operator,

$$\Delta^{\mu\nu} = g^{\mu\nu} - u^\mu u^\nu \,, \tag{3.23}$$

which projects onto the 3-space orthogonal to the normalized timelike four-vector, u^μ, i.e. $\Delta^{\mu\nu} u_\mu = 0$. In the LRF, the transverse projection operator reads

$$\Delta^{\mu\nu}_{\text{LRF}} = \begin{pmatrix} 0 & 0 & 0 & 0 \\ 0 & -1 & 0 & 0 \\ 0 & 0 & -1 & 0 \\ 0 & 0 & 0 & -1 \end{pmatrix} . \tag{3.24}$$

We have also introduced the equilibrium distribution function,

$$f_{\text{eq}}(x,p) \equiv \left(e^{\frac{p^\mu u_\mu - \mu}{T}} + a \right)^{-1} . \tag{3.25}$$

Here $a = -1(+1)$ corresponds to bosons (fermions), and $a = 0$ corresponds to Boltzmann particles. In this work we do not take into account any quantum effects such as Bose enhancement or Pauli blocking, i.e., we restrict our calculations and discussion to Boltzmann particles.

We have introduced the temperature, T, and chemical potential, μ, in Eq. (3.25), which together with the velocity, $\vec{v}$, are referred to as the primary fluid dynamical variables. The LRF equilibrium quantities for a constant and nonzero mass, m, are given in terms of T and μ,

$$n(T,\mu) = \frac{g}{2\pi^2} m^2 T e^{\mu/T} K_2(m/T) \,, \tag{3.26}$$

$$p(T,\mu) = n(T,\mu)T \,, \tag{3.27}$$

$$e(T,\mu) = 3p(T,\mu) + \frac{g}{2\pi^2} m^3 T e^{\mu/T} K_1(m/T) \,, \tag{3.28}$$

$$s(T,\mu) = \frac{e(T,\mu) + p(T,\mu) - \mu n(T,\mu)}{T} \,. \tag{3.29}$$

Here $K_n(x)$ is the modified Bessel function of the second kind [144]. In the ultrarelativistic limit, i.e., $m = 0$, Eqs. (3.26), (3.27), (3.28) and (3.29) simplify to

$$\lim_{m\to 0} n(T,\mu) = \frac{\lambda g}{\pi^2} T^3 \,, \tag{3.30}$$

$$\lim_{m\to 0} p(T,\mu) = n(T,\mu)T \,, \tag{3.31}$$

$$\lim_{m\to 0} e(T,\mu) = 3p(T,\mu) \,, \tag{3.32}$$

$$\lim_{m\to 0} s(T,\mu) = (4 - \ln\lambda)\, n(T,\mu) \,. \tag{3.33}$$

So far, we have introduced the general tensors that specify the state of a perfect fluid. However, in order to obtain the dynamical description of any fluid, we need the

conservation of energy, momentum, and particle number, which can be expressed by the following continuity equations,

$$\partial_\mu T^{\mu\nu}_{\text{eq}} = 0 \,, \tag{3.34}$$

$$\partial_\mu N^{\mu}_{\text{eq}} = 0 \,. \tag{3.35}$$

The conservation laws (3.34) and (3.35) provide five equations while e, p, n, and u^μ correspond in total to six unknowns. In order to close this system of equations we have to introduce an equation of state (EoS) for the fluid,

$$p = p(e, n) \,, \tag{3.36}$$

which relates the pressure to other thermodynamical quantities. For the simple case of a massless Boltzmann gas with no conserved charges, the equation of state is

$$p = \frac{1}{3} e \,, \tag{3.37}$$

which is mainly used throughout this work. With the equation of state, the above system of equations is closed and provides the time evolution of the conserved currents.

3.3. Framework of relativistic dissipative hydrodynamics

In this section we introduce the general formalism of relativistic dissipative hydrodynamics. In contrast to the previous Sec. 3.2, where we have assumed a perfect fluid, i.e., the fluid is always in local thermal equilibrium during its evolution, we now consider more realistic fluids, i.e., where dissipative effects are taken into account.

We know from thermodynamics that every closed system is driven towards thermodynamic equilibrium. Such a thermalization process is an irreversible process. The H-Theorem implies that the entropy production is always positive, see Eq. (3.12), and has its maximum value when the system reaches equilibrium. In fluids, dissipation originates from irreversible thermodynamic processes. In order to obtain local equilibrium, each fluid element exchanges heat and dissipates energy by friction with its surrounding fluid elements. Such processes have to be included into the relativistic hydrodynamic equations in order to obtain a more realistic description of relativistic fluids.

3.3.1. Basic tensorial decompositions and definitions

In this subsection we introduce the most general tensorial decomposition allowed by symmetry from the mathematical point of view. As discussed in Sec. 3.2 for perfect fluids, the particle and energy-momentum conservation laws provide the basic equations of motion for the fluid

$$\partial_\mu T^{\mu\nu} = 0 \,, \tag{3.38}$$

$$\partial_\mu N^{\mu} = 0 \,. \tag{3.39}$$

With the general decomposition using the transverse projection operator (3.23) and collective four-velocity of the fluid (3.14), the particle four-flow and energy-momentum tensor can be decomposed into the equilibrium (N^μ_{eq}, $T^{\mu\nu}_{\text{eq}}$) and dissipative parts (δN^μ, $\delta T^{\mu\nu}$), i.e.,

$$N^\mu = N^\mu_{\text{eq}} + \delta N^\mu = n u^\mu + V^\mu \, , \tag{3.40}$$

$$T^{\mu\nu} = T^{\mu\nu}_{\text{eq}} + \delta T^{\mu\nu} = e u^\mu u^\nu - (p + \Pi)\, \Delta^{\mu\nu} + W^\mu u^\nu + W^\nu u^\mu + \pi^{\mu\nu} \, . \tag{3.41}$$

We define the LRF particle density as

$$n \equiv N^\mu u_\mu \, , \tag{3.42}$$

and the LRF energy density as

$$e \equiv u_\mu T^{\mu\nu} u_\nu \, . \tag{3.43}$$

The two relations above are known as the Landau matching conditions, which we discuss in Sec. 3.3.2. Let us first continue the discussion of the other hydrodynamic quantities.

The sum of the equilibrium pressure, p, and bulk viscous pressure, Π, denotes the isotropic pressure

$$P = p + \Pi = -\frac{1}{3} \Delta_{\mu\nu} T^{\mu\nu} \, . \tag{3.44}$$

The flow of particles in the LRF reads

$$V^\mu = \Delta^\mu_\nu N^\nu \, , \tag{3.45}$$

while the flow of energy-momentum in the LRF is given by

$$W^\mu = \Delta^{\mu\alpha} T_{\alpha\beta} u^\beta \, . \tag{3.46}$$

The heat flow is defined as

$$q^\mu = W^\mu - h\, V^\mu \, , \tag{3.47}$$

with $h = (e + p)/n$ denoting the enthalpy per particle.

The shear-stress tensor is given by, $\pi^{\mu\nu} = T^{\langle\mu\nu\rangle}$, where

$$T^{\langle\mu\nu\rangle} \equiv \left[\frac{1}{2}\left(\Delta^\mu_\alpha \Delta^\nu_\beta + \Delta^\nu_\alpha \Delta^\mu_\beta \right) - \frac{1}{3} \Delta^{\mu\nu} \Delta_{\alpha\beta} \right] T^{\alpha\beta} \, . \tag{3.48}$$

Hence the shear-stress tensor is that part of $T^{\mu\nu}$ that is symmetric, traceless, and orthogonal to the flow velocity.

In a simplified one-dimensional setup, i.e., assuming an expansion only in x-direction and homogeneity in the transverse plane $y - z$, we define the shear pressure

$$\pi = \pi^{xx}/\gamma^2 = -2\pi^{yy} = -2\pi^{zz} \, , \tag{3.49}$$

which is shown to be a useful quantity in the upcoming chapters.

In local equilibrium all dissipative terms vanish, i.e., $\Pi = V^\mu = W^\mu = \pi^{\mu\nu} = 0$. Therefore the particle four-current and energy-momentum tensor, as given in Eqs. (3.40) and (3.41), again take the simpler form given by Eqs. (3.20) and (3.21). In local equilibrium, the particle four-current, N^μ_{eq}, the energy-momentum tensor, $T^{\mu\nu}_{\text{eq}}$, and the entropy four-current, S^μ_{eq}, are uniquely defined for any time-like four-velocity, u^μ. The LRF particle density and energy density are given by $n_{\text{eq}} \equiv N^\mu_{\text{eq}} u_\mu$ and $e_{\text{eq}} \equiv u_\mu T^{\mu\nu}_{\text{eq}} u_\nu$, respectively. The importance of the reference frame for the four-velocity is demonstrated in Sec. 3.3.3.

3.3.2. Matching conditions

We get in trouble when introducing dissipative currents, since the equilibrium variables are not well-defined in viscous fluids. The equilibrium pressure, p, is only known as a function of the equilibrium energy density, e_{eq}, and particle density, n_{eq}, but not known as a function of the actual energy density, e, and particle density, n. In order to resolve the problem we use the Landau matching conditions [44, 145, 146, 147]. They match the equilibrium energy density and particle density in the LRF to their non-equilibrium quantities

$$
\begin{aligned}
e_{\mathrm{eq}} &= e\,, \\
n_{\mathrm{eq}} &= n\,,
\end{aligned}
\tag{3.50}
$$

which allows us to define Eqs. (3.42) and (3.43). The matching conditions (3.50) imply the following constraints to the dissipative currents:

$$
u_\mu \delta N^\mu = 0\,,
\tag{3.51}
$$

$$
u_\mu u_\nu \delta T^{\mu\nu} = 0\,.
\tag{3.52}
$$

These conditions together with the Gibbs equation [142] ensure that the equilibrium part of the pressure is given by the equation of state, $p(e, n) = p(e_{\mathrm{eq}}, n_{\mathrm{eq}})$. Therefore, the temperature, T, and chemical potential, μ, correspond to a given energy density and particle density, which we introduce in Sec. 3.3.4.

In order to get a better understanding of the matching conditions, we consider an example from kinetic theory. We imagine a small volume element, $\mathrm{d}V$, in its local rest frame with a given distribution function, $f(p)$, for a massless classical Boltzmann gas. If matter is in thermal equilibrium, Eq. (3.25) holds with a given equilibrium temperature, T, the energy distribution has the form

$$
\frac{\mathrm{d}N}{NE^2\mathrm{d}E} = \frac{1}{2T^3}e^{-E/T}\,.
\tag{3.53}
$$

The energy density and particle density are e_{eq} and n_{eq}, respectively. Now, let us assume that the particle distribution function is not thermal, but for example, a delta function of the form

$$
\frac{\mathrm{d}N}{NE^2\mathrm{d}E} = \delta(E - 3T)\,.
\tag{3.54}
$$

This implies that all particles have the same kinetic energy, $E = 3T$, so that in the end the same amount of energy is in the system as it would be in the thermal case[4].

Although both systems have the same energy, the energy per particle is distributed in a different way. The Landau matching conditions tells us that we cannot distinguish between the two different setups. In other words, the local energy and particle density do not depend on the distribution function itself.

---

[4]Here, T is not the equilibrium temperature anymore.

3.3.3. Choice of reference frame for dissipative fluids

For a system that deviates from local thermodynamical equilibrium the LRF is ambiguous, because there is energy and particle diffusion. There are two special reference frames in which either the particle or the energy-momentum diffusion current vanishes.

Using Eckart's definition of the flow velocity [148],

$$u_E^\mu = \frac{N^\mu}{\sqrt{N^\nu N_\nu}}\,, \tag{3.55}$$

the LRF flow of particles vanishes, $V^\mu = 0$, while the flow of energy is given by the heat flow, $W^\mu = q^\mu$.

In Landau's frame [139] the flow of matter is tied to the flow of energy,

$$u_L^\mu = \frac{T^{\mu\nu} u_\nu}{\sqrt{u_\alpha T^{\beta\alpha} T_{\beta\gamma} u^\gamma}}\,; \tag{3.56}$$

hence the flow of energy vanishes, $W^\mu = 0$.

For processes close to equilibrium, the above definitions and decompositions are related to each other [43]. Up to second order in deviations from local equilibrium, $\delta u^\mu \sim q^\mu/e \ll 1$, we obtain

$$u_L^\mu = u_E^\mu + \frac{q^\mu}{e+p}\,. \tag{3.57}$$

This means that the non-equilibrium part of the particle four-flow in Landau's frame is related to the heat flow in Eckart's frame, that is, $V^\mu = -q^\mu/h$.

As we discuss later on, the number of independent components is reduced when one specific reference frame for the velocity is defined. This is important in order to solve the hydrodynamic equations in an easier way.

3.3.4. Definition of temperature and fugacity

For a gas of classical particles in equilibrium, the temperature is given by the ratio of the equilibrium pressure and equilibrium particle density

$$T_{\mathrm{eq}} \equiv \frac{p}{n_{\mathrm{eq}}}\,. \tag{3.58}$$

In order to define a temperature for a non-equilibrium state in any reference frame - Landau or Eckart - we essentially need the Landau matching conditions [44, 145, 146, 147]. Equation (3.58) then still holds for massless particles and refers to an effective temperature of a non-equilibrium state

$$T = \frac{P}{n}\,. \tag{3.59}$$

Here, we have replaced the equilibrium pressure, p, by the isotropic pressure, P, since the bulk pressure, Π, for massless particles always vanishes. For massive particles the relation above does not hold, because bulk viscous pressure can appear. Therefore, we use the energy density, e, and particle density, n, to determine the temperature for massive particles, which is discussed in greater detail in Appendix H.

The fugacity which accounts for deviations from the chemical equilibrium state is defined as

$$\lambda \equiv e^{\mu/T} = \frac{n}{n_{\mathrm{eq(T,\mu=0)}}} \,, \tag{3.60}$$

where $n_{\mathrm{eq(T,\mu=0)}}$ is the particle density in thermal and chemical equilibrium.

3.3.5. Description of hydrodynamic quantities with more than one species

In this section we briefly introduce the hydrodynamic description of fluids with more than one species of particles. This description is needed when extracting the hydrodynamic quantities from the numerical calculations. For a more detailed discussion we refer to Refs. [147, 149, 150, 151].

We consider a system of N_{spec} different particle species. Each particles species, i, is represented by its own distribution function, $f_i(x,p)$. Therefore, the general decomposition of the particle four-flow and energy-momentum tensor for each fluid component reads

$$N_i^\mu = n_i u^\mu + V_i^\mu \,, \tag{3.61}$$

$$T_i^{\mu\nu} = e_i u^\mu u^\nu - (p_i + \Pi_i)\, \Delta^{\mu\nu} + W_i^\mu u^\nu + W_i^\nu u^\mu + \pi_i^{\mu\nu} \,, \tag{3.62}$$

similar to Eqs. (3.40) and (3.41). The reader will notice that we use only one four-velocity, u^μ, instead of a velocity for each particle species, u_i^μ. The reason for that is discussed in the following.

We start with the following expressions,

$$T^{\mu\nu} = \sum_{i=1}^{N_{\mathrm{spec}}} T_i^{\mu\nu} \,,\ N^\mu = \sum_{i=1}^{N_{\mathrm{spec}}} N_i^\mu \,, \tag{3.63}$$

$$n = \sum_{i=1}^{N_{\mathrm{spec}}} n_i \,,\ P = \sum_{i=1}^{N_{\mathrm{spec}}} P_i \,,\ e = \sum_{i=1}^{N_{\mathrm{spec}}} e_i \,, \tag{3.64}$$

$$\Pi = \sum_{i=1}^{N_{\mathrm{spec}}} \Pi_i \,,\ V^\mu = \sum_{i=1}^{N_{\mathrm{spec}}} V_i^\mu \,,\ W^\mu = \sum_{i=1}^{N_{\mathrm{spec}}} W_i^\mu \,,\ \pi^{\mu\nu} = \sum_{i=1}^{N_{\mathrm{spec}}} \pi_i^{\mu\nu} \,. \tag{3.65}$$

We obtain the quantities for the whole system by summing up the quantities for each particle species. In order to fulfill relations (3.64) and (3.65) we have to define only one reference frame using one four-velocity, u^μ. This is explained next:

We consider two particle species, A and B. For each particle species we have an energy-momentum tensor, $T_A^{\mu\nu}$, $T_B^{\mu\nu}$, and particle four-flow, N_A^μ, N_B^μ. Using the energy-momentum tensor or particle four-flow for each particle species, choosing either the Eckart- or Landau-frame characterized by Eqs. (3.55) and (3.56), respectively, we obtain a velocity for each species, v_A and v_B. In general, the obtained velocities are not equal, i.e., $v_A \neq v_B$. Using these velocities we calculate for example the energy density, e_A and e_B. Using then Eq. (3.64) we obtain the energy density of the whole system via

$e_{A+B} = e_A + e_B$. We compare this to the energy density obtained from the energy-momentum tensor and particle-four flow of the whole system, which we refer to as e^w_{A+B}. Here we calculated the velocity v^w directly for the whole system, i.e., using $T^{\mu\nu}$ and N^μ. We get $e^w_{A+B} \neq e_{A+B}$.

As mentioned above, in order to get a consistent picture as given by Eqs. (3.64) and (3.65), we have to define one four-velocity, u^μ, for the whole system. This is also true for the temperature and chemical potential[5]. Using the method discussed in Appendix H, we use the temperatures, T_i, and chemical potential, μ_i, of each particle species to construct a temperature, T, and chemical potential, μ, for the whole system. The quantities for each particle species, T_i and μ_i, have no further physical meaning. The reason for this special construction for velocity, temperature, and chemical potential is that the description of hydrodynamics assumes (almost) local thermal and chemical equilibrium. Two particle species which differ with respect to their velocity, temperature, or chemical potential, are not thermalized with each other. We have to wait until both fluid components are in local thermal equilibrium with each other, so that $v_A \simeq v_B$, $T_A \simeq T_B$, and $\mu_A \simeq \mu_B$. We conclude that a velocity, v_i, temperature, T_i or chemical potential, μ_i, for each particle species itself has no important or significant meaning[6].

3.4. Derivation of relativistic dissipative hydrodynamics

In Sec. 3.3 we have introduced the basic framework of relativistic dissipative hydrodynamics. The total number of independent components from the symmetric energy-momentum tensor, $T^{\mu\nu}$, (ten) and particle four-flow, N^μ, (four) is fourteen. Via the tensor decomposition as realized in Sec. 3.3.1, we get:

- $\pi^{\mu\nu} \to 5$ symmetric, traceless and orthogonal to u^μ

- $q^\mu \to 3$ orthogonal to u^μ

- $u^\mu \to 3$ one component is eliminated by the normalization

- $\Pi \to 1$ scalar

- $p, n, e \to 2$ one is eliminated by the EoS

In this section we will give an overview of different methods for the derivation of dissipative relativistic hydrodynamics, which are partly used in this work. First, we introduce methods to approximate the off-equilibrium distribution function, $f(x,p)$, then we introduce the derivations of dissipative hydrodynamics.

3.4.1. Hydrodynamics as an approximation to kinetic theory: Knudsen number expansion and Grad´s 14-moment theory

Hydrodynamics is an effective theory for the slow, long-wavelength dynamics of a given system. For systems with well-defined quasi-particles, hydrodynamics can be derived

---

[5]or equivalently the fugacity.
[6]Except for the fact, that each species can be in thermal equilibrium among itself.

in terms of a power series in the Knudsen number (3.1), where

$$\lambda_{\text{mfp}} = \frac{1}{n\sigma} \tag{3.66}$$

is the mean free path of the particles with σ being the cross section. In Eq. (3.1) we refer to L as a macroscopic length scale over which macroscopic fields such as energy density, particle density, or temperature vary. Hydrodynamics as an effective theory can be systematically improved by successively including higher-order terms in Kn. This is discussed in detail in Ref. [107].

To zeroth order in Kn we obtain an effective theory that does not contain any powers of Kn, corresponding to the limit $Kn \to 0$, that is, the (unphysical) limit where $\lambda_{\text{mfp}} \to 0$. This corresponds to infinite scattering rates, and thus the system instantaneously assumes local thermodynamical equilibrium. This is the perfect-fluid limit we have discussed in Sec. 3.2. To first order in Kn, we obtain the relativistic generalization of Navier-Stokes theory presented in Sec. 3.4.2. This effective theory is plagued by instabilities and acausalities [152, 153, 154]. These problems can be circumvented by including terms of second order in Kn as it is done in the fluid-dynamical theory of Israel and Stewart described in Sec. 3.4.3. The fluid-dynamical limit can be derived for any kind of system, that is, its applicability is not restricted to dilute gases, as is the case for the Boltzmann equation. However, since it is an expansion around the perfect-fluid limit, we expect its validity to be restricted to dynamics close to local thermodynamical equilibrium.

The coefficients of hydrodynamics as an effective theory can be computed by matching to an underlying microscopic theory, for example the kinetic theory of ultrarelativistic Boltzmann particles, described by the Boltzmann equation (3.2) with elastic binary collisions. One has to note, however, that the matching procedure of dissipative quantities is not unique [155].

The matching condition can be as follows. We expand the single-particle distribution function around local thermodynamical equilibrium,

$$f(x, p) = f_{\text{eq}}(x, p) + \delta f, \tag{3.67}$$

where δf measures the deviation from the equilibrium distribution function (3.25). The validity of the expansion around f_{eq} requires that $\phi = \delta f / f_{\text{eq}} \ll 1$. In order to match to fluid dynamics as an expansion in powers of Kn, one possibility is to assume that ϕ is a series in powers of Kn. This approach was pioneered by Hilbert, and by Chapman and Enskog [40].

Another method has been proposed by Grad [42] and generalized to relativistic systems by Israel and Stewart [44, 156]. In this approach,

$$\phi(x, p) = \epsilon + \epsilon_\mu p^\mu + \epsilon_{\mu\nu} p^\mu p^\nu, \tag{3.68}$$

where the coefficients ϵ, ϵ_μ, and $\epsilon_{\mu\nu}$ are the expansion parameters and therefore $\sim O(Kn)$. For each non-equilibrium state given by f the corresponding equilibrium state f_{eq} is defined by the Landau matching conditions [44].

The coefficients of the expansion, ϵ, ϵ_μ, and $\epsilon_{\mu\nu}$, are determined using Eq. (3.68) together with Eqs. (3.8) and (3.9). Comparing the result with Eqs. (3.40) and (3.41), one

finds that the parameters of the expansion are proportional to the dissipative quantities Π, V^μ, q^μ, and $\pi^{\mu\nu}$. Thus, the deviation from equilibrium is proportional to the ratio of dissipative quantities to local equilibrium quantities, that is, $\phi \sim \Pi/e, q^\mu/e, \pi^{\mu\nu}/e$. However, if the dissipative quantities are close to the Navier-Stokes values[7], then these ratios are proportional to the local Knudsen number.

3.4.2. The Navier-Stokes theory

A simple way to obtain the first-order equations of hydrodynamics, which are also referred to as Navier-Stokes equations, is to apply the second law of thermodynamics, (3.12), to the simplest form of the entropy current, i.e.,

$$S^\mu = su^\mu + \frac{q^\mu}{T}\,. \tag{3.69}$$

We then obtain, as discussed in details in Refs. [44, 157], the Navier-Stokes equations:

$$\Pi_{\text{NS}} \equiv -\zeta \nabla_\mu u^\mu\,, \tag{3.70}$$

$$q^\mu_{\text{NS}} \equiv \kappa \frac{nT^2}{e+p} \nabla^\mu \left(\frac{\mu}{T}\right)\,, \tag{3.71}$$

$$\pi^{\mu\nu}_{\text{NS}} \equiv 2\eta \nabla^{\langle \mu} u^{\nu \rangle}\,. \tag{3.72}$$

The gradient operator is $\nabla^\mu = \Delta^{\mu\nu}\partial_\nu$ and $\langle...\rangle$ denotes the projection in order to obtain a traceless symmetric tensor. The dissipative currents in the Navier-Stokes limit, (3.70), (3.71) and (3.72), are proportional to the gradients of thermodynamic variables and velocity fields, which are considered as thermodynamic forces. We have introduced the proportionality factors ζ, κ, and η, which are the bulk viscosity, heat conductivity, and shear viscosity, respectively. They are referred to as transport coefficients and they have to be non-negative in order to satisfy the second law of thermodynamics (3.12).

Furthermore, Eqs. (3.70), (3.71), and (3.72) imply that thermodynamic forces can be switched on and off instantaneously, which violates causality and is intrinsically unstable. This is undesirable for relativistic systems. This fact is well-known in the hydrodynamic community and has been investigated in detail in several publications [152, 153, 158].

Another problem in the Navier-Stokes theory is the following: Eqs. (3.70), (3.71), and (3.72) imply that dissipative quantities only exist if there are spatial gradients. This is definitively not true as shown in Ref. [151]. Although there are no spatial gradients, the distribution function itself can be non-thermal. Thus, the Navier-Stokes equations fail in describing such a particular case.

These presented problems can be solved by introducing more terms in the hydrodynamic derivation. The obtained equations are called second-order equations. They are equations of relaxation type and have been introduced by Israel and Stewart, which we discuss in the following.

---

[7]see later

3.4.3. Transient relativistic fluid dynamics: The Israel and Stewart theory

The Navier-Stokes theory provides a reasonable description for a wide set of non-relativistic fluids, but it is unstable and acausal in the relativistic regime and, for this reason, unable to describe any relativistic fluid. Israel and Stewart have formulated a hydrodynamic theory which is stable and causal even in the relativistic regime [43, 44]. The main difference to the Navier-Stokes theory is the appearance of relaxation times which imply that $\pi^{\mu\nu}$, q^{μ}, and Π are dynamical variables. The relaxation times corresponds to the time scales on which the dissipative currents react to gradients of thermodynamic variables and velocity fields.

The macroscopic equations for the evolution of dissipative quantities can be obtained from the third moment of the single-particle distribution function [44]. The method is similar to one of the first-order equations, whereas the entropy four-current (3.69) is extended by introducing second-order corrections. Here we just recall the result of this laborious calculation by Israel and Stewart as presented by Huovinen and Molnár [45] for a massless gas, which implies that the bulk viscous pressure vanishes. Then the Israel-Stewart (IS) equations for the heat flow and the shear-stress tensor are

$$Dq^{\mu} = \frac{1}{\tau_q}\left(q^{\mu}_{NS} - q^{\mu}\right) - \omega^{\mu\lambda}q_{\lambda} \tag{3.73}$$

$$-u^{\mu}q_{\nu}Du^{\nu} - \frac{1}{2}q^{\mu}\left(\nabla_{\lambda}u^{\lambda} + D\ln\frac{\beta_1}{T}\right)$$

$$+\frac{\alpha_1}{\beta_1}(\partial_{\lambda}\pi^{\lambda\mu} + u^{\mu}\pi^{\lambda\nu}\partial_{\lambda}u_{\nu}) - \frac{a_1}{\beta_1}\pi^{\lambda\mu}Du_{\lambda}\,,$$

$$D\pi^{\mu\nu} = \frac{1}{\tau_{\pi}}\left(\pi^{\mu\nu}_{NS} - \pi^{\mu\nu}\right) - 2\pi_{\lambda}^{\langle\mu}\omega^{\nu\rangle\lambda} \tag{3.74}$$

$$-(\pi^{\lambda\mu}u^{\nu} + \pi^{\lambda\nu}u^{\mu})Du_{\lambda}$$

$$-\frac{1}{2}\pi^{\mu\nu}\left(\nabla_{\lambda}u^{\lambda} + D\ln\frac{\beta_2}{T}\right)$$

$$-\frac{\alpha_1}{\beta_2}\nabla^{\langle\mu}q^{\nu\rangle} + \frac{a'_1}{\beta_2}q^{\langle\mu}Du^{\nu\rangle}\,,$$

where the proper-time derivative is denoted by $D \equiv u^{\mu}\partial_{\mu}$, and the vorticity tensor

$$\omega^{\mu\nu} = \frac{1}{2}\Delta^{\mu\alpha}\Delta^{\beta\nu}\left(\partial_{\beta}u_{\alpha} - \partial_{\alpha}u_{\beta}\right)\,. \tag{3.75}$$

The coefficients $\alpha_1, \beta_1, \beta_2$, and a_1 are thermodynamic functions, and

$$a'_1 = [\partial(\beta\alpha_1)/\partial\beta]_{\mu/T} - a_1\,. \tag{3.76}$$

These coefficients depend on whether we choose the Landau or Eckart frame. The relaxation times of heat conductivity and shear viscosity are proportional to the heat conductivity and shear viscosity coefficient, respectively, that is, $\tau_q = \kappa_q T\beta_1$ and $\tau_{\pi} = 2\eta\beta_2$.

The microscopic time scales in the IS equations are given by the relaxation times of dissipative quantities, τ_{π} and τ_q, which are of the order of the mean free path between collisions. The relevant macroscopic scales can be estimated from the gradients of

the primary fluid-dynamical variables. For example, these can be given in terms of the expansion rate $L_\theta = 1/\theta$, or in terms of the energy density gradient $L_e^{-1} = \sqrt{\nabla^\mu e \nabla_\mu e}/e$.

If the Knudsen number is sufficiently small, then at late times $t > \tau_\pi, \tau_q$, heat flow and shear viscosity will approach their Navier-Stokes values, that is, $q^\mu \sim q_{NS}^\mu$ and $\pi^{\mu\nu} \sim \pi_{NS}^{\mu\nu}$. When this happens, the dissipative quantities can be estimated to be of order 1 in the Knudsen number, and Eqs. (3.73) and (3.74) include contributions up to second order in Kn.

In the limit $\tau_q, \tau_\pi \to 0$, with constant η and κ_q, the IS equations reduce to the Navier-Stokes equations. Here, the relaxation time is the time scale over which the dissipative currents relax to their Navier-Stokes values. Furthermore, in the limit where all dissipative quantities approach zero, the IS equations reduce to the perfect-fluid equations.

In this work the Israel-Stewart equations (3.73) and (3.74) are numerically solved using the vSHASTA (viscous SHarp And Smooth Transport Algorithm) [159]. Although solving the hydrodynamic equations it is not the main part of this work, it is important for the overall discussion in this work. Therefore, we shall introduce the equations in $(1 + 1)$-dimensions in Appendix A.

3.4.4. Resummed Transient Relativistic Fluid Dynamics

In the last couple of years, the IS theory introduced above has been widely applied to ultrarelativistic HIC in order to describe the time evolution of the QGP and the freeze-out of the hadron resonance gas appearing in the late stages of the collision. However, in heavy-ion collisions extreme conditions occur which question the validity of hydrodynamics. The QGP created at RHIC and, recently, at LHC is not only the fluid with the smallest space-time extension (~ 10 fm) ever created in nature but also the one where the space-time gradients of the fluid fields, for instance energy density, e, are the largest ($\sim |\partial_\mu e|/e \sim 1/$fm) ever encountered. On the other hand, Israel and Stewart's derivation lacks a small parameter, such as the Knudsen number, with which one can do power counting and systematically improve the approximation to describe higher-order gradients. Thus, the applicability of IS theory to the extreme conditions reached in heavy-ion collisions is, at the very least, not clear.

As shown in this work in Sec. 7.1.2 and also the corresponding publication [34], the IS formalism is unable to describe heat flow even when the Knudsen number is very small. Recently, a systematic derivation of hydrodynamics from the Boltzmann equation has been introduced [35, 46, 47]. The main difference between IS theory and the theory derived in Refs. [35, 46, 47] is that the latter does not truncate the moment expansion of the single-particle distribution function. Instead, dynamical equations for all its moments are considered and solved by separating the slowest microscopic time scale from the faster ones. Then, the resulting fluid-dynamical equations are truncated according to a systematic power-counting scheme using the inverse Reynolds number, $R^{-1} \sim |V^\mu|/n \sim |\pi^{\mu\nu}|/p$ and the Knudsen number, $Kn = \lambda_{\mathrm{mfp}}/L$, with λ_{mfp} being the mean free path and L a characteristic macroscopic distance scale, e.g. $L^{-1} \sim \partial_\mu u^\mu$. The values of the transport coefficients of fluid dynamics are obtained by resumming the contributions from all moments of the single-particle distribution function, which is similar to the Chapman-Enskog expansion [160].

In Appendix B, we briefly describe this recently derivation of viscous hydrodynamics, which is an approximation to the relativistic Boltzmann equation and is named RTRFD (Resummed Transient Relativistic Fluid Dynamics). For more details we refer to the original works [35, 46, 47]. The application of this theory in this work is shown in Sec. 7.3 and Sec. 7.4, when comparing the IS theory and RTRFD[8] to the numerical solutions of the relativistic Boltzmann equation.

---

[8]The IS theory and RTRFD are solved by the numerical solver vSHASTA.

4. Sound waves, shock waves, and Mach cones

We have introduced the framework of ideal and viscous hydrodynamics which govern the motion of fluids. This chapter provides an overview of the general definitions of sound waves and shock waves assuming a perfect fluid. Furthermore, we discuss the appearance of conical structures, such as Mach cones, caused by moving supersonic perturbations. For a more detailed discussion we refer to Refs. [139, 140, 161, 162].

4.1. Sound waves in a perfect fluid

A small oscillation with a small amplitude in a compressible fluid is called a sound wave. A sound wave can be referred to as a small perturbation moving through a fluid at rest. In a fluid, a sound wave causes alternating compression and rarefaction. The elements of a fluid propagate in the same direction as the sound wave itself. Therefore, they are longitudinal waves. In addition, we remind that the propagation of a sound wave is an adiabatic process such as all continuous solutions in perfect fluids. This is not true anymore for shock waves which belong to the class of discontinuous solutions.

The speed of sound, i.e., the speed of propagation of a sound wave in a perfect fluid, is given by

$$c_s = \sqrt{\left(\frac{\partial p}{\partial e}\right)_{s/n}}, \tag{4.1}$$

which is the square root of partial derivative of the pressure, p, with respect to energy density, e. The speed of sound (4.1) is the solution of the wave equation, a homogeneous differential equation of second order, which is discussed in more details in Refs. [139, 140].

For an ultrarelativistic gas of massless particles with $e = 3p$, see Eq. (3.37), the speed of sound is given by

$$c_s = \frac{1}{\sqrt{3}}. \tag{4.2}$$

We notice that for a massless gas the speed of sound does not depend on the local temperature or chemical potential, i.e., it is overall constant. In contrast, the speed of sound for a massive Boltzmann gas depends locally on the temperature and chemical potential. For a vanishing chemical potential this reads,

$$c_s(T) = \sqrt{\left.\frac{2TK_2 - \frac{m}{2}(K_1 + K_3)}{6TK_2 - \frac{3m}{2}(K_1 + K_3) + mK_1 + \frac{m^2}{2T}(K_0 + K_2)}\right|_{\mu=0}}. \tag{4.3}$$

where $K_n = K_n(m/T)$ are the modified Bessel functions of second kind. The derivation of Eq. (4.3) is shown in Appendix C.

4.2. Moving perturbation in a perfect fluid

So far, we have only discussed the propagation of sound waves in fluids at rest. If the fluid itself is moving, or equally, a perturbation is moving through the fluid, then we observe additional phenomena. We assume a projectile or source of the sound wave propagating with a given velocity towards an observer at rest, then the emitted frequency of the sound wave seems to have a higher frequency than it actually has. The other way around, the sound wave seems to have a lower frequency if the source is moving away from the observer. This can be understood when one considers that the sound waves are compressed and decompressed, respectively. This phenomenon is known as the *Doppler effect*.

The usual situation, when the source of disturbance moves slower than the speed of sound in the fluid, i.e., $v_{\mathrm{source}} < c_s$, is called *subsonic flow*. Therefore, the interfering sound waves which originate from the source reach an observer in front before the source could reach him/her. This is shown in the left part in Fig. 4.1. However, this situation changes when the source propagates faster than the speed of sound, $v_{\mathrm{source}} > c_s$, as shown in the right part of Fig. 4.1. This case is called *ultrasonic flow*. Here, the speed of the source is faster than the speed of sound, so that the interfering sound waves emitted from the source are confined inside a 3-dimensional conical structure. Therefore the sound cannot be heard outside the cone and the source reaches the observer in front before the sound wave.
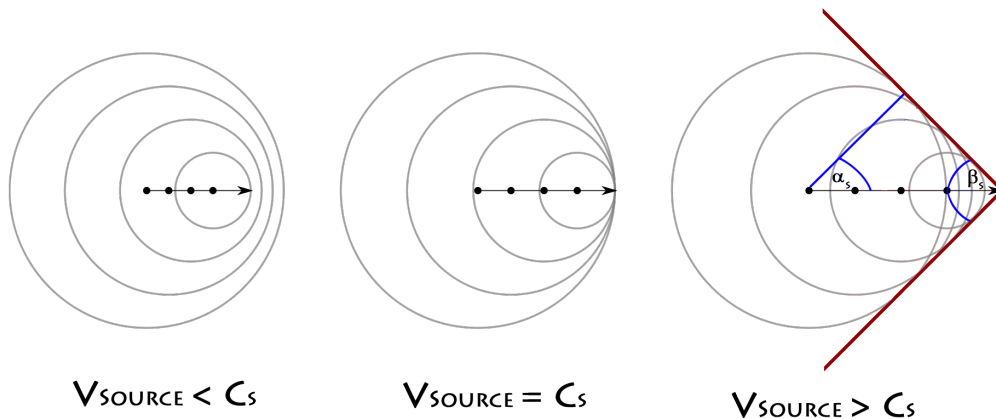
Figure 4.1.: The propagation of a weak perturbation through a fluid at rest. The perturbation emits sound waves propagating with the speed of sound. On the left, the perturbation is slower than the local speed of sound, in the middle, the perturbation is as fast as the speed of sound, and on the right, the perturbation exceeds the speed of sound. In the latter case the sound waves lie on a cone which is referred to as a Mach cone.

The cone is often referred to as *Mach cone*[1] in literature, and has an emission angle,

---
[1]Ernst Mach (1838-1916) was an Austrian physicist and philosopher who was a professor in Graz and

α_s, with

$$\cos \alpha_s = \frac{c_s}{v_{\text{source}}} \, , \tag{4.4}$$

and an opening angle, $2\beta_s$, with

$$\sin \beta_s = \frac{c_s}{v_{\text{source}}} \, . \tag{4.5}$$

We can read off the above relations from Fig. 4.1. The opening angle, $2\beta_s$, is also often referred to as *Mach angle* in literature. Furthermore, the ratio of v_{source}/c_s is defined as *Mach number*:

$$Ma = \frac{v_{\text{source}}}{c_s} \, . \tag{4.6}$$

The area which the perturbation touches during its evolution is called *Mach area* or *characteristic area.*

The appearance of a Mach cone in ultrasonic flow is not only interesting because of its geometrical structure, but is often connected to the existence of shock waves. This is the case, insofar the perturbation is not considered as weak anymore. In case of stronger perturbations the source emits shock waves instead of sound waves. In contrast to sound waves, shock waves are characterized by an abrupt and discontinuous change of the properties of the fluid such as pressure, energy density, or velocity. Moreover, they propagate with a speed faster than the speed of sound, which we refer to as the velocity of the shock front, v_{shock}. We introduce the properties of shock waves in the next section.
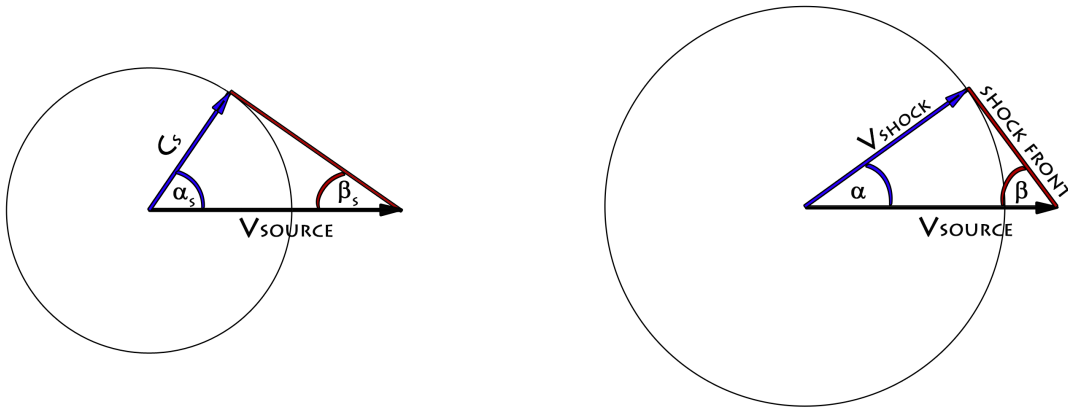
Figure 4.2.: The propagation of a perturbation, which emits sound waves (left) and shock waves (right). The angles of the Mach cone depends on the ratio of the velocity of the source, v_{source}, and the velocity of the emitted waves.

We above introduced the classical description and definition of a Mach cone, as usually presented in literature for a weak perturbation. We will extend the discussion

Prague.

a little bit more. In Fig. 4.2 we show the angle dependence of the emission angle of the Mach cone [163]. On the left we still consider a weak perturbation, where the emitted waves are sound waves propagating with c_s. Now the perturbation is not assumed to be weak anymore. Then the emitted waves are shock waves propagating with v_{shock}. As illustrated in the right part of Fig. 4.2, the emission angle of the Mach cone changes since the ratio of v_{shock} to v_{source} is smaller. Moreover, the length of the linear cone region, i.e., the shock front, is shorter.

Thus, we generalize the previously introduced angles of the Mach cone to

$$\cos \alpha = \frac{v_{\mathrm{shock}}}{v_{\mathrm{source}}} \, , \tag{4.7}$$

and

$$\sin \beta = \frac{v_{\mathrm{shock}}}{v_{\mathrm{source}}} \, , \tag{4.8}$$

which serve as a good approximation in case of not too strong perturbations. For the case that $v_{\mathrm{shock}} = v_{\mathrm{source}}$, the conical structure in the right part of Fig. 4.2 will vanish to one point. Furthermore, if the shock wave is faster than the source the Mach cone disappears. All shock-wave scenarios are illustrated in Fig. 4.1, when replacing c_s with v_{shock} and α_s (β_s) with α (β).

In the above discussion we have assumed that the source moving through the medium emits sound or shock waves isotropically in its LRF. This need not to be the case if one considers for example a highly energetic projectile depositing energy and momentum into the medium, which induce a different pattern of the generated Mach cone. Furthermore, increasing the strength of the perturbation for any kind of source induces the appearance of non-linear effects[2] along the shock front and behind the shock [139, 162, 163, 164, 165]. Moreover, the angle dependence of the Mach cone in the form introduced above serves also only as a good approximation for not too large perturbations, and may deviate for larger perturbations as well as for different sources due to the appearance of non-linear effects. This and more will be discussed in detail when presenting the numerical results in Chapter 8 using the numerical framework BAMPS.

4.3. Shock waves and discontinuities

In the previous section we have found out that in ultrasonic flow shock waves may form. We discuss now in more detail, what shock waves exactly are and introduce the theoretical description.

As mentioned in the previous section, the most important feature which characterizes shock waves is the abrupt and discontinuous change of hydrodynamic quantities such as pressure, energy density, flow velocity, etc. When the shock front hits the undisturbed medium, matter is heated up such the pressure and energy density rises instantaneously. The undisturbed medium has no chance to react fast enough since it is limited due to the speed of sound. Therefore, matter is pushed forward and the pressure progressively increases, respectively. This also implies that not a normal sound is emitted from the

---

[2]These are for example head shock or (anti-)diffusion wake and discussed in Chapter 8.

shock front, but a strong and loud bang. This is what happens for example when supersonic aircrafts travel faster than the speed of sound of air. Another example is the explosion of a bomb or the explosion of stars, like supernovae. The existence of shock waves in outer space are interesting and exciting phenomena, whereas the shock waves created in supernovae are of unimaginable strength.

The velocity of the shock wave, i.e., the signal propagation, as well as its strength depend strongly on the difference of the pressure in the shock wave and the pressure of the undisturbed medium in front of it. In the following we introduce the theoretical description of relativistic shock discontinuities. We still consider a perfect fluid without dissipation since viscous solutions of shock waves, at least in the relativistic regime, do not exist. The following discussion is analogous to that in Ref. [147]. For even more information considering shock discontinuities we also refer to Refs. [139, 161, 163, 166].

As mentioned above, shock waves represent discontinuous solutions of ideal hydrodynamics, where the general conservation equations introduced in Sec. 3.2 cannot be applied. At such discontinuities, the partial derivatives of the hydrodynamic quantities, $\partial_\mu N^\mu$ and $\partial_\mu T^{\mu\nu}$, are ill-defined. However, the general conservation equations can be replaced with pure algebraic equations which are well-defined across such discontinuities.

For this purpose we consider the shock discontinuity in its LRF. We also refer to it as shock front. For simplification, we assume the transverse direction to be homogeneous, and consider only the x-direction as relevant for the following problem. The matter, which enters the shock discontinuity (on the left) is denoted by the subindex 0, referring to the initial state. Now, matter enters that discontinuity with a given velocity, v_0. The matter is in local equilibrium, and is characterized by e_0, n_0, and p_0. In the following we are interested in the quantities behind the discontinuity. In other words, we aim to determine the final state of the quantities v, e, n, and p, which emerge from the shock front. For this purpose we define a small volume V, which encloses the shock discontinuity as shown in Fig. 4.3.

In the next step, we have to integrate the conservation equations (3.34) and (3.35) over the infinitely small volume V:

$$\partial_t \int_V \mathrm{d}^3x \, N^0 + \int_V \mathrm{d}^3x \, \partial_x N^x = 0 \,,$$
$$\partial_t \int_V \mathrm{d}^3x \, T^{00} + \int_V \mathrm{d}^3x \, \partial_x T^{x0} = 0 \,, \tag{4.9}$$
$$\partial_t \int_V \mathrm{d}^3x \, T^{x0} + \int_V \mathrm{d}^3x \, \partial_x T^{xx} = 0 \,.$$

We assume in the following a stable propagating shock discontinuity, i.e., a stationary scenario. Then matter in the small volume V does not change with time, which implies that the time derivatives in the above equations vanish. We perform an integration by parts and obtain the *Rankine-Hugoniot-Taub* relations, which represent the conservation of energy, momentum ,and particle number across the shock front,

$$n_0 u_0 = n u \,,$$
$$(e_0 + p_0)\gamma_0 u_0 = (e + p)\gamma u \,, \tag{4.10}$$
$$(e_0 + p_0)u_0^2 + p_0 = (e + p)u^2 + p \,.$$
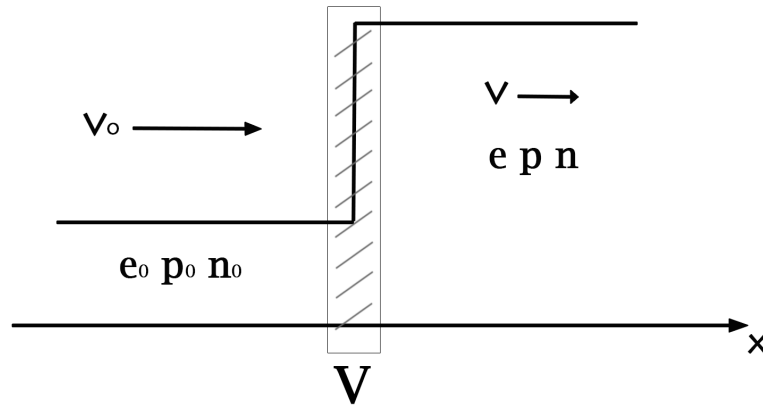
Figure 4.3.: A sketch of a shock discontinuity in its rest frame. On the left are the initial values v_0, e_0, n_0, and p_0. Matter propagates through the discontinuity, where the final values v, e, n, and p are obtained. A volume V encloses the shock discontinuity.

We have introduced here the four-velocity $u = \gamma v$ in the LRF of the shock front. The equations derived above are purely algebraic and valid for such shock discontinuities assuming a one-dimensional flow. For conical shock waves we refer to the discussion in [163].

The initial values on the left, v_0, e_0, n_0, and p_0, determine the final state, v, e, n, and p, on the right of the shock discontinuity. We require here that the equation of state, $p(e, n)$, is known. The introduced equations (4.10) are essential for the discussion of the relativistic Riemann problem in Chapter 5 and are partly used in Chapter 7 and 8, when discussing the numerical results of shock waves and Mach cones, respectively.

We have mentioned in Chapter 3 that in perfect fluids the entropy is conserved. This is true if we consider sonic perturbations, i.e., sound waves, which are considered as adiabatic processes. A remarkable feature of shock waves is that entropy is not conserved. As discussed in detail in Ref. [147], the specific entropy increases across the shock front, i.e.,

$$\frac{s}{n} \geq \frac{s_0}{n_0} \, . \tag{4.11}$$

The entropy conservation in perfect fluids is only valid for continuous, differentiable solutions. Shock discontinuities, as the name indicates, are not continuous such that Eq. (3.13) is not applicable. However, in the limit where the shock is infinitesimally small, the entropy is again preserved. Then the shock wave degenerates into an ordinary sound wave.

5. The relativistic Riemann problem

In this chapter we introduce the relativistic shock-tube problem, which is part of the famous Riemann problems in relativistic hydrodynamics. The Riemann problem has been first formulated by the mathematician Bernhard Riemann[1]. The problem deals with determining the temporal evolution of a perfect fluid which initially has a sharp discontinuity in velocity or thermodynamic variables, such as temperature or pressure. The initial discontinuity leads to the appearance of a shock wave and rarefaction wave. The final solution is totally determined by the initial values and the problem is self-similar. Under certain circumstances an analytic solution can be determined from the initial values, which is called self-similar solution.

Analytical solutions of the Riemann problem in the non-relativistic cases have been widely discussed in several publications in physics as well as in mathematics [139, 167]. However, in the relativistic regime such a solution is much more difficult to obtain. In many cases, a simple equation of state (EoS) and similarity methods have to be applied in order to get analytic expressions as shown in Refs. [33, 34, 168, 169, 170, 171]. Furthermore, solutions of the relativistic Riemann problem (rRP) in relativistic magnetohydrodynamics have been derived inter alia in Refs. [172, 173].

The analytic solution of the Riemann problem is quite often used to serve as a benchmark for numerical hydrodynamic solvers in the relativistic and non-relativistic regime. The almost exact reproduction of the analytic solutions proves that the numerical solvers are stable and trustworthy in capturing shock phenomena. After passing this benchmark, the hydrodynamic solvers can be applied to more complex hydrodynamic problems.

According to current knowledge, an analytic solution for the Riemann problem for dissipative fluids does not exist, not even for a simple ideal gas EoS. Therefore, the investigations of the rRP with nonzero dissipation have been performed via numerical solvers based on dissipative hydrodynamics [159, 174] and kinetic theory [33, 34]. From these works we can conclude that up to now only the results of kinetic transport models are trustworthy and able to describe any weakly coupled fluid covering ideal hydrodynamics and free streaming. This is part of this work and discussed in detail in Chapter 7. The solution of the rRP obtained in this section serves as a benchmark and is required for a deeper understanding of the evolution of shock waves.

In Sec. 5.1 we present the shock-tube problem which is a special case of the rRP and discuss the general procedure to obtain a solution. Using a simple EoS the problem admits an analytic solution, as discussed in Sec. 5.2. In Sec. 5.2.1 we will derive the equations for the rarefaction wave and, afterwards, in Sec. 5.2.2 the solution of the shock wave is discussed. In Sec. 5.2.3 we finally present our results.

---

[1]Bernhard Riemann (1826-1866) was a German mathematician who was a professor in Göttingen.

5.1. Phenomenological contemplation of the relativistic Riemann problem

We introduce the relativistic Riemann problem in the case of perfect fluids. The matter is assumed to be thermodynamically normal [171], e.g. an ideal gas, and, for the sake of simplicity, to be homogeneous in the transverse directions, such that the problem becomes $(1+1)$-dimensional.

In the Riemann problem we have matter in thermodynamical equilibrium separated by a membrane at $x = 0$. The pressures on the left $(x < 0)$ and right $(x \geq 0)$ sides of the membrane are p_0 and p_4, and the particle densities are n_0 and n_4, respectively. The velocities left and right of the discontinuity are v_0 and v_4. The "slab-on slab" collision problem where initially matter left or right of the discontinuity is moving, i.e., $v_0 \neq v_4$, is discussed in Ref. [171]. In the following we discuss only the shock-tube problem where the velocities on both sides of the membrane are zero, that is, $v_0 = v_4 = 0$, and with a pressure gradient $p_0 > p_4$.

In the shock-tube problem, removal of the membrane at time $t = 0$ leads to two propagating waves. A shock wave is propagating to the right with the velocity v_{shock}. Simultaneously, the tail of a rarefaction fan is propagating to the left with the speed of sound, c_s, into the matter with higher pressure. The region between these two waves includes a contact discontinuity propagating to the right with v_3 and a shock plateau which is bounded by the contact discontinuity and the shock front.

The solution for the ideal shock-tube problem is self-similar in time, that is, the solution keeps the same shape at all times, $t > 0$, without change. Therefore, the shape can only depend on the similarity variable

$$\xi = \frac{x}{t} \,. \tag{5.1}$$

Figure 5.1 shows the schematic representation of the particle density, pressure, and velocity profile against the similarity variable, ξ. Here, regions 0 and 4 represent the undisturbed matter at rest, 1 is the rarefaction wave, 2 denotes the constant region between the tail of the rarefaction wave and the contact discontinuity, while 3 is the shock plateau. The shock front is the discontinuity between regions 3 and 4.

The solution of the relativistic Riemann problem is obtained by matching the pressure, p_2, and velocity, v_2, at the rarefaction tail to the pressure and velocity of the shock plateau p_3 and v_3, that is, $p_2 = p_3$ and $v_2 = v_3$; see also Ref. [168]. In Sec. 5.2 we discuss the solution of the shock-tube problem using an EoS of the form

$$p = c_s^2 e \,, \tag{5.2}$$

which admits an analytical solution.

We have to determine the rarefaction wave using the conservation equations of particle number, energy, and momentum. In order to decouple the first-order differential equations, we use the similarity method. As mentioned above, this is possible, because the problem is self-similar. Therefore, we can replace position and time by the similarity variable (5.1). The procedure is discussed in Sec. 5.2.1. In Sec. 5.2.2 we discuss the part of the shock wave. The solution at the discontinuity is given by the Rankine-Hugoniot-Taub relations (4.10) in the LRF of the shock. The velocities of the shock
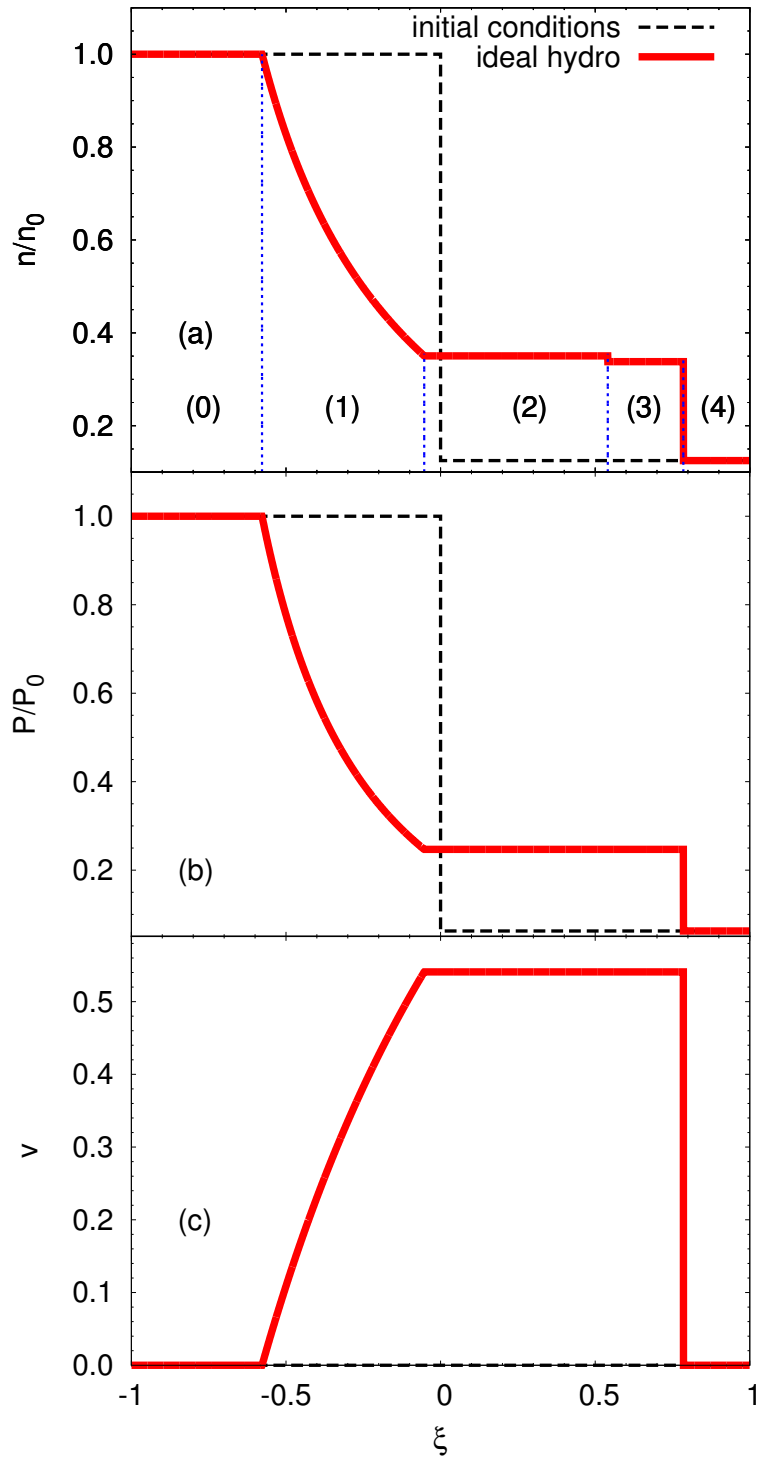
Figure 5.1.: Schematic representation of particle density (a), pressure (b), and velocity (c) as a function of the similarity variable, $\xi = x/t$, in the shock-tube problem.

plateau and the shock front in the LRF of the undisturbed matter can be expressed in terms of thermodynamic quantities before and after the discontinuity.

In general, using a more complicated EoS, the solution of the shock-tube problem requires a numerical integration of ordinary first-order differential equations, which is discussed in Ref. [168].

5.2. Analytic solution of the relativistic shock-tube problem in the perfect-fluid limit

5.2.1. The rarefaction wave

The rarefaction wave in the shock-tube problem can be determined using the conservation equations of particle number, Eq. (3.35), energy, and momentum, Eq. (3.34). We repeat the equations in $(1+1)$-dimensions with a different notation

$$\frac{\partial R}{\partial t} + \frac{\partial (Rv)}{\partial x} = 0 \,, \tag{5.3}$$

$$\frac{\partial M}{\partial t} + \frac{\partial (Mv)}{\partial x} = -\frac{\partial p}{\partial x} \,, \tag{5.4}$$

$$\frac{\partial E}{\partial t} + \frac{\partial (Ev)}{\partial x} = -\frac{\partial (pv)}{\partial x} \,. \tag{5.5}$$

Here $R = N^0$, $E = T^{00}$, and $M = T^{10}$ are the quantities in the laboratory frame, t is the time, p is the pressure, and v is the velocity in x-direction. We also introduce the following known relations which connect the quantities in the laboratory frame and LRF[2] in the case of perfect fluids,

$$R = N^0 = \gamma n \,, \tag{5.6}$$

$$E = T^{00} = \gamma^2(e+p) - p \,, \tag{5.7}$$

$$M = T^{10} = \gamma^2(e+p)v \,, \tag{5.8}$$

where e is the LRF energy density, n is LRF particle density, and $\gamma = 1/\sqrt{1-v^2}$ is the Lorentz factor. To close the conservation equations we have to use an EoS, $p = p(e, n)$. In the following we will restrict our calculations to an EoS which has a linear relation between the pressure and energy density via the speed of sound (5.2). We also define the specific enthalpy

$$w = e + p = \left(\frac{1}{c_s^2} + 1\right)p \,. \tag{5.9}$$

Due to the fact that the rRP is self-similar, we may use the similarity method [168]. The similarity method provides the possibility to decouple the differential equations (5.3), (5.4), and (5.5) and convert them into ordinary differential equations. This is realized by replacing the position and time with the similarity variable, ξ. In the following, we construct the solution of the rarefaction wave. First, we get the pressure and particle density, then we derive the velocity.

---

[2]See Eqs. (3.20) and (3.21).

Construction of the pressure $p_1(v)$ and particle density $n_1(v)$

Using expressions (5.6), (5.7), (5.8), and (5.9), we can write the conservation of energy (5.4) and momentum (5.5) in the following form

$$
\frac{\partial \left(w\gamma^2 - p \right)}{\partial t} + \frac{\partial \left(w\gamma^2 v \right)}{\partial x} = 0,
$$
$$
\frac{\partial \left(w\gamma^2 v \right)}{\partial t} + \frac{\partial \left(w\gamma^2 v^2 \right)}{\partial x} = -\frac{\partial p}{\partial x}. \tag{5.10}
$$

We perform a variable transformation using the similarity variable, $\xi = x/t$, and its relations

$$
\frac{\partial \xi}{\partial t} = -\frac{\xi}{t},
$$
$$
\frac{\partial \xi}{\partial x} = \frac{1}{t}. \tag{5.11}
$$

In the following, we multiply Eqs. (5.10) by $\partial \xi / \partial \xi = 1$ and use the relations (5.11). Afterwards, we multiply with t and $\partial \xi / \partial v$, such that both equations (5.10) are decoupled. We get

$$
(-\xi) \frac{\mathrm{d}\left(w\gamma^2 \right)}{\mathrm{d}v} + \frac{\mathrm{d}\left(w\gamma^2 v \right)}{\mathrm{d}v} + \xi \frac{\mathrm{d}p}{\mathrm{d}v} = 0,
$$
$$
(-\xi) \frac{\mathrm{d}\left(w\gamma^2 v \right)}{\mathrm{d}v} + \frac{\mathrm{d}\left(w\gamma^2 v^2 \right)}{\mathrm{d}v} + \frac{\mathrm{d}p}{\mathrm{d}v} = 0. \tag{5.12}
$$

Now, we equate both equations (5.12) to eliminate the variable ξ. Using the expression for the specific enthalpy (5.9) we obtain

$$
\frac{1}{(c_s^{-2} + 1)^2} \left(\frac{\mathrm{d}p}{\mathrm{d}v} \right)^2 - \frac{1}{c_s^{-2} + 1} \left(\frac{\mathrm{d}p}{\mathrm{d}v} \right) \frac{\mathrm{d}(p\gamma^2)}{\mathrm{d}v} + \left[\frac{\mathrm{d}(p\gamma^2 v)}{\mathrm{d}v} \right]^2
$$
$$
+ \frac{1}{c_s^{-2} + 1} \left(\frac{\mathrm{d}p}{\mathrm{d}v} \right) \frac{\mathrm{d}(p\gamma^2 v^2)}{\mathrm{d}v} - \left[\frac{\mathrm{d}(p\gamma^2 v^2)}{\mathrm{d}v} \frac{\mathrm{d}(p\gamma^2)}{\mathrm{d}v} \right] = 0. \tag{5.13}
$$

This relation can be rewritten as

$$
\left(\frac{\mathrm{d}p}{\mathrm{d}v} \right)^2 = c_s^2 \left(\frac{1}{c_s^2} + 1 \right)^2 p^2 \gamma^4. \tag{5.14}
$$

We obtain two solutions where only the solution with negative sign has a physical meaning

$$
\frac{\mathrm{d}p}{\mathrm{d}v} = -c_s \left(\frac{1}{c_s^2} + 1 \right) p\gamma^2. \tag{5.15}
$$

The solution for which $\mathrm{d}p/\mathrm{d}v > 0$ is unphysical since it describes a fluid compressing itself. As the next step, we integrate the equation above by separation of variables, i.e.,

$$
\int_{p_0}^{p} \frac{1}{p}\mathrm{d}p = -\left(\frac{1}{c_s} + c_s \right) \int_{v_0}^{v} \frac{1}{1 - v^2}\mathrm{d}v. \tag{5.16}
$$

The integral on the right-hand side can be calculated via a partial fraction leading to

$$
\begin{aligned}
\ln\left(\frac{p}{p_0}\right) &= -\left(\frac{1}{c_s} + c_s\right) \int_{v_0}^{v} \left[\frac{1}{1-v}\frac{1}{1+v}\right] dv \\
&= \frac{1}{2}\left(\frac{1}{c_s} + c_s\right)\left[\ln\frac{1-v}{1+v}\right]_{v_0}^{v}.
\end{aligned}
\tag{5.17}
$$

The final expression for the pressure of the rarefaction wave reads

$$
\boxed{p_1(v) = p_0\left(\frac{1-v}{1+v}\right)^{\frac{1}{2}\left(\frac{1}{c_s}+c_s\right)}},
\tag{5.18}
$$

where we have replaced $p \to p_1(v)$ for the correct notation.

In contrast to the propagation of the shock wave, the entropy is conserved during the expansion of the rarefaction wave. Therefore, we can use the adiabatic expansion rule [140] to determine the particle density

$$
\frac{p}{p_0} = \left(\frac{n}{n_0}\right)^{\Gamma}.
\tag{5.19}
$$

Here Γ is the adiabatic coefficient, which is determined by the EoS. Using the expressions (5.18) and (5.19), and the notation $n \to n_1(v)$, we can write for the particle density of the rarefaction wave

$$
\boxed{n_1(v) = n_0\left(\frac{1-v}{1+v}\right)^{\frac{1}{2\Gamma}\left(\frac{1}{c_s}+c_s\right)}}.
\tag{5.20}
$$

Construction of the velocity $v_1(\xi)$

We use again the conservation of energy (5.4) and momentum (5.5) and apply the similarity method to decouple both equations. Multiplying both equations with t we get

$$
\begin{aligned}
(-\xi)\frac{\partial M}{\partial \xi} + \frac{\partial (Mv)}{\partial \xi} + \frac{\partial p}{\partial \xi} &= 0, \\
(-\xi)\frac{\partial E}{\partial \xi} + \frac{\partial (Ev)}{\partial \xi} + \frac{\partial (pv)}{\partial \xi} &= 0,
\end{aligned}
\tag{5.21}
$$

and, after some transformations, we can rewrite

$$
\begin{aligned}
(v-\xi)\frac{dM}{d\xi} + M\frac{dv}{d\xi} + \frac{dp}{d\xi} &= 0, \\
(v-\xi)\frac{dE}{d\xi} + v\frac{dp}{d\xi} + (E+p)\frac{dv}{d\xi} &= 0.
\end{aligned}
\tag{5.22}
$$

Using expressions (5.7) and (5.8) we obtain after some algebraic transformations

$$(v - \xi)v\gamma^2 \frac{\mathrm{d}e}{\mathrm{d}\xi} + \left[1 + (v - \xi)v\gamma^2\right]\frac{\mathrm{d}p}{\mathrm{d}\xi} + \gamma^2(e + p)\left[(v - \xi)(1 + 2v^2\gamma^2) + v\right]\frac{\mathrm{d}v}{\mathrm{d}\xi} = 0,$$

$$(v - \xi)\gamma^2 \frac{\mathrm{d}e}{\mathrm{d}\xi} + \left[v + (v - \xi)v^2\gamma^2\right]\frac{\mathrm{d}p}{\mathrm{d}\xi} + \gamma^2(e + p)\left[2v\gamma^2(v - \xi) + 1\right]\frac{\mathrm{d}v}{\mathrm{d}\xi} = 0,$$

$$(5.23)$$

where we have used the following relations

$$\frac{\mathrm{d}\gamma}{\mathrm{d}\xi} = v\gamma^3 \frac{\mathrm{d}v}{\mathrm{d}\xi},$$

$$\frac{\mathrm{d}(\gamma v)}{\mathrm{d}\xi} = \gamma^3 \frac{\mathrm{d}v}{\mathrm{d}\xi}, \qquad (5.24)$$

$$\frac{\mathrm{d}\gamma^2}{\mathrm{d}\xi} = 2v\gamma^4 \frac{\mathrm{d}v}{\mathrm{d}\xi}.$$

Next, we use relation (5.2) to eliminate the pressure:

$$\left[v\gamma^2(v - \xi)(1 + c_s^2) + c_s^2\right]\frac{\mathrm{d}e}{\mathrm{d}\xi} + \gamma^2 e(1 + c_s^2)\left[(v - \xi)(1 + 2v^2\gamma^2) + v\right]\frac{\mathrm{d}v}{\mathrm{d}\xi} = 0,$$

$$\left[\gamma^2(v - \xi)(1 + v^2 c_s^2) + v c_s^2\right]\frac{\mathrm{d}e}{\mathrm{d}\xi} + \gamma^2 e(1 + c_s^2)\left[2v\gamma^2(v - \xi) + 1\right]\frac{\mathrm{d}v}{\mathrm{d}\xi} = 0.$$

$$(5.25)$$

We equate both equations to eliminate $\mathrm{d}e/\mathrm{d}\xi$. By means of algebraic transformations we then obtain the velocity of the rarefaction wave

$$\boxed{v_1(\xi) = \frac{\xi + c_s}{1 + \xi c_s}}, \qquad (5.26)$$

where we replaced $v \rightarrow v_1(\xi)$.

5.2.2. The shock wave

The conservation equations (5.3), (5.4), and (5.5) can not be applied to shock waves, since the derivatives are ill-defined at such discontinuities as discussed in Sec. 4.3. Thus, we apply the Rankine-Hugoniot-Taub relations (4.10) which represents the conservation of particle density and energy-momentum across the shock discontinuity[3], in order to derive the necessary equations for the shock wave.

We repeat the Rankine-Hugoniot-Taub relations (4.10) with a different notation,

$$n_3\widehat{u}_3 = n_4\widehat{u}_4,$$

$$(e_3 + p_3)\widehat{\gamma}_3\widehat{u}_3 = (e_4 + p_4)\widehat{\gamma}_4\widehat{u}_4, \qquad (5.27)$$

$$(e_3 + p_3)\widehat{u}_3^2 + p_3 = (e_4 + p_4)\widehat{u}_4^2 + p_4.$$

The "~" denotes that the quantities are taken in the rest frame of the shock front. The subindex 3 denotes the quantities entering the shock discontinuity, the subindex 4 denotes the quantities emerging from the shock front. $\widehat{u} = \widehat{\gamma}\widehat{v}$ is the four-velocity in the rest frame of the shock front.

---

[3]We also call it shock front.

The velocities

First, we derive the velocities, $\widehat{v}_3$ and $\widehat{v}_4$, of matter in the rest frame of the shock front. We start with the energy and momentum conservation across the shock discontinuity (5.27), which leads to

$$
\begin{aligned}
(e_3 + p_3)\widehat{\gamma}_3\widehat{u}_3 &= (e_4 + p_4)\widehat{\gamma}_4\widehat{u}_4, \\
(e_3 + p_3)\widehat{u}_3^2 + p_3 &= (e_4 + p_4)\widehat{u}_4^2 + p_4.
\end{aligned}
\tag{5.28}
$$

We can rewrite the above equations as

$$
(e_3 + p_3)\widehat{\gamma}_3^2\widehat{v}_3 = (e_4 + p_4)\widehat{\gamma}_4^2\widehat{v}_4 , \tag{5.29}
$$

$$
(e_3 + p_3)\widehat{\gamma}_3^2\widehat{v}_3^2 + p_3 = (e_4 + p_4)\widehat{\gamma}_4^2\widehat{v}_4^2 + p_4. \tag{5.30}
$$

The relation (5.29) is inserted into Eq. (5.30), which yields

$$
\widehat{\gamma}_3^2\widehat{v}_3^2 = \frac{(e_4 + p_4)}{(e_3 + p_3)}\widehat{\gamma}_4^2\widehat{v}_3\widehat{v}_4, \tag{5.31}
$$

$$
\widehat{\gamma}_4^2\widehat{v}_4^2 = \frac{(e_3 + p_3)}{(e_4 + p_4)}\widehat{\gamma}_3^2\widehat{v}_3\widehat{v}_4, \tag{5.32}
$$

such that we obtain the following equations:

$$
\widehat{v}_3^2(e_3 + p_4) - \widehat{v}_3\widehat{v}_4(e_3 + p_3) = (p_4 - p_3) , \tag{5.33}
$$

$$
\widehat{v}_4^2(e_4 + p_3) - \widehat{v}_3\widehat{v}_4(e_4 + p_4) = -(p_4 - p_3). \tag{5.34}
$$

We have used the relations $\widehat{\gamma}_3^2 = 1/(1 - \widehat{v}_3^2)$ and $\widehat{\gamma}_4^2 = 1/(1 - \widehat{v}_4^2)$ to expand all terms. Now, we add both equations, i.e.,

$$
\widehat{v}_3^2(e_3 + p_4) + \widehat{v}_4^2(e_4 + p_3) - \widehat{v}_3\widehat{v}_4(e_3 + p_3 + e_4 + p_4) = 0 , \tag{5.35}
$$

and divide them by $\widehat{v}_3\widehat{v}_4$. Applying the following expression $x = \widehat{v}_3/\widehat{v}_4$, we obtain

$$
x^2(e_3 + p_4) - x(e_3 + p_3 + e_4 + p_4) + (e_4 + p_3) = 0. \tag{5.36}
$$

The solution of the above equation is

$$
x = \frac{\widehat{v}_3}{\widehat{v}_4} = \frac{e_4 + p_3}{e_3 + p_4}. \tag{5.37}
$$

In order to obtain $\widehat{v}_3$ and $\widehat{v}_4$ in terms of the pressure and energy density the expression (5.37) is inserted into Eq. (5.30). This leads to

$$
\begin{aligned}
\widehat{v}_3 &= -\left(\frac{(p_4 - p_3)(e_4 + p_3)}{(e_4 - e_3)(e_3 + p_4)}\right)^{\frac{1}{2}} , \\
\widehat{v}_4 &= -\left(\frac{(p_4 - p_3)(e_3 + p_4)}{(e_4 - e_3)(e_4 + p_3)}\right)^{\frac{1}{2}} .
\end{aligned}
\tag{5.38}
$$

As expected, the velocities, $\widehat{v}_3$ and $\widehat{v}_4$, depend only on the pressure and energy density on both sides of the shock front. Using the relativistic velocity-addition formula, we can transform the velocities into the laboratory frame, i.e.,

$$v_3 = \frac{\widehat{v}_3 - \widehat{v}_4}{1 - \widehat{v}_3 \widehat{v}_4}, \qquad v_4 = 0. \tag{5.39}$$

We are able to determine the velocity of the shock plateau and shock front, respectively,

$$v_{\text{plat}} \equiv v_3 = \left[\frac{(p_3 - p_4)(e_3 - e_4)}{(e_4 + p_3)(e_3 + p_4)} \right]^{\frac{1}{2}}, \tag{5.40}$$

$$v_{\text{shock}} \equiv -\widehat{v}_4 = \left[\frac{(p_4 - p_3)(e_3 + p_4)}{(e_4 - e_3)(e_4 + p_3)} \right]^{\frac{1}{2}}. \tag{5.41}$$

For the velocity of the shock front, v_{shock}, there are two limits. For $p_3 \gg p_4$ and $e_3 \gg e_4$, the velocity of the shock front approaches the speed of light,

$$\lim_{p_3 \gg p_4, e_3 \gg e_4} v_{\text{shock}} \approx 1, \tag{5.42}$$

whereas for $p_3 \to p_4$ and $e_3 \to e_4$ we obtain the speed of sound

$$\lim_{p_3 \to p_4, e_3 \to e_4} v_{\text{shock}} \approx c_s = \left(\frac{\partial p}{\partial e} \right)^{\frac{1}{2}}. \tag{5.43}$$

In the latter case, the shock wave degenerates to a sound wave. In contrast, the velocity of the shock plateau covers the regime $0 \le v_{\text{plat}} \le 1$.

The pressure

As the next step, we derive the pressure, $p_3(v)$, for the shock wave, which is necessary to complete the solution of the rRP. For this purpose, we insert Eqs. (5.38) into Eq. (5.39). Using the expression for the EoS given in Eq. (5.2), and squaring the equations to get rid of the square roots, we get after some simple algebraic transformations the following quadratic expression,

$$p_3^2 + p_3 p_4 A + p_4^2 = 0, \tag{5.44}$$

with

$$A = \frac{2\left(c_s^2 - 1\right)\left(1 - c_s^2\right) - c_s^2 v^2 \left(1 - c_s^2\right)^2 - \frac{v^2}{c_s^2}\left(1 - c_s^2\right)^2}{\left(c_s^2 - 1\right)^2 \left(1 - v^2\right)}. \tag{5.45}$$

Only the positive solution has a physical meaning. It is given by

$$p_3(v) = -\frac{p_4 A}{2} + \sqrt{\left(\frac{p_4 A}{2}\right)^2 - p_4^2}, \tag{5.46}$$

which is the expression we are searching for.

5.2.3. Discussion for the ultrarelativistic gas of massless particles

In the following, we discuss the results we have achieved in our calculations for the shock-tube problem. We assume an ultrarelativistic gas of massless particles for which $p = e/3$ and the speed of sound is given by $c_s = 1/\sqrt{3}$. The corresponding adiabatic coefficient in this case is $\Gamma = 4/3$. We mention that the initial values are fixed, i.e., $p_0 > p_4$, n_0, n_4, $v_0 = v_4 = 0$. The discussion for a different EoS of the form $p = c_s^2 e$ is analogous.

The solution of the shock tube problem is obtained by matching the pressure and velocity at the rarefaction tail and at the shock front, i.e.,

$$p_2 = p_3 , \quad v_2 = v_3 . \tag{5.47}$$

For this purpose we use *Newton´s method* to determine the intersection point of Eq. (5.18),

$$p_1(v) = p_0 \left(\frac{1-v}{1+v} \right)^{\frac{2}{\sqrt{3}}} , \tag{5.48}$$

and Eq. (5.46),

$$p_3(v) = \gamma^2 p_4 \left[1 + \frac{5}{3}v^2 + 4v \left(\frac{1}{3} + \frac{1}{9}v^2 \right)^{\frac{1}{2}} \right] . \tag{5.49}$$

The intersection point represents the tail of the rarefaction wave and its connection to the constant plateau p_2. We obtain the velocity $v_2 = v_3$. This automatically leads to the determination of the pressure at the tail of the rarefaction wave and the shock plateau, where $p_2(v_2) = p_3(v_3)$. In addition, using Eq. (5.20) we get,

$$n_2 = n_1(v_2) = n_0 \left(\frac{1-v}{1+v} \right)^{\frac{\sqrt{3}}{2}} , \tag{5.50}$$

which corresponds to the particle density at the tail of the rarefaction wave.

The rarefaction wave propagates with the speed of sound to the left, which is our starting point to draw the profile. The velocity in the rarefaction wave is given by Eq. (5.26),

$$v_1(\xi) = \frac{1 + \xi\sqrt{3}}{\sqrt{3} + \xi} . \tag{5.51}$$

Here we use the similarity variable, which covers the range $-1 \leq \xi \leq 1$. The pressure and particle density at the rarefaction wave are given by $p_1(v)$ and $n_1(v)$, respectively.

In the following, we have to determine the velocities in the rest frame of the shock, Eq. (5.38). Thereon, we are able to determine the velocity of the plateau, v_{plat}, given by Eq. (5.40), the shock front, v_{shock}, given by Eq. (5.41), as well as the particle density,

$$n_3 = n_4 \frac{\widehat{\gamma}_4 \widehat{v}_4}{\widehat{\gamma}_3 \widehat{v}_3} . \tag{5.52}$$

The region left of the rarefaction wave and right of the shock front are given in terms of the values of the undisturbed matter at rest. Now, the solution of the shock-tube problem which is a special case of the relativistic Riemann problems is complete.

However, the solution discussed here is restricted to a simple EoS which has the form as shown in Eq. (5.2). When considering another EoS which has a more complicated form or simply the pressure has an additional dependence on the particle density an analytical solution is not possible anymore. Thus, the solution of the rarefaction wave has to be calculated via numerical integration.

In Chapter 7 we discuss in particular the solutions of the shock-tube problem using numerical solvers where the analytical solution is used as a reference to check the perfect-fluid limit. In addition, using the numerical solvers we are able to produce viscous solutions of the rRP. We will observe how the sharp profiles smoothen out and the characteristic structures are washed out due to dissipation. Furthermore, we show the solutions for a different EoS and a system with more than one particle species.

6. The kinetic transport model BAMPS

In this chapter we introduce the relativistic microscopic transport model BAMPS (**B**oltzmann **A**pproach **T**o **M**ulti-**P**arton **S**cattering) which has been developed by Z. Xu and C. Greiner [41] in order to investigate and to understand the early evolution and thermalization of the hot and dense quark-gluon matter created in heavy-ion collisions (HIC) at RHIC and LHC energies[1]. This has been realized by implementing perturbative QCD (pQCD) interactions for binary collisions as well as for creation and annihilation processes. Furthermore, the model delivers a facility to investigate two different HIC-phenomena, jet quenching and elliptic flow, within one framework. Since then it has been updated and successfully applied to a wide range of phenomena and its applications. These are the comparison of kinetic to hydrodynamic theory, understanding and calculating transport coefficients, and the investigation of shock-wave phenomena. Furthermore, it has been extended and improved by several people, which makes this model a powerful framework for many present and future studies.

In this work, the main emphasis is on the investigation of shock-wave phenomena which are realized within a static box scenario as well as in full simulations of HIC. The feature of pQCD scattering processes, as introduced in the original version of BAMPS [41], is not treated here. In this work, we concentrate on the feature of BAMPS in dealing with an accurate numerical solution of the relativistic Boltzmann equation using momentum-independent matrix elements, i.e., isotropic cross sections.

This chapter is organized as follows: We start with the basic numerical framework of BAMPS in Sec. 6.1 where the idea of the core model is discussed. In Sec. 6.2 and 6.3 we introduce the space-time geometry and initial momentum sampling, respectively. The implementation of the momentum-independent cross sections is shown in the following section. Afterwards, in Sec. 6.5 we describe the method to extract several hydrodynamic quantities from BAMPS. In Sec. 6.6 we finally introduce other works realized with BAMPS in order to present the other abilities and achievements of the model.

6.1. The basic numerical framework

6.1.1. Basic idea

BAMPS is a full (3+1)-dimensional kinetic transport model which solves the relativistic Boltzmann equation (rBE),

$$p^\mu \partial_\mu f(x,p) = C = C_{22} + C_{23} + \cdots ,$$ (6.1)

for a semi-classical Boltzmann gas using a stochastic collision algorithm [175, 176, 177, 178]. Bose enhancement and Pauli blocking are currently not taken into account. The

---

[1]Thus, BAMPS is often referred to as a partonic cascade, because it is originally designed to study the early partonic phase of HIC.

Boltzmann equation[2] describes the time evolution of the single-particle distribution function, $f(x, p)$, in presence of collisions represented here by the collision term, C. For $C = 0$ the solution is given by free streaming, represented by the left part of the equation. For $C \neq 0$, the time evolution of the phase-space distribution is altered by binary $2 \leftrightarrow 2$ and/or inelastic scattering $2 \leftrightarrow 3$ processes.

As mentioned above, BAMPS solves the rBE using a stochastic collision algorithm, which makes it so powerful compared to different approaches based on a geometrical interpretation of cross sections. For example, ZPC [179, 180] is a partonic cascade which implements the partonic dynamics with elastic scatterings and a geometric interpretation of the cross section. It turns out that when the mean free path, λ_{mfp}, of the particles is not much larger than the interaction length, $\sqrt{\sigma/\pi}$, causality violation arises. In order to solve this limitation, the subdivision or *test particle method* has been introduced in MPC [181]. This method preserves covariance. However, the geometric interpretation of cross sections is limited inter alia due to the following facts: applying the models based on the geometrical interpretation of cross sections to dense matter where the mean free path is very small compared to the system size, the computation time is very high since one has to use a large number of test particles in order to preserve covariance and correct collision rates. Moreover, due to the fact that one has to go through the list of all particles to check the next collision time, the computation time increases quadratically with the number of test particles. This can be avoided by dividing space in smaller areas, in order to decrease the checking of collision partners. However, the numerical accuracy suffers especially in the region at the borders of these areas. Another disadvantage is that a consistent implementation of inelastic processes in the geometrical picture is difficult and almost impossible for the annihilation process $3 \rightarrow 2$.

In BAMPS the incorporation of inelastic processes is possible since the model relies on the stochastic algorithm. Inelastic processes are important when the system has to achieve chemical equilibrium. In order to maintain detailed balance, a consistent incorporation of $3 \rightarrow 2$ processes besides $2 \rightarrow 3$ has to be realized. As we will show in this work the stochastic algorithm has the advantage that it allows for an accurate solution of the rBE even in the almost perfect-fluid limit. In addition, due to the natural division in cells, the computation time for small mean free paths compared to the system sizes does not increase as fast as in the geometrical method. In the following, we introduce the general fundamental operation method.

In order to numerically calculate the space-time evolution of the distribution function, $f(x, p)$, via the rBE, space and time in BAMPS are discretized into small cells with a volume, $\Delta V = \Delta x \cdot \Delta y \cdot \Delta z$, and small time steps, Δt, respectively. The distribution function is represented by a certain number of point particles located in each cell as illustrated in Fig. 6.1. Here, we require that the cell size has to be sufficiently small in order to resolve spatial gradients. Only if this condition is fulfilled, each cell represents the distribution function properly. Every particle in these cells has a well defined four-momentum, $p^\mu = (E, \vec{p})$. At each time step, particles may interact only with other particles in the same cell, without regarding their spatial difference, by a given collision probability, P. This is calculated dynamically for all particles. Before and

---

[2] The Boltzmann equation Eq. (6.1) including the collision term is introduced in Sec. 3.1.
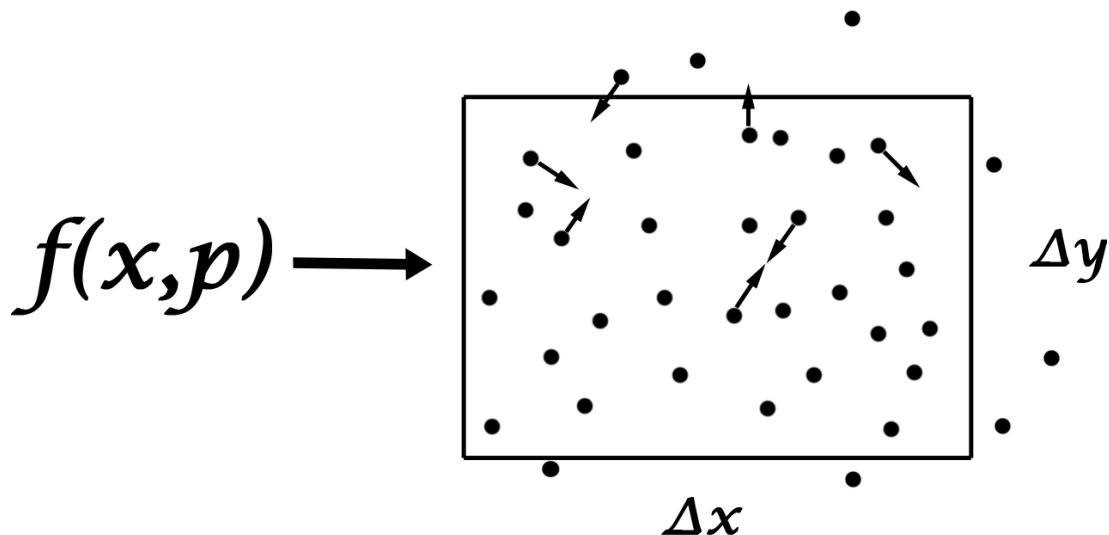
Figure 6.1.: In BAMPS, each cell with a given number of particles corresponds to a single-particle distribution function, $f(x,p)$. The time evolution of the distribution function via the rBE is realized as follows: Within a time step, Δt, particles propagate freely but they may collide with other particles in the same cell with a given collision probability, irrespectively of their spatial separation.

after the collision, particles propagate via free streaming.

The probability of a collision is a number in the range $(0 < P \leq 1]$, which is one important difference to the geometric method where the collision probability is either 0 or 1. Using the Monte Carlo sampling in BAMPS, a random number is diced and compared to the calculated probability. If the random number is smaller than P the collision occurs, otherwise it does not. Of course, one has to ensure that P is not larger than one. Therefore, the time step, Δt, as well as the volume element, ΔV, have to be chosen appropriately.

However, if the volume element is too small and does not contain enough particles, one encounters a problem when using the stochastic algorithm. As we mentioned above, the distribution function is represented by the particles in each volume element. The stochastic method only works properly if the number of particles in the cells is sufficiently large. For example, if less than two particles are in the cells, the distribution function is not represented in an appropriate way. Moreover, the collision algorithm does not work, since no collision partners are available. This leads to a wrong collision rate, as discussed in Ref. [41].

In order to solve this problem, the test particle method is used. The real number of particles is multiplied with the test particle number, N_{test}, and therefore adjusts the test particles in the simulation to an appropriate number[3]. Of course, the test particle number is implemented in such a way that the mean free path is not changed. In

---

[3]The motivation to implement the test particle number, N_{test}, in models based on the stochastic interpretation of the cross section is thus different to models based on the geometrical one.

order to accomplish this, the probability, P, is scaled with N_{test}. Furthermore, several extracted physical observables have to be rescaled with N_{test} as well. This is discussed in particular in Sec. 6.5.

Note that the test particle number can be in the range of $[0 < N_{\text{test}} < \infty]$. Depending on the densities and volumes we use in our simulations, N_{test} has to be chosen accordingly.

For the given limits, $\Delta t, \Delta V \to 0$ and $N_{\text{test}} \to \infty$, the rBE is solved exactly [33,34]. However, this is computationally very expensive, but a good choice of parameters is sufficient to solve the rBe in a very accurate way. These choice are as follows:

- The time step should be at least one order of magnitude smaller than the local mean free path λ_{mfp} of the particles[4]. Among other things this is important in order to ensure the correct collision rate.

- The cell sizes, Δx, Δy, and Δz, have to be smaller than the local mean free path, λ_{mfp}. Moreover, the cell sizes have to be small enough to resolve spatial gradients.

- The number of particles in each cell should be at least $8 - 10$ to represent the distribution function in an accurate way.

If the above conditions are fulfilled we can conclude that the physical results are almost independent of the discretization of space and time in cells and time steps, respectively, as well as of the approximation of the distribution function by test particles located in cells. If one violates these conditions numerical artifacts arise as discussed in Refs. [34, 41]. The magnitude of the numerical artifacts depends on the level of the violation of the conditions listed above. We will discuss in Chapter 7 some ot those limitations when presenting the accurate solution of shock waves. In particular Sec. 7.5.1 provides a detailed discussion on the numerical convergence when varying the number of test particles per cell and the cell length with respect to the local mean free path.

6.1.2. Probabilities and cross sections

So far we have introduced the core of the model based on the stochastic algorithm. This method allows us to incorporate certain scattering processes: elastic $2 \to 2$ scattering, inelastic process $2 \to 3$ and its reverse channel $3 \to 2$. The collision probability for a $2 \to N$ process is expressed by

$$P_{2N} = v_{\text{rel}} \frac{\sigma_{2N}}{N_{\text{test}}} \frac{\Delta t}{\Delta V} \, , \tag{6.2}$$

where $N = 2, 3$ and σ_{2N} is the cross section. The relative velocity of two incoming particles is defined as

$$v_{\text{rel}} = \frac{\sqrt{(p_1^\mu p_2^\mu)^2 - m_1^2 m_2^2}}{E_1 E_2} \, . \tag{6.3}$$

---

[4]This value is based on personal experience.

In the massless case, the above relation simplifies to

$$v_{\text{rel}} = \frac{s}{2E_1 E_2} \, , \tag{6.4}$$

with

$$s = (p_1^\mu + p_2^\mu)^2 = (E_1 + E_2)^2 - \sum_{i=1}^{3} \left(p_1^i + p_2^i\right)^2 \, , \tag{6.5}$$

being one of the Mandelstam variable, while $\sqrt{s}$ denotes the center of mass energy, i.e., the invariant mass of the particle pair. The probability for the annihilation process $3 \to 2$ for three particles 1, 2, and 3 is given by

$$P_{32} = \frac{1}{8E_1 E_2 E_3} \frac{I_{32}}{N_{\text{test}}} \frac{\Delta t}{(\Delta V)^2} \, , \tag{6.6}$$

where I_{32} is the phase-space matrix element corresponding to the cross section σ_{2N}. The introduced probabilities are scaled with the test particle number, N_{test}, which we have introduced above.

The collision terms, C_{22} and C_{23}, and their definitions have been introduced in Sec. 3.1. From these terms we can read off the usual definitions of the momentum-dependent cross sections, i.e.,

$$\sigma_{22} = \frac{1}{2s} \frac{1}{2} \int \frac{d\Gamma'_1}{2} \frac{d\Gamma'_2}{2} |M_{12 \to 1'2'}|^2 (2\pi)^4 \delta^{(4)} \left(p_1 + p_2 - p'_1 - p'_2\right) \, , \tag{6.7}$$

$$\sigma_{23} = \frac{1}{2s} \frac{1}{3!} \int \frac{d\Gamma'_1}{2} \frac{d\Gamma'_2}{2} \frac{d\Gamma'_3}{2} |M_{12 \to 1'2'3'}|^2 (2\pi)^4 \delta^{(4)} \left(p_1 + p_2 - p'_1 - p'_2 - p'_3\right) \, . \tag{6.8}$$

The phase-space matrix element [41] reads

$$I_{32} = \frac{1}{2!} \int \frac{d\Gamma'_1}{2} \frac{d\Gamma'_2}{2} |M_{123 \to 1'2'}|^2 (2\pi)^4 \delta^{(4)} \left(p_1 + p_2 + p_3 - p'_1 - p'_2\right) \, . \tag{6.9}$$

The matrix elements in the expressions for cross sections are, in general, momentum dependent and have to be derived from the underlying field theory. In the original version of BAMPS the matrix elements have been implemented as given by pQCD, which is discussed in detail in Refs. [41, 182]. In this work, we use momentum-independent matrix elements, as shown in Sec. 6.4.

6.2. Space-time geometry in BAMPS

There are two main geometry types in BAMPS used in this as well as in other works. We will briefly discuss them.

6.2.1. Heavy-ion collisions

BAMPS has been designed for the simulation of ultrarelativistic heavy-ion collisions [41]. For this purpose, the transverse cell structure is kept constant, $\Delta x = \Delta y = \text{const}$, since the expansion in transverse direction is small compared to the expansion

in longitudinal direction. The grid in the transverse direction is always set to be large enough for the individual setup. In contrast, the cell size in the longitudinal direction, Δz, is dynamically adjusted in space-time rapidity according to

$$\eta_{\text{rap}} = \frac{1}{2} \ln \frac{t+z}{t-z} \, . \tag{6.10}$$

Due to the fact that the system behaves approximately Bjorken-like [21] in the longitudinal direction, it turns out that we automatically obtain almost equally sized bins in space-time rapidity, η_{rap}. We adjust N_{test} such that in average there are enough particles in each cell. In order to reduce numerical artifacts, the sizes of the cells are adjusted in such a way that the mean free path is of the order or larger than the cell sizes. Since this is not always possible and densities and the corresponding mean free paths vary a lot, the cells are "joggeled". This procedure prevents also other numerical artifacts due to the static cell structure, which are discussed in Ref. [41]. As a final remark, there are no special boundary conditions in this scenario, since we have an expansion into vacuum.

6.2.2. Static box

The stationary problems are simulated in a static box. Here, we have a better control of the boundary conditions. As the name indicates, all cell sizes are constant during the whole simulation, i.e., $\Delta x = \Delta y = \Delta z = \text{const}$.

Depending on the individual problem, we can set our boundary conditions appropriately. We have to decide what happens to particles colliding with the static walls in each direction. We discuss the scenarios at the point when a particle hits the boundary. We do so for the x-direction since the generalization for the y and z-direction is then straightforward.

- Periodic boundary conditions are used in the case where the specific direction is homogeneous.

  When a particle with position X collides with the boundary in x-direction, then its position changes the sign, $X = -X$. Therefore, it moves to the other side of the box. The particle momentum does not change.

- Elastic walls are used in the case where the border in the specific direction is a hard wall.

  When a particle with momentum P_X collides with the wall in x-direction, then its momentum changes sign, $P_X = -P_X$. It is reflected by the wall without loosing any energy. The particle position does not change.

- Reservoirs: They are used where we simulate a constant thermal reservoir with a given temperature, T, fugacity, λ, and collective velocity, $\vec{v}$.

  When a particle collides with the boundary in x-direction, the particle is instantaneously removed from the whole simulation. Independent from the removal, particles are inserted at a specific rate. This is discussed in Appendix F.2.

6.3. Initial momentum sampling

6.3.1. Heavy-ion collisions

We discuss the initial momentum sampling for heavy-ion collisions in Chapter 8.

6.3.2. Static box

When performing numerical calculations in BAMPS, we have to initialize the system according to some distribution function. If not stated otherwise, we sample for each particle species with a temperature, T, chemical potential, μ, collective velocity, $\vec{v}$, and constant or vanishing mass, m, a thermal distribution for a Boltzmann gas,

$$f(x,p) = e^{-\frac{u^\mu p_\mu - \mu}{T}} . \tag{6.11}$$

The four-velocity is $u^\mu = \gamma(1, \vec{v})$, and the four-momentum vector is $p^\mu = (E, \vec{p})$ with $E^2 = p^2 + m^2$. We briefly introduce the numerical implementation to sample the momenta in Appendix F.1. The method is based on the rejection sampling method introduced in Appendix E.

6.4. Implementation of momentum-independent cross sections

If not stated otherwise, we use isotropic cross sections for elastic and inelastic processes throughout this work such that the matrix elements introduced previously in Sec. 6.1 are momentum-independent. Furthermore, the cross sections are calculated locally in each cell. We begin with the cross sections for elastic processes and continue with the inelastic processes afterwards. Depending on the implemented method, we need to know different hydrodynamic quantities in each cell and time step during the simulation. These quantities are computed using the procedure introduced in Sec. 6.5.

Before discussing the methods to implement the cross section into BAMPS, we introduce the main definitions related to the cross section which are employed in this work. The first one is the mean free path which is related to the cross section by

$$\lambda_{\mathrm{mfp}} = \frac{1}{n\sigma} , \tag{6.12}$$

where n is the LRF particle density. Hence, for a given density and the cross section, the mean free path is given by the relation above.

For elastic and isotropic processes in an ultrarelativistic gas of massless particles, a simple relation exists between the cross section and the shear viscosity[5] over entropy density ratio. The general formula for the shear viscosity [105] is given in terms of the collision rate:

$$\eta = \frac{4e}{15R^{\mathrm{tr}}} . \tag{6.13}$$

---

[5]We introduced the transport coefficient η in Chapter 3.

e is the LRF energy density. In case of binary isotropic cross sections the transport collision rate [45] is given by

$$R^{\mathrm{tr}} = \frac{2}{3} n \sigma_{22} \,, \tag{6.14}$$

where n is the LRF particle density and σ_{22} is the cross section for isotropic binary collisions. Inserting the above expression into (6.13) we obtain,

$$\eta = \frac{2e}{5n\sigma_{22}} \,. \tag{6.15}$$

This equation relates the cross section to the transport coefficient η for isotropic binary collisions, as derived in Ref. [39]. We have to mention that Eq. (6.15) is approximately true. Recent calculations extracting the shear viscosity from kinetic theory using BAMPS [183, 184], show a tiny deviation from the above relation. This has also been found in Refs. [35, 47]. However, unless stated otherwise, we exclusively use Eq. (6.15) throughout this work.

For the case where we also consider inelastic processes, Eq. (6.15) has to be modified. The relation between the cross sections and the shear viscosity for elastic and inelastic scatterings reads

$$\eta = \frac{2e}{5n\left(\sigma_{22} + \frac{3}{2}\sigma_{23}\right)} \,. \tag{6.16}$$

Here, σ_{23} is the isotropic cross section for inelastic processes. The formula above is derived in Ref. [185] and confirmed using BAMPS in Ref. [183]. For vanishing inelastic processes, i.e., $\sigma_{23} = 0$, Eq. (6.16) reduces to Eq. (6.15). We mention that the relation above is only valid for massless particles.

The relationship between the heat conductivity and the cross section [39, 186] in IS theory, which is partly used in this thesis for the numerical solver vSHASTA, is given by

$$\kappa = \frac{2}{\sigma} \,. \tag{6.17}$$

The above relation does not hold in all cases, as shown in recently published works [35, 187]. Part of the work done in Ref. [35] is shown in this thesis, see Chapter 7.

6.4.1. Elastic processes: constant cross section

This is the most trivial case in BAMPS and requires no further assumptions. For a single-component system, the cross section σ_{22} is overall constant and independent of the densities during the whole simulation.

In the case of more than one particle species, we set different but constant cross sections[6] for each particle species separately. For example, considering two particle species, A and B, we have a cross section for species A to species A, $\sigma_{22}(\mathrm{A} \leftrightarrow \mathrm{A})$, and species species B to species B, $\sigma_{22}(\mathrm{B} \leftrightarrow \mathrm{B})$. Moreover, we have to specify a mixed cross section $\sigma_{22}(\mathrm{A} \leftrightarrow \mathrm{B})$.

---

[6]These have also no local space or time dependence.

6.4.2. Elastic processes: constant mean free path

This method implies an overall constant local mean free path during the whole simulation, $\lambda_{\mathrm{mfp}} = C$, where C is a constant. This scenario is useful when huge differences in densities exist, for example, due to strong local energy depositions. In order to prevent numerical artifacts originating from a smaller mean free path compared to the cell size, the cross section in each cell is locally adjusted at every time step, which results to a constant mean free path. The cross section is calculated via

$$\sigma_{22} = \frac{1}{nC} \, . \tag{6.18}$$

If large densities exist the cross section is automatically reduced and vice versa.

6.4.3. Elastic processes: constant shear viscosity over entropy density ratio, η/s

In the following, we introduce the method to keep the shear viscosity over entropy density ratio constant in a simulation with massless particles. The motivation to do so arises from viscous hydrodynamic models applied to heavy-ion collisions. While kinetic models have the cross section, σ, as input parameter, the input in viscous hydrodynamics are the transport coefficients, such as the shear viscosity coefficient, η. Therefore, a relation between those two input parameters is essential for a direct comparison between both theories.

In the following, we divide both sides of Eq. (6.15) by the entropy density, s, see Eq. (3.33), and obtain an expression for the shear viscosity over entropy density ratio:

$$\frac{\eta}{s} = \frac{2e}{5n^2(4 - \ln\lambda)\sigma_{22}} \, . \tag{6.19}$$

Reshaping the relation above we obtain a formula for the cross section which depends on the ratio of shear viscosity over entropy density,

$$\sigma_{22} = \frac{2e}{5n^2(4 - \ln\lambda)} \left(\frac{\eta}{s}\right)^{-1} \, . \tag{6.20}$$

The cross section is adjusted locally at each time step in such a way, that the shear viscosity over entropy density ratio is achieved.

6.4.4. Inelastic processes

In this work we also apply simulations which include inelastic scattering processes in addition to the usual binary collisions. However, we restrict this scenario to a single species of massless particles. Furthermore, we apply only constant cross sections.

The isotropic cross sections for the elastic processes, $2 \to 2$, is given by σ_{22}. In addition, we have the isotropic cross section, σ_{23}, for the creation process, $2 \to 3$, and also the cross section for the annihilation process, $3 \to 2$, which is given by the phase-space matrix-element, I_{32}. We choose the cross section for the inelastic process to be equal to the elastic one, i.e., $\sigma_{23} = \sigma_{22}$. In order to maintain detailed balance,

the expression I_{32} for momentum-independent matrix elements is given in terms of the cross section σ_{23}:

$$I_{32} = \frac{192\pi^2}{g}\sigma_{23}\,. \tag{6.21}$$

For more details see Ref. [41]. The implemented method discussed above implies that the system can achieve chemical equilibrium. The amount of time the system needs to chemically equilibrate strongly depends on the cross section and initial conditions. The numerical realization for such a scenario is shown in Sec. 7.2.1.

6.5. Computation and extraction of hydrodynamic quantities

In this section we discuss the extraction of hydrodynamic quantities, which is highly important and necessary for the whole discussion of the numerical results coming up later[7]. Moreover, the extracted hydrodynamic quantities are partially required to calculate the cross section, as introduced above.

We will describe the extraction of the hydrodynamic quantities in both reference frames[8], Eckart and Landau, as well the extraction for a multi-component system in a detailed way. In the following discussion, we introduce the method directly for a multi-component system. The only restriction is that the procedure is only valid for a Boltzmann gas where the mass for each particle species is constant or zero. For a more detailed discussion related to hydrodynamic quantities, see Chapter 3.

6.5.1. Computing the energy-momentum tensor and particle four-flow

The first step in computing the hydrodynamic quantities is to determine all components of the particle four-flow and the energy-momentum tensor as a function of time and position. We consider a system of N_{spec} different particle species. For each particle species, i, we identify

$$N_i^{\mu}(x^{\mu}) = \frac{g_i}{(2\pi)^3} \int \frac{d^3p}{E}\, p^{\mu} f_i(x,p)\,,$$
$$T_i^{\mu\nu}(x^{\mu}) = \frac{g_i}{(2\pi)^3} \int \frac{d^3p}{E}\, p^{\mu}p^{\nu} f_i(x,p)\,, \tag{6.22}$$

where $f_i(x,p)$ is the distribution function and g_i is the degeneracy factor of each particle species. So far, we have repeated the relevant definitions from Sec. 3.3.5. Next, we have to perform the transition from the continuous integral to the numerical summation in

---

[7]A big advantage of BAMPS is its possibility to obtain the dissipative quantities directly from the off-equilibrium distribution function in the simulation.

[8]There are more reference frames, but these are the most familiar ones. They have also a physical motivation.

BAMPS. This leads to

$$N_i^\mu(x^\mu) = \frac{1}{\Delta V N_{\text{test}}} \sum_{j=1}^{N_i} \frac{p_{ij}^\mu}{p_{ij}^0}, \tag{6.23}$$

$$T_i^{\mu\nu}(x^\mu) = \frac{1}{\Delta V N_{\text{test}}} \sum_{j=1}^{N_i} \frac{p_{ij}^\mu p_{ij}^\nu}{p_{ij}^0} \ . \tag{6.24}$$

The integral has been replaced by a discrete summation over all particles, N_i, of each species. As mentioned above, in BAMPS we can reconstruct the distribution function $f(x,p)$ from the momentum distribution of the particles inside an arbitrary volume[9], ΔV, i.e., the position, x^μ, and momentum, p^μ, of each particle is explicitly given at any time step and position. Due to the test-particle method, the number of particles has to be rescaled with N_{test} in order to obtain the correct physical values in the end. Finally, we obtain $N^\mu(x^\mu)$ and $T^{\mu\nu}(x^\mu)$ from Eqs. (6.23) and (6.24) via summing over all particle species[10], i.e.,

$$N^\mu(x^\mu) = \sum_{i=1}^{N_{\text{spec}}} N_i^\mu(x^\mu), \tag{6.25}$$

$$T^{\mu\nu}(x^\mu) = \sum_{i=1}^{N_{\text{spec}}} T_i^{\mu\nu}(x^\mu). \tag{6.26}$$

As mentioned above, space in BAMPS is discretized naturally. When computing the hydrodynamic quantities during the simulation in order to calculate the cross sections, the size of the volume, ΔV, is equal to the volume of the cell. However, if hydrodynamic quantities are computed in order to extract them off line for the analysis, the size of the volume element can be chosen freely. The finer the grid is, the better is the resolution[11], but unfortunately, the size of statistical fluctuations also increases. In order to reduce the statistical fluctuations, we have to perform an ensemble average of the particle four-flow $N_i^\mu(x^\mu)$ and energy-momentum tensor $T_i^{\mu\nu}(x^\mu)$ of each particle species.

In the following we introduce the calculation of the hydrodynamic quantities in the Eckart and Landau frame. Furthermore, we assume that $N_i^\mu(x^\mu)$ and $T_i^{\mu\nu}(x^\mu)$ are extracted numerically. Moreover, we omit the index (x^μ), since it is clear that we calculate the quantities in discretized space at different time steps.

6.5.2. Numerical extraction in the Landau and Eckart frame

Except for the calculation of the velocity, the procedure for the numerical extraction of hydrodynamical quantities coincides in both the Landau and Eckart frame. We start with the procedure for the Landau frame for a general multi-component system. Then, we briefly introduce the difference compared to the Eckart frame. The general definitions of the hydrodynamic quantities have been provided in Chapter 3.

The extraction procedure for the Landau frame is given as follows:

---

[9]The coordinate of the volume is always defined in the center.
[10]This is also true for the continuous integrals in Eqs. (6.22).
[11]It is clear that the grid should always be chosen appropriately in order to resolve spatial gradients.

1. We determine the energy density, e, as well as the components of the velocity, $\vec{v}$, via the global $N^{\mu\nu}$ and $T^{\mu\nu}$ using Eq. (3.56). The procedure is discussed in Appendix G.

2. With e, $\vec{v}$, $N^{\mu\nu}$, and $T^{\mu\nu}$, we determine the particle density, n, and isotropic pressure, P.

3. Now, we go through all particle species separately. We adopt the velocity of the global system, i.e., $\vec{v}_i = \vec{v}$, instead of calculating the velocity for each particles species. The reason for this is discussed in Sec. 3.3.5.

4. Using $\vec{v}_i$, $N_i^{\mu\nu}$, and $T_i^{\mu\nu}$ we determine the energy density, e_i, using Eq. (3.43). Moreover, we determine the particle density, n_i, and isotropic pressure P_i,

5. We calculate the pseudo[12]-temperature, T_i', and pseudo-fugacity, λ_i', using the procedure discussed in Appendix H.

6. Using T_i' and λ_i' we calculate the temperature, T, and fugacity, λ, as discussed in Appendix H.

7. In the next step we require that $T_i = T$ and $\lambda_i = \lambda$ as motivated in Sec. 3.3.5.

8. We determine entropy density, s (s_i), equilibrium pressure, p (p_i), and bulk pressure, Π (Π_i), for the global system (each particle species).

9. Finally, we determine the shear-stress tensor, $\pi^{\mu\nu}$ ($\pi_i^{\mu\nu}$), the flow of energy-momentum and particles, W^μ (W_i^μ) and V^μ (V_i^μ), respectively, and heat flow, q^μ (q_i^μ), for the global system (each particle species).

The extraction procedure for the quantities in the Eckart frame is the same as listed above, except the first step. Using $N^{\mu\nu}$ and $T^{\mu\nu}$, the global velocity, $\vec{v}$, is calculated via Eq. (3.55), and the global energy density, e, is determined via Eq. (3.43).

6.6. Further application of the model

BAMPS is an appropriate tool in order to study off-equilibrium physics and both, low- and high-p_T phenomena, within one framework. It has been applied to study the early phase of ultrarelativistic heavy-ion collisions. Furthermore, since the model solves the rBE, it is a perfect tool to study several transport coefficients as well as to serve as a benchmark to viscous hydrodynamics. We briefly introduce the topics on which the framework of BAMPS has been already applied in several studies. The results have been published in several notable journals.

---

[12]We name them pseudo, because they have no physical meaning, and we denote them with "$\prime$". For more details see Sec. 3.3.5.
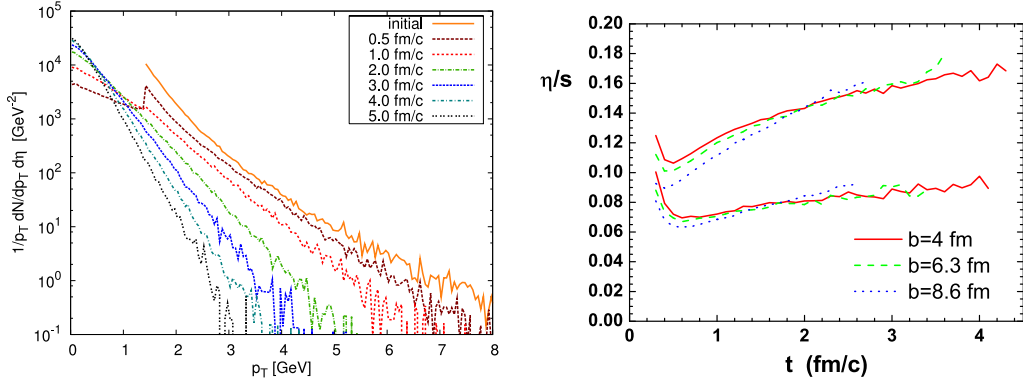
(a) Time evolution of the p_T-spectrum at mid-rapidity and central $b = 0$ fm Au + Au at 200 A GeV collisions. The initial spectrum is the distribution given from mini-jet initial conditions with $p_0 = 1.4$ GeV. Figure from Ref. [196].

(b) Time evolution of the ratio of the shear viscosity to the entropy density, η/s, extracted from the central region of simulations of Au + Au collisions at 200 A GeV with different impact parameters. The upper band shows the results with $\alpha_s = 0.3$ and the lower band the results with $\alpha_s = 0.6$. Figure from Ref. [105].

Figure 6.2.: Early thermalization and time evolution of η/s from previous studies with BAMPS.

6.6.1. Application to heavy-ion phenomenology

Early thermalization and low shear viscosity

The issue of thermal and chemical equilibration of the QGP created in relativistic heavy-ion collisions has been already addressed in certain studies [179, 181, 188, 189, 190, 191, 192, 193]. Initially, BAMPS has been employed to study the early evolution of hot gluon matter in relativistic heavy-ion collisions at RHIC energies, focusing on the understanding of rapid thermalization [41]. Such a rapid thermalization is not possible with elastic scattering processes only unless unphysically high cross sections are used instead of pQCD-based cross sections. It has been shown that including inelastic particle production and annihilation processes with pQCD-based cross sections solves the problem of the rapid thermalization, as shown in Fig. 6.2a. Moreover, studies focusing on the "bottom-up" scenario using BAMPS have been realized in Refs. [194, 195]. The fast thermalization observed in non-central collisions of heavy-ions correlates with the appearance of a small shear viscosity over entropy density ratio, η/s. Comparison of ideal and viscous hydrodynamics [10, 69, 104, 197, 198, 199] to data from RHIC suggests a rather small value of η/s, which seems to be very close to the conjectured lower bound of $\eta/s = 1/(4\pi)$ [19] from a correspondence between conformal field theory and string theory in Anti-de-Sitter space. Such a small ratio has also been confirmed by calculations with BAMPS including both elastic and inelastic processes [105, 106, 200, 201, 202]. These findings indicate a rather small $\eta/s \approx 0.08 - 0.15$ depending on the coupling constant, α_s. In Fig. 6.2b we show the time evolution of the shear viscosity over entropy density ration in Au + Au collisions at 200 A GeV with different impact parameters and
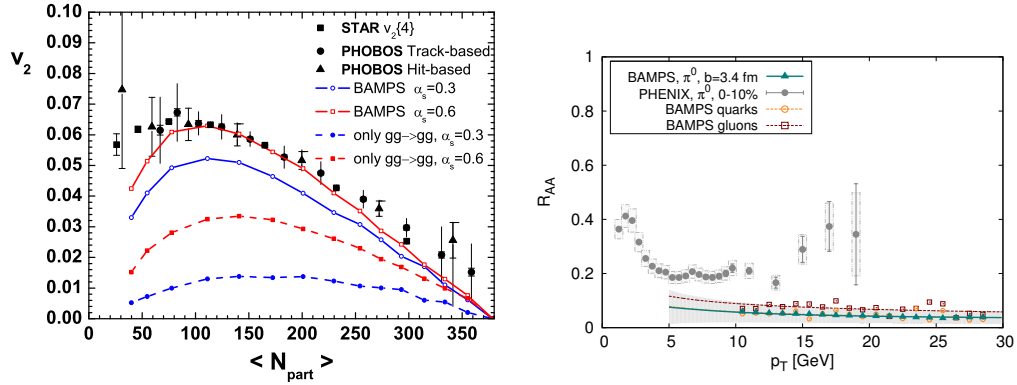
(a) Integrated elliptic flow, v_2, vs. number of participants, N_{part}, for the central region of Au + Au collisions using $\alpha_s = 0.3$ and 0.6 compared with RHIC data. The initial spectrum is the distribution given from mini-jet initial conditions with $p_0 = 1.4\,\text{GeV}$. Figure from Ref. [105].

(b) The nuclear modification factor, R_{AA}, for neutral pions, quarks, and gluons, extracted from BAMPS calculations with an impact factor of $b = 3.4\,\text{fm}$, compared with experimental data for central collisions. Figure from Ref. [182].

Figure 6.3.: Integrated elliptic flow, v_2, and the nuclear modification factor, R_{AA}, from previous studies with BAMPS.

coupling constants, α_s.

Flow phenomena and jet suppression

BAMPS provides the possibility to study both low- and high-p_T phenomena within one framework, i.e., to study the bulk and jet properties of QCD matter in the perturbative coupling regime. Calculations of the elliptic flow, v_2, which are shown in Fig. 6.3a, are found to be in good agreement with experimental data for the coupling regime $\alpha_s = 0.3...0.6$ [105, 201]. For the hadronization, a simple picture has been employed, where gluons turn into pions[13] when the local energy density drops lower than a specified critical value. The results are in very good agreement with the experimental data, and one observes the importance of inelastic scattering processes included in BAMPS. Whereas the bulk properties are well-described in BAMPS using pQCD-based scattering processes, the nuclear modification factor, R_{AA}, shown in Fig. 6.3b, is found to be below the data, i.e., a too strong suppression of highly energetic jets traversing the medium created in HIC [182]. Here, BAMPS has been already extended to light quarks, with all scattering channels, while the cross sections are based on pQCD. Recently, it has been demonstrated in Ref. [203], that the Gunion-Bertsch approximation of the leading-order perturbative QCD radiation matrix element, which is used in BAMPS, is not exact and has to be improved. The improved Gunion-Bertsch approximation may resolve the bad description of the nuclear modification factor, R_{AA}, but simultaneously will change also the results for the elliptic flow, v_2. This work is still in progress.

---

[13]This is named "parton-hadron duality" [182].
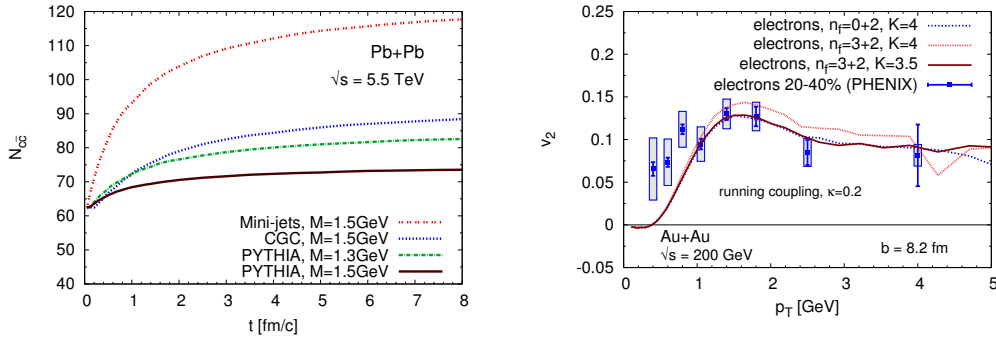
(a) Charm production in a central Pb + Pb collision at LHC as simulated within the BAMPS framework for different charm quark masses and initial conditions. Figure from Ref. [204].

(b) Heavy quark flow for an impact parameter $b = 8.2$ fm in Au + Au collision at RHIC as simulated within BAMPS. The $gQ \to gQ$ cross section is enlarged by a factor K. For comparison experimental data for electrons from heavy-flavor decays [205] is shown. Figure from Ref. [206].

Figure 6.4.: Heavy quark flow at RHIC and charm production at LHC as studied within the BAMPS framework in Refs. [204] and [206].

Heavy quarks

As shown in Ref. [182], BAMPS has been extended to light quarks in order to provide a more complete description of the phenomena in heavy-ion collisions at RHIC and LHC. However, BAMPS has also been extended to heavy quarks which enables the study of production and space-time evolution of charm and bottom quarks in central and non-central heavy-ion collisions at RHIC and LHC energies for various initial conditions [204,206]. It has been found that the in-medium production of charm quarks from $gg \to Q\bar{Q}$ processes is negligible for RHIC collisions. In contrast, it contributes significantly to the total charm yield at LHC energies, which is shown in Fig. 6.4a. In a recently published study the nuclear modification factor, R_{AA}, and elliptic flow, v_2, of electrons emerging from open heavy-flavor decays have been extensively investigated as shown in Fig. 6.4b. It has been found that the elastic $gQ \to gQ$ cross section is too small in order to provide a good description. A scaling factor of K for the elastic cross section has to be introduced in order to reproduce the experimental data. Further studies require the extension to inelastic processes for heavy quarks, such as $gQ \to gQg$, based on the improved Gunion-Bertsch matrix element. This will allow for the investigation of radiative contributions to the energy loss and collective behavior of charm and bottom quarks.

6.6.2. Application to nearly ideal and viscous hydrodynamics

Comparison to viscous hydrodynamics

BAMPS is an excellent tool to compare with, insofar as the exact solution of the rBE is required. In certain studies, BAMPS has been used as benchmark for newly developed

theories of viscous hydrodynamics. In Ref. [207], a new third order dissipative hydro-dynamic theory has been derived from the entropy principle and extensively compared to the numerical results generated with BAMPS. This is depicted in Fig. 6.5a. The main question which has been tried to answer is, in which regime the theory of viscous hydrodynamics is applicable and which are the conditions where it fails. It has been shown that the standard theory of Israel and Stewart which is the so-called second-order theory of viscous hydrodynamics, does not provide a reasonable description of systems which are far from thermal equilibrium. In contrast, in a simplified model assuming Bjorken scaling, a newly derived third-order theory covers a larger regime of applicability, i.e., larger values of Knudsen number[14], Kn. Moreover, when effectively considering contributions from all orders, the agreement with BAMPS is improved even more.

The above work has been extended to systems with more than one particle species, as shown in Ref. [150, 151]. The main emphasis has been put on the issue whether a system containing many species can be treated as a single component hydrodynamical system. In this work, novel hydrodynamic equations for each component of a multi-component system have been derived and compared to the solution of the rBE via BAMPS, as shown in Fig. 6.5b. It has been found that especially in a static system where no spatial and velocity gradients appear the shear viscosity coefficient for each particle species as well as the effective shear viscosity of the mixture depend on the ratios of the shear pressures. Although similar relaxation-type equations exist, there are differences between single- and multi-component systems. Therefore, using only a single-component description unavoidably leads to the wrong description of a multi-component system. However, it has been shown, that with the appearance of spatial and velocity gradients, the differences become smaller [208].

Extraction of transport coefficients

The determination of transport coefficients of the medium which is created in relativistic HIC is of big interest. The most important ones are the shear viscosity, η, the bulk viscosity, ζ, and the heat conductivity, κ. The transport coefficients describe the properties of the medium on a macroscopic length scale, which are an important input for viscous hydrodynamic models. Furthermore, with the knowledge of these coefficients, one can qualitatively learn about the interactions in the system on the microscopic level.

As BAMPS solves the rBE, it is a perfect tool to extract these coefficients on the level of a simplified Boltzmann gas. In Ref. [184], BAMPS has been employed in a more or less phenomenological Ansatz to extract the shear viscosity coefficient, η, using the relativistic Navier-Stokes equations, where η is proportional to the velocity gradient. For this purpose, left and right of a one-dimensional system two moving plates were simulated by thermal reservoirs. Using a sufficiently high momentum-independent cross section with only binary collisions, a velocity gradient has been established after a certain period of time, which is non-linear due to relativistic effects. On the other hand, the rapidity shows a linear behavior, as demonstrated in Fig. 6.6a. The extraction of

---

[14]The Knudsen number is the ratio of a microscopic to a macroscopic length scale.
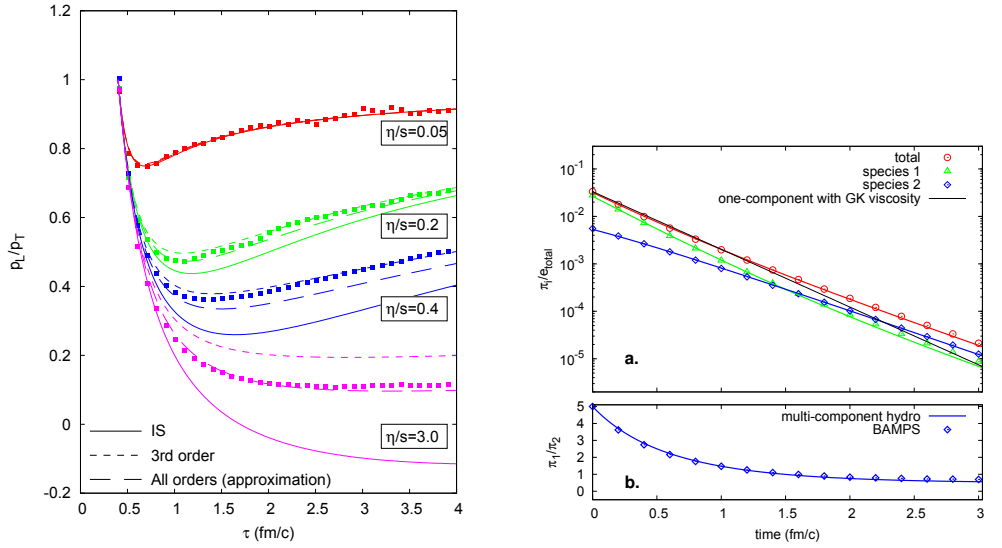
(a) Time evolution of the pressure isotropy for various η/s values. Symbols present the results of BAMPS calculations. The solid, short-dashed and long-dashed curves show the solutions of Israel-Stewart theory, of third-order hydrodynamics, and of the heuristic consideration of all-orders contributions. Figure from Ref. [207].

(b) (a) Time evolution of the partial and total shear pressures normalized by total energy density and (b) ratio of the partial shear pressures from BAMPS (symbols) and hydrodynamic calculations (lines). Solid grey lines represent the effective one-component solution. Figure from Ref. [151].

Figure 6.5.: Applicability of hydrodynamics investigated within BAMPS in Refs. [207] and [150, 151].

the shear-stress tensor components in BAMPS makes it possible to determine the shear viscosity, whereas for simplification the gradient of the velocity and rapidity have been derived analytically. Using a similar method the heat conductivity, κ, is extracted in the Navier-Stokes limit using BAMPS [187]. To this end, a temperature gradient has been established using thermal reservoirs, where a non-vanishing heat flow exists. In order to obtain a static profile, the pressure gradient has to vanish. Furthermore, another method to extract the shear-viscosity coefficient, η, is realized within the Green-Kubo formalism. The details are discussed in Ref. [183]. As expected, the results agree with those obtained in the work discussed above [184].

Both, the shear viscosity, η, and heat conductivity, κ, for a massless Boltzmann gas with isotropic cross sections have been compared to different values extracted from different derivations of viscous hydrodynamics. BAMPS has been able to clarify which method reflects the best manner of derivation. In case of the shear viscosity, the results from all second-order theories are close to the values extracted from BAMPS. This changes dramatically for the heat conductivity, where a big discrepancy between the different theories exists as shown in Fig. 6.6b.

Besides that, the different methods to extract the shear-viscosity coefficients makes it possible to determine the shear viscosity of a medium with momentum-dependent
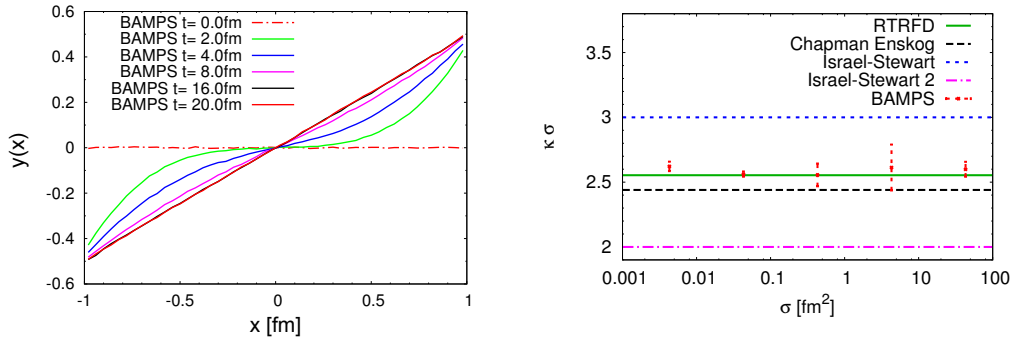
(a) Build-up of the rapidity profile in BAMPS. Two thermal reservoirs with a given velocity are simulated left and right, indicating two moving plates. A non-linear velocity and linear rapidity gradient develops after a certain time, which approaches a stationary solution. Figure from Ref. [184].

(b) Using a stationary temperature gradient the heat conductivity κ can be extracted from BAMPS. The heat conductivity κ for isotropic cross sections σ derived from different viscous hydrodynamic theories (lines) is compared to the extracted results from BAMPS (dots). For a better illustration we show the dimensionless quantity $\kappa\sigma$ in dependence of the cross section σ. Figure from Ref. [187].

Figure 6.6.: Extraction of transport coefficients within BAMPS in the Navier-Stokes limit as realized in Refs. [184] and [187].

cross sections. This has been realized in Refs. [183,184] for a medium with pQCD-based elastic and inelastic scattering processes.

7. Investigation of shock-wave phenomena in kinetic theory and viscous hydrodynamics

In this work, the main emphasis is put into the investigation of ideal and viscous shock waves using kinetic theory. For this purpose we use the microscopic transport model BAMPS which solves the relativistic Boltzmann equations (rBE). In order to obtain a better structure and keep track of the whole discussion, we partitioned the numerical results into two parts: In this Chapter 7, we present the numerical results of shock waves in various scenarios in a simplified $(1+1)$-dimensional[1] setup, while in the subsequent Chapter 8, we study the evolution and properties of Mach cones which belong to the class of shock-wave phenomena but require a two or three-dimensional framework.

In order to obtain a more comprehensive discussion, we also make use of the hydrodynamic solver vSHASTA[2] in this chapter. Using both, BAMPS and vSHASTA, we determine the range of applicability of the relativistic viscous hydrodynamic theory by simulating shock waves appearing in the context of the relativistic Riemann problem (rRP), which is introduced in the perfect-fluid limit in Chapter 5, and other numerical setups. The comparison of viscous hydrodynamics to kinetic theory considering shock wave scenarios has turned out to be a fundamental and notably study [33,34,35]. Thus, this chapter is an elaborate discussion of these publications and contains additional material useful for the investigation of shock waves and the comparison between viscous hydrodynamics and kinetic theory.

In the forthcoming discussion, we exclusively use a 3-dimensional static box of fixed size with various boundary conditions. Since we consider the shock-wave propagation in one dimension, we assume that the matter is homogeneous in the $y - z$ plane[3]. The shock wave propagates along the longitudinal x–direction. Furthermore we also use different cross sections. Unless stated otherwise, however, we only use isotropic cross sections and the extracted hydrodynamic quantities are calculated in the Landau frame, both for BAMPS and for vSHASTA. The method to extract those quantities using BAMPS has been introduced in Sec. 6.5.

We now introduce the structure of this chapter: In Sec. 7.1 we study the influence of the η/s ratio on the formation and evolution of shock waves by solving the rRP with the microscopic transport model BAMPS and the viscous hydrodynamic solver vSHASTA. Here vSHASTA solves the Israel-Stewart (IS) theory. We benchmark both vSHASTA

---

[1]The transverse directions are assumed to be homogeneous.

[2]The numerical calculations of vSHASTA have been performed by H. Niemi and E. Molnar.

[3]Thus, the cell sizes in transverse direction are equal to the corresponding arbitrarily large size of the box.

and BAMPS to the ideal solution as a proof of their applicability. In the following, we consider shock waves for different viscosities by adjusting the η/s ratio, where results from BAMPS are used as a reference for vSHASTA in order quantify the applicability of IS theory. We find that for large η/s ratio the IS theory breaks down. Furthermore, we encounter a strong limitation in the description of heat flow, which is identified as a limitation of the IS theory. In the end of this section we discuss the scaling behavior and formation time of shock waves. In the following Sec. 7.2, we discuss the implementation of inelastic processes in BAMPS and the effects compared to the case where only binary scattering processes are taken into account. Furthermore, we extend our discussion by solving the rRP for a gas of massive particles and to a system of more than one component. In Sec. 7.3 we use a modified setup to investigate the heat-flow problem as encountered in Sec. 7.1. We demonstrate the improvements of RTRFD compared to IS theory when comparing them to the solutions of BAMPS. In Sec. 7.4 we introduce another modified setup to investigate the formation of a shock front. Here, we move to the frame where the shock front is in rest and use both, BAMPS and vSHASTA, to compare relativistic kinetic theory to relativistic dissipative hydrodynamics. We encounter strong limitations when applying dissipative hydrodynamics to describe the shock-front region for large propagation speeds of the shock front. In Sec. 7.5, we finally provide a brief discussion of the numerical convergence of BAMPS by varying the parameters, such as cell size and test-particle number. Moreover, we show some details regarding the calculating time of BAMPS.

7.1. The Riemann problem in the ultrarelativistic limit

In this section, we consider the rRP in order to investigate shock waves in one dimension. The initial conditions are the same as for the shock-tube problem discussed in Chapter 5. Furthermore, we use an ultrarelativistic gas of massless particles characterized by the equation of state (EoS) $e = 3p$. The size of the static box is chosen to be $L_x = 6.4\,\text{fm}$. In order to obtain the results in BAMPS we average over many different ensembles. Unless otherwise stated, vSHASTA solves the standard IS theory, see Appendix A. In the following, we shall also use the relationship between the heat conductivity and the cross section. We use the relation (6.17). Furthermore, we use the relation (6.15) to relate the shear viscosity to the cross section for binary collisions.

7.1.1. The perfect-fluid limit

The Riemann problem which is analytically solvable in the perfect-fluid limit is an important test case for both kinetic and hydrodynamical calculations. In this section, we show that both approaches can reproduce the analytic solution very accurately, and therefore are usable for investigations of shock-wave phenomena. Furthermore, we also discuss possible numerical uncertainties which always appear in numerical approaches.

The initial conditions we use are those of the shock-tube problem discussed in Chapter 5. This implies that we initialize the left and the right part of the box. We initialize the system in thermal equilibrium with the initial values summarized in Tab. 7.1. The initial dissipative quantities, q^μ and $\pi^{\mu\nu}$, vanish and the bulk viscous pressure in the ultrarelativistic limit is always zero. A sharp discontinuity appears in the temperature

profile, which implies a strong initial pressure gradient. In the end, the initial pressure gradient leads to the development of a shock wave and a rarefaction wave, as discussed in detail for the ideal solution in Chapter 5.

initial variables	left	right	further settings
$T\,(\mathrm{GeV})$	0.4	0.2	one species: $m = 0\,\mathrm{GeV}$
λ	1	1	degeneracy factor $g = 16$
v	0	0	isotropic elastic $2 \to 2$ collisions
$\Pi\,(\mathrm{GeV/fm^3})$	0	0	constant η/s or σ
$q^\mu\,(\mathrm{GeV/fm^3})$	0	0	runtime = 3.2 fm/c; system size $L_x = 6.4$ fm
$\pi^{\mu\nu}\,(\mathrm{GeV/fm^3})$	0	0	walls in x-direction; periodic boundary conditions in transverse y- and z-directions

Table 7.1.: The initial conditions and settings used in BAMPS and vSHASTA in the rRP for an ultrarelativistic gas of massless particles.

In BAMPS we cannot exactly reach the perfect-fluid limit, but we can choose a very small physical viscosity $\eta = 0.001s$ to simulate an ideal fluid numerically. The use of even smaller viscosities or, equivalently, larger cross sections would require a better resolution[4] which is computationally very time consuming. On the other hand, we can choose $\eta = \kappa = 0$ for vSHASTA which solves the relativistic Euler equations instead of the IS equations. As explained in Appendix D, however, because of the approximative nature of the numerical algorithm we always have some residual numerical viscosity in the calculations.

Figure 7.1 shows a snapshot of the particle density n, the fugacity, λ, the isotropic pressure, P, the shear pressure, π, the velocity, v, and the heat flow, q^x, at $t = 3.2$ fm/c. The shear pressure is defined as $\pi = \pi^{xx}/\gamma^2$, because we identify the x-direction as the longitudinal one, whereas y and z span the transverse plane[5].

The results from BAMPS for n, P, and v in Fig. 7.1 agree well with those of the ideal fluid-dynamical calculation, except for small deviations around the discontinuities separating the different regions. These deviations are expected to appear because of the small but non-vanishing physical viscosity used in BAMPS calculations and are best seen in the fugacity profile. The solution of vSHASTA demonstrates that this effect originates from the small nonzero viscosity. Nevertheless, the results from BAMPS also deviate from vSHASTA using the same η/s value. This is especially distinctive in the heat-flow profile, which is not zero but positive around the constant plateau. Furthermore, one observes a peak in the BAMPS result. We demonstrate later that this deviation arises from numerical fluctuations.

Figure 7.1 shows that BAMPS is indeed able to reproduce the almost perfect-fluid limit. The small deviations of the ideal solution indicate that particles in regions around discontinuities are out of thermal equilibrium in the BAMPS calculations. However,

---

[4]This implies a smaller Δx and a larger N_{test}.

[5]However, this definition of the shear pressure holds for a one-dimensional expanding system only.

Figure 7.1.: The analytical and numerical solutions of the relativistic Riemann problem for the particle density (a), the fugacity (b), the isotropic pressure (c), the shear pressure (d), the velocity (e), and the heat flow (f). The initial conditions and settings are listed in Tab. 7.1. The full lines are the analytic solutions at $t = 3.2$ fm/c. The results from vSHASTA for the perfect-fluid limit are shown by the dashed-dotted lines. The results from BAMPS and vSHASTA at $\eta/s = 0.001$ are displayed by the dashed and dotted line, respectively.

this is only a small fraction of the whole system. The development of the (shock) plateau as well as of the sharp discontinuities indicates that matter reaches thermal equilibrium. In order to demonstrate this, we calculate the energy distribution, $\mathrm{d}N/(N\,\mathrm{d}E)$, of particles in the region of the shock plateau and compare it to the thermal one, which
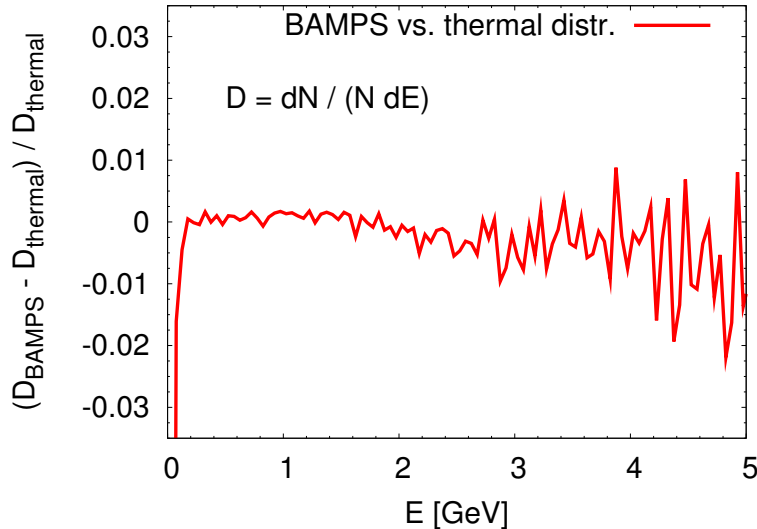
Figure 7.2.: Relative difference of the energy distribution for particles in the plateau region between the results extracted from BAMPS and from a local thermal equilibrium distribution given by Eq. (3.25) with $a = 0$.

is obtained from Eq. (3.25) with $a = 0$, i.e.,

$$\frac{\mathrm{d}N}{N\,\mathrm{d}E} = \frac{e^{-\gamma E/T}\sinh(v\gamma E/T)E}{2T^2\gamma^2 v} \ . \tag{7.1}$$

The results are shown in Fig. 7.2, where we see agreement within a few percent.

If the system is exactly in thermal equilibrium as described by the ideal fluid-dynamical solution, the dissipative quantities such as the heat flow, q^x, are expected to vanish. As already mentioned above, the heat-flow profile as shown in Fig. 7.1f demonstrates that this is not the case for BAMPS. Here, BAMPS deviates from vSHASTA with the same $\eta/s = 0.001$. The heat flow in vSHASTA is practically zero, while in BAMPS it has a small positive value between the rarefaction fan and the shock front. This deviation between BAMPS and vSHASTA is already noticeable in the fugacity and shear pressure profile, although the difference is hardly distinctive. Moreover, we see a large peak in the fugacity, the shear pressure, and the heat flow in the region of the shock front. The particle density, pressure, and velocity are not sensitive enough on this numerical artifact, such that the same effect is not visible.

The deviation of q^x from zero observed in Fig. 7.1f seems to be a numerical artifact[6], because it disappears when using a constant cross section instead of a constant value of η/s. In Fig. 7.3 we show the numerical result from BAMPS and from vSHASTA for the fugacity, the shear pressure, and the heat flow for constant η/s and for a constant cross section in the left and in the right panel, respectively. We have chosen $\sigma = 224.431$ mb, which corresponds to $\eta/s = 0.002$ in the medium with the higher initial temperature. Furthermore, in contrast to Fig. 7.1 we use a smaller number of test particles in the left part of Fig. 7.3. This effectively leads to an on average smaller number of particles per cell.

---

[6]except for the peak
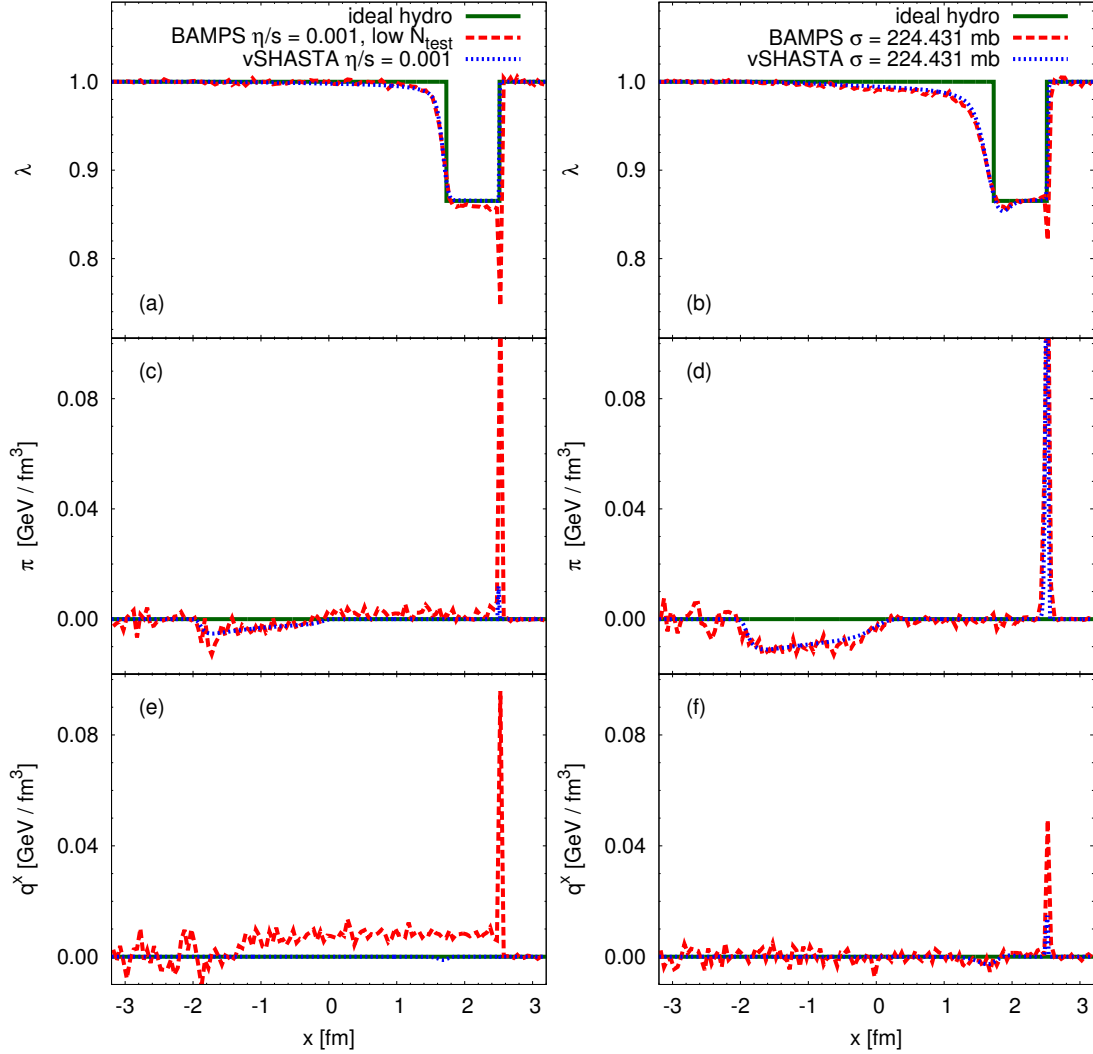
Figure 7.3.: The fugacity, λ, the shear pressure, π, and the heat flow, q^x, obtained from BAMPS and from vSHASTA using a constant $\eta/s = 0.001$ (left panel) and a constant cross section $\sigma = 224.431$mb (right panel).The initial conditions and settings are listed in Tab. 7.1. In contrast to the results displayed in Fig. 7.1, we use in BAMPS a smaller number of test particles in the left panel. The value of η/s for the case of a constant cross-section simulation varies from 0.002 to 0.008.

For the quantities in the right panel of Fig. 7.3, we see a perfect agreement between the results from BAMPS and vSHASTA. This is especially distinctive for the small drop at $x \approx 1.6$ fm. The peak at the shock front becomes smaller, although it is larger than the peak from the vSHASTA calculation. One can infer from the left panel of Fig. 7.3 that using a smaller number of test particles the size of the numerical artifact increase when comparing them to Fig. 7.1. This demonstrates that this numerical artifact originates from the method of cross section and local fluctuations. This is

explained in the following: On the shock plateau, where the flow velocity and the LRF particle and energy density (v, n, e) are constant, one expects that the cross section is also constant for a constant η/s. In a single event, however, thermodynamic quantities fluctuate, such that one would use a smaller cross section (larger shear viscosity) in a cell with larger energy (entropy) density in order to keep η/s constant, and a larger cross section in a cell with smaller energy density. Therefore, although the results shown in Figs. 7.1 and 7.3 (left panel) are averaged over 1000 events, the deviations between BAMPS and vSHASTA results are likely to come from the fluctuations in single BAMPS events. These can be reduced by performing simulations with much larger N_{test}.

Using a larger number of test particles in Fig. 7.1 than we have used in Fig. 7.3, we have confirmed that the difference between BAMPS and vSHASTA solutions decreases. The scenario of using a constant σ is independent of this effect.

7.1.2. Viscous solutions

In this section we study the relativistic Riemann problem at different non-zero viscosities. We show that for small viscosities both the hydrodynamical and kinetic approaches are in good agreement, especially at late times. With increasing viscosity, however, this agreement fades and ultimately breaks down when the hydrodynamical description leads to results which are inconsistent with kinetic calculations. Thus, the main motivation of this section is to find the conditions of this break-down and then to quantify the range of applicability and the limitations of the dissipative hydrodynamical description.

We note that all results shown below are calculated in the Landau frame. In the cases considered here the heat flow is small[7] such that the differences between the Landau and Eckart frames are very small, even for large values of η/s.

Relativistic kinetic theory can correctly treat the Riemann problem from the nearly perfect-fluid limit to the free-streaming limit. This has been demonstrated before and has been published in Refs. [33, 34, 209, 210]. Another promising method to investigate the Riemann problem is based on the lattice Boltzmann approach and has been recently reported in Refs. [211, 212, 213, 214]. In contrast to kinetic theory, the applicability of IS theory requires that the system stays close to local thermal equilibrium and that the Knudsen number, Kn, is small during the whole evolution.

In the special case of the Riemann problem the local Knudsen number is large at early times of the evolution when large density gradients appear even for small viscosities. Furthermore, the system is far from equilibrium around the discontinuity. Hence, the IS theory of dissipative hydrodynamics is expected to fail to correctly describe the evolution in this region.

However, the gradients will be smoothened out later because of the viscosity and heat conductivity, which provides better conditions for the IS hydrodynamical description. The degree of agreement with the kinetic description depends on the value of the Knudsen number which we demonstrate later.

In the next subsections, we show results at fixed times but for different values of η/s.

---

[7]except for the free streaming case.
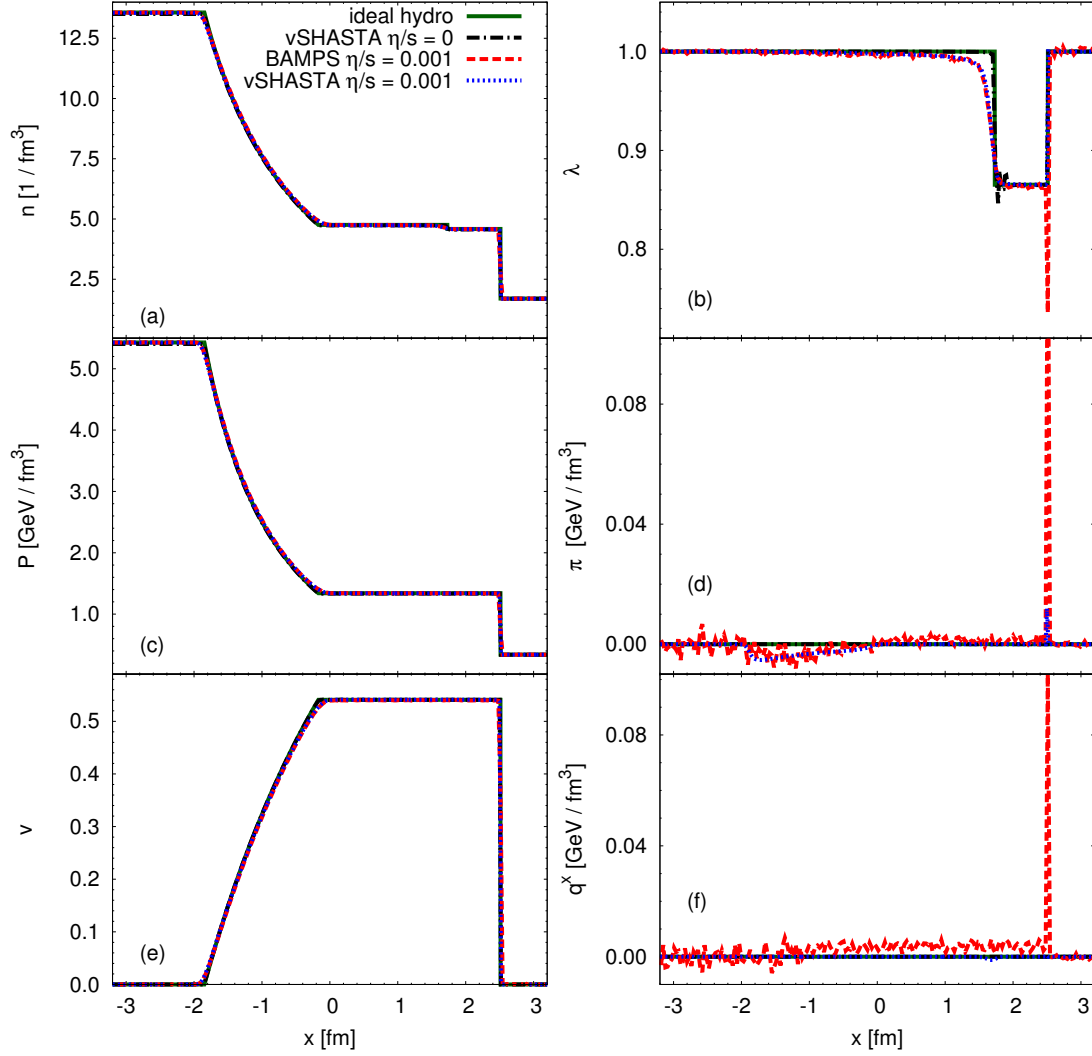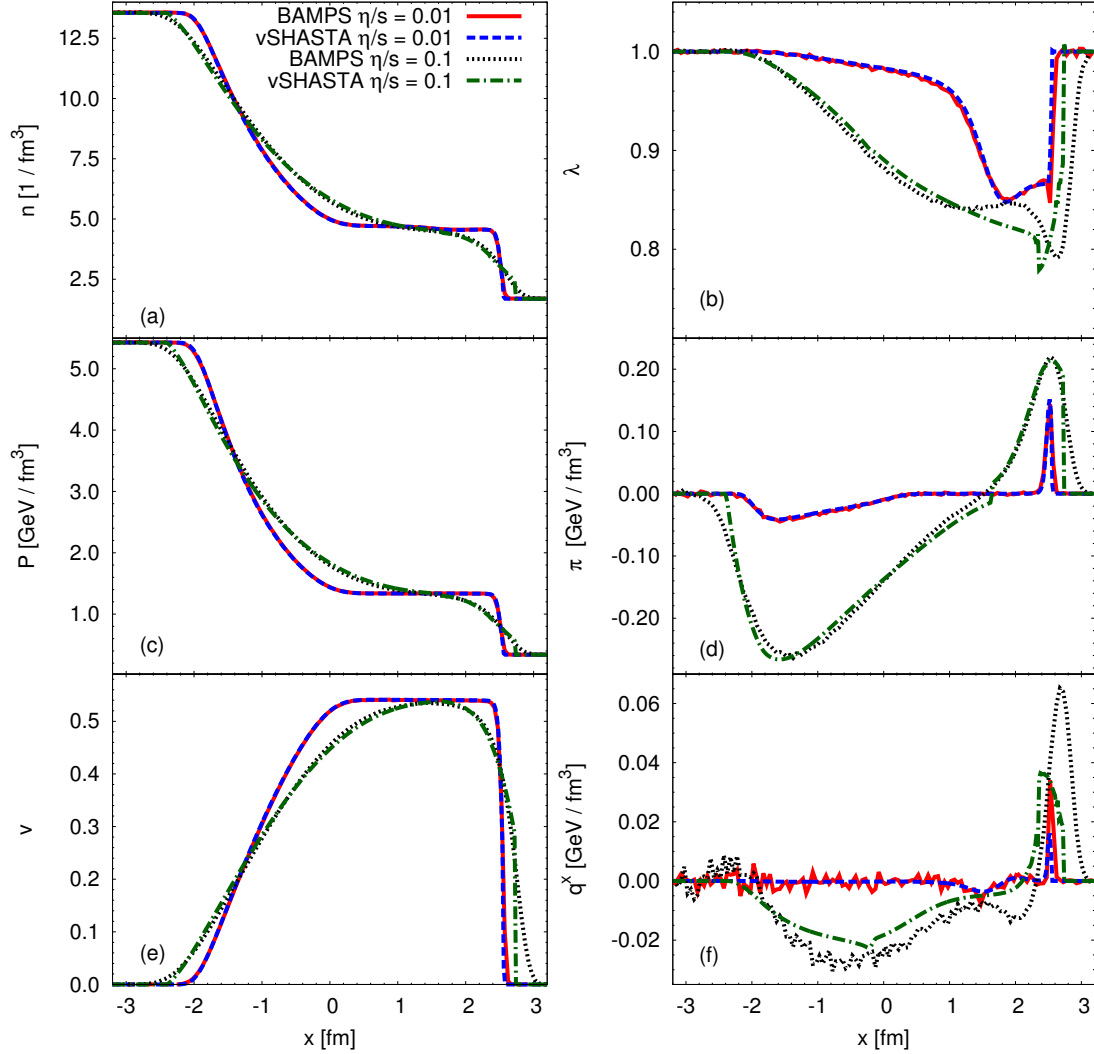
Figure 7.4.: The numerical solutions of the relativistic Riemann problem for the particle density (a), the fugacity (b), the isotropic pressure (c), the shear pressure (d), the velocity (e) and the heat flow (f). The initial conditions and settings are listed in Tab. 7.1. The results are shown for BAMPS and vSHASTA for $\eta/s = 0.01$ and 0.1 at $t = 3.2$ fm/c.

However, solutions at time t with shear-viscous coefficient η correspond to solutions at time $a\,t$ with a shear-viscous coefficient $a\,\eta$, where a is some arbitrary constant. This scaling behavior is discussed later in Sec. 7.1.4.

Small viscosity

We use the same initial conditions as in the previous Sec. 7.1.1, but we consider two different values of the shear viscosity to entropy density ratio, $\eta/s = 0.01$ and $\eta/s = 0.1$. Figure 7.4 shows the particle density, n, the fugacity, λ, the isotropic pressure, P, the shear pressure, π, the velocity, v, and the heat flow, q^x, at $t = 3.2$ fm/c for BAMPS

and vSHASTA calculations.

In the dissipative case, the characteristic structures of the perfect-fluid solution still can be found in the late stages of the evolution since it takes a finite time for the structures to form. We demonstrate this in Sec. 7.1.4. Instead of a discontinuous shock front, a contact discontinuity, and sharp rarefaction tails, however, we obtain continuously changing profiles, i.e., dissipation leads to the smoothening and the broadening of these characteristic structures.

Another difference compared to the perfect-fluid case is that the head and the tail of the rarefaction fan and the shock front propagate faster into the undisturbed matter. However, for the shock wave this happens only until the shock plateau is formed. After that, the velocity of the shock wave is the same as for the perfect-fluid case. Similarly, the velocity of the plateau does not change compared to the perfect-fluid solution. The width of the shock front strongly depends on the dissipation. In the perfect-fluid case the width vanishes, whereas it increases with increasing η/s. However, as we will show in Sec. 7.4, the total width of the shock front is proportional to the shear viscosity coefficient η in the limit $t \to \infty$ [40, 215, 216, 217].

For the smaller shear viscosity to entropy density ratio, $\eta/s = 0.01$, the agreement between BAMPS and vSHASTA results is excellent within statistical fluctuations for all macroscopic quantities, although any definite conclusions regarding the heat fluxes are hard to draw because of large fluctuations. The shock front from both calculations is also in very good agreement. However, a closer inspection reveals that vSHASTA results in slightly steeper profiles than BAMPS.

Increasing the viscosity to $\eta/s = 0.1$ leads to noticeable differences between the approaches. The most pronounced difference can be again seen in the shock front: vSHASTA provides a too sharp profile at the right edge of the front, while the matter in the low-density region is diffused faster in the BAMPS calculation. It is an important question whether this is only a specific failure of the IS theory or a general failure of viscous hydrodynamics. A deeper investigation of the shock front is performed in Sec. 7.4.

Further differences are visible in the region of the rarefaction fan where the kink at the left edge survives. Another difference can be seen by inspecting the fugacity and shear pressure in the region where one would find the contact discontinuity in the perfect-fluid case. In this region the vSHASTA calculation leads to an overall smaller fugacity, and to a sharp kink in the shear-pressure profile. These differences are enhanced for larger viscosities as seen in the next subsection.

Large viscosity

If the value of η/s is increased further to $\eta/s = 0.2$, deviations between the results of vSHASTA and BAMPS become more significant. They are shown in Fig. 7.5 for the same quantities as in Fig. 7.4. In addition, we also present the free-streaming solution which has been discussed in Appendix I.

The most salient difference occurs in the pressure profile. In the vSHASTA calculation a part of the initial discontinuity survives near the contact discontinuity located at $x \sim 1.5$ fm even after $t = 3.2$ fm/c. In contrast, this kind of structure is not seen in the BAMPS calculation. A similar shock structure has also been observed
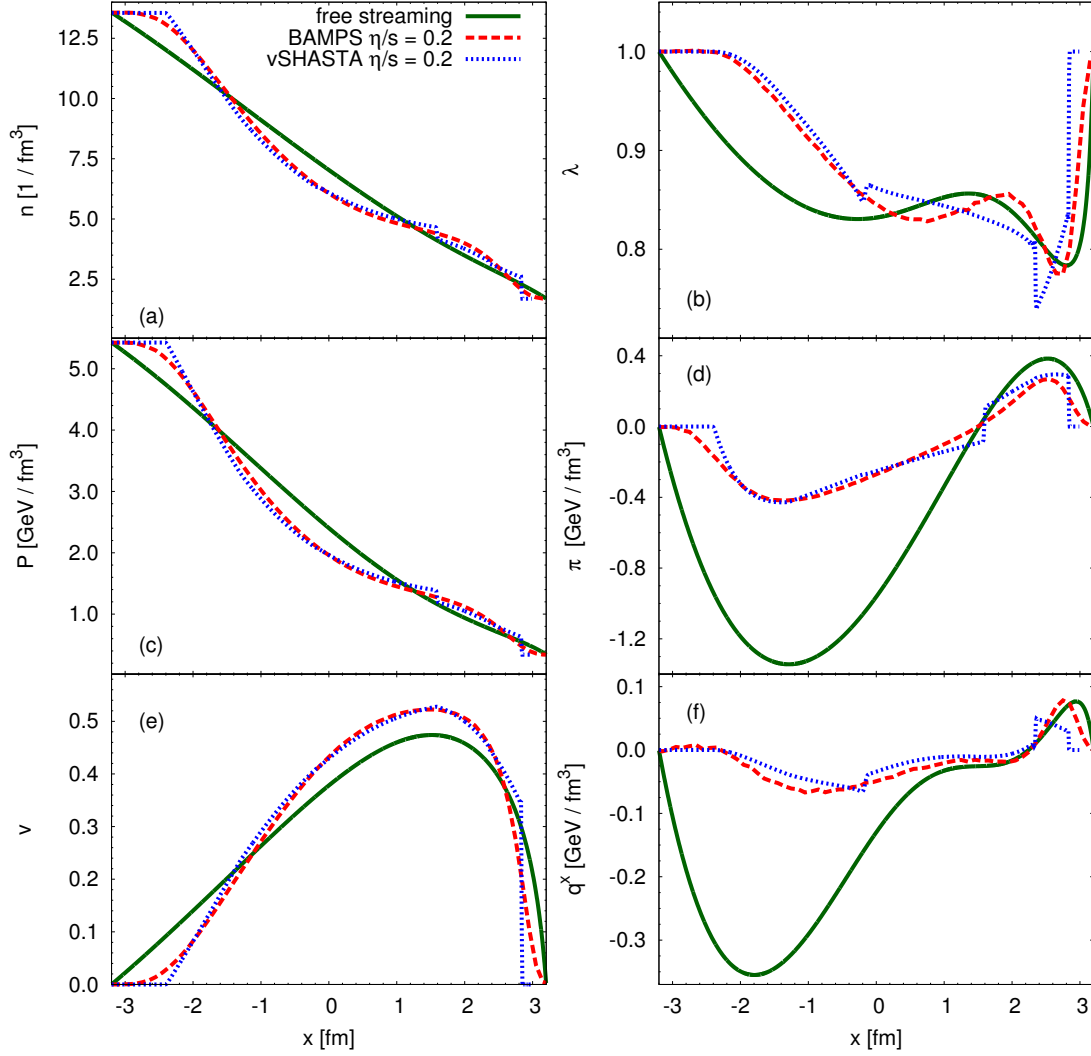
Figure 7.5.: Same quantities as shown in Fig. 7.4 but for $\eta/s = 0.2$. In addition, the free-streaming solution, as discussed in Appendix I, is shown. The initial conditions and settings are listed in Tab. 7.1.

in Ref. [174], called the "double-shock" phenomenon by the authors. It is important to note that within this reference smoothed-particle hydrodynamics (SPH) has been used to solve the equations of dissipative hydrodynamics, corresponding to the simplified IS equations without heat conductivity. The simplified or truncated IS equations take into account the relaxation term only to describe the time evolution of dissipative quantities.

In the hydrodynamical calculation, this discontinuity originates from the initial discontinuity. In the early stage of the evolution the effective pressure, $P + \pi$, and the velocity acquire almost constant values near the discontinuity. The velocity and the gradient of the effective pressure are the driving forces of the expansion. Therefore, if they are constant nothing happens to the structures in the solution and the original

discontinuity disappears very slowly such that parts of it are still visible in the later stages of the evolution.

A similar difference between the BAMPS and vSHASTA results is seen at the right edge of the shock wave. This part of the profile is again not described correctly by the IS theory, and the difference is already visible for smaller values of η/s. The same is also true for the head of the rarefaction fan, although it is less visible for small viscosities. This kind of discontinuous behavior can be seen in all relevant hydrodynamical quantities.

In the BAMPS calculation, the original discontinuity disappears immediately. This is because in kinetic theory, the evolution near the very steep density gradient is well approximated by free streaming or diffusion of particles, which smoothen out all sharp structures very rapidly. Free streaming of particles drives the system far out of thermal equilibrium immediately, such that it cannot be described correctly by second-order dissipative hydrodynamics.

This phenomena has been studied and explained in non-relativistic systems by M. Torrilhon *et al*. [218, 219, 220]. They concluded that the viscous hydrodynamical solutions of the Riemann problem actually lead to discontinuous solutions. For example, in the non-relativistic 13-field equations the system has five instead of three characteristic waves. Although dissipation leads to the attenuation of these waves and the smoothening of discontinuities, this can only happen after a sufficiently long time. In case we include higher moments of the distribution function we will find more characteristics and therefore more discontinuities but with smaller amplitude. There is an infinite number of moments, which form a hierarchy of equations. Therefore, by taking into account higher moments the approximations to the Boltzmann equation become more precise, which in turn leads to a better approximation for smooth profiles. On this account we note that there are more recent studies showing that the Grad's 13-moment method leads to much better results with a special regularization technique [221, 222]. So far these methods have been studied only in the non-relativistic case, but they nevertheless point towards a solution.

Heat-flow problem in the IS-Theory

As shown in Appendix A, we have neglected the term that couples the shear pressure to the heat-flow equation (A.14). The reason is that, if this term is included, the good agreement of heat flow and fugacity between BAMPS and vSHASTA is lost even for small viscosities. This is demonstrated in Fig. 7.6, where we show the fugacity, λ, and heat flux, q^x, for $\eta/s = 0.1$ with and without this coupling term. The profiles change completely, and there is no support from BAMPS for structures induced by the coupling. For the other quantities this coupling term has only a very small effect.

The reason that this single term can become dominant is that for the viscous Riemann problem, the heat flow is typically one order of magnitude smaller than the shear pressure. Thus, the coupling term in the heat equation can be large when the shear pressure is large, even if it formally is a second-order correction only.

The origin of the heat-flow problem is hence not due to strong dissipation, but it is a general failure of the standard theory of Israel and Stewart. We assume that the IS theory suffers from wrong values for the transport coefficients and does not
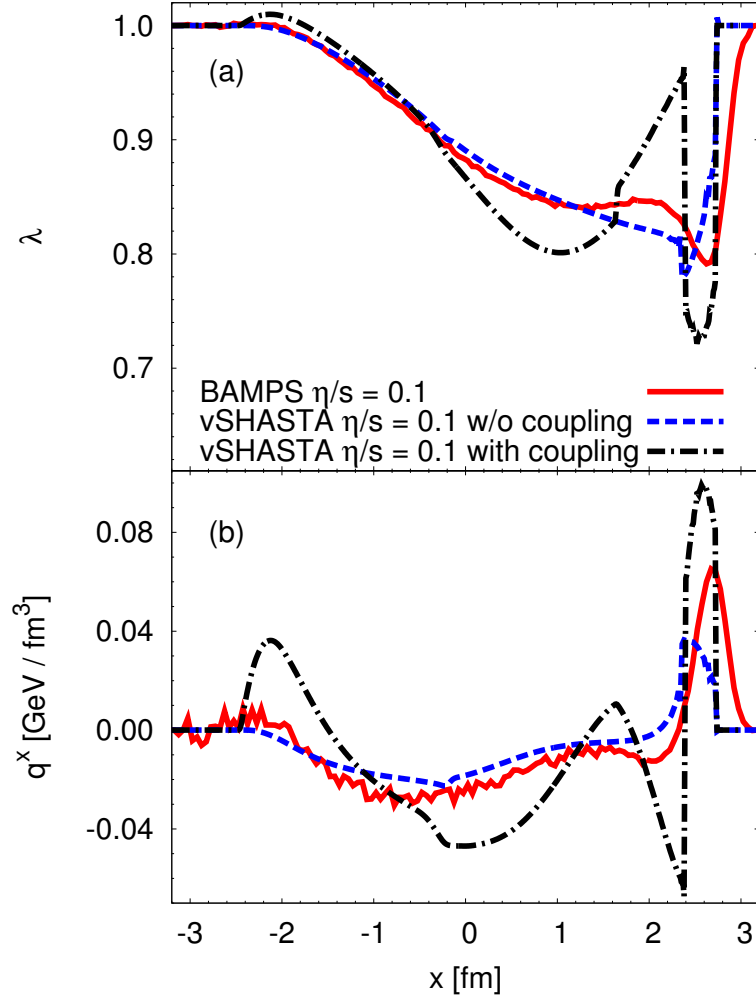
Figure 7.6.: The fugacity (a) and heat flow (b) profiles with and without the coupling, I_{q3}^x, of the shear pressure in the heat-flow equation (A.14).

include all terms which are necessary for a sufficiently good description. In order to resolve the heat-flow problem, it is necessary to go beyond the standard 14-moment approximation, which has been pointed out in Sec. 3.4.4 and is discussed in greater detail in Refs. [35, 47]. In Sec. 7.3, we show the results and improvements of this recently derived RTRFD theory compared to the IS theory again using BAMPS as a reference.

Global Knudsen number analysis

In order to better quantify and measure the applicability of IS theory, we define the relative difference between the BAMPS and vSHASTA calculations as

$$\left\langle \frac{\delta e}{e} \right\rangle^2 = \frac{1}{\Delta x} \int \mathrm{d}x \left(\frac{\delta e}{e} \right)^2, \tag{7.2}$$
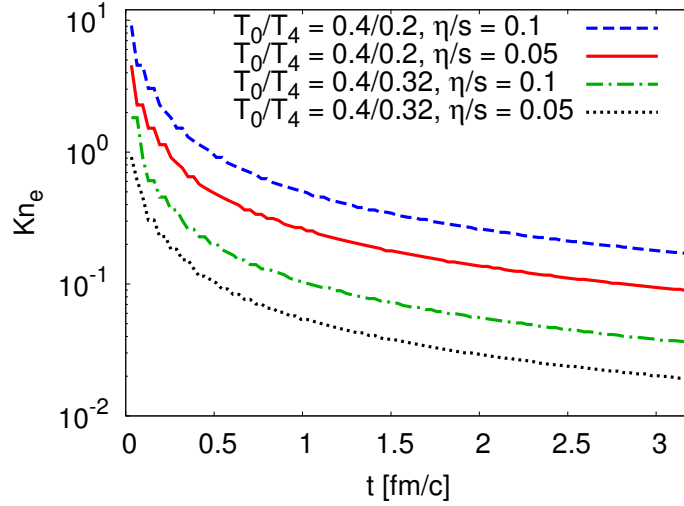
Figure 7.7.: Time evolution of the average Knudsen number, Kn_e, for different initial temperature ratios and different values of η/s.

where δe is the difference in energy density between the BAMPS and the vSHASTA calculations. We recall that $e = 3p$ for a massless gas. The integral is evaluated from the head of the rarefaction fan to the tail of the shock wave. As a consequence the constant temperature regions to the left and the right are not included. The width of this region is denoted as Δx. Similarly, the average macroscopic length scale can be estimated from the average energy density gradient as

$$L_e^{-1} = \left| \frac{1}{\Delta x} \int \frac{1}{e} \frac{\partial e}{\partial x} \mathrm{d}x \right| = \frac{1}{\Delta x} \ln \frac{e_0}{e_4}, \tag{7.3}$$

where e_0 and e_4 are the initial energy densities on the left- and the right-hand side of the initial discontinuity, respectively. Hence, an average Knudsen number relevant for this study can be defined as

$$Kn_e = \frac{\lambda_{\mathrm{mfp}}}{L_e}, \tag{7.4}$$

where λ_{mfp} is the mean free path in the low-temperature region, i.e., where the mean free path is largest. This definition smoothens the rapid changes compared to a local Knudsen number and makes the comparisons between calculations feasible. Note that the Knudsen number (7.4) is similar to that introduced in Ref. [33].

Since $\lambda_{\mathrm{mfp}} \sim \eta/(Ts)$ and $L_e \sim t$, where t is a typical time scale of the evolution, we also have

$$Kn_e \sim \frac{\eta}{s} \frac{1}{Tt}. \tag{7.5}$$

Therefore, Kn_e stays constant for a given temperature if we scale η/s and t by the same factor.

Figure 7.7 shows the time evolution of the average Knudsen number for two different initial conditions and two different viscosities. In all cases the Knudsen number is
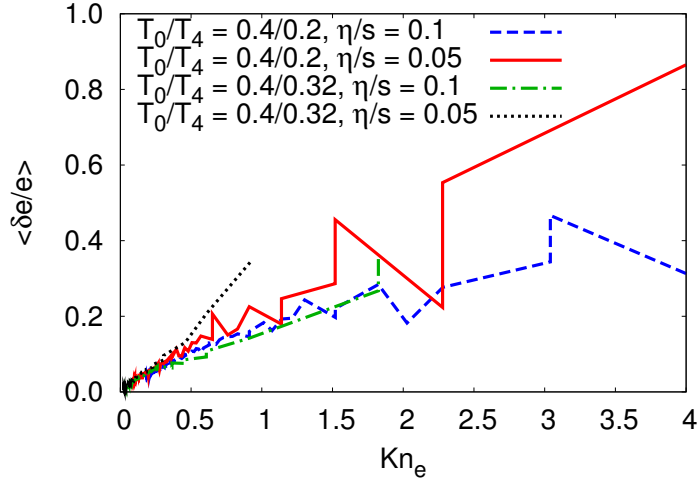
Figure 7.8.: The relative difference of kinetic and hydrodynamical calculations for different initial temperature ratios and different values of η/s as a function of the average Knudsen number.

initially large but then decreases rapidly as the system expands. This happens as a function of the initial temperature difference and viscosity.

On the other hand, the relative difference between BAMPS and vSHASTA calculations decreases with a decreasing averaged Knudsen number. This is shown in Fig. 7.8 where we can see that for small Knudsen numbers the different solutions converge to approximately one curve. This also means that to good approximation the Knudsen number alone determines the applicability of IS theory. We can infer from Fig. 7.8 that the differences between BAMPS and vSHASTA are less than 10% for $Kn_e < 1/2$.

7.1.3. The weak and the strong shock-wave limit

initial variables	left	right	further settings
$T\,(\mathrm{GeV})$	0.4	0.32 and 0	one species: $m = 0\,\mathrm{GeV}$
λ	1	1	degeneracy factor $g = 16$
v	0	0	isotropic elastic $2 \rightarrow 2$ collisions
$\Pi\,(\mathrm{GeV/fm^3})$	0	0	constant η/s
$q^\mu\,(\mathrm{GeV/fm^3})$	0	0	runtime = 3.2 fm/c; system size $L_x = 6.4$ fm
$\pi^{\mu\nu}\,(\mathrm{GeV/fm^3})$	0	0	walls in x-direction; periodic boundary conditions in transverse y- and z-direction

Table 7.2.: The initial conditions and settings used in BAMPS solving the rRP in the ultrarelativistic limit for weak and strong shock waves.

In Sec. 7.1.1 and 7.1.2, we have discussed in detail the numerical solutions of the rRP

using BAMPS and vSHASTA. The initial conditions have been chosen as $T_L = 0.4$ GeV and $T_R = 0.2$ GeV, resulting in a specific profile. However, keeping all other initial values the same, but using a different initial ratio, the profile of the shock-tube problem changes. For this purpose, we discuss two other initial ratios for the shock-tube problem, which we call the weak limit with $T_R = 0.32$ GeV, and the strong limit with $T_R = 0$ GeV. The latter limit corresponds exactly to the expansion into the vacuum. The designation *weak limit* is not totally correct, since one has to use an infinitely small difference between initial pressures to obtain the weak-shock limit, i.e., $P_0/P_4 \approx 1$. For our discussion, however, the values are appropriate enough. A smaller ratio would require a considerably larger computational power in order to get rid of statistical fluctuations. In contrast to Secs. 7.1.1 and 7.1.2 we discuss the numerical solutions from BAMPS only. The initial conditions are listed in Tab. 7.2.

We discuss both cases simultaneously, and compare always with the cases discussed in Secs. 7.1.1 and 7.1.2. In Fig. 7.9 and 7.10, we show the results for various η/s values as computed with BAMPS, demonstrating the gradual transition from the ideal hydrodynamical limit to free-streaming of particles. We show a snapshot at the time $t = 3.2$ fm/c from BAMPS for the particle density, n, the fugacity, λ, the isotropic pressure, P, the shear pressure, π, the velocity, v, the shear pressure, π, and the heat flow, q^x. In addition, the analytical solution for a massless gas of particles is depicted for the corresponding initial ratio both for the perfect-fluid case[8] and the free-streaming case[9]. At first glance we observe that the perfect-fluid limit is reproduced by BAMPS very accurately using a small shear viscosity over entropy density ratio of $\eta/s = 0.001$ although we find the same numerical artifact for the dissipative quantities as in Sec. 7.1.1. In order to resolve this numerical artifact, we have to use a higher number of test particles.

Comparing the results to the case discussed in Sec. 7.1.1, we find differences in the profiles of the pressure, P, the particle density, n and the velocity, v. First of all, the plateau itself is wider in the weak limit shown in Fig. 7.9, and the rarefaction wave is almost not curved. Moreover, the velocity of the shock front is smaller, i.e., the shock front propagates more slowly into the right medium at rest. Furthermore, the drop of the fugacity is not that strong. On the other hand, the expansion into the vacuum shown in Fig. 7.10, has a dramatically different profile. Due to the fact, that there is no medium on the right side initially, an infinitely strong shock wave evolves. However, because this shock wave approaches the speed of light the width of the shock wave shrinks to zero and is not visible anymore. Hence, the only part we observe is the characteristic structure of a rarefaction wave which is strongly curved due to relativistic effects.

The viscous solutions are obtained by varying the shear viscosity over entropy density ratio to larger values. A larger η/s value results in a finite transition layer where the quantities change smoothly rather than discontinuously as in the case of a perfect fluid. We make the clear observation that in the weak limit presented in Fig. 7.9 the shock plateau shrinks with larger viscosity. A nonzero viscosity smears out the profiles and impedes a clean separation of the shock front from the rarefaction fan.

---

[8]discussed in Chapter 5.
[9]discussed in Appendix I.
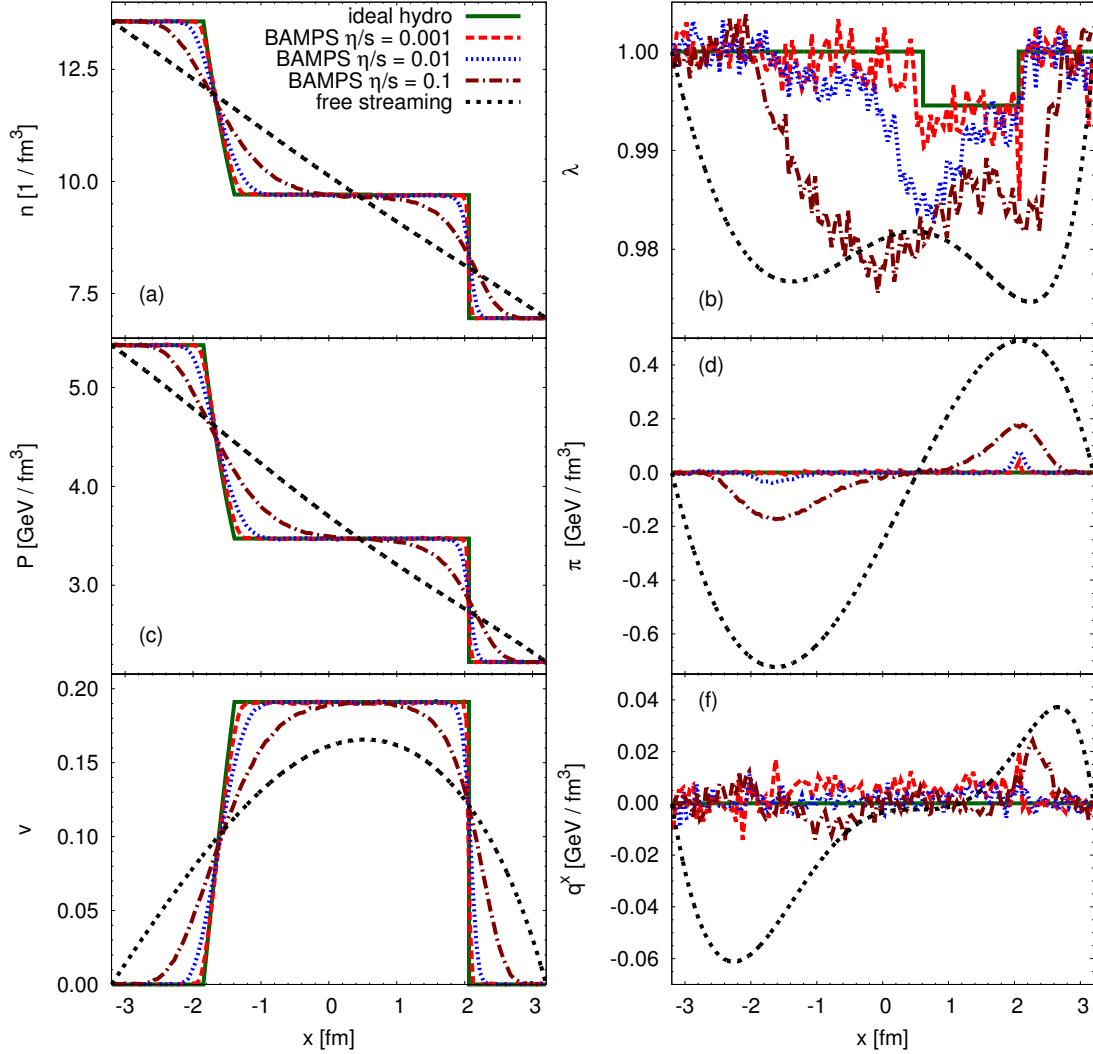
Figure 7.9.: The analytical and numerical solutions of the relativistic Riemann problem for the particle density (a), the fugacity (b), the isotropic pressure (c), the shear pressure (d), the velocity (e), and the heat flow (f). The initial conditions at $t = 0$ fm/c are listed in Tab. 7.2. The initial temperatures are $T_L = 0.4$ GeV and $T_R = 0.32$ GeV. The results from BAMPS are shown for various η/s at $t = 3.2$ fm/c. The full lines represent the analytic solution for $\eta = 0$.

The expansion into the vacuum presented in Fig. 7.10 undergoes a similar behavior with larger viscosity. The difference here is that only the shape of the rarefaction wave changes, since there is no shock wave part at all. In both cases the dissipative quantities grow with larger viscosity. Depending on the strength of the viscosity a different shape of the shear pressure and heat flow appear. For a non-interacting gas we have depicted the free-streaming solution where the characteristic structure of the Riemann problem for a perfect fluid is completely washed out. A clear distinction between the shock
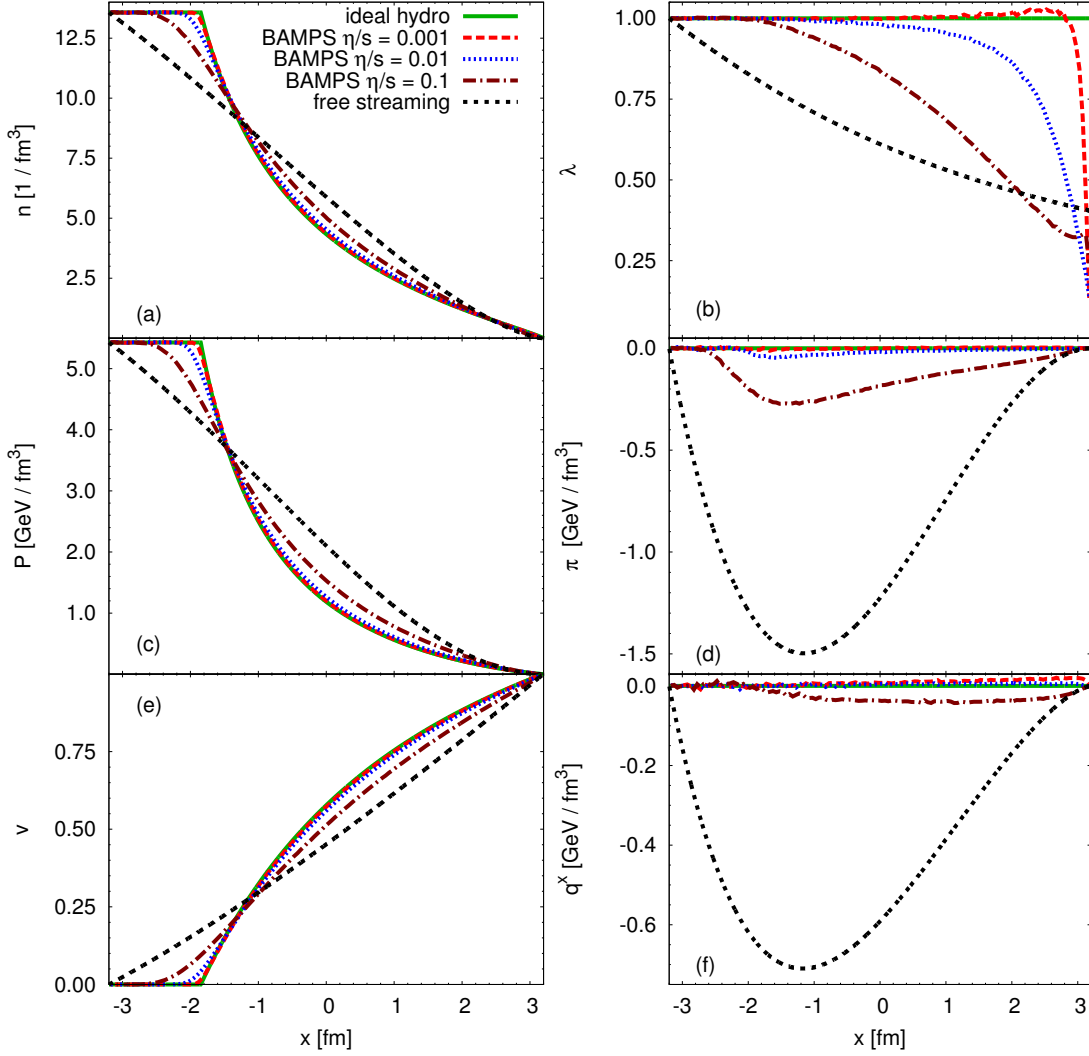
Figure 7.10.: Same quantities as shown in Fig. 7.9. The initial conditions at $t = 0\,\mathrm{fm}/c$ are listed in Tab. 7.2. The initial temperatures are chosen as $T_\mathrm{L} = 0.4\,\mathrm{GeV}$ and $T_\mathrm{R} = 0\,\mathrm{GeV}$ which represents the expansion into the vacuum.

wave and the rarefaction fan is no longer possible.

Finally, we can conclude that BAMPS is able to describe all the initial pressure ratios of the rRP, even though there are some limitations. The most difficult case is the expansion into the vacuum since no particles exist on the corresponding side initially. But in BAMPS we require a sufficient number of particles per cell in order to solve the rBE in an accurate way. For the weak limit presented in Fig. 7.9 we find a very good agreement to the analytical solution of the perfect-fluid limit. The only problem we encounter here is the fact that the dissipative quantities are almost of the same magnitude as the statistical fluctuations. Thus, we need more computational power in order reduce these fluctuations. An even smaller initial pressure ratio compared to this presented in Fig. 7.9 aggravates this problem.
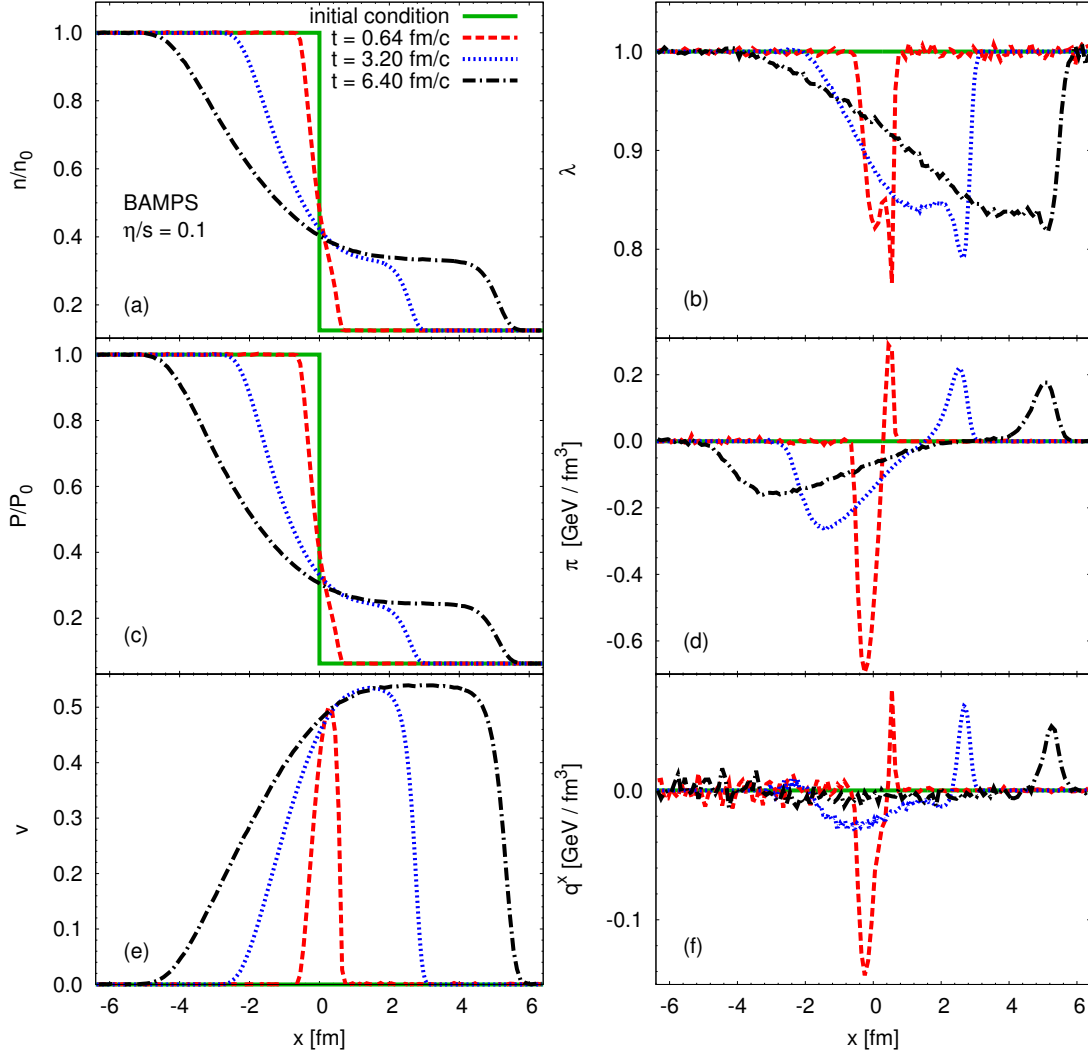
Figure 7.11.: The time evolution of the rRP for $\eta/s = 0.1$. The quantities and the initial conditions are the same as shown in Fig. 7.1.

7.1.4. Time evolution and scaling behavior

In ideal hydrodynamics, shock waves are formed immediately after removing the membrane that separates matter with different temperatures. This happens because the Knudsen number, Kn_e, vanishes at any time. For non-vanishing viscosity, Kn_e is large at early times and, as a consequence, the formation of shock waves occurs later, when Kn_e becomes smaller. For example, this happens in the case of constant η/s value as demonstrated in Fig. 7.7.

Figure 7.11 shows the profiles of the particle density, n, the isotropic pressure, P, the velocity, v, the fugacity, λ, the shear pressure, π, and the heat flow, q^x, at various times for $\eta/s = 0.1$ and initial temperatures $T_L = 0.4\,\text{GeV}$ and $T_R = 0.2\,\text{GeV}$. At the early time $t = 0.64$ fm/c shock waves have not yet developed. The pressure profile looks like that in the strongly diffusive case of free-streaming particles. At $t = 6.4$ fm/c
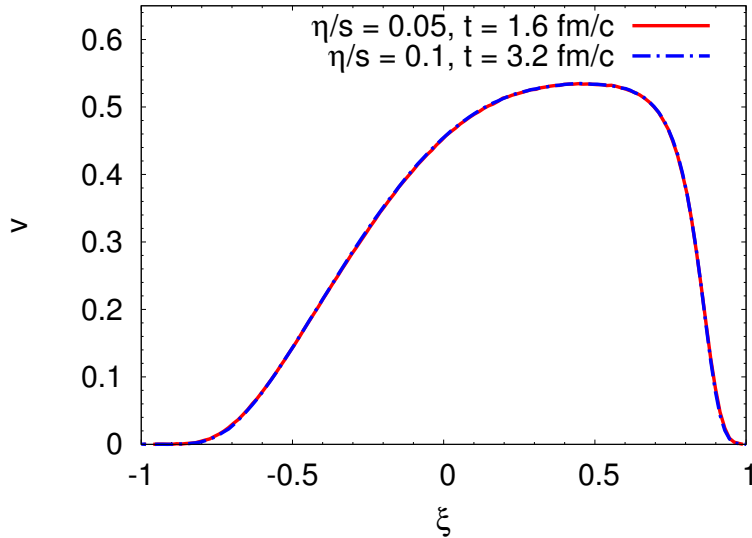
Figure 7.12.: The scaling behavior of the rRP. The initial conditions and settings are listed in Tab. 7.1. The velocity profiles are shown as a function of the similarity variable $\xi = x/t$ for $\eta/s = 0.1$ and $\eta/s = 0.05$ at the times $t = 3.2$ fm/c and $t = 1.6$ fm/c, respectively.

we observe a characteristic shock plateau that clearly separates the shock front from the rarefaction wave as in the ideal-fluid case. The intermediate time $t = 3.2$ fm/c is approximately the time scale at which the shock plateau is being formed and the maximum of the velocity distribution, $v(x)$, reaches the value v_{plat} of the ideal-fluid solution. We define this time scale as the formation time of shocks.

The only intrinsic length scale in the microscopic approach is the particle mean free path. Therefore, if we rescale the mean free path by a constant factor of a, we expect the time scale for the evolution of matter to change accordingly. Since $\eta/s \sim \lambda_{\text{mfp}}$ we expect that profiles calculated at time t for a given value of η/s agree with those at a time $a\,t$ for a viscosity-to-entropy density ratio of $a\,\eta/s$. This is demonstrated in Fig. 7.12 where we show the velocity profiles as a function of the similarity variable, $\xi = x/t$.

The pressure and the velocity profile as a function of ξ are determined by the Knudsen number given by Eq. (7.4). According to Eq. (7.5), Kn_e is the same for the calculation with $\eta/s = 0.1$ at $t = 3.2$ fm/c and that with $\eta/s = 0.05$ at $t = 1.6$ fm/c. Therefore, the pressure $P(x,t;\eta/s)/P_0$ and velocity $v(x,t;\eta/s)$ are functions of ξ and Kn_e only, i.e., $P(x,t;\eta/s)/p_0 = F(\xi; Kn_e)$, with the same relation holding for the velocity. For decreasing Kn_e, the plateau of the velocity profile in Fig. 7.12 grows and approaches the shape of the ideal-fluid case discussed in previous sections.

This scaling behavior holds for initial conditions with a discontinuity in the pressure only. If the discontinuity is replaced by a smooth transition, the non-zero width, Γ_{tr}, of the transition region introduces another length scale. This transition region then changes as a function of the transition variable under the rescaling $t \to at$, $\xi_{\text{tr}} = \Gamma_{\text{tr}}/t \to \Gamma_{\text{tr}}/(at)$, which causes a different gradient in the transition region as a function of ξ.

Because of the different initial situations, evolutions in ξ are not identical for the same Knudsen number, Kn_e.

7.1.5. Formation time of shock waves

In the following, we estimate the upper limit of the η/s ratio, for which shocks can still be observed experimentally on the timescale of an ultrarelativistic heavy-ion collision. As mentioned in the previous section 7.1.4, a criterion for a clear separation, and thus for the observability of a shock wave, is the formation of a shock plateau as in the ideal-fluid case. The formation of a shock plateau takes a certain amount of time, as demonstrated in Fig. 7.11 for a specific initial pressure ratio.

From Fig. 7.11, we see that the shock wave develops between $3.2 < t < 6.4$ fm/c for a fixed $\eta/s = 0.1$. Thus, the shock plateau has not yet developed at $t = 3.2$ fm/c, but for sure at $t = 6.4$ fm/c. There is a critical time t_f for a given η/s where the shock plateau has been formed. However, there is also a dependence on the initial pressure ratio, which is not negligible for the formation time of a shock wave. The larger the initial pressure ratio, the longer time the shock plateau needs to develop.

In order to understand the timescale of the formation of a shock wave, we use the general definition of the Knudsen number [45, 202, 223]

$$K = \frac{\lambda_{\mathrm{mfp}}}{L} , \tag{7.6}$$

where we define $L \equiv t\,(v_{\mathrm{shock}} + c_s)$ as the width of the region bounded by the rarefaction wave traveling to the left and the shock front moving to the right[10]. Here, v_{shock} is the velocity of the shock front and c_s is the speed of sound. Note that λ_{mfp} is not constant. We approximate it by its maximum value which is assumed to be found on the low-pressure side[11] in front of the shock wave. The quantity K can be viewed as a "global" Knudsen number for the Riemann problem. K goes to zero at late times, which implies that the medium behaves more and more like an ideal system.

The value of K at which the shock wave forms, called K_f, is universal for given P_4/P_0. With Eq. (6.15) we obtain $\lambda_{\mathrm{mfp}} = 10/(3T_4)\eta/s$ in the undisturbed medium with the lower pressure. As an example, for the case with $T = 320$ MeV the shock wave forms at $t = 3.2$ fm/c for $\eta/s = 0.1$. We find that $K_f = 0.053$.

Inserting $\lambda_{\mathrm{mfp}} = 10/(3T)\eta/s$ into Eq. (7.6), the formation time of shock waves is given by

$$t_f = \frac{10}{3} \frac{1}{K_f(v_{\mathrm{shock}} + c_s)T} \frac{\eta}{s} . \tag{7.7}$$

Figure 7.13 shows the relation (7.7) with $T = 350$ MeV and for various initial pressure discontinuities, P_4/P_0.

The difference in slopes reflects the dependence of K_f and v_{shock} on the ratio P_4/P_0. For $\eta/s = 0.2$, no shock will be visible until $6-7.2$ fm/c, which most likely exceeds the lifetime of the QGP at RHIC. This implies that if shock phenomena are discovered at RHIC, this could be an indication that the QGP has a small η/s ratio of probably less

---

[10]in the ideal-fluid case.
[11]the undisturbed medium.
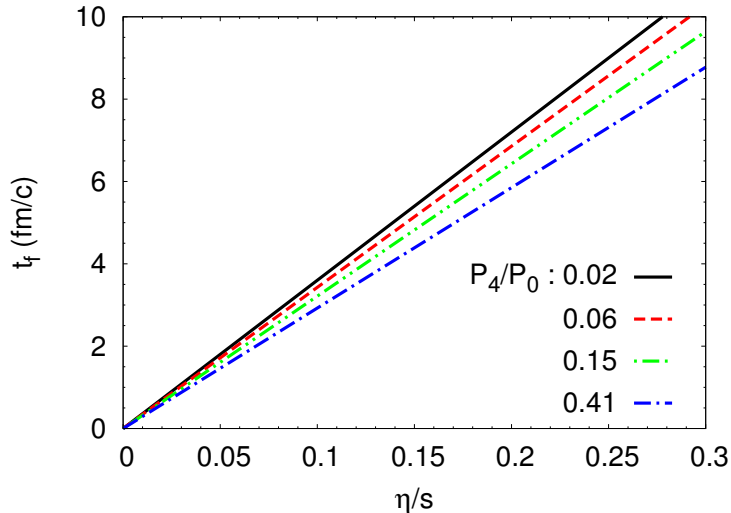
Figure 7.13.: Formation time of shock waves as a function of η/s.

than 0.2. For a more viscous QGP no shock waves and thus no Mach cones will be formed. In a relativistic heavy-ion collision, the temperature is decreasing during the expansion. Thus, according to Eq. (7.7), t_f is even larger and shock waves may be even harder to observe.

This kind of study is useful for our further discussions about Mach cones which are a special form of shock waves. We demonstrate in Chapter 8 that the viscosity as well as the energy deposition rate play an important role for the observation of Mach cones.

7.1.6. The difference between the Eckart and the Landau frame

In Chapter 6 we have mentioned that we are able to calculate the hydrodynamic quantities either in the Eckart or the Landau frame. In this Chapter 7 we have so far focused exclusively on the Landau frame, so far. The reason is that the difference between the Eckart and Landau frame is small and does not play any important role for the discussions and conclusions we have made. This is definitely true in the case of small dissipation. However, the difference between Eckart and Landau frame becomes significant with larger viscosity and gradients, which is reflected by the appearance of heat flow. In this section we briefly discuss the origin of heat flow and demonstrate the difference between Eckart and Landau frame using BAMPS.

In Fig. 7.14, we show the velocity profile in the Eckart and the Landau frame of the rRP in the almost ideal case (upper panel) and in the case with huge dissipation (lower panel). The initial conditions are listed in Tab. 7.1. In the upper left panel we use a large constant cross section of $\sigma = 224\,\mathrm{mb}$, which results in a very small Knudsen number Kn, because the mean free path is small compared to the macroscopic length scale. We find that there is no visible difference between Eckart and Landau frame in the velocity profile $v(x)$. This results in a vanishing heat flow, q^x, as shown in the upper right panel. Since we cannot go to the limit of the perfect-fluid case, some finite heat flow remains, which is indicated by the peak at the shock front. On the other
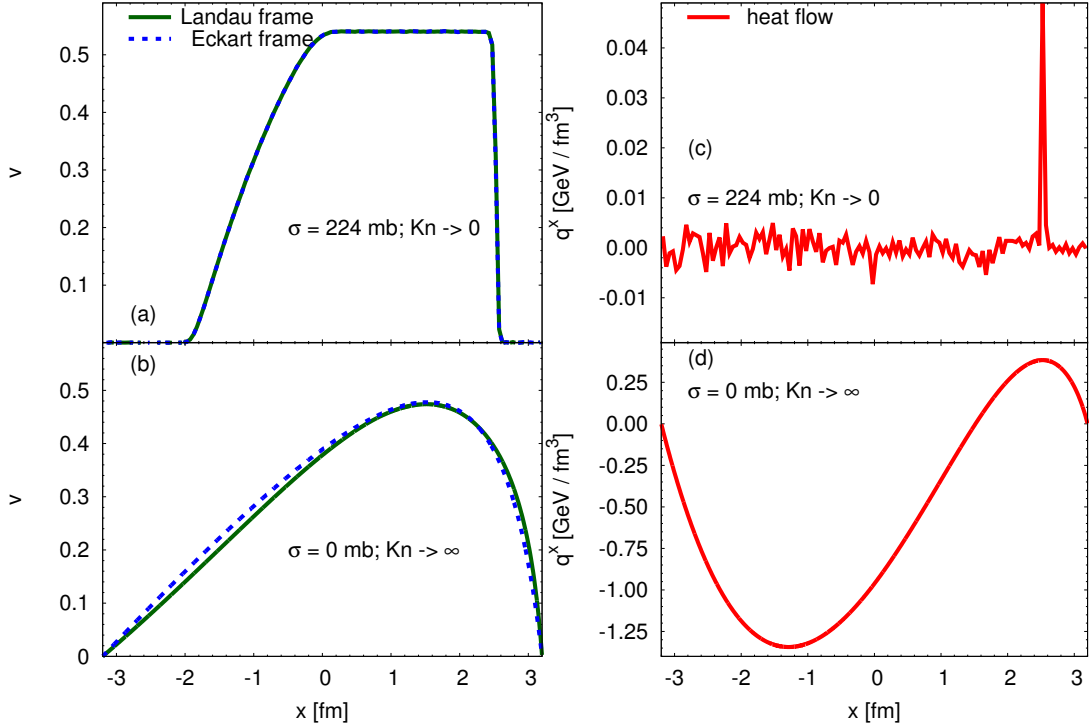
Figure 7.14.: The difference between the Eckart and the Landau frame for a specific ratio in the rRP. In the left panels, we show the velocity profile in the Eckart and the Landau frame. The right panels depict the corresponding heat flow. In the upper panels we show the almost ideal case, whereas we show the free-streaming case in the lower panels. The initial conditions and settings are listed in Tab. 7.1.

hand, for an infinitely large Knudsen number, as shown in the lower left panel, we find an explicit difference between Eckart and Landau frame. This obviously results in a strong heat flow, as shown in the lower right panel. When comparing the upper and lower right panel, we see that heat flow is different by $3 - 4$ orders of magnitude.

The heat flow is directly connected to the difference between Eckart and Landau frame. For the special case of a one-dimensional system which is homogeneous in transverse direction, we can find a simple expression to illustrate this. We start from the general definition of the heat flow (3.47) as discussed in Chapter 3, i.e.,

$$q^{\mu} = W^{\mu} - h\,V^{\mu}\,. \tag{7.8}$$

The heat flow is the difference between the flow of energy W^{μ} and flow of particles V^{μ}, where h is the enthalpy per particle. In the Landau frame the flow of energy vanishes, while the flow of particles vanishes in the Eckart frame. In the following, we use the Landau frame. Thus, the heat flow reads

$$q_L^{\mu} = -h\,V^{\mu}\,. \tag{7.9}$$

Using the definition of V^μ from Eq. (3.45), we can rewrite this as

$$q_L^\mu = -h\,\Delta_\nu^\mu N^\nu\,. \tag{7.10}$$

With the definition of the space-like transverse projection operator (3.23), the first component of the heat flow reads

$$q_L^x = h\left(\gamma_L^2 v_L N^0 - N^x - \gamma_L^2 v_L^2 N^x\right)\,, \tag{7.11}$$

where v_L (γ_L) is the velocity (Lorentz factor) in the Landau frame. Now, factorizing out N^0, we obtain

$$q_L^x = hN^0\left(\gamma_L^2 v_L - v_E - \gamma_L^2 v_L^2 v_E\right)\,, \tag{7.12}$$

where $v_E = N^x/N^0$ is the definition of the velocity in the Eckart frame. In the following, we use the relation $\gamma^2 = 1 + \gamma^2 v^2$, leading to

$$q_L^x = h\gamma_L^2 N^0\left(v_L - v_E\right)\,. \tag{7.13}$$

This relation indicates that heat flow only appears if $v_L \neq v_E$. In the perfect-fluid case we have $v_L = v_E$, such that the heat flow has to vanish. In case of particle or energy diffusion, i.e., if we have dissipation, the heat flow is proportional to the difference between the velocities in the Landau and Eckart frame, respectively.

7.2. Further solutions of the relativistic Riemann problem

In this section, we solve the rRP for different properties of the matter using BAMPS. We still consider the shock-tube problem and the size of the static box is chosen to be $L_x = 6.4\,\text{fm}$.

We start in Sec. 7.2.1 using a massless gas of particles, but in contrast to Sec. 7.1 we include the possibility of production and annihilation of particles, which in the end affects the fugacity and particle-density profile. In the following Sec. 7.2.2, we employ BAMPS to simulate the shock-tube problem for a gas of massive particles, with only binary collisions and constant cross sections. The nonzero mass of the particles leads to a nonzero viscous bulk pressure which grows with larger dissipation. In Sec. 7.2.3 we finally simulate a system of two massless particle species with various cross sections. We will observe an interesting coupling between both particle species.

7.2.1. A system of massless particles including inelastic processes

In Sec. 7.1 we have restricted our investigations of the rRP to binary collisions. This implies that the particle number is conserved during the whole simulation and leads to a drop of the fugacity in the region of the shock plateau, even in the nearly perfect-fluid limit. This can be inferred from Fig. 7.1b. This drop of the fugacity also appears in the analytical solution and is not a numerical artifact.

In this section we employ BAMPS to solve the rRP for an ultrarelativistic gas of massless particles as we have done in Sec. 7.1, but we now include particle production and annihilation processes. This results in chemical equilibration depending on the chosen values of the cross sections. For an infinite scattering rate, we would observe

initial variables	left	right	further settings
$T\,(\mathrm{GeV})$	0.4	0.25	one species: $m = 0\,\mathrm{GeV}$
λ	1	1	degeneracy factor $g = 16$
v	0	0	isotropic elastic $2 \to 2$ and inelastic $2 \leftrightarrow 3$ collisions
$\Pi\,(\mathrm{GeV/fm^3})$	0	0	$\sigma_{22} = \sigma_{23} = 25\,\mathrm{mb}$, $I_{32} = (196/g)\pi^2\sigma_{23}$
$q^\mu\,(\mathrm{GeV/fm^3})$	0	0	runtime $= 3.2\,\mathrm{fm}/c$; system size $L_x = 6.4$ fm
$\pi^{\mu\nu}\,(\mathrm{GeV/fm^3})$	0	0	walls in x-direction; periodic boundary conditions in transverse y- and z-direction

Table 7.3.: The initial conditions and settings used in BAMPS to describe the rRP for an ultrarelativistic gas of massless particles including binary and inelastic processes.

an instantaneous chemical equilibration. Then, the chemical potential would vanish, i.e., the fugacity would always be equal to unity. However, BAMPS always has a finite cross section, and therefore the chemical potential does not vanish.

In Fig. 7.15 we show a snapshot of the particle density, n, the fugacity, λ, the isotropic pressure, P, the shear pressure, π, the velocity, v, and the heat flow, q^x, at time $t = 3.2\,\mathrm{fm}/c$. The initial conditions are listed in Tab. 7.3. For binary collisions we use a constant cross section of $\sigma_{22} = 25\,\mathrm{mb}$. In addition, the cross section for particle creation is $\sigma_{23} = 25\,\mathrm{mb}$ and the phase-space matrix element is accordingly given by $I_{32} = (196/g)\pi^2\sigma_{23}$. All scattering processes are isotropic and the inelastic scattering processes are adjusted in such a way that we maintain detailed balance.

In Fig. 7.15, we compare the numerical results of BAMPS to the analytical solution of the rRP. For the analytic solution we assume particle-number conservation in order to demonstrate the differences arising from chemical equilibration. At first glance we observe an almost perfect agreement in most quantities. However, there are differences which results from two effects. The first one results from the nonzero dissipation emerging from the finite cross sections in BAMPS. We observe a smearing out of the profile around the shock front as well in the region of the rarefaction wave. Still, the cross sections are large enough to lead to the appearance of a shock plateau. The second effect results from chemical equilibration, which manifests itself in the profile of the fugacity and the particle density.

In the region of the shock plateau the temperature is higher, since the particles in this region have a higher kinetic energy. When assuming particle-number conservation, as done for the analytical solution, this is unavoidable, and results in a drop of the fugacity and the particle density. When including inelastic processes in BAMPS, for which the results are shown in Fig. 7.15, we see that the fugacity is almost equal to unity even in the region of the shock plateau and as a further consequence the discontinuity in the particle-density profile vanishes.

The chemical equilibration also affects the heat-flow profile. Although we have nonzero dissipation, as seen in the profile of the shear pressure, depicted in Fig. 7.15d,
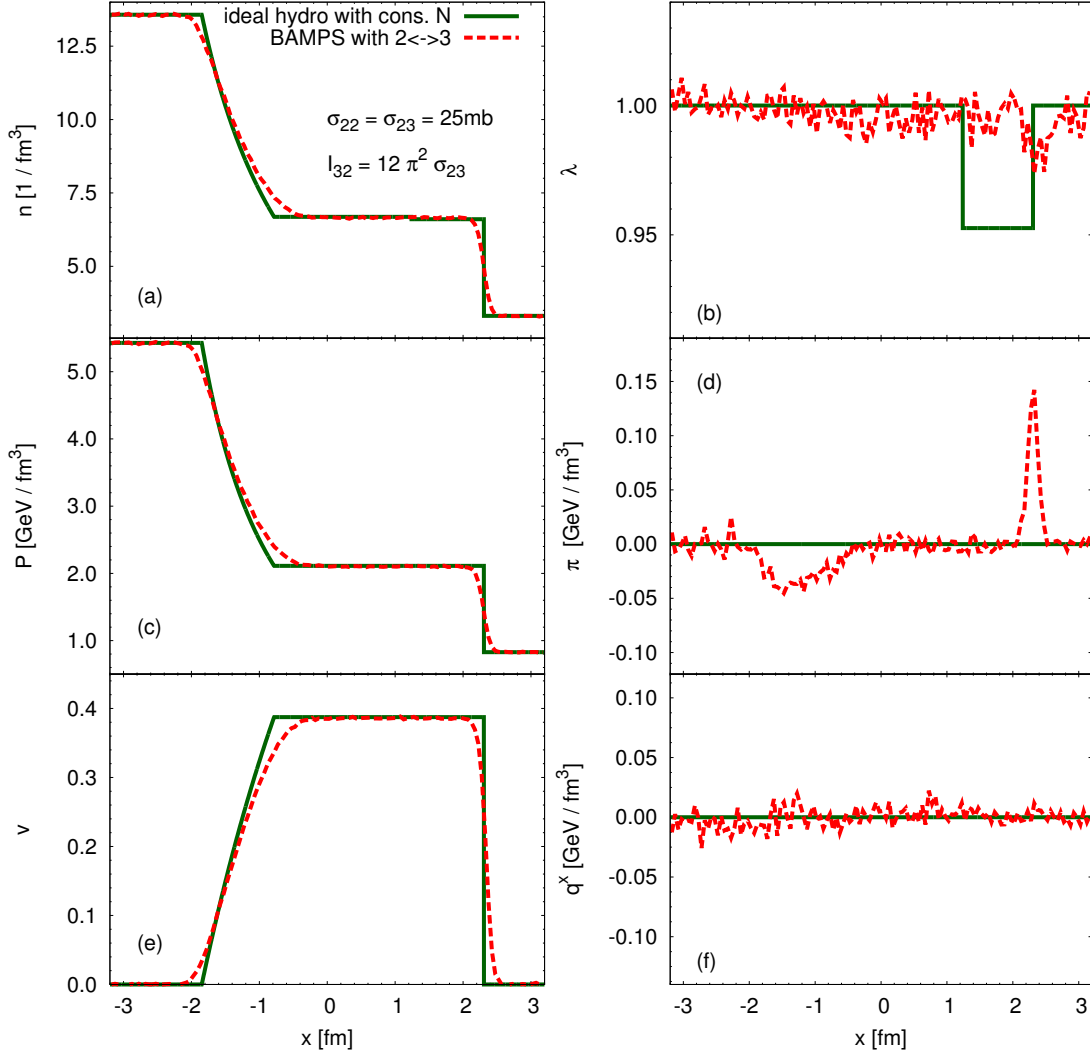
Figure 7.15.: The analytical and numerical solutions of the rRP for an ultrarelativistic gas of massless particles including inelastic processes. We show the particle density (a), the fugacity (b), the isotropic pressure (c), the shear pressure (d), the velocity (e), and the heat flow (f). The initial conditions and settings are listed in Tab. 7.3. The full lines are the analytic solutions at $t = 3.2$ fm/c assuming particle-number conservation. The results from BAMPS are shown for constant and isotropic cross sections for elastic and inelastic processes.

the heat flow almost vanishes and it has no peak in the region of the shock front, see Fig. 7.15f. However, the effect here is small, because the heat flow is very small even for the case of only binary collisions, see Fig. 7.3f. A vanishing heat flow indicates that the Eckart and Landau velocity are closer to each other compared to the case assuming particle-number conservation[12].

---

[12]See Sec. 7.1.6 for more details to the origin of heat flow.

We can conclude that the consistent implementation of inelastic processes in BAMPS is a very important and interesting feature [41]. Inelastic processes[13] become very important when dealing with energies in the relativistic regime as they occur in HIC. The effect and importance of chemical equilibration has been discussed in several works dealing with hydrodynamic models of relativistic HIC [224, 225, 226, 227, 228].

7.2.2. A system of massive particles

initial variables	left	right		further settings
$T\,(\text{GeV})$	0.4	0.3		one species: $m = 1\,\text{GeV}$
λ	1	1		degeneracy factor $g = 16$
v	0	0		isotropic elastic $2 \to 2$ collisions
$\Pi\,(\text{GeV}/\text{fm}^3)$	0	0		constant σ
$q^\mu\,(\text{GeV}/\text{fm}^3)$	0	0		runtime $= 3.2$ fm/c; system size $L_x = 6.4$ fm
$\pi^{\mu\nu}\,(\text{GeV}/\text{fm}^3)$	0	0		walls in x-direction; periodic boundary conditions in transverse y- and z-direction

Table 7.4.: The initial conditions and settings used in BAMPS to describe the rRP for a massive gas of particles for binary collisions only.

BAMPS is a kinetic transport model which allows also the propagation and scattering of particles with nonzero masses. In this section, we want to investigate the behavior of a gas of massive particles by considering the rRP. The main motivation is the investigation of bulk viscous pressure which vanishes in the ultrarelativistic limit, as discussed in Sec. 7.1. The bulk viscosity, ζ, is another transport coefficient similar to the shear viscosity, η. In viscous hydrodynamic models, the bulk viscosity is mostly neglected. This is reasonable, since the effects of bulk viscosity are small. However, the effects of a nonzero mass are not small even with low viscosity and result in a different profile in the quantities of interest. The analytical solution of the rRP with nonzero fixed mass is not possible, since it requires the numerical integration of three coupled nonlinear differential equations. However, since BAMPS can handle the rRP in the ultrarelativistic limit, we expect no problems simulating the rRP at nonzero mass.

Figure 7.16 shows the transition from ideal to viscous shock waves for a massive gas in the shock-tube problem. We show a snapshot at time $t = 3.2$ fm/c of the particle density, n, the fugacity, λ, the isotropic pressure, P, the shear pressure, π, the energy density, e, the bulk viscous pressure, Π, the velocity, v, and the heat flow, q^x. The initial conditions are listed in Tab. 7.4, where the initial temperatures are $T_\text{L} = 0.4\,\text{GeV}$ and $T_\text{R} = 0.3\,\text{GeV}$. We use a gas of massive particles with $m = 1\,\text{GeV}$, which interacts only via isotropic and binary collisions. The mass is kept constant during the simulation. Due to the constant mass and changing local temperature, the EoS as well as the speed of sound are not fixed. The speed of sound for a massive gas and vanishing chemical potential is given in Appendix C. The results are shown for

---
[13]In HIC, they are known as Bremsstrahlung processes.
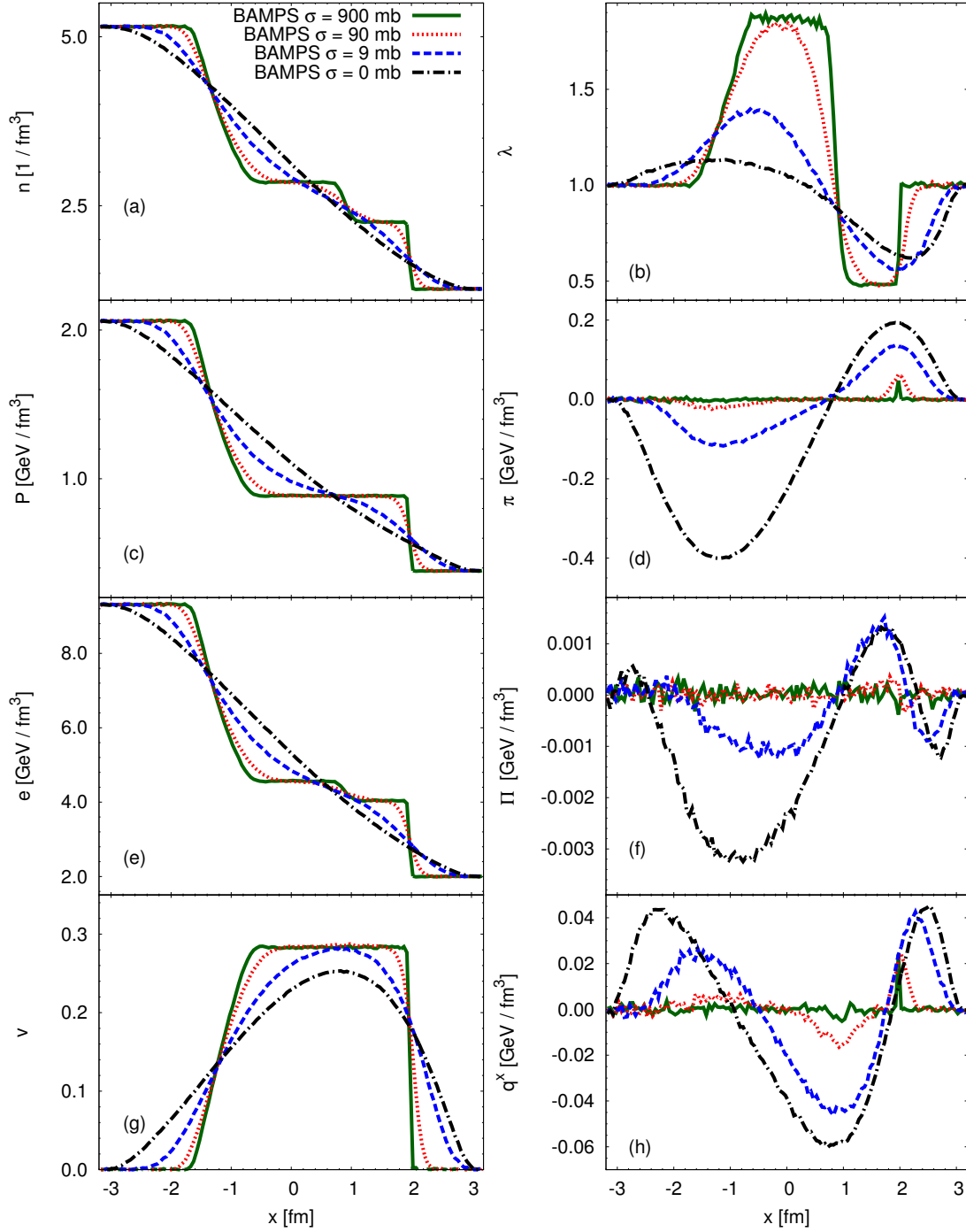
Figure 7.16.: Transition from ideal to viscous shock waves in BAMPS using the rRP for a gas of massive particles. We show the particle density (a), the fugacity (b), the isotropic pressure (c), the shear pressure (d), the energy density (e), the bulk pressure (f), the velocity (g), and the heat flow (h). The initial conditions and settings are listed in Tab. 7.4. The results from BAMPS are shown for constant and isotropic cross sections and a constant mass of $m = 1$ GeV.

various constant cross sections, where $\sigma = 900$ mb represents an almost ideal fluid and $\sigma = 0$ mb the free-streaming solution. The results for $\sigma = 90$ mb and $\sigma = 9$ mb are the viscous solutions.

We can infer from Fig. 7.16a that for $\sigma = 900$ mb the particle density features different regions separated by discontinuities . The discontinuities are not sharp, which is the main effect of the nonzero but small viscosity. However, when comparing the results to the ultrarelativistic case calculated from BAMPS we observe a similar structure for the particle density, except for the fact that there is a larger drop in the shock plateau region, see Fig. 7.1a. At first glance, the fugacity in Fig. 7.16b considerably differs from the fugacity which is shown in Fig. 7.1b. The main difference is that in the region of the rarefaction wave as well as in the constant region in front of the shock plateau, the fugacity is above 1. In this region we have particles with less kinetic energy, which implies that the temperature is lower. In contrast to that, the temperature is very high in the region of the shock plateau, because we have particles with more kinetic energy. As expected, there is no discontinuity in the pressure profile between the shock plateau and the constant region, which can be inferred from Fig. 7.16c. This is the main requirement in the shock-tube problem and is discussed in Chapter 5. Furthermore, there is no discontinuity in the velocity profile depicted in Fig. 7.16g.

In the ultrarelativistic limit, the energy density is exactly proportional to the pressure, i.e., $e = 3p$. Thus, we have not shown the energy-density profile in Sec. 7.1. However, for a gas of massive particles this relation does not hold any longer, which is shown in Fig. 7.16e. We clearly observe another contact discontinuity similar to the one in the particle density. The fact that the energy density is no longer proportional to the pressure is also a direct consequence inferred from Eqs. (3.26) - (3.28).

Since we use a very large cross section, the dissipative quantities such as the shear pressure, the bulk viscous pressure, and the heat flow almost vanish. This is shown in Figs. 7.16d, 7.16f, and 7.16h, respectively. The bulk viscous pressure, Π, is another quantity we have not yet considered in the ultrarelativistic limit, since the bulk viscous pressure for massless particles is always zero.

By adjusting the cross section to smaller values, we are able to investigate the viscous solutions of the rRP and for a massive gas. In Fig. 7.16, this is demonstrated for $\sigma = 90$ mb, $\sigma = 9$ mb and $\sigma = 0$ mb, where the latter represents the free-streaming solution. Instead of a discontinuous shock front, a contact discontinuity, and sharp rarefaction tails, we get continuously changing profiles for the particle density, n, the fugacity, λ, the isotropic pressure, P, the energy density, e, and the velocity, v. Dissipation leads to the smoothening and the broadening of these characteristic structures. For $\sigma = 90$ mb, the separation of these structures is weak, but still visible. Due to increasing viscosity for $\sigma = 9$ mb and $\sigma = 0$ mb, a clear separation is not possible anymore. For the dissipative quantities, such as the shear pressure, π, the bulk viscous pressure, Π, and the heat flow, q^x, the dissipation in these quantities becomes large with smaller cross section.

Similar to the massless case, the dissipative quantities build up in different regions. The shear pressure is positive in the front, but negative in the region of the rarefaction wave. The heat flow shows up in three regions. It is positive in the front and back but negative in between. This kind of behavior is different from the one in the ultrarelativistic limit, as discussed in Sec. 7.1. Due to the constant and nonzero mass the bulk
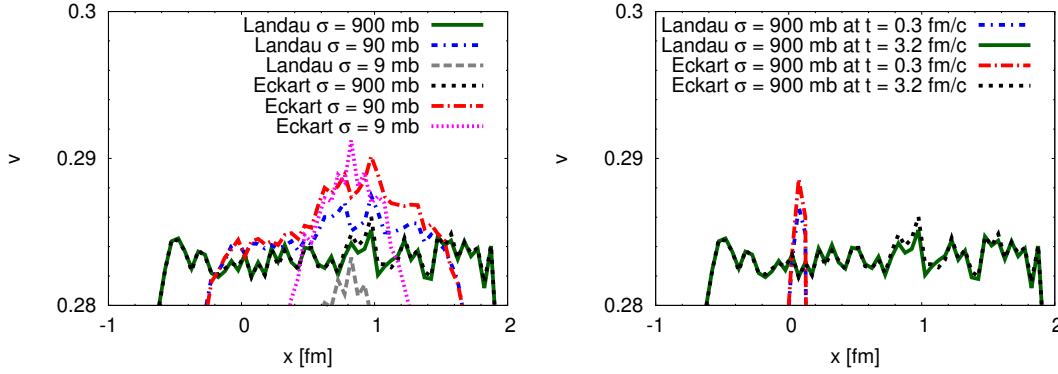
Figure 7.17.: Same setup as shown in Fig. 7.16. In the left panel we show the velocity both in the Eckart and the Landau frame for various cross sections. In the right panel we show the velocity for $\sigma = 900\,\mathrm{mb}$ in both the Eckart and the Landau frame at $t = 0.3\,\mathrm{fm}/c$ and $t = 3.2\,\mathrm{fm}/c$. In order to enhance the visibility we show only a small fraction of the velocity profile.

viscous pressure also appears and develops differently in four separate regions. When comparing the order of magnitude of the bulk viscous pressure to the heat flow or to the shear pressure, one notices that the bulk viscous pressure is one (two) order(s) of magnitude smaller than the heat flow (shear pressure).

We have to pay attention to the velocity profile which shows an interesting and unexpected structure. When comparing the solution for $\sigma = 900\,\mathrm{mb}$ and $\sigma = 90\,\mathrm{mb}$ in Fig. 7.16g, we notice that the velocity profile for $\sigma = 90\,\mathrm{mb}$ exceeds the velocity for $\sigma = 900\,\mathrm{mb}$ in a small part of the region at the plateau. From the solution in the ultrarelativistic limit in Sec. 7.1 we have obtained that the maximum velocity never exceeds the velocity of the ideal solution, v_{plat}. This kind of behavior seems not be true anymore for a massive gas and this fact is also visible if the velocity is considered in the Eckart frame. In the left panel of Fig. 7.17, we show the velocity profile in the Landau and the Eckart frame for various cross sections. We show a small fraction of the velocity profile only, in order to enhance the visibility in this region. For $\sigma = 900\,\mathrm{mb}$, there is almost no difference while for $\sigma = 90\,\mathrm{mb}$ there is a noticeable difference between the velocities in the Eckart and the Landau frame. The Eckart velocity is higher than the Landau velocity in that specific region. This is also reflected in the heat-flow profile where for $\sigma = 90\,\mathrm{mb}$ we observe a noticeable drop towards negative values[14]. For the low cross section of $\sigma = 9\,\mathrm{mb}$ we observe that the velocity in the Landau frame is below the solution with $\sigma = 900\,\mathrm{mb}$, whereas the solution of the Eckart frame at $\sigma = 9\,\mathrm{mb}$ is still higher than the solution for $\sigma = 900\,\mathrm{mb}$ and almost on the same level as the one for $\sigma = 90\,\mathrm{mb}$.

For a deeper inspection we show the time evolution of the velocity both in the Eckart and the Landau frame in the right panel of Fig. 7.17, where the solution is displayed for $\sigma = 900\,\mathrm{mb}$, at $t = 0.3\,\mathrm{fm}/c$ and $t = 3.2\,\mathrm{fm}/c$. Since we solve the shock-tube problem

---

[14]See Sec.7.1.6 for more details on the heat flow and the relation between the Eckart and the Landau frame.

which features a sharp initial discontinuity, we can make use of the scaling behavior introduced in Sec. 7.1.4. The solution for $\sigma = 900\,\text{mb}$ at $t = 0.3\,\text{fm}/c$ is approximately the same as for $\sigma = 90\,\text{mb}$ at $t = 3\,\text{fm}/c$. Therefore, we can check whether the velocity in the early phase of the solution for $\sigma = 900\,\text{mb}$ is higher than in the later phase. As shown in the right panel of Fig. 7.17, this is indeed the case. For both the Eckart and the Landau frame the velocity is higher in the early phase and decreases in time. As expected, the velocity in the Eckart frame is higher than the velocity in the Landau frame.

We have to mention that in the scenario discussed in this section, the EoS is not constant, since in contrast to the ultrarelativistic case the proportionality constant between the pressure and the energy density varies with m/T. Therefore, the expectation that the maximum velocity of the plateau in the perfect-fluid limit is always the maximum velocity for any value of the viscosity, is untenable.

In order to clarify that this is no possible numerical artifact we adjusted the cell length and increased the test-particle number. We have used a four times smaller cell length than the smallest average mean free path appearing in this simulation. The results do not change significantly, and we therefore conclude that it is a feature and not a numerical artifact. Thus, BAMPS can serve as a benchmark for viscous hydrodynamics when considering massive gases. Moreover, using BAMPS we can easily investigate the effects of the bulk viscous pressure in various scenarios. The effects of nonzero masses is clearly visible in the evolution of shock waves.

7.2.3. A multi-component system

initial variables	left	right		further settings
$T_A(\text{GeV})$	0.4	0.2		species A: $m = 0\,\text{GeV}$
$T_B(\text{GeV})$	0.35	0.3		species B: $m = 0\,\text{GeV}$
λ_A	1	1		degeneracy factor $g_A = 8$, $g_B = 8$
λ_B	1	0.5		isotropic elastic $2 \to 2$ collisions
$v_A = v_B$	0	0		scenario (high): $\sigma_{A\leftrightarrow A} = 80\,\text{mb}$, $\sigma_{A\leftrightarrow B} = 40\,\text{mb}$, $\sigma_{B\leftrightarrow B} = 20\,\text{mb}$
$\Pi_A = \Pi_B\,(\text{GeV}/\text{fm}^3)$	0	0		scenario (low): $\sigma_{A\leftrightarrow A} = 20\,\text{mb}$, $\sigma_{A\leftrightarrow B} = 10\,\text{mb}$, $\sigma_{B\leftrightarrow B} = 5\,\text{mb}$
$q_A^\mu = q_B^\mu\,(\text{GeV}/\text{fm}^3)$	0	0		runtime $= 3.2\,\text{fm}/c$; system size $L_x = 6.4$ fm
$\pi_A^{\mu\nu}\,(\text{GeV}/\text{fm}^3)$	0	0		walls in x-direction; periodic boundary conditions in transverse y- and z-direction
$\pi_B\,(\text{GeV}/\text{fm}^3)$ approx.	-1.6	-0.4		

Table 7.5.: The initial conditions and settings used in BAMPS in the rRP for a multi-component system.

In this section, we solve the rRP for a system with two different particle species, A and B, which both interact with constant isotropic and binary collisions. We intro-

duce the cross sections σ_{AA}, σ_{AB}, and σ_{BB}, which represent the different cross sections between the two particle species. Here, σ_{AA} is the cross section between two particles of species A, σ_{AB} the intermediate cross section between particles of species A and B, and σ_{BB} the cross section between two particles of species B. Due to the different cross sections and the different initial conditions for each particle species, we expect an interesting interaction between the particle species. A similar study with two different interacting particle species, but no spatial gradients using BAMPS and viscous hydrodynamics has already been performed in Refs. [150, 151], where the main focus was on the extraction of the shear viscosity, η, of such a composite system. However, in this section we investigate the final hydrodynamic quantities in a one-dimensional system using BAMPS only. Moreover, we restrict our calculations to massless particles.

In Fig. 7.18, we show a snapshot of the particle density, n, the fugacity, λ, the isotropic pressure, P, the shear pressure, π, the energy density, e, the bulk viscous pressure, Π, the velocity, v, and the heat flow, q^x, for both particle species together ($A+B$), and each particle species separately at time $t = 3.2\,\text{fm}/c$. The initial conditions are listed in Tab. 7.5, where two scenarios for the cross sections are employed. The first scenario (high) uses $\sigma_{AA} = 80\,\text{mb}$, $\sigma_{AB} = 40\,\text{mb}$, and $\sigma_{BB} = 20\,\text{mb}$, whereas the second scenario (low) uses $\sigma_{AA} = 20\,\text{mb}$, $\sigma_{AB} = 10\,\text{mb}$, and $\sigma_{BB} = 5\,\text{mb}$. The initial conditions are as follows: Particle species A is initialized with $T_{\text{L}} = 0.4$ GeV and $T_{\text{R}} = 0.2$ GeV, and vanishing chemical potential on both sides. Furthermore, the system is initialized in thermal equilibrium. The second particle species is initialized with $T_{\text{L}} = 0.35$ GeV and $T_{\text{R}} = 0.3$ GeV, where on the right side the fugacity is $\lambda_{\text{R}} = 0.5$. In contrast to the particle species of A, the particles of B are initially not in thermal equilibrium. The momenta of the particles in the transverse directions y and z are isotropic, but they have no momentum in x-direction. The initial shear pressure is therefore very large. However, we will find that this anisotropic initialization has no significant effect for the further evolution of the system.

We remind that the initial conditions given in Tab. 7.5 are chosen for each species separately. Hence, initially each particle species has no clue about the other particle species. The initial temperatures we have listed in this table have no further physical meaning, because the temperature for each particle species differs from that of the other one. This changes during the evolution, when the system rapidly thermalizes via interactions between both particle species. In Sec. 3.3.5 we have already introduced the definitions and problems corresponding to a system with more than one particle species.

Figure 7.18 shows the results for both scenarios. We first focus on the first scenario with the large cross sections, where we can identify the appearance of a shock wave as well as a rarefaction wave in the particle density, the isotropic pressure, the energy density, and the velocity profile. This is true when considering both particle species together, where the pressure has a constant plateau. However, when we take a view on each particle species separately, we can see that for particle species, A or B, there is no constant plateau in the pressure. For particle species A the pressure drops in the region of the shock plateau, whereas for particle species B the pressure increases in this region. However, this is not a problem, since one has to keep in mind that only the whole system has the whole information, since both particle species interact with each other. Therefore, it is to be expected that there is no constant pressure region
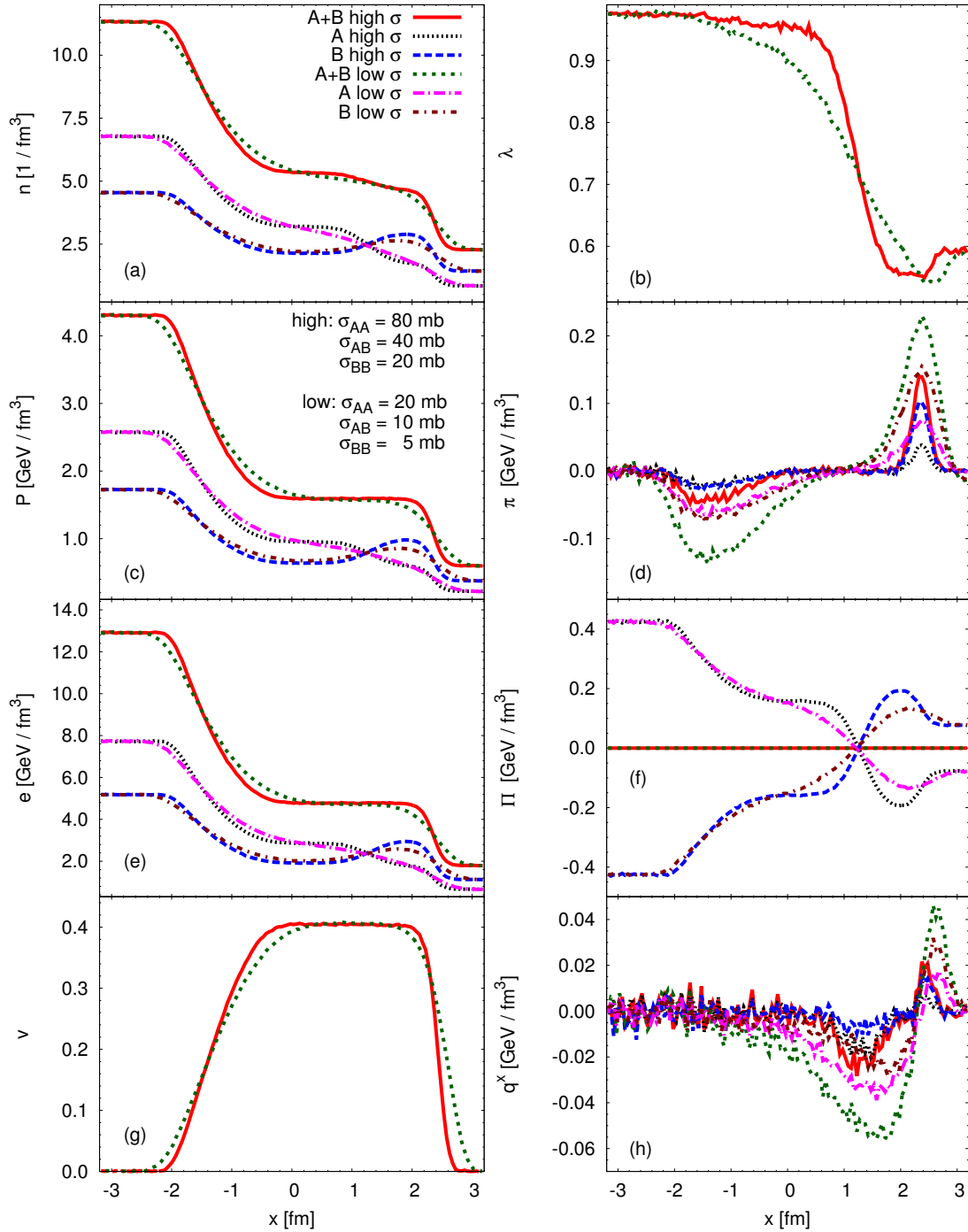
Figure 7.18.: Transition from ideal to viscous shock waves in BAMPS using the rRP for a multi-component system of massless particles. We show the particle density (a), the fugacity (b), the isotropic pressure (c), the shear pressure (d), the energy density (e), the bulk pressure (f), the velocity (g), and the heat flow (h). The initial conditions and settings are listed in Tab. 7.5. The results from BAMPS are shown for two different sets of constant and isotropic cross sections.
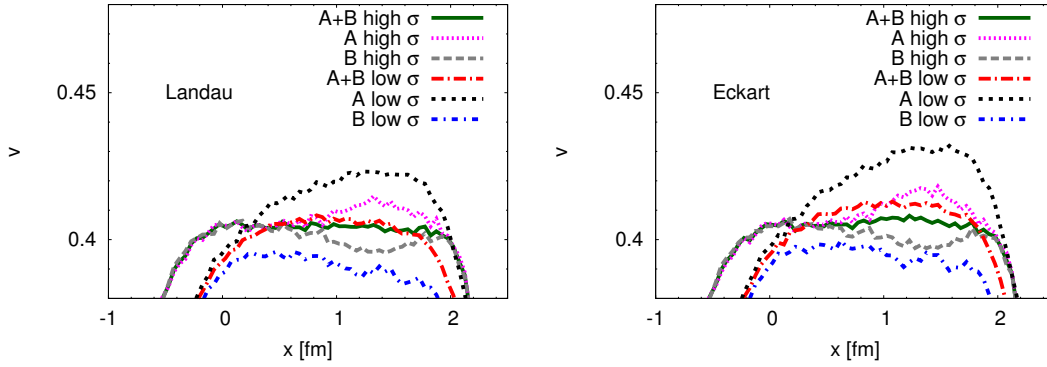
Figure 7.19.: We show the velocity profile for the same setup as depicted in Fig. 7.18. The left (right) panel shows the velocities in the Landau (Eckart) frame. We show only a small fraction of the profiles in order to enhance the visibility.

when considering each particle species separately.

If one deactivates the interaction between the particle species A and B, i.e., $\sigma_{AB} = 0\,\mathrm{mb}$, the profiles would evolve separately. If instead one deactivates the cross section of each particle species, i.e., $\sigma_{AA} = \sigma_{BB} = 0\,\mathrm{mb}$, each particle species could only equilibrate via interactions with the other particle species. If all interaction cross sections were exactly the same we would not distinguish between each particle species, except for the facts that the initial conditions make the difference. For $t \to \infty$, the system would behave as a one-component system [150, 151].

Considering the second scenario with lower cross sections, we observe the expected behavior: The profiles smear out and the discontinuities vanish. This is also visible for the dissipative quantities such as the shear pressure and the heat flow, which grow with increasing viscosity. Due to the initially smaller fugacity for the particle species B on the right side, the heat flow develops differently as if it would have been the case for $\lambda = 1$, i.e., the heat flow is larger because of the additional gradient in fugacity. The bulk viscous pressure vanishes for the whole system, since we have no masses for both particle species. However, considering the bulk viscous pressure for each particle species, we get a nonzero bulk viscous pressure. This is due to the construction of the temperature, the fugacity, and the velocity which has been discussed in Sec. 3.3.5 in greater detail.

The initially nonzero and large shear pressure for particle species B has no significant effect on the final profile as depicted in Fig. 7.18. Due to the interactions the system equilibrates very fast. Furthermore, the shear pressure for particle species A first grows due to the intermediate cross section and then relaxes similar to particle species B. This happens within a very short time in the beginning of the simulation and does not have any significant effect to the final profile.

As discussed in Sec. 7.1, the velocity in the plateau region is the highest for the most ideal system. In the case that dissipation appears, the velocity should not exceed the maximum velocity in the plateau, v_{plat}. We have already shown in Sec. 7.2.2 that this is not valid anymore for nonzero masses. We also find such an observation in our

multi-component system, which is depicted in Fig. 7.19. Here we show the velocities in the Landau (left panel) and in the Eckart frame (right panel). Furthermore, we show the velocities of each particle species separately.

Considering the velocity of both particle species together, $A + B$, which is done in the left panel of Fig. 7.19 the velocity for the low cross section is higher than the one for large cross sections. This is also shown in the right panel for the Eckart frame where the difference is even larger. However, an explanation of our finding is difficult to formulate. First, the initial fugacity gradient of the particles of species B may play a role. Another point are the different initial temperatures for each particle species. And one last effect might arise from the individual cross sections we use in our scenarios. However, most probably all these referred points together result in this unexpected behavior in the velocity profile, whereas the initial fugacity gradient is the most probable candidate leading to the largest effect. In Fig. 7.19 we see that, with larger viscosity, the velocity of species A increases at a larger rate than the velocity of the particles of species B is decreasing. However, clarifying this point requires further studies. The best way to do this is to systematically investigate each effect separately.

We can conclude that a system with two or more particle species with different cross sections and initial conditions is much more complex than a simple system of one component. Especially in the early phase, when both particle species are not equilibrated with each other, the multi-component system cannot be reduced to a system with only one species of particles. Using in addition inelastic processes in such kind of scenarios, the complexity changes dramatically which is of great interest for future investigations. We expect that with a possible chemical equilibration the final profiles depend even more on the chosen cross sections and initial conditions.

7.3. Solving the heat-flow problem

In Sec. 7.1, we have investigated the rRP using BAMPS and vSHASTA. We found that for small Knudsen numbers the standard IS theory provides a reasonable description for most hydrodynamic quantities, such as the shear pressure. However, in Sec. 7.1.2, we found that even for small Knudsen numbers the description of heat flow was in a bad agreement with the microscopic theory. This observation indicated that the IS theory suffers from wrong values for the transport coefficients and does not include all terms which are necessary for an appropriate description.

In this section, we compare the equations of motion of Resummed Transient relativistic Fluid Dynamics (RTRFD), which has been reviewed in Refs. [46,47] and briefly reviewed in Sec. 3.4.4, at various levels of approximation with numerical solutions of the Boltzmann equation. In order to obtain a detailed discussion we perform the calculations for two different types of initial conditions[15]. We demonstrate that this recently derived formalism, RTRFD, is able to handle problems with strong initial gradients in pressure or particle-number density, whereas the theory of IS fails especially to describe the heat flow. Both hydrodynamic theories are solved using vSHASTA, while the solution of the rBE is performed by BAMPS. We have to notice that we do not solve the

---

[15]labeled case I and II as explained in the following.

rRP, but use smooth initial conditions, as explained in the following. The following part is a strict summary of the work presented in Ref. [35].
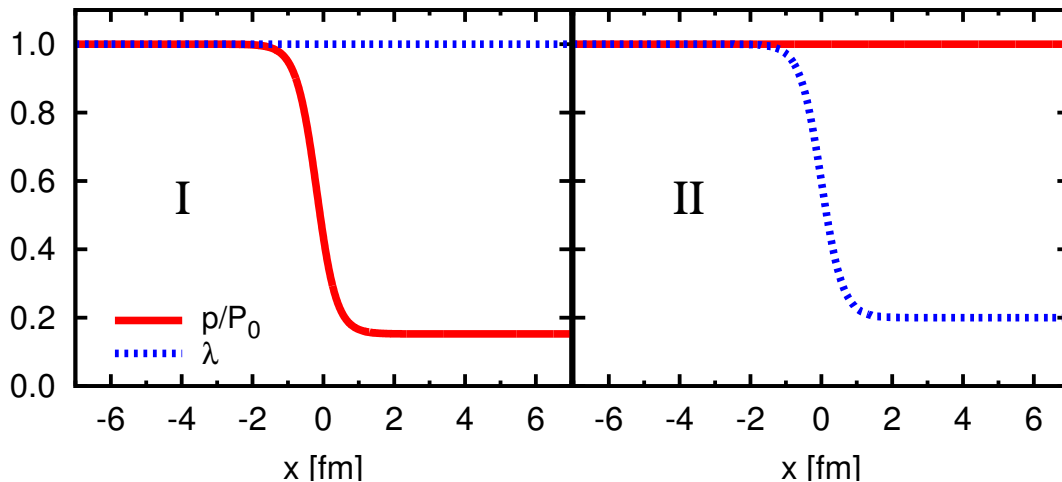
Figure 7.20.: Initial conditions for cases I and II.

We consider two different initial conditions. In case I, the system is initialized with a homogeneous fugacity of $\lambda_0 \equiv 1$, but with an inhomogeneous pressure profile in the longitudinal direction. In practice, we smoothly connect the two temperature states $T_{(-\infty)} = 0.4\,\text{GeV}$ and $T_{(+\infty)} = 0.25\,\text{GeV}$ via the Woods-Saxon parametrization

$$T(x) = \frac{T_{(-\infty)} - T_{(+\infty)}}{\exp\left(\frac{x}{D}\right) + 1} + T_{(+\infty)} \tag{7.14}$$

with the thickness parameter given by $D = 0.3$ fm. In case II, the pressure is homogeneous with $P_0 = gT_{(-\infty)}^4/\pi^2$ and the fugacity distribution is given by a Woods-Saxon profile[16] with $D = 0.3$ fm, interpolating between $\lambda_{(-\infty)} = 1$ and $\lambda_{(+\infty)} = 0.2$. For the degeneracy factor we use $g = 16$. In both cases, matter is initialized in local thermodynamical equilibrium, i.e., with all dissipative currents[17] set to zero, and at rest, i.e., with a vanishing collective velocity $u^\mu = 0$. These initial conditions are shown in Fig. 7.20.

In both cases, we consider two exemplary values for the cross section of $\sigma = 2$ mb and 8 mb, and consider the solutions after the system has evolved for 6 fm/c in time. We compare the solution of the Boltzmann equation with that of traditional IS theory[18], as well as with RTRFD at various levels of approximation. In the following, we shall compare RTRFD with 13 dynamical degrees of freedom and with the transport coefficients computed with 13 and with 37 moments. We shall term these variants of RTRFD "13/13" and "13/37". In addition, we also solve Eqs. (B.6). These contain 21 dynamical degrees of freedom. We compute the corresponding transport coefficients using 37 moments. We shall refer to this variant of RTRFD as "21/37". For more details we refer to Refs. [35, 47] and Sec. 3.4.4.

---

[16]We replace the corresponding values of the temperature by those of the fugacity in Eq. (7.14).

[17]and eigenmodes of the Boltzmann equation.

[18]including terms omitted in the original work [44, 229, 230] but quoted in Ref. [231, 232, 233].
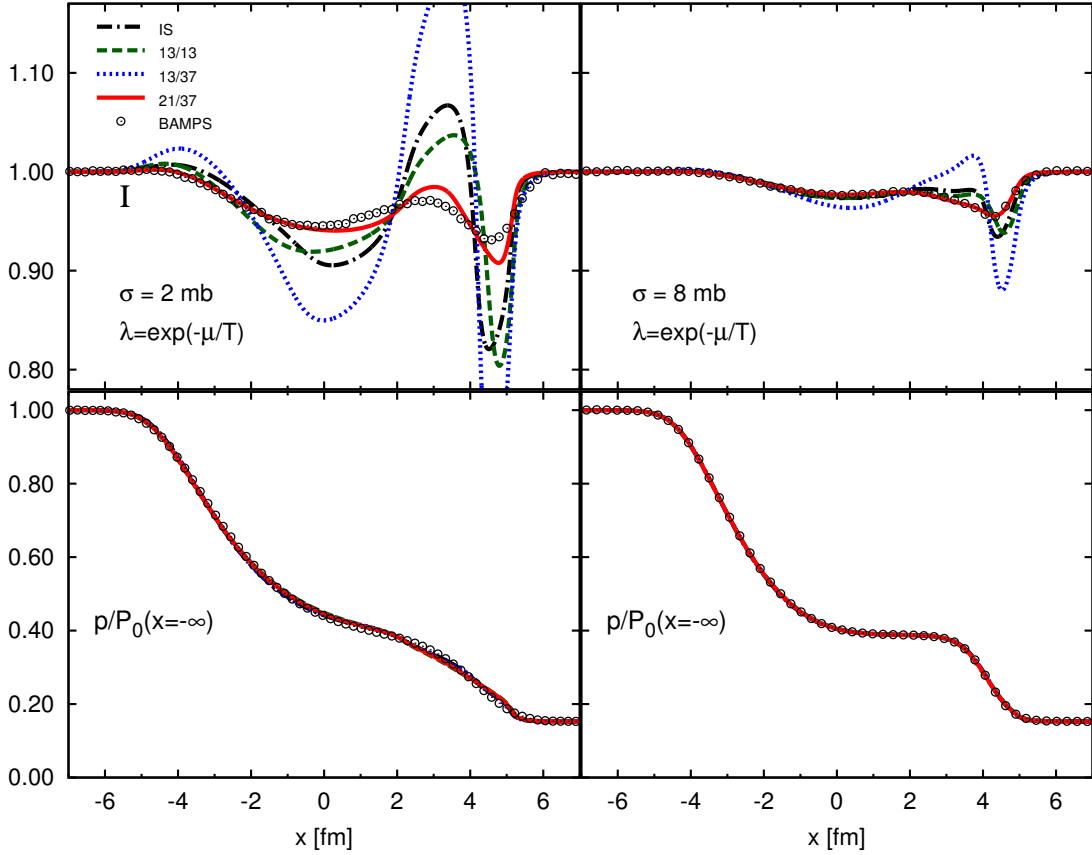
Figure 7.21.: Fugacity and thermodynamic pressure profiles at $t = 6$ fm/c for case I, for $\sigma = 2$ mb (left panels) and $\sigma = 8$ mb (right panels) .

In the following figures, the numerical solutions of the Boltzmann equation shall always be displayed by open dots, the results of IS theory by black dash-dotted lines, the solution of RTRFD "13/13" by green dashed lines, that of RTRFD "13/37" by blue dotted lines, and that of RTRFD "21/37" by solid red curves.

In order to verify the different fluid-dynamical theories discussed in this section the solutions of the Boltzmann equation must be calculated to a very high precision. For this purpose we performed $5 \cdot 10^4$ BAMPS runs and computed the fluid-dynamical quantities as averages over these runs.

In Fig. 7.21 we show the fugacity (top) and thermodynamic pressure (bottom) and in Fig. 7.22 the heat flow (top) and shear-stress tensor (bottom) for case I. The initial pressure gradient in case I drives, via conservation of momentum, the creation of velocity gradients. On the other hand, the gradient of fugacity is initially zero and turns out to remain small throughout the evolution. The Boltzmann equation and the fluid-dynamical theories have been solved for $\sigma = 2$ mb (shown in the left panels of each figure) and for $\sigma = 8$ mb (shown in the right panels). For $\sigma = 8$ mb, the thermodynamic pressure and shear-stress tensor computed in all fluid-dynamical theories are in good agreement with the numerical solutions of the Boltzmann equation. As we decrease the cross section we expect the agreement between macroscopic and microscopic theory to
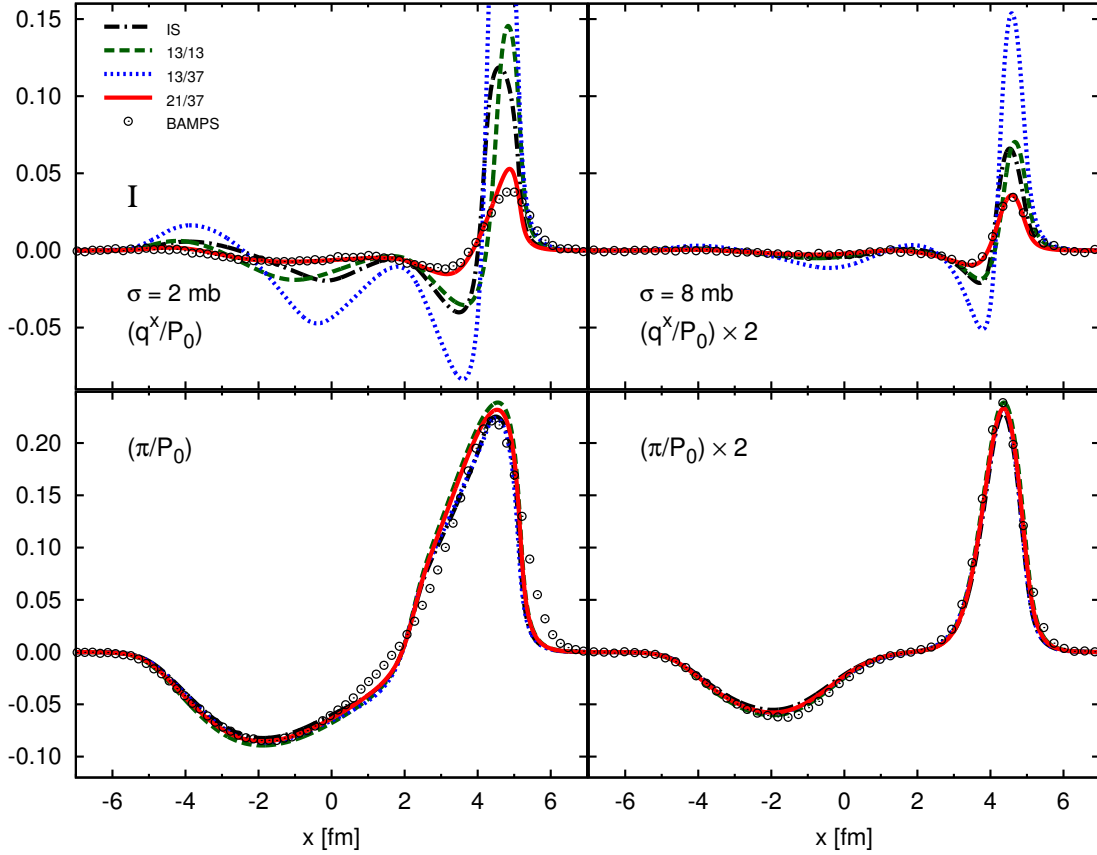
Figure 7.22.: Heat flow and shear-stress tensor profiles at $t = 6$ fm/c for case I, for $\sigma = 2$ mb (left panels) and $\sigma = 8$ mb (right panels).

become worse. This explains why, for $\sigma = 2$ mb, the pressure and shear-stress tensor computed within fluid-dynamical theories deviate more strongly from those computed via the microscopic theory. Nevertheless, compared to the fugacity and heat-flow profiles, the agreement is not too bad, even for the smaller value of the cross section.

In Fig. 7.23 we show the fugacity (top) and thermodynamic pressure (bottom) and in Fig. 7.24 the heat-flow (top) and shear-stress tensor profiles (bottom) for case II. As before, the Boltzmann equation and the fluid-dynamical theories considered have been solved for $\sigma = 2$ mb (shown in the left panels) and for $\sigma = 8$ mb (shown in the right panels). Since, in case II, the initial pressure gradient is zero and turns out to remain small throughout the evolution, the velocity gradients remain small as well. Again, we expect, and see, better agreement between fluid dynamics and the Boltzmann equation for the larger value of the cross section. While the fugacity profiles are in good agreement with the solution of the Boltzmann equation for all fluid-dynamical theories and both values of the cross section, the heat flow is not well described in IS theory and in RTRFD "13/13": IS theory predicts values for the heat flow which are smaller in magnitude than the Boltzmann equation, while RTRFD "13/13" predicts larger values, even for $\sigma = 8$ mb. On the other hand, both RTRFD "13/37" and RTRFD "21/37"
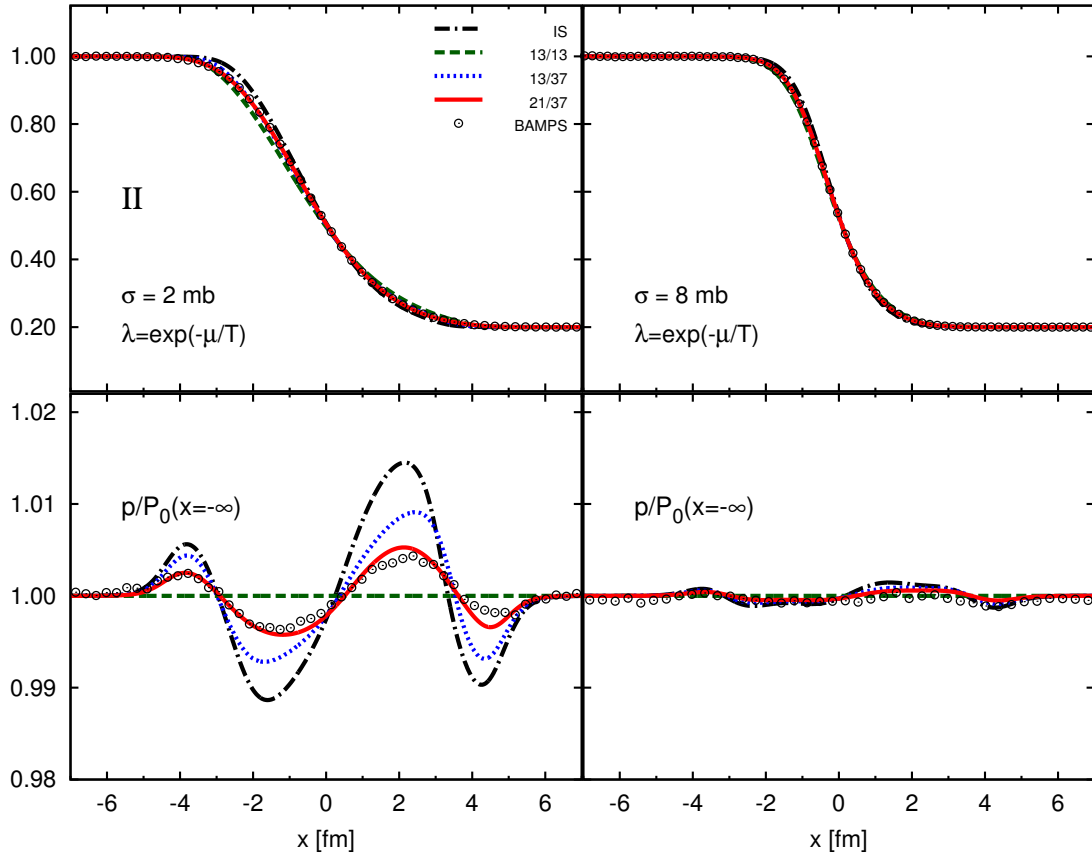
Figure 7.23.: Fugacity and thermodynamic pressure at $t = 6$ fm/c for case II, for $\sigma = 2$ mb (left panels) and $\sigma = 8$ mb (right panels).

describe the heat flow very well or even perfectly, respectively, for both values of the cross section. The reason is that the diffusion coefficient, κ, has the correct value in these theories[19], see Refs. [47, 187].

Note that in Fig. 7.24 the BAMPS results for the shear-stress tensor are strongly fluctuating. This happens because, in this special case, the values of the shear-stress tensor are of the same magnitude as the statistical fluctuations in BAMPS. In order to reduce the statistical fluctuations and to achieve a better resolution, a significantly larger amount of runs would be required.

In conclusion, the resummation of irreducible moments for the computation of the transport coefficients, as introduced in Sec. 3.4.4 and described in Refs. [35, 47], has been essential to obtain a good agreement with the microscopic theory. It provides not only the correct values for the shear-viscosity and heat-conduction coefficients, but also for the transport coefficients that couple the respective dissipative currents. This recent derivation of viscous hydrodynamics resolved the previously observed differences between the solution of IS theory and of the Boltzmann equation discussed in Sec. 7.1.2 and the corresponding published work [34].

---

[19]while it deviates by $\sim 30\%$ in both IS theory and RTRFD "13/13".
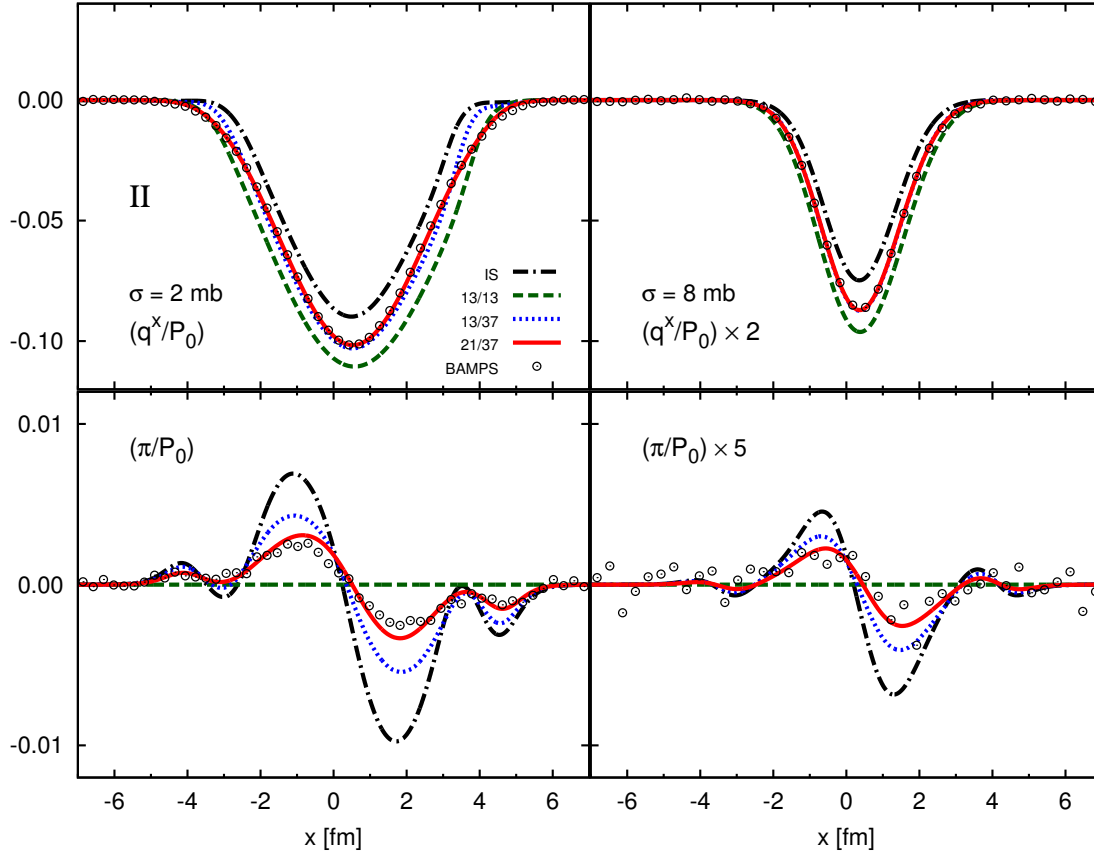
Figure 7.24.: Heat flow and shear-stress tensor profiles at $t = 6$ fm/c for case II, for $\sigma = 2$ mb (left panels) and $\sigma = 8$ mb (right panels).

As expected, and explicitly demonstrated in this section, the agreement between solutions of RTRFD and the Boltzmann equation depends on the value of σ. For the cases considered in this section, we obtained a good agreement for $\sigma = 8$ mb, while for $\sigma = 2$ mb we started to notice small deviations. In order to improve the agreement for smaller values of the cross section, more moments of the Boltzmann equation have to be included.

7.4. Investigation of the shock front

In Chapter 5, we have discussed the analytical solution of the rRP for a perfect fluid in the massless limit, which for initially zero velocities is called the shock-tube problem. The rRP consists of three main regions: the propagation of the rarefaction wave in one direction, the propagation of the shock wave in the opposite direction, and the part in between, which is the constant plateau. The shock-wave part is characterized by the shock plateau and the shock front, while in the perfect-fluid limit the width of the shock front is exactly zero.

However, as discussed in Sec. 7.1, we have introduced the numerical viscous solutions

of the rRP. With nonzero and not too large viscosity we still found a rarefaction wave, constant plateau, and shock plateau, as well as a shock front, but all regions were smoothed out due to dissipation. The shock front had a nonzero width, where we have assumed, but not confirmed, that the total width of the shock front in the limit $t \to \infty$ is proportional to the shear viscosity, η [40, 215, 216]. In the shock-tube problem a detailed investigation of the shock plateau and front is not easy since in the laboratory frame this part is moving with a high velocity. In order to investigate the shock plateau and front, it is reasonable to transfer into the frame of the shock front. Then, this problem becomes stationary, and we disregard the rarefaction wave as well as the constant plateau region.

initial/reservoir values	left	right		further settings
$T \, (\text{GeV})$	0.272416	0.19912		one species: $m = 0 \, \text{GeV}$
λ	0.913437	1		degeneracy factor $g = 16$
v	-0.441552	-0.754912		isotropic elastic $2 \to 2$ collisions
$\Pi \, (\text{GeV}/\text{fm}^3)$	0	0		constant $\sigma = 100 \, \text{mb}$
$q^\mu \, (\text{GeV}/\text{fm}^3)$	0	0		runtime $=$ $10 \, \text{fm/c}$, system size $L_x = 1 \, \text{fm}$
$\pi^{\mu\nu} \, (\text{GeV}/\text{fm}^3)$	0	0		thermal reservoirs in x-direction; periodic boundary conditions in transverse y- and z-direction

Table 7.6.: The settings used in BAMPS and vSHASTA for the simulation of the shock front using thermal reservoirs for an ultrarelativistic gas of massless particles. The values for T, λ, and v are the values given in the reservoirs and the initial conditions left and right of the discontinuity. The pressure ratio of the initial discontinuity and the reservoirs is given by $P_\text{L}/P_\text{R} = 3.2$.

The stationary solution of the shock front can be found from the Rankine-Hugoniot-Taub relations (4.10), as discussed in Sec. 4.3. By fixing a pressure ratio, all other quantities, such as the energy density, the particle density, and the velocities are given in front of and after the discontinuity. Initializing a sharp discontinuity in pressure and using special boundary conditions in form of thermal reservoirs with the values given from the Rankine-Hugoniot-Taub relations, a stationary solution of the shock wave is obtained. It is obvious that the final stationary solution is reached after a certain time, which strongly depends on the chosen value for the cross section and the size of the system. In the end, the initial sharp discontinuity will smoothen out, where we expect that the shock front will approach a final width, which is proportional to the shear viscosity or ultimately the cross section.

In this section we apply BAMPS in order to simulate the shock wave in its rest frame. The advantage of this scenario is that we can investigate the shock wave with a higher resolution than in the previous scenario shown in Sec. 7.1. Moreover, using vSHASTA we can simulate the same scenario using the 13 and 21 moment approxima-
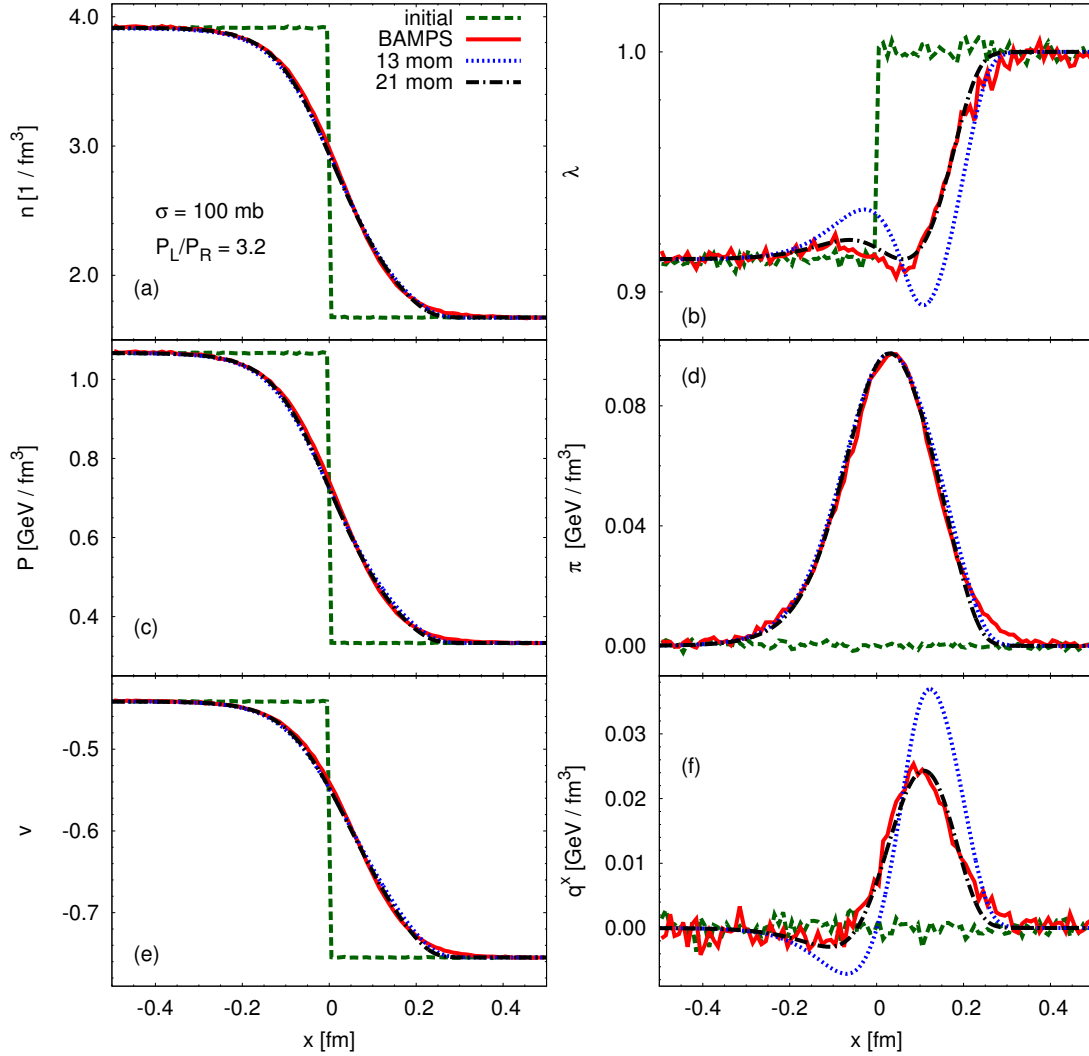
Figure 7.25.: Stationary numerical solutions of the shock front in BAMPS and vSHASTA. The initial conditions as well as the parameters given in the thermal reservoirs are listed in Tab. 7.6. The pressure ratio is $P_L/P_R = 3.2$. We use isotropic and binary collisions. We show the particle density (a), fugacity (b), isotropic pressure (c), shear pressure (d), velocity (e), and heat flow (f). The results of vSHASTA are shown for 13 and 21 moments.

tion of RTRFD, as introduced in Sec. 3.4.4. The comparison to BAMPS will reveal the limitations of both theories when applied to strong gradients as given in this scenario. We will see that both theories have no reasonable agreement with the results from kinetic theory for large Knudsen numbers. We will discuss this in the following.

We begin with the scenario as shown in Fig. 7.25 for the pressure ratio $P_L/P_R = 3.2$. Here we show the particle density, n, the fugacity, λ, the isotropic pressure, P, the shear pressure, π, the velocity, v, and the heat flow, q^x, initially and after $t = 10$ fm/c.

We use binary collisions only with an isotropic angular distribution. As constant cross section we use $\sigma = 100$ mb. The size of the system is $L_x = 1$ fm. The system is initialized as listed in Tab. 7.6, where the initial sharp discontinuity at $x = 0$ fm is clearly visible for most of the quantities in Fig. 7.25, while the dissipative quantities are zero initially. We use thermal reservoirs with the values as listed in Tab. 7.6 as well. The implementation of thermal reservoirs in BAMPS is discussed in Sec. 6.2 and in Appendix F. The initial conditions for vSHASTA are identical with those for BAMPS.

The initial sharp discontinuity in Fig. 7.25 in the particle density, the isotropic pressure, and the velocity in Fig. 7.25a, Fig. 7.25c, and Fig. 7.25e, respectively, smoothens out and reaches an almost stationary solution after a sufficiently long time of $t = 10$ fm/c, i.e., the profiles will not change their shape anymore. The final shape of the profile is determined by the pressure ratio, the cross section, σ, and the size of the system, L_x. This can be expressed in terms of the Knudsen number (3.1). If we used a higher cross section but the same system size, the width of the shock front would decrease, and vice versa. However, this fact indicates that the absolute width of the shock front is indeed proportional to a kind of microscopic length scale, such as the shear viscosity, η, the mean free path, λ, or the cross section, σ, and is universal for a given pressure. These observations agree very well with those in Refs. [40, 215, 216].

initial/reservoir values	left	right		further settings
$T\,(\mathrm{GeV})$	0.292228	0.19912		one species: $m = 0\,\mathrm{GeV}$
λ	0.862245	1		degeneracy factor $g = 16$
v	-0.423659	-0.786796		isotropic and elastic collisions
$\Pi\,(\mathrm{GeV/fm^3})$	0	0		constant $\sigma = 100\,\mathrm{mb}$
$q^\mu\,(\mathrm{GeV/fm^3})$	0	0		runtime = $10\,\mathrm{fm}/c$, system size $L_x = 1$ fm
$\pi^{\mu\nu}\,(\mathrm{GeV/fm^3})$	0	0		thermal reservoirs in x-direction; periodic boundary conditions in transverse y- and z-direction

Table 7.7.: The settings used in BAMPS and vSHASTA for the simulation of the shock front using thermal reservoirs for an ultrarelativistic gas of massless particles. The values for T, λ, and v are the values given in the reservoirs and the initial conditions left and right of the discontinuity. The pressure ratio of the initial discontinuity and the reservoirs is given by $P_\mathrm{L}/P_\mathrm{R} = 4.0$.

A further investigation of the other quantities shows the detailed shape of the shock front for the dissipative quantities. The possibility to investigate the shock front in its rest frame allows an improved and detailed comparison to the results of viscous hydrodynamics, as realized via vSHASTA. As introduced above, we compare two different theories, 13 and 21 moments of viscous hydrodynamics, where the one with the higher moments is expected to have a better agreement with the results from BAMPS. This fact is clearly visible in all quantities. While in the particle density, the isotropic
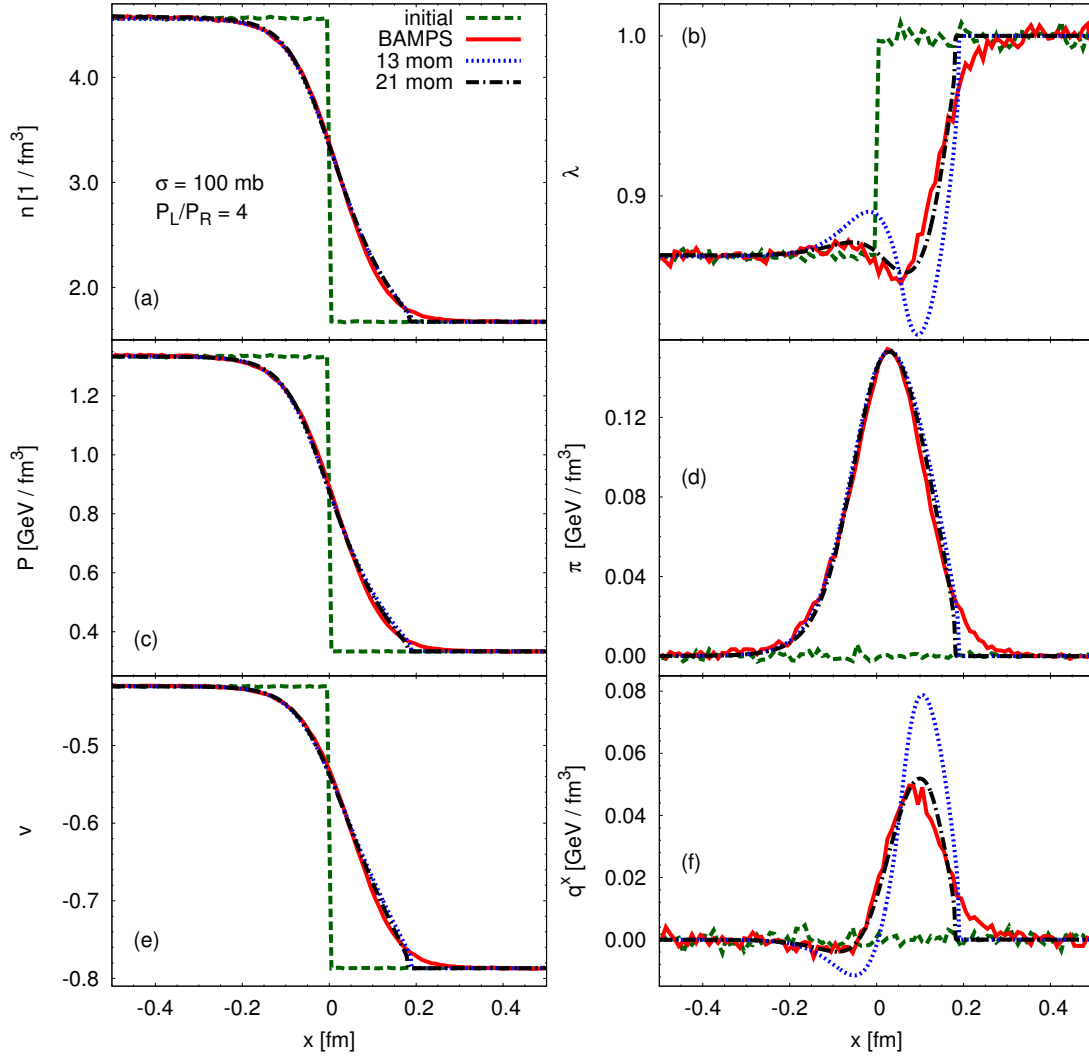
Figure 7.26.: Same quantities as shown in Fig.7.25. The initial conditions and settings are listed in Tab. 7.7. We show the results for $P_L/P_R = 4$.

pressure, and the velocity[20] in Fig. 7.25a, Fig. 7.25c, and Fig. 7.25e, respectively, the agreement of both theories is overall very good and the deviations are not noticeable, we identify a disagreement with BAMPS in the dissipative quantities. For the shear pressure the agreement is almost perfect, except for the frontmost part, where a small discontinuity appears and does not smoothen out. For the fugacity and the heat flow depicted in Fig. 7.25b and Fig. 7.25f, respectively, the disagreement of the theory with 13 moments has been discussed in Secs. 7.1.2 and 7.3. The improvement using 21 degrees of freedom in viscous hydrodynamics is clearly visible, while we have to mention again the small disagreement in the frontmost part where again a discontinuity appears.

---

[20] A negative value of the collective velocity displays that matter propagates from right to the left.

This very small disagreement in the frontmost part of the shock front seems to be a general failure or limitation of the present form of viscous hydrodynamics, i.e., the IS theory or RTRFD. Although the inclusion of higher moments is necessary in order obtain a better agreement with the rBE, see also Sec. 7.3, it does not help to obtain a better agreement in the region of the shock front. In order to clarify this fact, we use a stronger gradient in pressure, as shown in Fig. 7.26. Here we have $P_L/P_R = 4$ and the values used in the simulation are listed Tab. 7.7. As visible in every quantity in Fig. 7.26, we observe a sharp discontinuity appearing in vSHASTA for both theories, but not in BAMPS.

So far the explanation of this limitation of viscous hydrodynamics is the following: The signal speed in the IS theory and RTRFD, which are both variants of transient relativistic hydrodynamics[21], is limited. This is exactly the property that makes those kind of theories causal, i.e., no superluminal signal propagation exists. This for example occurs in the theory of Navier and Stokes[22] where the signal speed is not limited.

Actually, in viscous hydrodynamics we have a few modes each of which propagates with the corresponding signal velocity[23]. When we start to solve the discontinuity in the rRP, as shown in Sec. 7.1 and discussed for the non-relativistic case in Refs. [218, 219, 220], we initially get several "steps" in the solution, corresponding to each mode and propagating with the corresponding signal velocity. One of them has the maximum propagation speed. All the other steps will eventually smoothen out, expect the fastest if the speed of the shock front is larger than the maximum propagation speed.

Now the actual maximum propagation speed depends on the values of the transport coefficients heat conductivity, shear viscosity, and the corresponding relaxation times. For actual values derived in IS theory or RTRFD from the Boltzmann equation the propagation speed is clearly below the speed of light and that is why we obtain the discontinuity in the shock problem.

In principle, if we would include more and more dynamical moments into the equations we would get more and more of these small steps and also the maximum propagation speed would approach the speed of light. With an infinite number of moments we would go back to the Boltzmann equation with an infinite number of propagating modes with always smooth solutions, as shown in BAMPS. In RTRFD only the 1st and 2nd rank moments are included. In order to really see the increase in the number of modes we would need to include also higher rank moments. This is a similar procedure as discussed in Refs. [218, 219, 220].

Thus, this discussion demands a deeper investigation by the authors of Ref. [35] and remains a future task [38].

7.5. Numerical performance in BAMPS

7.5.1. Numerical convergence

In the previous sections we have already figured out some limitations of BAMPS when solving the evolution of an interacting gas. In Sec. 7.1 we have found, that BAMPS

---

[21]see Sec. 3.4.3 and 3.4.4, respectively.
[22]see Sec. 3.4.2.
[23]In ideal fluid dynamics we have only the speed of sound.
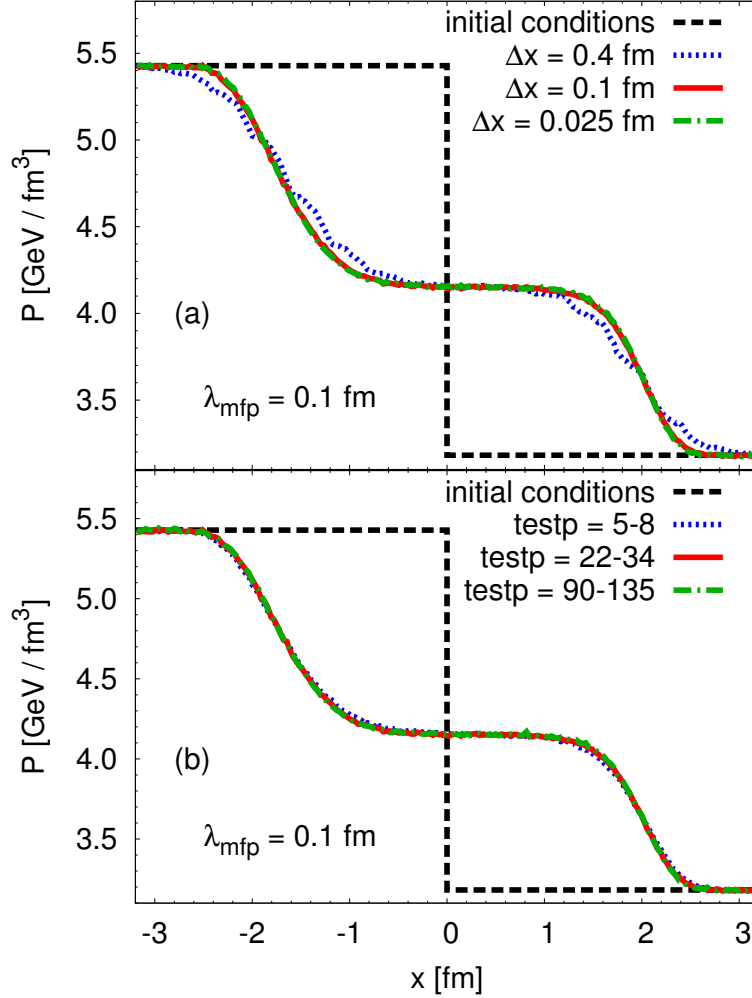
Figure 7.27.: Cell size (a) and number of test particles (b) dependence in the BAMPS simulation at $t = 3.2$ fm/c. The initial conditions are chosen as $T_\mathrm{L} = 0.4$ GeV and $T_\mathrm{R} = 0.35$ GeV. The mean free path is $\lambda_\mathrm{mfp} = 0.1$ fm. In (a) the pressure profile is shown for different cell sizes $\Delta x = 0.4, 0.1, 0.025$ fm and constant N_test. In (b) we use a fixed $\Delta x = 0.1$ fm and different numbers of test particles per cell.

produces numerical artifacts if we try to simulate a constant η/s. The magnitude of the numerical artifact strongly depends on the average number of particles in the cells. In case we use a constant cross section, this numerical artifact does not appear.

In this section we want to illustrate the effects of the test-particle number and cell length on the physical results using a massless Boltzmann gas. As already discussed in Chapter 6, the relevant parameters in BAMPS that control the numerical accuracy are the cell size, Δx, the time step, Δt, and the test-particle number, N_test. The cell sizes in the transverse directions, Δy and Δz, are not relevant, because the system is

assumed to be homogeneous in the transverse plane[24]. In addition, Δt is always chosen to be smaller than Δx as to avoid possible large local variations within one time step. If one decreases Δx one has to simultaneously increase N_{test} to ensure that each cell contains a sufficiently large number of test particles. Thus, using BAMPS the rBE will be exactly solved in the limit $\Delta x \to 0$ and $N_{\text{test}} \to \infty$. In practice, we do, of course, use a non-vanishing value of Δx and a finite value of N_{test}. In the following, we show how the numerical solutions converge when Δx is decreased and N_{test} is increased.

The initial conditions for this study are $T_{\text{L}} = 0.4$ GeV and $T_{\text{R}} = 0.35$ GeV. Figure 7.27 shows the pressure profile at a time $t = 3.2$ fm/c for a constant mean free path of $\lambda_{\text{mfp}} = 0.1$ fm. Results in the upper panel are obtained by varying Δx and keeping N_{test} unchanged. The number of test particles in the cells is between 22 and 34, depending on the local temperature. We see that convergence is reached when $\Delta x = \lambda_{\text{mfp}}$. Further decrease of Δx does not lead to noticeable changes. The lower panel of Fig. 7.27 shows the results for fixed Δx and a varying number of test particles per cell. Here we do not see significant changes even for a small test-particle number in the cells.

The number of test particles per cell plays an important role when not using a constant cross section, but e.g. a constant shear viscosity over entropy density ratio, η/s, or constant mean free path, λ_{mfp}. When inspecting various dissipative quantities we have found small numerical artifacts, as shown in Sec. 7.1. These are in general very small and negligible.

We conclude that using a cell length smaller than the mean free path in the system is enough to avoid numerical artifacts originating from the cell length. Furthermore, a sufficient number of test particles is also enough to avoid numerical artifacts.

7.5.2. Calculating time

So far, in this chapter, we have not mentioned the required computational run time for each setup. Moreover, we have not listed all numerical parameters, such as N_{test} or cell length Δx.

It is obvious that the calculating time strongly depends on the chosen parameters N_{test} and Δx. The more test particles we use, the longer is the runtime. It is also clear that the smaller the cell length, the more test particles we have to use in order to avoid numerical artifacts. The reason why we have not displayed these numerical parameters is that they should not matter for the physical results. These parameters are always chosen accordingly, such that BAMPS solves the rBE in an accurate way.

The corresponding runtime varies with the chosen numerical parameters. It is to be expected that performing BAMPS in the almost perfect-fluid limit, i.e., for small Knudsen number, the runtime is very large and takes a couple of hours. In contrast, when we perform BAMPS in the highly viscous limit, the cell length does not have to be so small as in the almost perfect-fluid limit such that the runtime per simulation decreases significantly. However, we always average over many ensembles to get rid of statistical fluctuations and, therefore, depending on the statistics we frequently require to perform more than $10^3 - 10^4$ parallel simulations.

---

[24]In case we do not have a one-dimensional problem, the cell sizes in transverse direction are relevant and have to be adjusted accordingly.

We can conclude that BAMPS is a very accurate rBE solver, but requires large computational resources especially when considering the almost perfect-fluid limit.

8. Investigation of Mach cones in a kinetic transport model

In the previous chapter we have shown a detailed study of the formation and the evolution of shock waves in a simplified $(1+1)$-dimensional setup. It has been demonstrated that BAMPS is suitable to describe the complete transition from ideal to viscous shock waves in a very accurate manner. This implies that BAMPS is also an appropriate framework to study "Mach cone"-like structures, which is the main topic of this chapter.

In Chapter 4, we have introduced the physical motivation for Mach cones and the framework in which they may appear. As discussed there, the most important prerequisites in order to observe Mach cones are that we have to assume an almost perfect fluid and a perturbation, i.e., a source or projectile, which propagates faster than the local speed of sound in the medium. If these two requirements are fulfilled, a Mach cone may appear. As we will observe in the forthcoming sections, however, the shape of the Mach cone strongly depends on the implementation of the moving projectile which in the end deposits energy and/or momentum into the medium.

The motivation for studying Mach cones is not only of academical interest. Mach cones have been a topic of great interest in the community of the heavy-ion physics [29, 30,51,114,117,118,120,121,122,123,124,125,126,127,128,129,130,131,132,133,163] over the last decades. The almost perfect-fluid behavior and strong jet suppression indicate that shock waves in form of Mach cones have to exist. Furthermore, the extracted two-particle correlations from experiments at RHIC and LHC indicated that under some circumstances the appearance of a double-peak structure is found [113, 234, 235, 236, 237,238]. Initially, it was considered that such double-peak structures originated solely from the jet-medium interaction. Recent studies of hot spots and triangular flow from initial-state fluctuations have shown to have a very large contribution to the double-peak structure in the azimuthal two-particle correlations [15, 31, 32, 115, 135, 136, 239]. In this work, however, we address the question whether a Mach cone can contribute to the signal of a double-peak structure and whether it is indeed an appropriate observable for it. The naive picture of a Mach cone implies that a double-peak structure appears because the Mach cone in the transverse plane is mainly characterized by two wings where matter propagates at a certain emission angle with respect to the propagating source. It has to be checked whether this naive picture is indeed true. For this purpose, we inspect the jet-medium interaction and quantify which properties of the medium and/or jet prevents a double-peak structure. The influence of a non-static medium has also to be considered [30, 51]. Therefore, it is reasonable to split our forthcoming discussion about Mach cones into two parts: studies in a static medium where only the effects of the Mach cone itself are analyzed, and a scenario in full relativistic heavy-ion collisions (HIC), which by default includes an expansion of the medium.

Although the shear viscosity over entropy density ratio, η/s, seems to be very small in relativistic HIC, the short lifetime of the QGP possibly prevents the full development of shock waves and thus of Mach cones. As shown in Sec. 7.1.4, shock waves need a certain time to develop when the viscosity is not exactly zero. Thus, as discussed in Sec. 7.1.5, the formation time of shock waves depends on η/s and the lifetime of the system. The larger η/s the more time shock waves need to develop. Therefore, the effects of dissipation on the development of shock waves and Mach cones have to be taken into account, which is part of our study and the main advantage of the kinetic transport model BAMPS.

We now introduce the structure of this chapter: In order to understand the origin of the double-peak structure associated originally with Mach cones, we start in Sec. 8.1 with the discussion of the particle-momentum distribution emitted from a shock front of an ideal Mach cone in a perfect fluid. In the subsequent Sec. 8.2, we use BAMPS in order to investigate the transition from ideal to viscous Mach cones using different projectiles in a static system. We note that we use a $(2+1)$-dimensional setup[1] in order to reduce the required computational power when performing the almost perfect-fluid limit. In particular, a dependence of the Mach-cone angle on the details and rate of the energy deposition from the projectile to the matter is investigated. Similarly to the relativistic Riemann problem we also encounter a characteristic scaling behavior. In the end of this section we discuss the two-particle correlations of the Mach cones in the perfect-fluid limit as well for various η/s, where we compare the numerical results with our findings from Sec. 8.1. In the following Sec. 8.3 we still maintain our studies in a static system, but we switch to highly energetic jets losing energy and momentum to the medium and thus decelerating and study the corresponding two-particle correlations. In Sec. 8.4 we finally extend our study to relativistic heavy-ion collisions in $(3+1)$-dimensions, which imply a longitudinal and radial expansion which affects the evolution of the Mach cone induced by highly energetic jets. We study possible scenarios of the jet path and the resulting two-particle correlations.

We note that in the following we will investigate the jet-medium interaction in several setups. Depending on the properties of the medium and projectile/jet shock waves in form of a "Mach cone"-like structure will appear. The shape will always deviate from the strict conical structure due to non-linear effects. Nevertheless, we will always call this "Mach cone"-like structure Mach cone.

In this chapter, all further hydrodynamic quantities are calculated in the Landau frame. The method to extract those quantities has been introduced in Sec. 6.5.

8.1. Particle momentum distribution in the shock front of an idealized Mach cone

In this section, we derive a simple model for the particle emission from a Mach cone in a perfect fluid omitting non-linear effects resulting from a diffusion wake or head shock[2]. This will clarify whether the naive picture of a Mach cone leading to a double-peak

---

[1]This is realized using periodic boundary conditions in z-direction.
[2]More details regarding those effects come later when introducing the numerical results.

structure in the particle-momentum distribution is supported. Before that, we repeat some basic details from Chapter 4 using an adapted notation.

8.1.1. Basic details of Mach cones

In Chapter 4, we have illustrated the main features of Mach cones in a perfect fluid. We have found that if the velocity of the source or projectile, v_{source}, is faster than the generated waves propagating with the speed of sound, c_s, the waves lie on a cone. In this case, the propagating modes are called sound waves. In the following, we refer to the surface of the cone as the Mach cone or shock front[3].

The resulting emission angle of this Mach cone with respect to the direction of the projectile with $v_{\text{source}} = 1$ is given by the weak-perturbation Mach angle which for an ultrarelativistic gas of massless particles characterized by the EoS $e = 3p$ reads

$$\alpha_{\text{w}} = \arccos\left(\frac{c_s}{v_{\text{source}}}\right) = \arccos\left(\frac{1}{\sqrt{3}}\right) = 54,73° \,. \tag{8.1}$$

As discussed in Chapter 4, we have to mention that in nature perturbations are not always small. In this case, shock waves are generated instead of sound waves and we expect a change of the Mach angle due to different propagation velocities of these waves. Therefore, the Mach angle has to be generalized to the case of stronger perturbations[4] as

$$\alpha = \arccos\left(\frac{v_{\text{shock}}}{v_{\text{source}}}\right) \,. \tag{8.2}$$

We require here $v_{\text{source}} > v_{\text{shock}}$, where v_{shock} is the velocity of the shock front propagating through the medium. The velocity of the shock front depends on the pressure (energy density) behind the cone, p_{cone} (e_{cone}), and in front of it, i.e., of the medium, p_{med} (e_{med}), i.e.,

$$v_{\text{shock}} = \left[\frac{(p_{\text{med}} - p_{\text{cone}})(e_{\text{cone}} + p_{\text{med}})}{(e_{\text{med}} - e_{\text{cone}})(e_{\text{med}} + p_{\text{cone}})}\right]^{1/2} \,. \tag{8.3}$$

The relation above corresponds to Eq. (5.41) with an adapted notation. Equation (8.3) has the following limits: If $p_{\text{cone}} \gg p_{\text{med}}$ we obtain $v_{\text{shock}} = 1$. If $p_{\text{cone}} \approx p_{\text{med}}$, i.e., if the perturbation is very weak, we get the expected limit of the speed of sound, i.e., $v_{\text{shock}} \approx c_s$. As expected, Eq. (8.2) turns into α_{w} in the latter case. A useful and required quantity for our forthcoming discussion is the collective velocity of matter in the shock wave, i.e., in the wings of the Mach cone. This is different from the signal propagation velocity (8.3), and reads

$$v_{\text{coll}} = \left[\frac{(p_{\text{cone}} - p_{\text{med}})(e_{\text{cone}} - e_{\text{med}})}{(e_{\text{med}} + p_{\text{cone}})(e_{\text{cone}} + p_{\text{med}})}\right]^{1/2} \,, \tag{8.4}$$

which is just Eq. (5.40) with an adapted notation. In the case of a very weak perturbation the collective velocity of matter vanishes, i.e., $v_{\text{coll}} \approx 0$, whereas for stronger perturbations v_{coll} can increase up to the speed of light.

---

[3]The name shock front is in general only valid in case of stronger perturbations, as we will discuss in the following.

[4]These are shock waves.

8.1.2. Derivation of particle-momentum distribution on the shock front

In order to understand the origin of the double-peak structure induced by Mach cones in our forthcoming analysis of the numerical results, we shall derive a simple model of particle emission from the shock front of a Mach cone in the 2-dimensional xy-plane. We restrict our model to a projectile depositing its energy isotropically into the medium, i.e., there is no momentum deposition. We furthermore assume a perfect fluid, i.e., no dissipation.
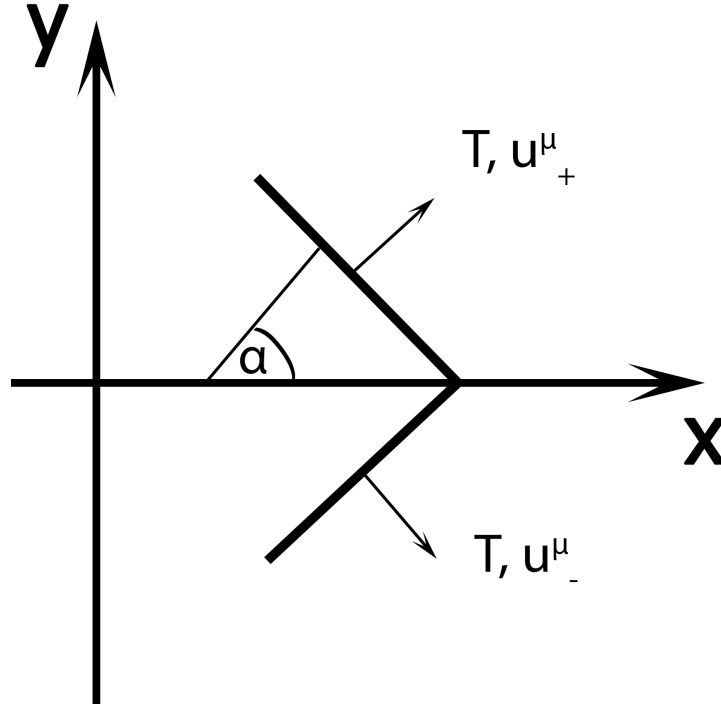
Figure 8.1.: A sketch of an idealized Mach cone in a two-dimensional plane. The perturbation propagates in x-direction and induces two wings, which symbolizes the shock front of the cone. The Mach cone has an emission angle α. The matter on the cone is characterized by the velocity, u^μ, and temperature, T. There is no diffusion wake, head shock, or any other non-linear effect.

As depicted in Fig. 8.1, we assume two sources modeling the two wings of a Mach cone[5] with a constant temperature, T, and collective four-velocity, $u^\mu = \gamma(1, \vec{v})$, where $\gamma = 1/\sqrt{1 - v^2}$ is the Lorentz factor. Each source consists of massless particles with to the thermal distribution

$$f(x, p) = \exp\left(\frac{-u_\mu p^\mu}{T}\right), \tag{8.5}$$

where $p^\mu = (E, \vec{p})$ is the particle four-momentum. Choosing the x-axis to be the symmetry axis of the cone, which is simultaneously the propagation direction of the

---

[5]We omit the contribution of a possible diffusion wake or head shock, which will be discussed later on when showing the numerical results. These contributions affect the final particle distribution emitted from a Mach cone.

projectile, we can write

$$u_\pm^\mu = \gamma \begin{pmatrix} 1 \\ v\cos\alpha \\ \pm v\sin\alpha \\ 0 \end{pmatrix}. \tag{8.6}$$

The $\pm$ corresponds to each wing of the cone. We identify $v = v_{\text{coll}}$ with Eq. (8.4) as the collective velocity of the matter in the shock wave and α is the Mach angle defined in Eq. (8.2). Using the same coordinate system we write for the four-momentum vector

$$p^\mu = p \begin{pmatrix} 1 \\ \cos\phi\sin\theta \\ \sin\phi\sin\theta \\ \cos\theta \end{pmatrix}. \tag{8.7}$$

ϕ is the azimuthal angle in the $x-y$-plane and θ is the polar angle with respect to the z-axis. The distribution function is defined as

$$\frac{\mathrm{d}N(2\pi)^3}{\mathrm{d}V\mathrm{d}^3p} = f(x,p), \tag{8.8}$$

where $\mathrm{d}V\,\mathrm{d}^3p/(2\pi)^3$ is the phase-space volume element. We are interested in the normalized azimuthal particle distribution, $\mathrm{d}N/(N\mathrm{d}\phi)$, which can be calculated as an integral over the thermal distribution in a certain volume, V, over the Mach-cone surface. We use $\mathrm{d}^3p = \sin\theta p^2\,\mathrm{d}p\,\mathrm{d}\phi\,\mathrm{d}\theta$ and write

$$\frac{\mathrm{d}N}{N\mathrm{d}\phi} = \frac{V}{N(2\pi)^3}\int_0^\pi \mathrm{d}\theta\sin\theta \int_0^\infty p^2\left(e^{-\frac{u_+^\mu p_\mu}{T}} + e^{-\frac{u_-^\mu p_\mu}{T}}\right)\mathrm{d}p. \tag{8.9}$$

We obtain $N = 8\pi\gamma T^3 V$ by integrating Eq. (8.8) over the entire phase-space volume. First, integrating Eq. (8.9) over $\mathrm{d}p$ leads to

$$\frac{\mathrm{d}N}{N\mathrm{d}\phi} = \frac{1}{8\pi\gamma^4}\int_0^\pi \sum_{i=1}^2\left[\frac{1}{1-b_i\sin^3\theta}\right]\sin\theta\mathrm{d}\theta, \tag{8.10}$$

and after the integration over $\mathrm{d}\theta$ we obtain

$$\frac{\mathrm{d}N}{N\mathrm{d}\phi} = \frac{1}{8\pi\gamma^4}\sum_{i=1}^2\left[\frac{2+b_i^2}{(1-b_i^2)^2} + \frac{3b_i}{(1-b_i^2)^{5/2}}A\right], \tag{8.11}$$

where $A = \pi/2 + \arctan(b_i/\sqrt{1-b_i^2})$, $b_1 = v\cos(\alpha-\phi)$ and $b_2 = v\cos(\alpha+\phi)$. Equation (8.11) mainly depends on the pressure (energy density) on the cone, p_{cone} (e_{cone}), and the medium itself, p_{med} (e_{med}), which determines the emission angle, α, and the collective velocity of matter, $v = v_{\text{coll}}$, on the cone.

Discussion of the solution

The naive picture of Mach cones suggests that both wings generate two peaks in the azimuthal particle distribution, $dN/d\phi$. Against all expectations, even in this simple model this does not always apply. In the left panel of Fig. 8.2 we show the normalized azimuthal particle distribution, $dN/(Nd\phi)$, according to Eq. (8.11) with respect to the angle, ϕ. We consider an energy density on the cone of $e_{cone} = 16.3$ GeV/fm^3, with a medium temperature of $T_{med} = 0.4$ GeV and an energy density of $e_{med} = 16.28$ GeV/fm^3. This specific case represents a very weak perturbation for which the emission angle is $\alpha = 54.72°$ and the collective velocity of matter is given by $v_{coll} = 0.0004$. Each of the wings leads to a peak around $\pm 54.72°$, but the sum of both wings results in a peak in direction of the projectile, $\phi = 0°$. One would expect such an outcome since the propagation of a shock front does not mean that all particles have the same propagation direction: In effect, they are distributed according to the thermal distribution function (8.5).
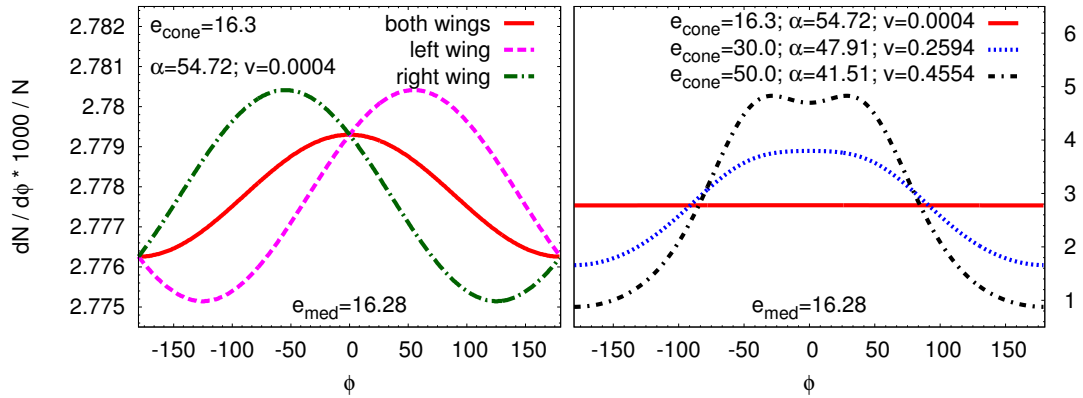
Figure 8.2.: We show the normalized azimuthal particle distribution, $dN/(Nd\phi)$, of a Mach cone in a simplified model for an ultrarelativistic gas of massless particles. The temperature of the medium is $T_{med} = 0.4$ GeV, and therefore we have $e_{med} = 16.28$ GeV/fm^3. In the left panel, we show the results for each wing separately and for the sum of both. We use $e_{cone} = 16.3$ GeV/fm^3, which results in $\alpha = 54.72°$ and $v_{coll} = 0.0004$. In the right panel, we show the particle distribution for various strength of the shock waves.

However, the results might change when increasing the strength of the shock wave, which induces a higher collective velocity of matter in the shock wave, as shown in the right panel of Fig. 8.2. If e_{cone} is much larger than e_{med}, a double-peak structure appears. This is due to the fact that the peaks originating from each wing become sharper, because of the increasing collective velocity of matter, which in the end affects the distribution function (8.5). Thus, although summing up both wings together, those peaks survive. When increasing the strength of the shock waves, the corresponding signal of the double-peak structure becomes even more dominant. Due to the dependence of the emission angle, α, on the strength of the shock wave, however, the peaks move

closer to the direction of the projectile.
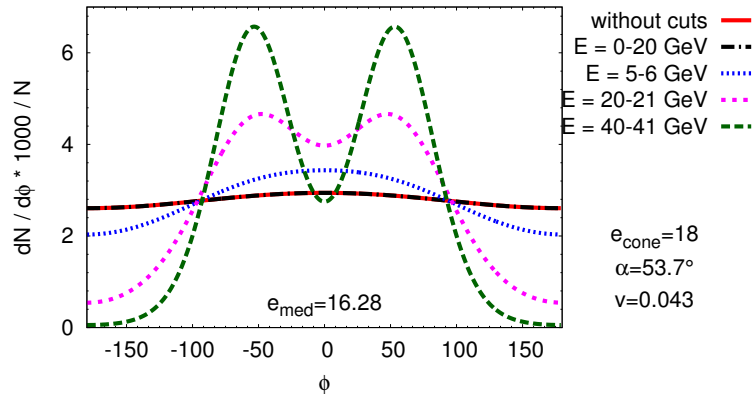
Figure 8.3.: We show the normalized particle distribution, $\mathrm{d}N/(N\mathrm{d}\phi)$, with several cuts in the energy E of a Mach cone in a simplified model for an ultrarelativistic gas of massless particles. The temperature of the medium is $T_{\mathrm{med}} = 0.4$ GeV which corresponds to $e_{\mathrm{med}} = 16.28$ GeV/fm^3. We show the results for $e_{\mathrm{cone}} = 18$ GeV/fm^3, which results in $\alpha = 53.7°$ and $v_{\mathrm{coll}} = 0.043$.

These results indicate that a Mach cone does not necessarily result in a double-peak structure in the azimuthal particle distribution, $\mathrm{d}N/(N\mathrm{d}\phi)$, but that such a phenomenon occurs for strong shocks only. However, this might change if one considers momentum cuts. If we do not carry out the full momentum integration in Eq. (8.9) but restrict it to a certain interval, a double-peak structure even appears for weak shocks, as demonstrated in Fig. 8.3 for $e_{\mathrm{cone}} = 18$ GeV/fm^3. This is shown for $E = 21-22$ GeV or $40-41$ GeV, which represent exemplary fractions of the high-momentum region[6]. On the contrary, the low-momentum region represented exemplary by $E = 5-6$ GeV particles does not support a double-peak structure. This indicates that the contribution for the double-peak structure originates mostly from high-momentum particles, while the contribution of the bulk medium[7] has a compensating effect on the phenomenon.

We have discussed the results for a specific scenario by assuming a gas of massless particles and a projectile propagating with the speed of light. It is clear that changing the EoS or speed of the projectile might play an important role when addressing the question under which conditions a double-peak structure will appear. For example, if the speed of sound is very small compared to the speed of the projectile, when considering a massive gas for instance, the double-peak structure appears even for very weak shock waves. This is due to the fact that in this case the emission angle of the Mach cone is very large. However, we restrict our forthcoming discussion of the numerical results to an ultrarelativistic gas of massless particles.

We can conclude that in our simplified model a double-peak structure does not always appear. The appearance of a double-peak structure depends on the strength of the shock wave, the speed of the projectile with respect to the propagation speed of

---

[6]We note that $p = E$ for massless particles.

[7]It consists of low-momentum particles.

the shock front, and, in general, on the EoS. Using special cuts in momentum, a double peak in the particle distribution may appear more easily since the contribution for the double-peak structure originates mostly from the high-momentum region. Nevertheless, we have to mention that our scenario omits any other non-trivial and non-linear effects which normally appear if a projectile moves through a medium[8], and which affects the final distribution. Moreover, the propagating projectile in our scenario deposits only energy to the medium, but no momentum. Therefore, our simple model here is merely a good approximation and just serves as a reference.

We will compare our results derived here to the numerical results from BAMPS. For a static system[9] and fixed projectile direction, the particle distribution is equivalent to the two-particle correlation, since the angle ϕ is always correlated to the direction of the projectile, which serves as a "trigger" particle.

8.2. Transition from ideal to viscous Mach cones using projectiles

In the following, we study the evolution of Mach cones with different assumptions of the interaction between the projectile and the medium using the microscopic transport model BAMPS. To our knowledge, the complete transition from ideal to viscous Mach cones, similar to the studies of shock waves in the previous Chapter 7, has not been realized by any other model or study.

In this section, we focus on the investigation of Mach-cone evolution in the absence of any other effects, i.e., we neglect such effects as initial fluctuations or longitudinal/transverse expansion, which are, however, relevant for heavy-ion collisions. For this purpose, the space-time evolution of particles is performed in a static box. If not stated otherwise, the box lengths are $L_x = L_y = L_z = 5$ fm. We initialize a static uniform medium of massless Boltzmann particles for a medium temperature of $T_{\mathrm{med}} = 0.4$ GeV which is in chemical equilibrium, i.e., $\lambda_{\mathrm{med}} = 1$. This corresponds to a LRF energy density of $e_{\mathrm{med}} = 16.28 \, \mathrm{GeV/fm}^3$, while the degeneracy factor is $g = 16$. The medium is initially in thermal equilibrium, i.e., all dissipative quantities are initially zero.

In order to keep our calculations simple, we consider only binary collisions with an isotropic cross section, i.e., a cross section with an isotropic distribution of the collision angle. Furthermore, as introduced in Sec. 6.4, we keep the mean free path of the medium particles constant in all spatial cells, i.e., $\lambda_{\mathrm{mfp}} = C$, by adjusting the cross section according to $\sigma = 1/(nC)$, where n is the LRF particle density in the cell[10]. In the forthcoming numerical results we always show the corresponding shear viscosity over entropy density ratio, η/s, of the medium in rest. The related shear viscosity for isotropic binary collisions is given by Eq. (6.15).

---

[8]We will see those effects when introducing the numerical results for Mach cones.

[9]There is no expanding medium.

[10]This is necessary, because due to the energy deposition originating from the propagating projectiles, the local energy and particle density will increase significantly. This would possibly lead to numerical artifacts. Adjusting the cross section according to $\sigma = 1/(nC)$, where C has to be chosen larger than the cell size, avoids this problem.

8.2.1. Number of dimensions

When performing the almost perfect-fluid limit, the computational time in BAMPS is already very high in the simplified one-dimensional problem considered in Chapter 7. In a full $(3+1)$-dimensional system the calculations would take too much time when performing the almost perfect-fluid limit. To this end, we reduce our problem to two space dimensions, which considerably decreases the computational time. Thus, we keep the z-direction homogeneous and use periodic boundary conditions. Collisions of particles against box boundaries in x- and y-direction are realized as elastic collisions off a wall. The x- and y-directions are the physically relevant dimensions.

As we show in Sec. 8.2.2, we implement two different projectiles depositing energy and momentum in order to simulate the evolution of the Mach cones. The shape of the Mach cone as well as the evolution is similar to the case of a full $(3+1)$-dimensional scenario. The restriction to $(2+1)$-dimensions does not affect the main results and conclusions we obtain in our discussion. Nevertheless, the corresponding energy-deposition rate, $\mathrm{d}E/\mathrm{d}x$, of the projectile in two dimensions is not directly comparable to systems with three dimensions.

8.2.2. The projectiles

In order to investigate the evolution of Mach cones, we introduce two different projectiles. Both projectiles are characterized by their different implementation of the energy- and momentum-deposition into the medium. We note that the projectiles are point-like.

1. **The pure-energy deposition scenario (PED)**
   In the so called pure-energy deposition scenario (PED) which is quite similar to the one introduced in Refs. [50, 240, 241] the projectile propagates and emits particles according to the thermal distribution

$$f(x,p) = \exp\left(-\frac{E}{T_{\mathrm{source}}}\right), \tag{8.12}$$

   such that the energy deposition is isotropic in the LRF of the projectile. The parameter T_{source} as well as the number of particles is chosen appropriately in order to obtain a specific energy-deposition rate, $\mathrm{d}E/\mathrm{d}x$. In this scenario only energy, but no net-momentum is deposited into the medium.

2. **The JET scenario**
   In the second scenario, referred to as JET, a highly energetic massless particle (jet) has a momentum in x-direction only, i.e., $p_x = E_{\mathrm{jet}}$. The jet propagates and deposits energy into the medium due to collisions with the medium particles. After each collision, the momentum of the jet is reset to its initial value. The jet-medium cross section is adjusted in such a way that we obtain a specific energy deposition rate, $\mathrm{d}E/\mathrm{d}x$. Using this scenario a constant energy- and momentum-deposition rate is achieved.

For both scenarios the projectiles are initialized at $t = 0$ fm/c at the position $x = -0.1$ fm and propagate in x-direction with $v_{\mathrm{source}} = 1$, i.e., with the speed of light.

We note that the JET scenario is a simplified model of a jet in heavy-ion physics, whereas the PED scenario vaguely resembles the hot spots studied in [135], but in its implemented form has no direct relation to heavy-ion collisions. Furthermore, the PED scenario provides the possibility to reproduce the Mach cone structure generated by a weak and sonic perturbation, see Chapter 4.

We expect clear differences between these two scenarios concerning the evolution of the entire system, but also concerning the final distribution of the particles.

The energy deposition rate $\mathrm{d}E/\mathrm{d}x$

In this section we use a constant energy-deposition rate, $\mathrm{d}E/\mathrm{d}x$, for the projectiles. The energy-deposition rate is given by

$$\frac{\mathrm{d}E}{\mathrm{d}x} = \frac{E_\mathrm{f} - E_\mathrm{i}}{\Delta x \, N_\mathrm{test}} \,, \tag{8.13}$$

where E_i denotes the energy of the whole system at $t = 0$ fm/c, E_f the energy at the end of the simulation, and Δx the path length the projectiles traverse.

Although the projectile is point-like, the energy is deposited in the smallest possible volume element, which is given in terms of the cell sizes. However, due to the fact that we choose the z-direction to be homogeneous, we numerically set the cell size in z-direction equal to the box length, L_z. Thus, we have to be careful when comparing the results for a specific $\mathrm{d}E/\mathrm{d}x$, but different lengths of L_z. The same amount of energy has a different influence on the medium when changing[11] L_z. Thus, in case we change the length in L_z, we have to rescale the energy deposition rate[12] by L_z. Then, two different simulations with a given energy-deposition rate and different L_z are directly comparable.

In this section we always use $L_z = 5$ fm, such that all numerical calculations are directly comparable.

8.2.3. Mach cones in the nearly perfect-fluid limit

In Fig. 8.4, we show the results for the PED scenario in the left panel and for the JET scenario in the right panel for three different energy-deposition rates into the medium, i.e., $\mathrm{d}E/\mathrm{d}x = 1$, 10, and 200 GeV/fm, and in the nearly ideal limit, i.e., we have chosen $\eta/s = 0.005$. We note that, in general, the maximum (minimum) energy density in the simulations is larger (smaller) than the maximum (minimum) of the energy density scales in the figures. As an overlay we show the velocity profile as arrows with a scaled length arrow. Both modifications are done to enhance the readability of the figures[13].

In both scenarios, PED and JET, we observe a conical structure but with obvious differences for all depositions. In the PED case with the isotropic energy deposition, a circle of perturbations propagating in backward direction is visible. This is missing in

---

[11]The energy per particle which is transferred to the medium by the projectile is large for small L_z and small for large L_z.

[12]The energy deposition rate has to be divided by L_z, i.e., $\frac{\mathrm{d}E^*}{\mathrm{d}x} = \frac{1}{L_z}\frac{\mathrm{d}E}{\mathrm{d}x}$.

[13]Those modifications are performed in all forthcoming figures concerning the demonstration of Mach cones in those 2-dimensional plots.

Figure 8.4.: Shape of a Mach cone in the nearly ideal limit ($\eta/s = 0.005$) shown for different jet scenarios and different energy-deposition rates into the medium, i.e., $dE/dx = 1$, 10, and 200 GeV/fm. The left panel shows the pure energy deposition scenario (PED), whereas the right panel shows the propagation of a highly energetic jet (JET) depositing energy and momentum in the x-direction. We have depicted the LRF energy density within a specific range. As an overlay we show the velocity profile as arrows with a scaled length arrow in order to improve the readability. The results are a snapshot of the evolution at $t = 2.5$ fm/c. In addition we show the analytical solution for the ideal Mach cone in the very weak perturbation case with the emission angle α_w.

the JET scenario because of the strong momentum deposition in x-direction. Another difference is that in the JET scenario a clearly visible head shock, i.e., a shock wave in the front of the jet perpendicular to the direction of the jet appears. This in turn is missing in the PED scenario. Furthermore, there is a clear difference in the behavior of the matter behind the Mach cones. In the JET case, the projectile induces a diffusion wake[14] where the matter is flowing in the direction of the projectile. On the contrary, a different behavior is observed within the PED scenario. In this scenario, we observe an anti-diffusion wake, for which the matter behind the cone is flowing in the backward direction. These observations are in qualitative agreement with the results from ideal hydrodynamics and transport calculations [50, 240, 241].

Angular dependence of the energy-deposition rate

Additionally, every scenario is compared to the ideal Mach cone with α_w for a very weak perturbation as shown in Fig. 8.4. Both scenarios provide evidence that the energy-deposition rate of the projectile influences the Mach angle, α. For a very small energy deposition of $\mathrm{d}E/\mathrm{d}x = 1$ GeV/fm, the profile in JET and PED is almost linear and, as expected, we reproduce the angle α_w. In addition, non-linear effects such as a diffusion wake and a head shock are almost negligible and do not influence the conical structure significantly due to the very weak perturbation[15]. This changes with larger energy deposition as shown for $\mathrm{d}E/\mathrm{d}x = 10$ GeV/fm. Here, the shock front in both, PED and JET, propagates faster through the medium and the Mach angle changes according to Eq. (8.2). Moreover, the shock front is already slightly curved, because the energy density and pressure in the wings decrease away from the projectile. Different energy densitiy and pressure mean a different local propagation velocity at each point of the wing according to Eq. (8.3). When increasing the energy deposition further the curved structure of the shock front is clearly visible, both, for JET and PED, and the Mach angle, α, strongly deviates from the weak-perturbation Mach angle, α_w.

Furthermore, near the projectile in the JET scenario the disturbance of the medium is strongest, resulting in a strong head shock, and the shock front moves much faster than the speed of sound. Farther away from the projectile, a part of the energy of the shock front has already dissipated into the medium and, as a result, the perturbation gets weaker and approaches a weak perturbation propagating with the speed of sound.

For the PED scenario, the curved profile is not the result from a head shock[16], but due to the fact that the linear conical region is shortened. Since the propagating waves are shock waves and not sound waves, the linear region where the shock waves lie on the cone is shortened, which is shown in the right part of Fig. 4.2. For example, if the propagation velocity of the shock waves approaches the velocity of the projectile, v_source, the linear region vanishes and we obtain only a circle-like structure. In order to demonstrate this, we show a very strong energy deposition of $\mathrm{d}E/\mathrm{d}x = 20000$ GeV/fm

---

[14]More details to the appearance of a diffusion wake are given in Refs. [50, 139, 164, 165, 242].

[15]However, by a deeper inspection we can see that only the PED scenario is able to reproduce the Mach cone generated by sonic perturbations (plotted as black lines), because it deposits its energy isotropically to the medium. In the JET scenario we see even for this small energy- and momentum deposition that the cone region has a significantly higher energy density as the medium in rest and a small but visible diffusion wake in direction of the projectile exists.

[16]As mentioned above, there is no head shock in the PED scenario.
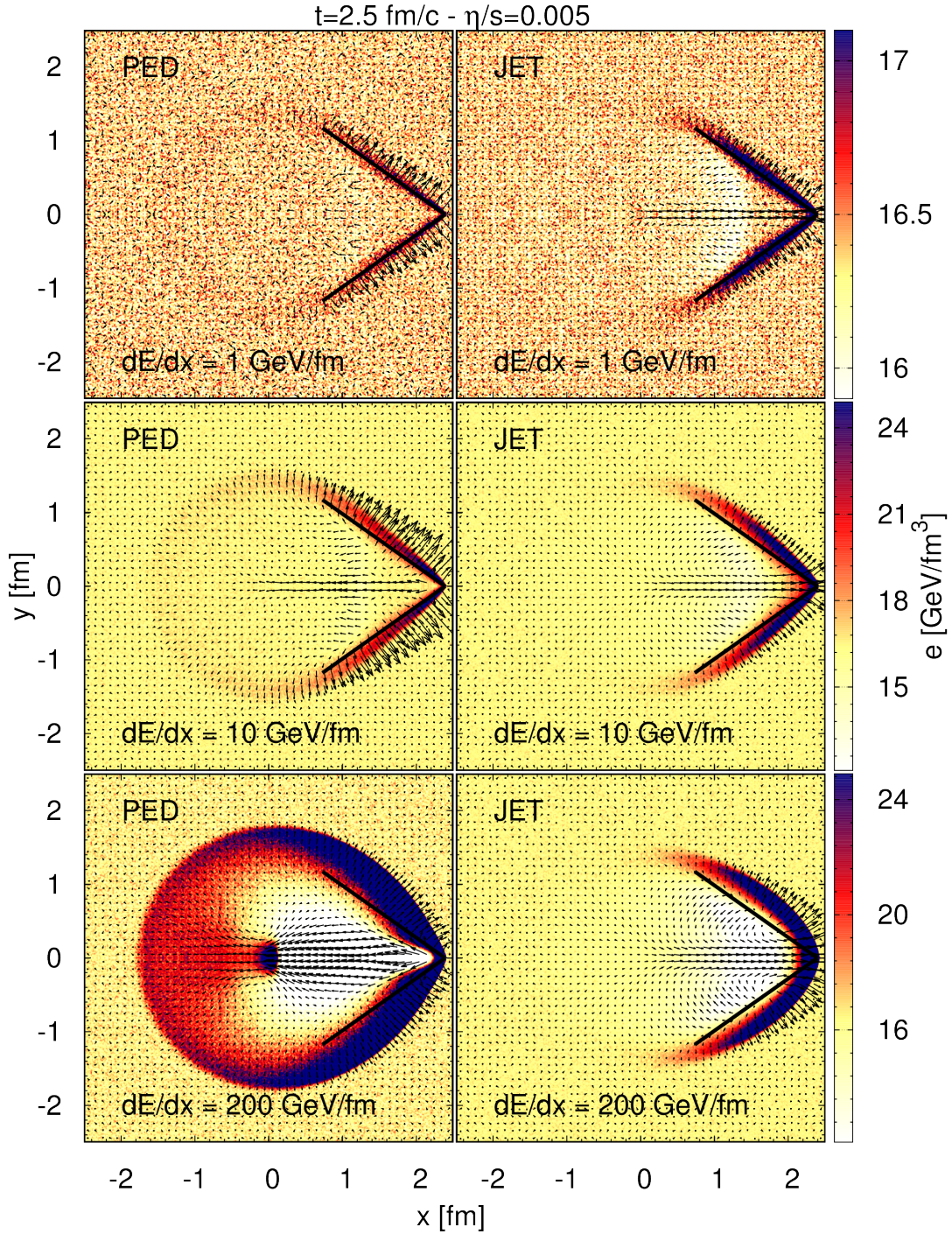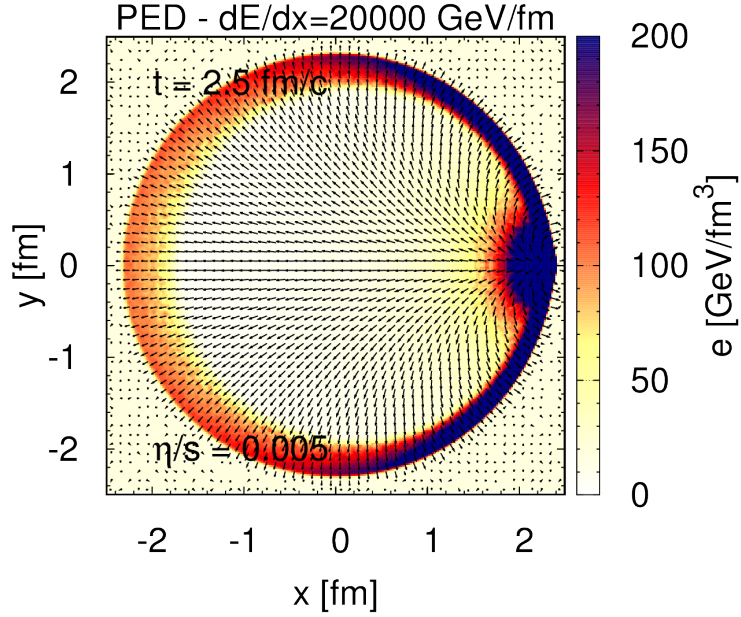
Figure 8.5.: Shape of a Mach cone in the nearly ideal limit ($\eta/s = 0.005$) shown for the PED scenario at energy deposition rate $\mathrm{d}E/\mathrm{d}x = 20000$ GeV/fm in the x-direction. Depicted is the LRF energy density within a specific range. As an overlay we show the velocity profile as arrows with a scaled length arrow. The results are a snapshot of the time evolution at $t = 2.5$ fm/c.

for the PED scenario in Fig. 8.5. The propagation velocity of the shock waves in the backward and the sidewards direction is almost 85% and 90% of the speed of light, respectively. Furthermore, they approach the speed of light in forward direction. Due to this incredibly fast shock-wave propagation in the forward direction, the conical linear region shortens to almost a point, and we hence observe a circle-like structure only.

Details on the implementation of the projectile

In the JET scenario the energy of the jet, E_{jet}, is 20, 200, and 20000 GeV, starting from the upper to the lower panel in Fig. 8.4, respectively. For our calculations in the nearly ideal limit, the energy of the jet does not play any significant role. The only parameter which matters is the average energy-deposition rate. We mention in Sec. 8.2.4 how the value of the jet energy, E_{jet}, changes the pattern of the Mach cone.

In the PED scenario we make a similar observation as in the JET scenario due to the free choice of the parameters of the projectile, which are T_{source} and the number of particles which are emitted by the projectile. In order to achieve a fixed energy-deposition rate, $\mathrm{d}E/\mathrm{d}x$, we can adjust those parameters in an arbitrary way. This free choice leads to different final profiles of the resulting Mach cones. In order to demonstrate this we show a Mach cone in the PED scenario for $\mathrm{d}E/\mathrm{d}x = 200$ GeV/fm,
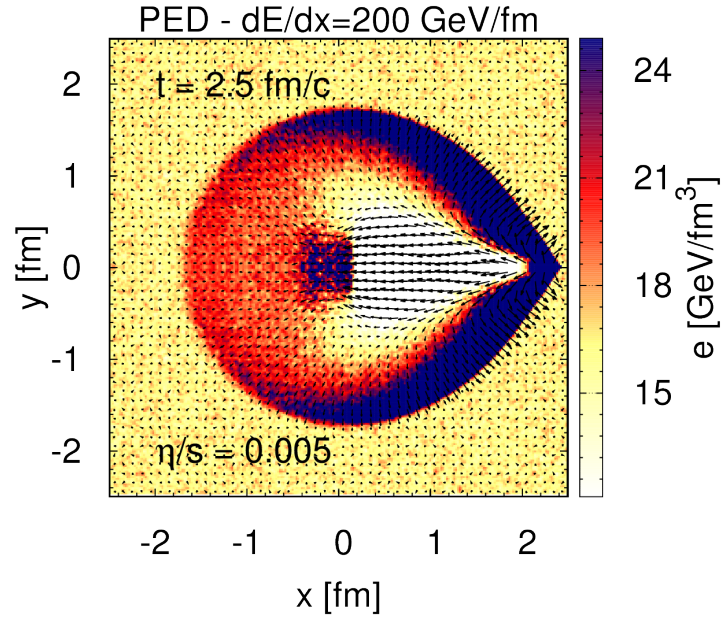
Figure 8.6.: Shape of a Mach cone in the nearly ideal limit ($\eta/s = 0.005$) shown for the PED scenario at energy deposition rate of $dE/dx = 200$ GeV/fm in the x-direction. The results are a snapshot of the time evolution at $t = 2.5$ fm/c. Depicted is the LRF energy density within a specific range. As an overlay we show the velocity profile as arrows with a scaled length arrow. The value T_{source} and the number of particles emitted from the projectile differs from those in Fig. 8.4 and results into a slightly different shape in the final profile.

$\eta/s = 0.005$, and at a time of $t = 2.5$ fm/c in Fig. 8.6. Although the choice of the settings is equal to the case shown in Fig. 8.4 for $dE/dx = 200$ GeV/fm (lower left panel), we observe a slightly different profile. This is due to the fact that the number of particles as well as their average kinetic energy are chosen differently in both simulations[17].

Mach cone or Mach shock?

An interesting issue is whether the specific case considered in Fig. 8.5 can be still called a Mach cone. In this case only shock waves propagate through the medium, which are still slower than the projectile itself, but there is almost no conical structure visible. A better name for such a scenario would be "Mach shock" [30, 163]. In the end, this is an issue of convention and should not affect our discussions and conclusions.
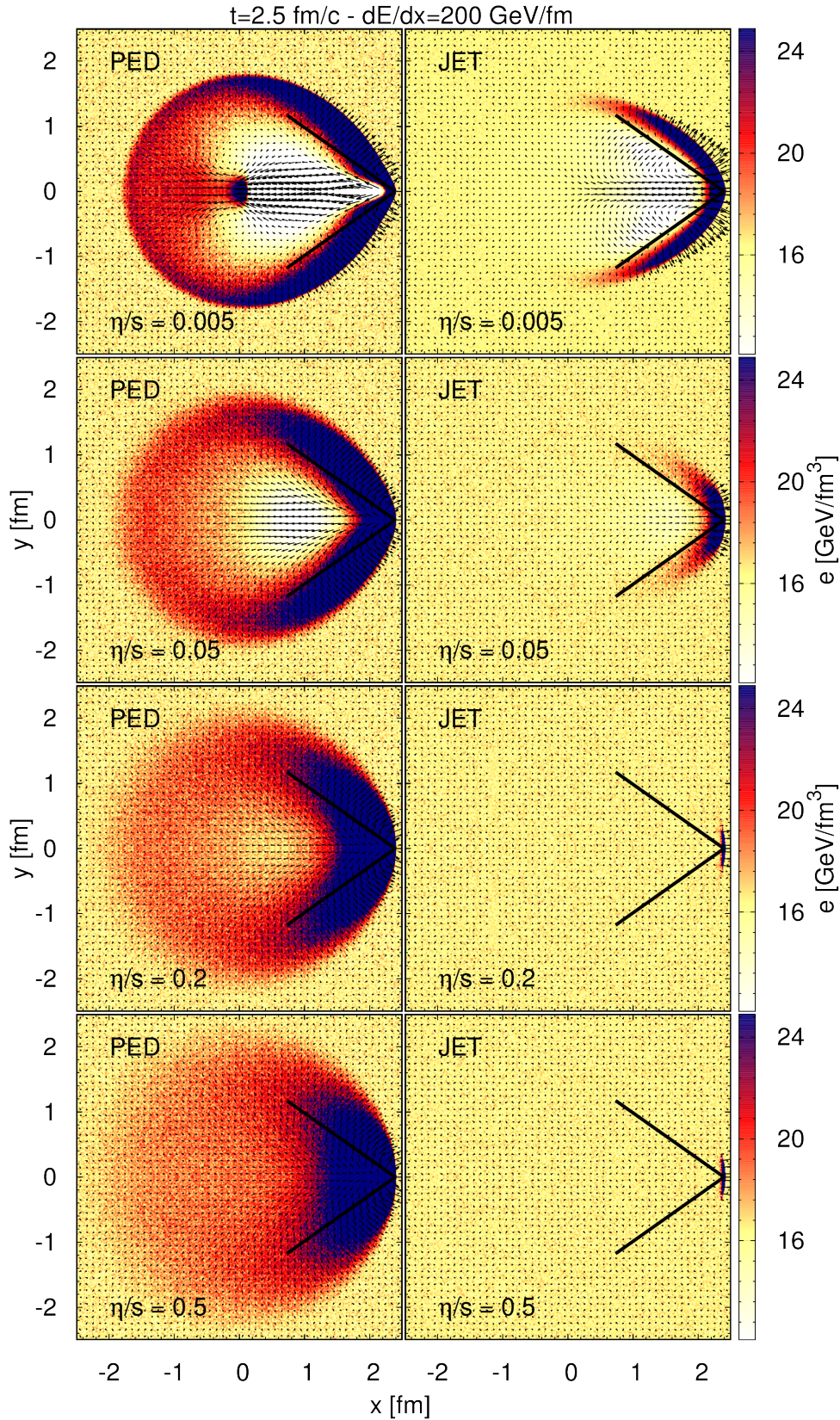
Figure 8.7.: Similar to Fig. 8.4. We show the transition from ideal to viscous Mach cones by adjusting the shear viscosity over entropy density ratio, $\eta/s = 0.005$, 0.05, 0.2, and 0.5. The energy deposition is $\mathrm{d}E/\mathrm{d}x = 200$ GeV/fm. The results are a snapshot of the time evolution at $t = 2.5$ fm/c. Depicted is the LRF energy density within a specific range. As an overlay we show the velocity profile as arrows with a scaled length arrow.

8.2.4. Effects of viscosity on the evolution of Mach cones

Similar to the consideration of shock waves in one dimension in Chapter 7, BAMPS also allows us to investigate Mach cones in different dissipative regimes. For this purpose, we show the Mach-cone structure for the PED scenario (left panel) and the JET scenario (right panel) for different values of η/s in Fig. 8.7. The energy-deposition rate has been fixed to $dE/dx = 200$ GeV/fm. In addition, $E_{\text{jet}} = 20000$ GeV is used in the JET scenario. The chosen η/s values are intended to cover the nearly-ideal limit ($\eta/s = 0.005$), the estimated QGP shear viscosity over entropy density ratio in heavy-ion collisions ($\eta/s = 0.05, 0.2$) [11, 105] and the highly viscous limit where dissipative hydrodynamical calculations are not reliable anymore ($\eta/s = 0.5$) [33].

First, we note that if we consider the system at fixed time of $t = 2.5$ fm/c, the Mach cone structure and the characteristic sharp structures smear out and eventually disappear almost completely within both scenarios as the viscosity increases. This is true for the shock front as well as for the (anti-)diffusion wake. The difference between both scenarios is that for increasing η/s the resulting Mach-cone solution covers approximately the same spatial region regardless of the value of η/s within the PED scenario, while in the JET case the structure is concentrated more and more near the projectile. The reason for this is that in the PED scenario, the momentum from the projectile is isotropically deposited into the medium, whereas in the JET scenario, the initial momentum dissipation is strongly peaked in the direction of the projectile[18]. With a large viscosity, the re-scattering of the emitted particles from the projectile is very rare. Thus, the larger the viscosity the more the resulting solution reflects the details of the projectile-matter interaction.

Dissipative quantities of Mach cones

So far, we have only investigated the energy-density profile which already reveal a lot about the structure end evolution of Mach cones in the low- and high-viscosity regime. As a further possibility, we can also inspect the dissipative quantities which reflect the non-equilibrated regions of the profiles. This is especially the case if the shear viscosity over entropy density ratio is large. For this purpose, we show some of the dissipative quantities in Fig. 8.8 ($\eta/s = 0.005$), Fig. 8.9 ($\eta/s = 0.05$), and Fig. 8.10 ($\eta/s = 0.5$). We show the time-like component of the shear-stress tensor, π^{00} (upper panel), the time-like component of the heat flow, q^0 (middle panel), and the fugacity λ (lower panel), at time $t = 2.5$ fm/c. The energy deposition has been fixed to $dE/dx = 200$ GeV/fm. The left and the right panel presents the PED and the JET scenario, respectively.

In Fig. 8.8, which represents the almost ideal limit, the dissipative quantities π^{00} and q^0 are only observable in the very small region of the shock front. In this case the dissipative quantities are not zero because the gradients are very large here. In the region away from the shock front, however, the medium is in thermal equilibrium. When increasing the shear viscosity over entropy density ratio to $\eta/s = 0.05$ as shown in Fig. 8.9, we observe that the region where the dissipative quantities are not zero

---

[17]The main conclusions we draw in this thesis are not affected by this choice.

[18]The effect in the JET scenario becomes even stronger with increasing energy E_{jet} of the jet, since the scattered particles are stronger forward-peaked.

Figure 8.8.: Shape of a Mach cone in the nearly ideal limit ($\eta/s = 0.005$), shown for different jet scenarios and a fixed energy-deposition rate into the medium of $dE/dx = 200$ GeV/fm. The left panel shows the pure energy-deposition scenario (PED), whereas the right panel shows the propagation of a highly energetic jet (JET) depositing energy and momentum into the x-direction. Depicted are the time-like component of the shear-stress tensor, π^{00} (upper panel), the time-like component of the heat flow, q^0 (middle panel), and the fugacity λ (lower panel) within a specific range. As an overlay we show the velocity profile as arrows with a scaled length arrow. The results are a snapshot of the time evolution at $t = 2.5$ fm/c.

Figure 8.9.: Shape of a Mach cone in the viscous regime ($\eta/s = 0.05$) shown for different jet scenarios and a fixed energy-deposition rate into the medium of $dE/dx = 200$ GeV/fm. The left panel shows the pure energy-deposition scenario (PED), whereas the right panel shows the propagation of a highly energetic jet (JET) depositing energy and momentum into the x-direction. Depicted are the time-like component of the shear-stress tensor, π^{00} (upper panel), the time-like component of the heat flow, q^0 (middle panel), and the fugacity λ (lower panel) within a specific range. As an overlay we show the velocity profile as arrows with a scaled length arrow. The results are a snapshot of the time evolution at $t = 2.5$ fm/c.

Figure 8.10.: Shape of a Mach cone in the highly viscous regime ($\eta/s = 0.5$) shown for different jet scenarios and a fixed energy-deposition rate into the medium of $\mathrm{d}E/\mathrm{d}x = 200 \, \mathrm{GeV/fm}$. The left panel shows the pure energy-deposition scenario (PED), whereas the right panel shows the propagation of a highly energetic jet (JET) depositing energy and momentum into the x-direction. Depicted are the time-like component of the shear-stress tensor, π^{00} (upper panel), the time-like component of the heat flow, q^0 (middle panel), and the fugacity λ (lower panel) within a specific range. As an overlay we show the velocity profile as arrows with a scaled length arrow. The results are a snapshot of the time evolution at $t = 2.5 \, \mathrm{fm}/c$.

becomes larger and the sharp profiles smear out. A higher dissipation as considered in Fig. 8.10 with $\eta/s = 0.5$ shows a further increase of π^{00} and q^0 for the PED scenario but not for the JET scenario. This is due to the fact that in the JET scenario particles are pushed almost only in forward direction due to the high energy and momentum deposition, as discussed previously and demonstrated in Fig. 8.7. Thus, only in the region at the very front around the projectile the dissipative quantities do not vanish. In the PED scenario, to the contrary, the emitted particles are distributed isotropically such that dissipation covers a larger region.

The pattern of the dissipative profiles obviously depends strongly on the implemented projectile. This fact is also reflected in the fugacity, λ, which in the affected region exceeds one within the PED scenario, whereas it remains below one within the JET scenario. This is due to the fact that in the JET scenario the number of particles is conserved but energy is deposited into the medium. In the PED scenario the energy is deposited via the emission of particles, where in this specific case the kinetic energy per particle is very low[19]. Thus, the fugacity develops differently compared to the JET scenario.

8.2.5. Scaling behavior and time evolution of Mach cones

In Figs. 8.11 and 8.12, we demonstrate the time evolution of the PED and the JET scenario, respectively. We fix the energy deposition to $dE/dx = 200$ GeV/fm and show the results for the nearly ideal-fluid limit characterized by $\eta/s = 0.005$. In both cases, we observe that the Mach cone takes some time to develop its final structure. Especially for the PED scenario we see that the high energy-density region around $x = -0.2$ fm for $t = 2.5$ fm/c has not yet developed at very early times.

We note that in both scenarios the projectiles are point-like and the matter is homogeneously distributed initially, i.e., there are no gradients and the medium does not expand. The only length scales that control the solution are the mean free path, $\lambda_{\mathrm{mfp}} \propto \eta$, and the energy deposition rate, dE/dx. Thus, we expect a similar scaling behavior as for the Riemann problem discussed in Sec. 7.1.4. For example, the energy density profiles for two different shear viscosities, η and η', are related by

$$e(t - t_0, x - x_0, y - y_0, \frac{dE}{dx}, \eta) = e'\left(\frac{t - t_0}{C}, \frac{x - x_0}{C}, \frac{y - y_0}{C}, \frac{1}{C^{N-1}}\frac{dE}{dx}, \eta'\right), \quad (8.14)$$

where the scaling factor is given by $C = \eta/\eta'$. Furthermore, x_0 and y_0 are the coordinates of the projectile at time t_0. Here, N counts the physically relevant number of dimensions in space. In our case we have $N = 2$ since we keep the z-direction as homogeneous[20].

Using this scaling behavior, we can also interpret Fig. 8.7 as a time-evolution of the solution, with a larger viscosity corresponding to an earlier time and with an appropriate scaling of the energy-deposition rate. In order to demonstrate this, we

---

[19]The shape of the fugacity depends strongly on T_{source} and the number of particles emitted from the projectile.

[20]In case we consider the evolution of a Mach cone in a full 3-dimensional setup with $N = 3$, then the relation (8.14) has to be modified, such that the signal propagation in z-direction has to be considered, too.
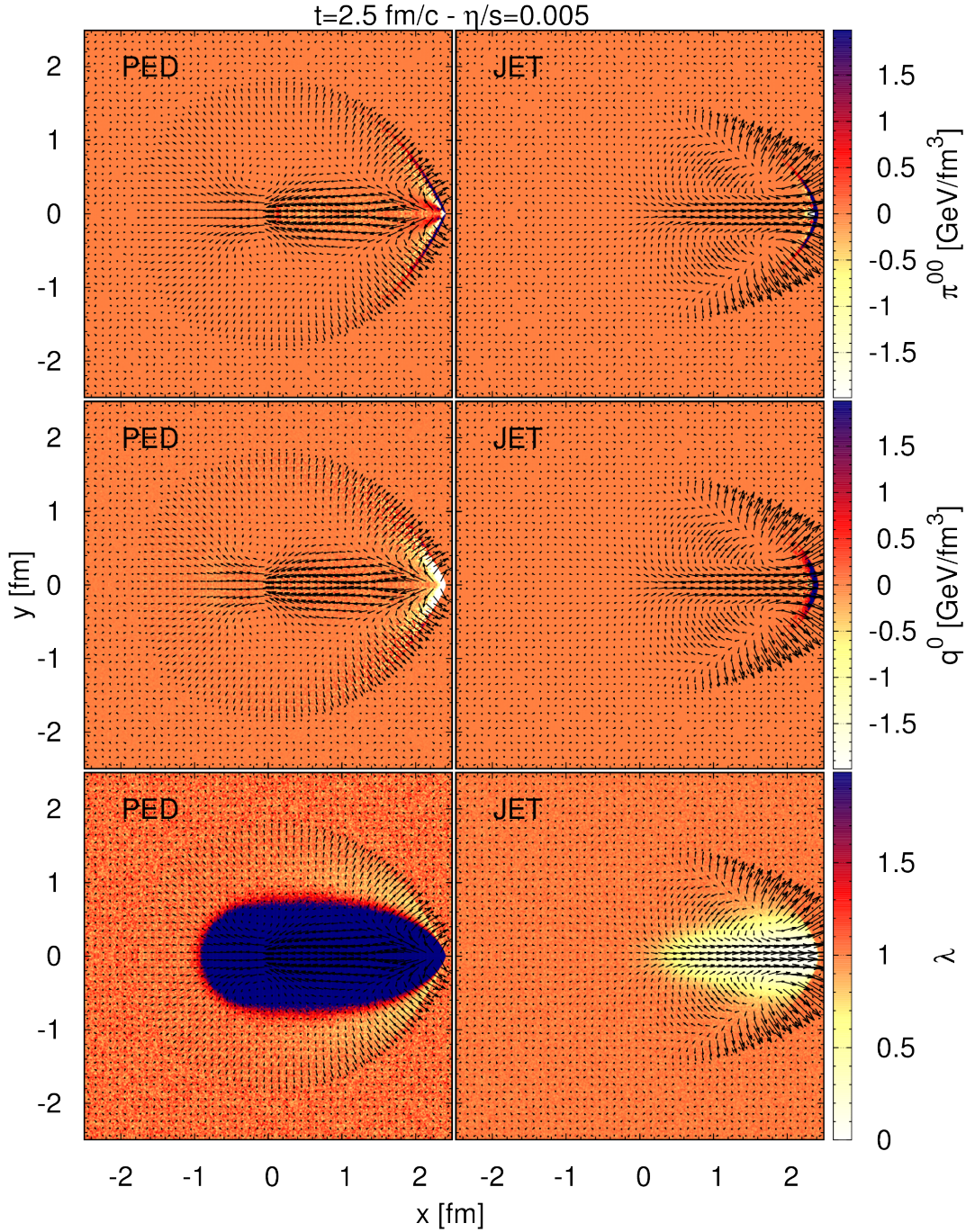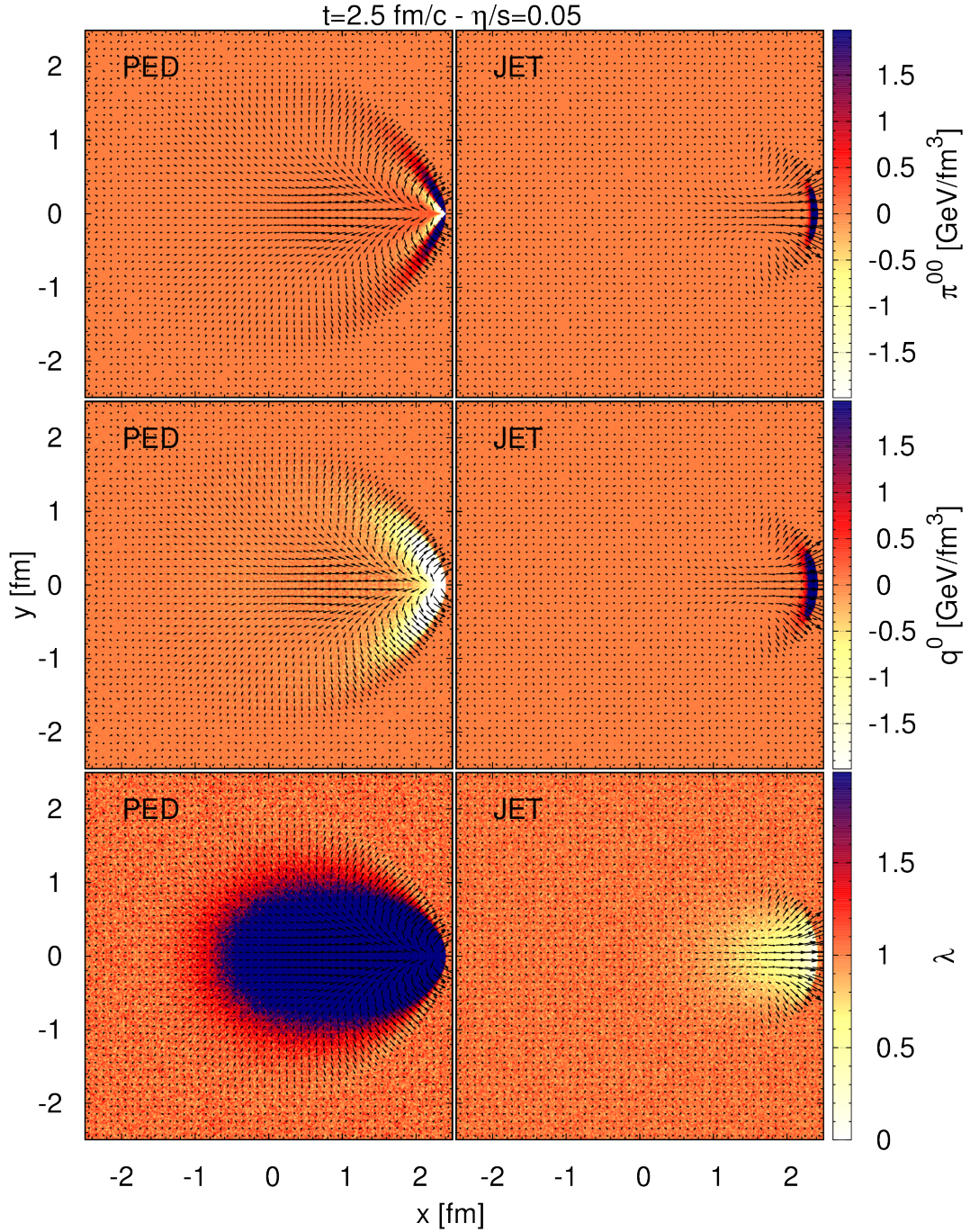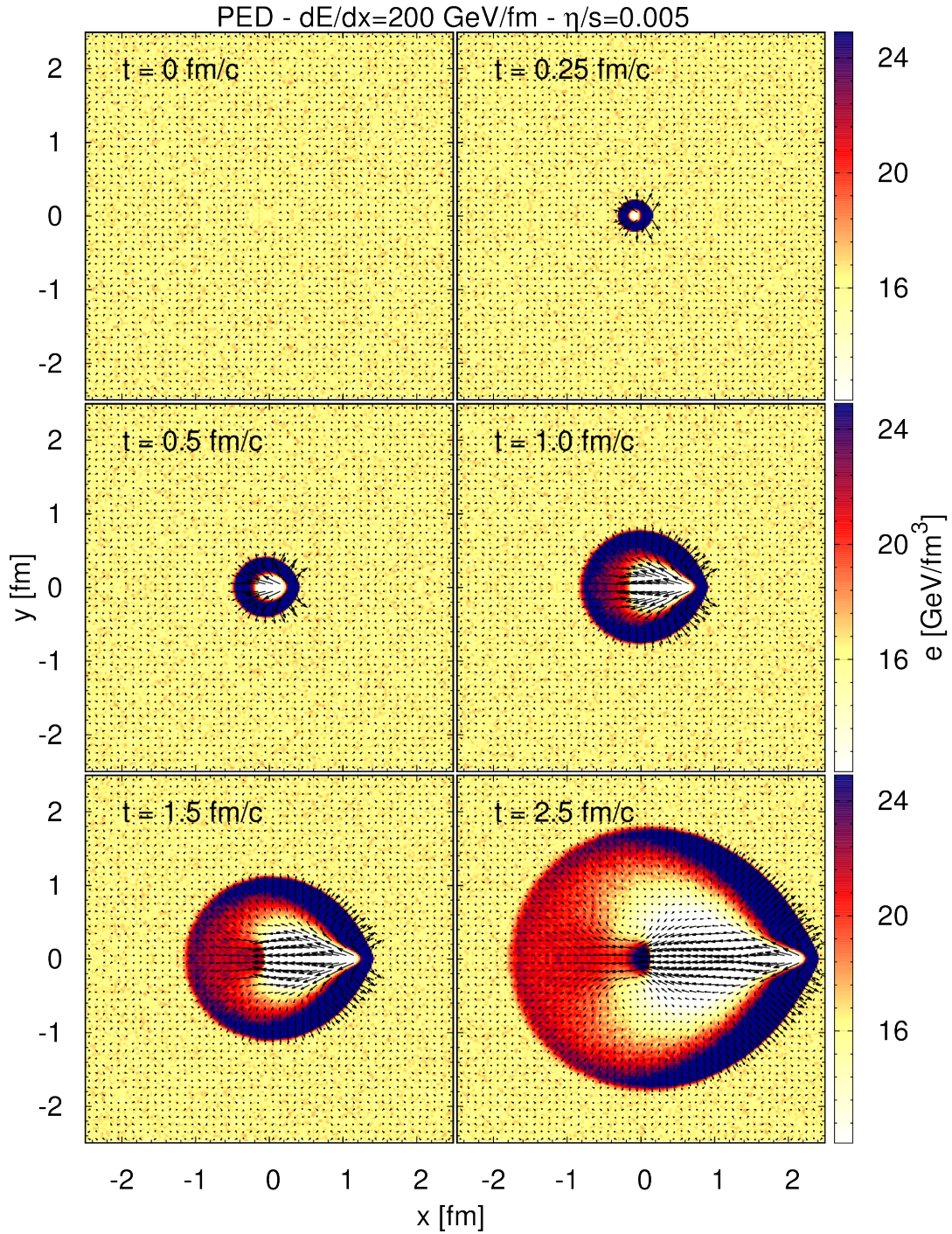
Figure 8.11.: Time evolution of a Mach cone in the nearly ideal limit ($\eta/s = 0.005$) shown for the PED scenario at a fixed energy-deposition rate $\mathrm{d}E/\mathrm{d}x = 200$ GeV/fm. Depicted is the LRF energy density within a specific range. As an overlay we show the velocity profile as arrows with a scaled length arrow.
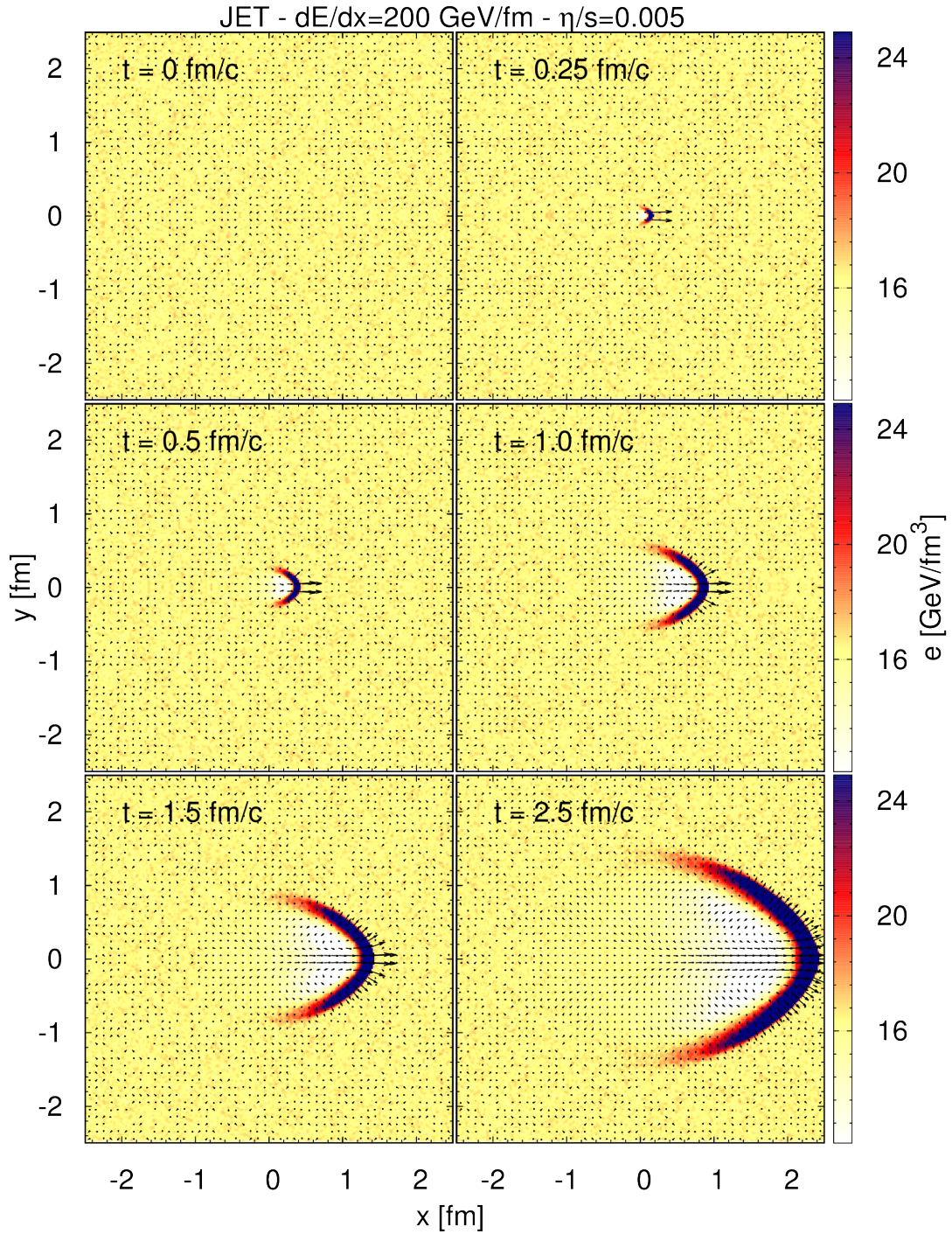
Figure 8.12.: Time evolution of a Mach cone in the nearly ideal limit ($\eta/s = 0.005$) shown for the JET scenario at a fixed energy-deposition rate $\mathrm{d}E/\mathrm{d}x = 200$ GeV/fm. Depicted is the LRF energy density within a specific range. As an overlay we show the velocity profile as arrows with a scaled length arrow.
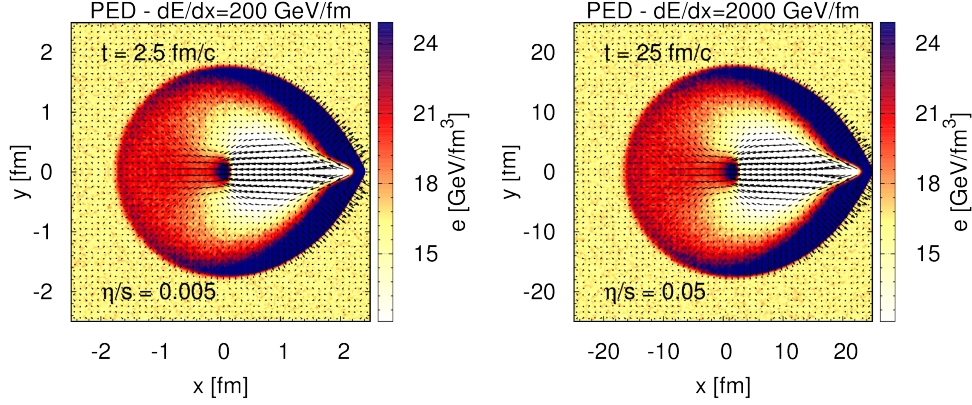
Figure 8.13.: We demonstrate the scaling behavior of a Mach cone using the PED scenario according to Eq. (8.14). Depicted is the LRF energy density within a specific range. As an overlay we show the velocity profile as arrows with a scaled length arrow. In the left (right) panel we show a snapshot at $t = 2.5$ (25) fm/c for $\eta/s = 0.005$ (0.05) and $\mathrm{d}E/\mathrm{d}x = 200$ (2000) GeV/fm. The box sizes are $L_x = L_y = 50$ (5) fm and $L_z = 5$ (5) fm. The starting position of the projectile is $x = -0.1$ fm at $t = 0$ fm/c.

show the solution for $\eta/s = 0.005$ (0.05), $t = 2.5$ (25) fm/c $\mathrm{d}E/\mathrm{d}x = 200$ (2000) GeV/fm in the left (right) panel of Fig. 8.13. The box sizes are $L_x = L_y = 50$ (5) fm and $L_z = 5$ (5) fm. The starting position of the projectile is $x = -0.1$ fm at $t = 0$ fm/c in both simulations. Both simulations are identical, which confirms the scaling behavior given by Eq. (8.14).

Although the Mach angle apparently changes with viscosity, see Fig. 8.7, this is a transient effect related to the finite formation time of the Mach cone with non-zero viscosity. The viscosity affects the width and formation time of the shock front, but not its speed of propagation, i.e., Eq. (8.3) still holds for non-zero viscosity. Asymptotically, the Mach-cone angle will be the same regardless of the value of η/s using the corresponding energy-deposition scaling given in Eq. (8.14).

From this discussion, we can conclude that in order to observe a fully developed Mach-cone structure, we have to wait for a sufficient long time, i.e., we have to keep the microscopic length scale small compared to the macroscopic one. This relation corresponds to a small Knudsen number Kn, which has been discussed in Sec. 7.1.4 and 7.1.5.

8.2.6. Two-particle correlations of Mach cones

Based on the naive assumption that the double-peak structures always result from the formation of Mach cones, we investigate the two-particle correlations in the PED and JET scenario for ideal and viscous Mach cones extracted from the numerical calculations in BAMPS. We further compare our numerical results with our findings in Sec. 8.1, where we have derived a simple model in order to understand the origin of

a double-peak structure induced by Mach cones. Since we have performed our calculations in a static system and the direction of the projectile is always in x-direction, the particle distribution extracted from BAMPS is equivalent to the two-particle correlation. The reason is that the angle ϕ is always correlated to the direction of the projectile, which serves as a "trigger" particle.

Two-particle correlations in the nearly perfect-fluid limit

We would now like to address the question whether the Mach-cone structures in the almost perfect-fluid limit as observed in Fig. 8.4 can be regarded as the source of a double-peak structure in two-particle correlations. For this purpose, we extract the normalized azimuthal particle distribution, $dN/(Nd\phi)$, from BAMPS calculations. In Fig. 8.14a, we show the numerical results for the energy-deposition rate $dE/dx = 10$ GeV/fm together with the analytical calculation as given by Eq. (8.11). In order to extract the contribution from the wings only and to exclude those from all regions such as the (anti-)diffusion wake and the back region[21], a lower energy-density cut of $20\,\text{GeV/fm}^3$ is applied[22]. Particles in cells with an energy density lower than this value are not considered for the extracted particle distribution[23]. For the analytical solution[24] taken from Eq. (8.11) we use $e_{\text{cone}} = 22.15\,\text{GeV/fm}^3$ and $v_{\text{coll}} = 0.137$. For both scenarios as well as for the analytical calculation we observe only a peak in the direction of the projectile, i.e., $\phi = 0°$, but no double-peak structure. As already mentioned in Sec. 8.1 this finding is against all expectations from the naive picture of a Mach cone.

However, with a sufficiently high energy-deposition rate the final picture changes significantly. In Fig. 8.14b the results from BAMPS calculations with $dE/dx = 200$ GeV/fm are shown. The lower energy-density cut has been increased to $50\,\text{GeV/fm}^3$ because of the much higher energy-deposition rate. For the analytic calculation $e_{\text{cone}} = 62.55\,\text{GeV/fm}^3$ with $v_{\text{coll}} = 0.537$ has been chosen. In the PED scenario as well as in the analytic model the double-peak structure finally appears as long as the energy-deposition rate and, consequently, v_{coll} are sufficiently large. In the JET scenario, however, only one peak in direction of the jet is visible.

There are two main contributions to the structure of the two-particle correlation. One arises from the wings of the Mach cone and the other one emerges from the head-shock region. The matter in the wings is moving in the direction perpendicular to the surface with some collective velocity, v_{coll}. The peaks in the local particle-distribution function are the stronger the larger the collective velocity is chosen. It follows from our simple analytical model that the mere existence of the wings does not necessarily lead to clearly visible peaks in the correlation, but that the local velocity of the matter has to be sufficiently large as well. This is also confirmed by the numerical simulations:

---

[21]especially in the PED scenario.

[22]We note that regardless of those lower energy-density cuts the contribution of the head shock in the JET scenario is included since this region features the largest energy density.

[23]We note that the contribution of the medium at rest is a constant. Thus, this contribution cancels out when inspecting the normalized particle distribution.

[24]e_{cone} is estimated by the average energy density on the Mach-cone wings extracted from the associated numerical calculations.
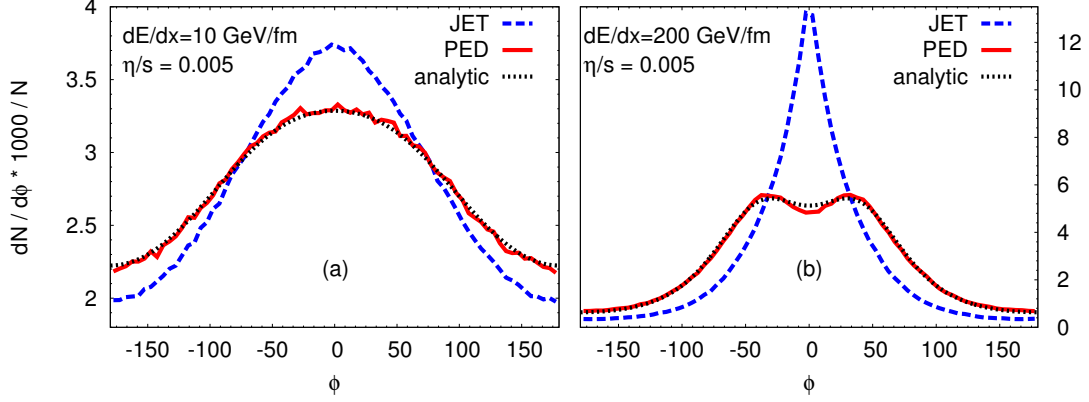
Figure 8.14.: Two-particle correlations, $dN/(Nd\phi)$, extracted from calculations for Mach cones in the nearly ideal limit shown in Fig. 8.4. The results are extracted from calculations with $dE/dx = 10$ GeV/fm (a) and $dE/dx = 200$ GeV/fm (b). Analytic solutions extracted from Eq. (8.11) are shown for $e_{\text{cone}} = 22.15\,\text{GeV/fm}^3$ (a) and $e_{\text{cone}} = 62.55\,\text{GeV/fm}^3$ (b).

If the energy-deposition rate is sufficiently large in the PED scenario, the double-peak structure appears.
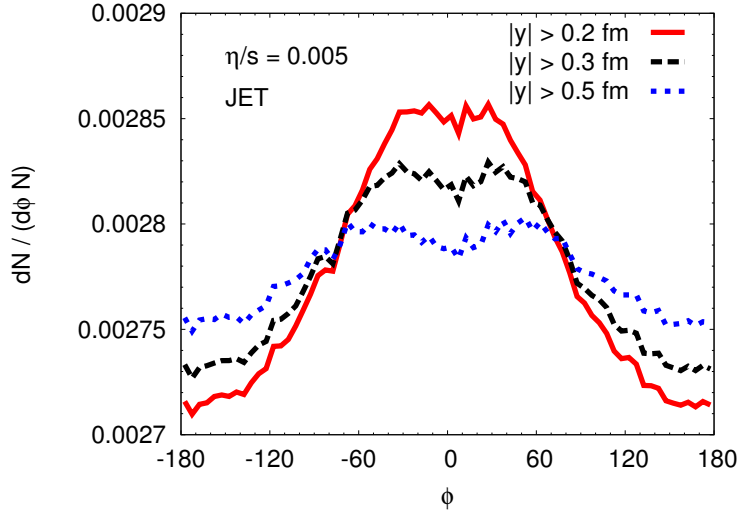
Figure 8.15.: Two-particle correlations, $dN/(Nd\phi)$, with spatial cuts in transverse position extracted from calculations as shown in Fig. 8.4. We have considered the JET scenario for $\eta/s = 0.005$ and $dE/dx = 200$ GeV/fm. Only particles with transverse positions $|y| > 0.2$, 0.3, and 0.5 fm, respectively, contribute to the final two-particle correlations.

In principle, the same argument also holds for the JET scenario. In this scenario,

however, there is also a strong contribution from the head-shock region[25], where the matter is moving with large collective velocity. This collective motion is in direction of the projectile and results in a particle-distribution function that is peaked in the same direction. Although a double-peak structure due to the Mach-cone wings may be formed, the contribution of head shock clearly dominates and overshadows the contribution from the wing regions.

A promising method to find a double-peak structure in the JET scenario are probably momentum cuts[26]. When considering only particles from the high-momentum region, the signal for the double peak becomes very strong. This is definitely true for the PED scenario and also leads to the appearance of a double-peak structure for weak-shock scenarios, i.e., for small v_{coll}. However, such an effect does not occur within the JET scenario. The reason is that within the JET scenario, one encounters a strong contribution from the head-shock region, where a huge amount of highly energetic particles exist. These highly energetic particles mostly propagate in the direction of the projectile.

In order to obtain a double-peak structure in the JET scenario, we have to perform a spatial cut in the transverse y-direction in order to get rid of the contribution of the diffusion wake and the strong head-shock region [243]. This is shown in Fig. 8.15, where only particles with $|y| > 0.2$, 0.3, and 0.5 fm are taken into account. For $|y| > 0.2$ fm the contribution of the head shock and the diffusion wake is still too strong. But for $|y| > 0.3$ fm as well as for $|y| > 0.5$ fm the double-peak structure originating from the wings becomes clearly visible. Figure 8.15 demonstrates that neglecting the head shock and the diffusion wake makes it possible to observe a double-peak structure originating from the wings. Therefore, it is justified to conclude that the head shock as well as the diffusion wake prevent the appearance of a double-peak structure in the above JET scenario .

Two-particle correlations in the low and highly viscous regime

An important question of interest is the effect of dissipation on the development of the two-particle correlations. In Fig. 8.16 we show the two-particle correlations for the distributions shown in Fig. 8.7. The procedure is similar to the one applied for the results presented in Fig. 8.14. The lower energy-density cut is chosen as $50\,\text{GeV}/\text{fm}^3$. For the JET scenario (a), the peak in direction of the projectile becomes sharper with larger viscosity and no other appreciable effects originating from viscosity are visible. On the contrary, for the PED scenario (b) the viscosity destroys the double-peak structure. If the viscosity is very large, only one peak in direction of the jet is visible.

As a matter of fact, dissipation does not lead to any important effect enhancing the appearance of a double-peak structure. Quite the reverse, without exception possible double-peak structures tend to disappear with larger dissipation. This is also shown in the forthcoming sections.

---

[25]The part of the diffusion wake is already excluded by the lower energy-density cuts.

[26]As shown for our simple model a double-peak structure in Fig. 8.3 appears when restricting the momentum or equivalent the energy integration in Eq. (8.9) to a certain interval.
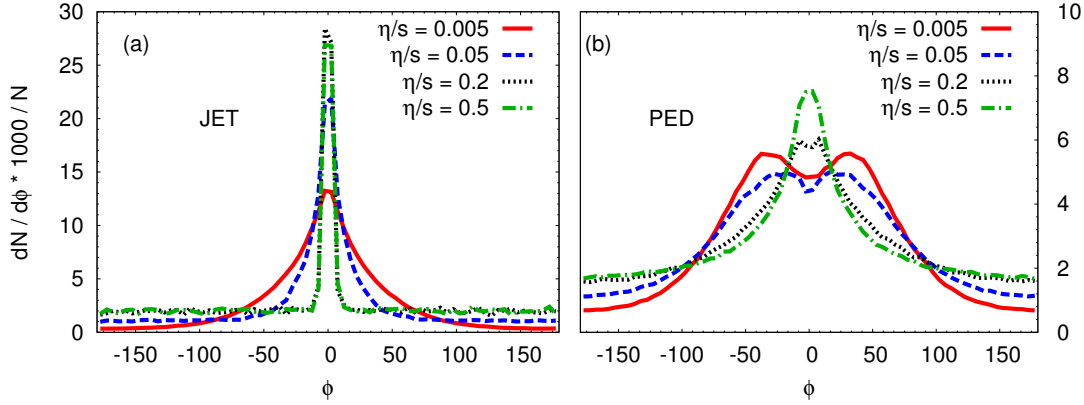
Figure 8.16.: Two-particle correlations, $\mathrm{d}N/(N\mathrm{d}\phi)$, for different viscosities extracted from the distributions shown in Fig. 8.7. The results are depicted for an energy-deposition rate of $\mathrm{d}E/\mathrm{d}x = 200$ GeV/fm for both scenarios.

8.3. Mach cones induced by decelerating or quenched jets in a static system

In the previous section, we have investigated the evolution of Mach cones induced by projectiles in a static system. In this section, we still keep the static system and the initial configuration, but instead of a projectile we use a highly energetic and massless jet[27] which interacts with the medium via isotropic and binary collisions. The main difference to the previous section is that we now take into account that the jet can lose energy and momentum when interacting with the medium and thus decelerates. This also implies that the energy loss, $\mathrm{d}E/\mathrm{d}x$, is not constant and changes in time. We also allow the deflection of the jet. The exact mechanism strongly depends, however, on the interaction strength with the medium which is characterized by the value of η/s.

Although the JET scenario as well as the scenario with the decelerating jet are both characterized by their energy and momentum deposition, we expect differences in the final energy-density profile of the Mach cone. This is to be expected, since the decelerating jet is quenched due to the interaction with the medium. In this section we address the issue whether this natural deceleration of the jet might change the final particle distribution in such a way that those strong contributions of head shock and diffusion wake become weaker or even vanish[28]. This would finally lead to the appearance of a double-peak structure.

The initial setup of the static system is equal to the one in Sec. 8.2, but we use a larger box size given by $L_x = L_y = L_z = 10$ fm. The method of calculating the cross section is also identical to the previous section. Moreover, we again use a $(2+1)$-dimensional setup. This is necessary in order to approach the almost perfect fluid limit,

---

[27]A jet is by definition a highly energetic particle whose energy is much larger than those of particles of the bulk medium.

[28]As discussed for the JET scenario in the previous section, the development of the head shock as well as the diffusion wake prevents the observation of a double-peak structure in the final azimuthal particle distribution.

because otherwise the computational time would be too large. This implies that the calculations done here are not directly comparable to those for a full (3+1)-dimensional setup.

8.3.1. The jet initialization and the issue with the test-particle method

In this work we have demonstrated that BAMPS is a very accurate relativistic Boltzmann solver with the distribution function locally represented by point-like particles. Using the test-particle method we ensure that we solve the rBE in a proper way. Thus, the test-particle method is of great necessity.

However, we encounter a problem when we initialize the bulk medium[29], but set a highly energetic particle on top, which should represent the jet. If we are interested in the effect of the medium on the jet only [244], then the test-particle number does not affect the numerical results. In our scenario, however, we are highly interested in the jet-medium interaction, i.e., we are interested in the effect of the medium on the jet and vice versa. Thus, the exact influence of the jet on the medium is lost when $N_{\text{test}} \neq 1$. The energy which the jet deposits in the medium is large if $N_{\text{test}} = 1$, but small if we choose $N_{\text{test}} = 100$, for instance. In the latter case, the effective energy deposition of the jet is reduced by 100 and thus does not correspond anymore to the scenario with $N_{\text{test}} = 1$.

In order to preserve the correct interaction between jet and medium, we have the possibility to rescale the jet energy, E_{jet}, for example. However, this is not the best way since the way how the momentum and the energy are transferred in each collision of a jet with $E_{\text{jet}} = 20$ GeV is not the same as for a rescaled jet with $E_{\text{jet}} = 2000$ GeV. Thus, we should not consider this scenario as a possible solution.

Another method is to rescale the number of jets by N_{test}. This implies that we do not have only one jet, but a jet bundle. Physically speaking, we still have only one jet, because if we divide the number of jets in the bundle by N_{test}, we again obtain a real physical jet. The advantage of this method is that we preserve the correct influence of the medium on the jet and vice versa[30], by multiplying the jet number with N_{test}.

The jet bundle is initialized within a small volume element characterized by $x_{\text{min}} = -0.53$ fm, $x_{\text{max}} = -0.07$ fm, $y_{\text{min}} = -0.2$ fm, $y_{\text{max}} = +0.2$ fm, $z_{\text{min}} = -5$ fm, and $z_{\text{max}} = +5$ fm. Concerning the cross section, we do not distinguish between medium and jet particles. The initial momenta of the jets are $p_x = E_{\text{jet}}$.

8.3.2. Transition from ideal to viscous Mach cones induced by decelerating jets

In Fig. 8.17, we show the results for the energy density as well the velocity profile for a jet with an initial energy and momentum of $p_x = E_{\text{jet}} = 20$ GeV. In the upper panel, we show the scenario for a small shear viscosity over entropy density ratio of $\eta/s = 0.01$. In the middle and the lower panel we consider the cases of $\eta/s = 0.1$ and 0.5, respectively. For the smallest value of η/s, a clear development of a shock front with a higher energy

---

[29]The medium in rest.

[30]In other words, rescaling the jet number by N_{test}, we represent the jet by a distribution function, which is physically correct, since we solve the rBE.
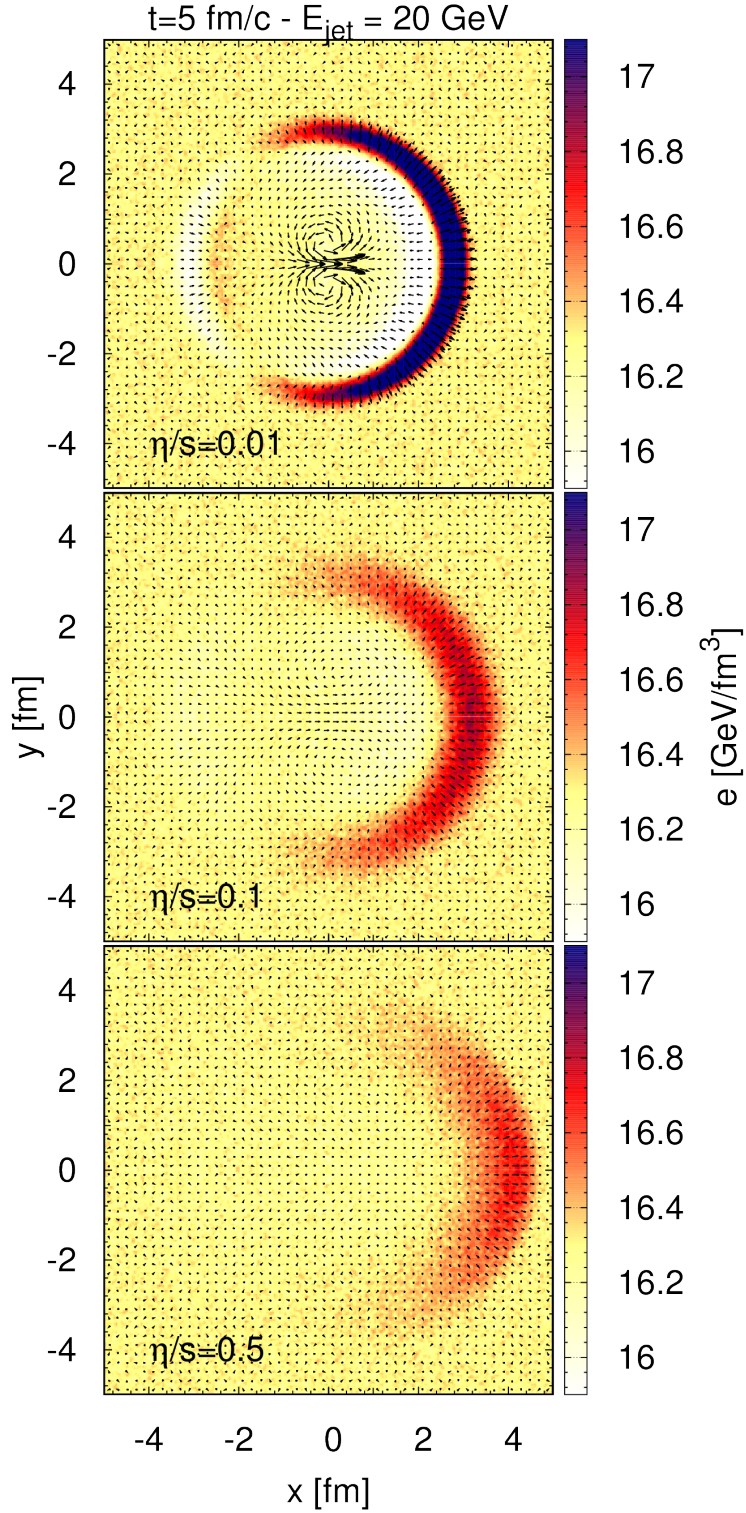
Figure 8.17.: Transition from ideal to viscous Mach cones induced by decelerating jets in a static medium. Depicted is the LRF energy density within a specific range. As an overlay we show the velocity profile as arrows with a scaled length arrow. We use a jet with an initial energy of $E_{\text{jet}} = 20$ GeV. The system size is $L_x = L_y = L_z = 10$ fm and we show a snapshot of the simulation at $t = 5$ fm$/c$ for different values of the shear viscosity over entropy density ratio, η/s.

density, which is strongly curved rather than conical can be observed. Furthermore we observe very characteristic velocity profiles. It is remarkable that strong vortices occur around $x = y = 0$ fm, while a diffusion wake and strong head shock are also visible. In the back as well as behind the shock front we observe a significantly lower energy-density region. All those effects result from the strong collective behavior of the medium[31].

The reason for this strongly curved structure of the shock front is perhaps due to the strong quenching of the jet and its deflection. A jet which interacts strongly with the medium reduces its energy in a very fast manner, which is demonstrated below. This energy reduction is commonly known as jet quenching [22, 24, 25, 26, 27, 28, 72, 245, 246, 247]. Due to the fact that the jet decelerates very fast it cannot punch through the matter. However, this changes when considering a jet with initially much larger energy. Then the scenario would approach the JET scenario discussed in Sec. 8.2.
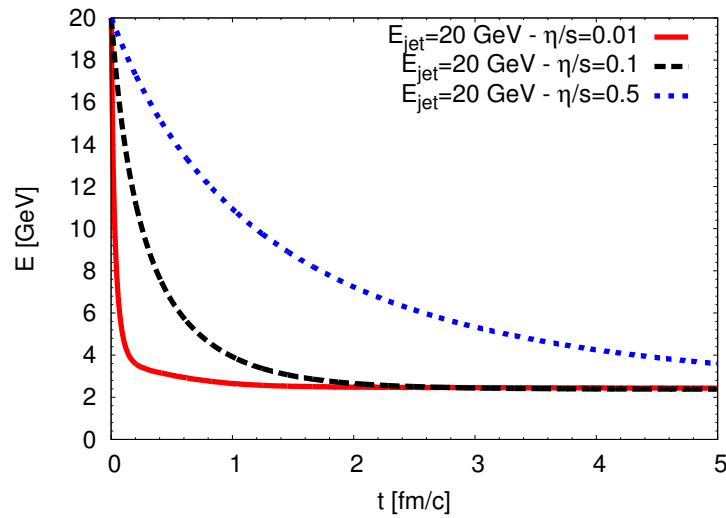
Figure 8.18.: Time evolution of the jet energy in a static medium at different values of the shear viscosity over entropy density ratio, η/s. The results are extracted from the scenarios shown in Fig. 8.17.

Increasing the value of η/s, as shown in the middle and lower panel of Fig. 8.17, an expected smearing out of the profile is observed. Features such as head shock, diffusion wake, and the vortices almost vanish. In case of $\eta/s = 0.5$, the shock front is more or less concentrated in the forward direction. However, although the diffusion wake disappears when increasing the value of η/s to even larger values, the head shock definitely persists, since the jet itself does not disappear. Moreover, we make an interesting observation: The velocity of the shock front moving through the matter in rest strongly depends on the strength of dissipation. The larger the dissipation is assumed, the faster the shock front is moving. This is to be expected, since the jet interaction with the medium is

---

[31]For jets with initially larger/lower energy the final profile would change. In case the jet has a significantly larger energy, the shock front would become more conical, because it can punch through the medium.

weaker at larger dissipation. Thus, the deceleration or quenching of the jet is smaller with larger values of η/s.
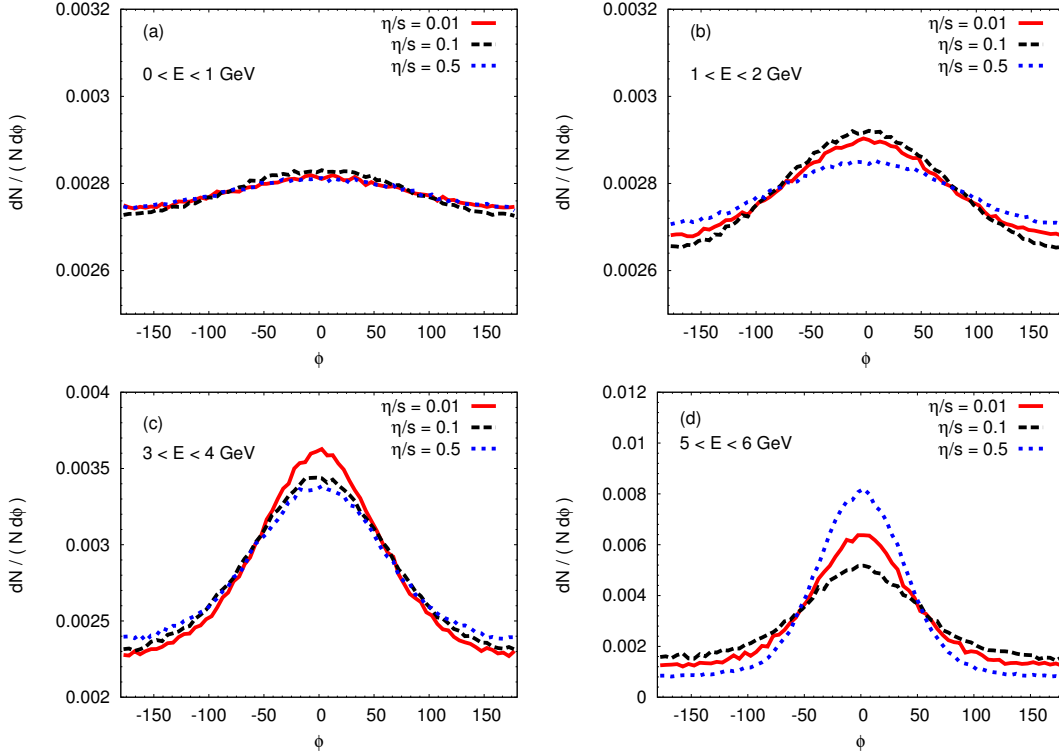
Figure 8.19.: Two-particle correlations, $\mathrm{d}N/(N\mathrm{d}\phi)$, extracted from BAMPS calculations for realistic jets as shown in Fig. 8.17. We show the results for several values of η/s in specific energy ranges.

A comparison to the JET scenario indicates that an influence of the medium on the decelerating jet is visible, which is the stronger the smaller the value of η/s is. The development of a head shock is more or less independent of whether the jet is quenched or not, while the diffusion wake disappears with increasing η/s.

In Fig. 8.18 we show the time evolution of the jet energy, E_{jet}, for three different values of the shear viscosity over entropy density ratio, η/s. As expected, the energy loss of the jet is the stronger the smaller η/s is chosen. For $\eta/s = 0.01$ the jet loses almost 80% of its initial energy within the first 0.2 fm/c. Afterwards the jet energy approaches the value $E_{\mathrm{jet}} = 2.2$ GeV at 5 fm/c, such that it can be considered as thermal. It is not a surprise that the jet does not approach the average kinetic energy of particles in the medium in rest given by $E = 3T = 1.2$ GeV, since a shock front with a higher energy density is created due to the jet-medium interaction. Particles in the shock-front region are characterized by a higher kinetic energy and thus the jet approximates the average kinetic energy of those particles. Furthermore, the region with lower energy density indicates that a huge amount of matter is pushed in the forward direction and increases the energy density on the shock front. This is the main

effect when considering jet-medium interaction: the jet influences the medium and vice versa.

With increasing viscosity the jet loses its energy more slowly. For $\eta/s = 0.1$ the jet energy is below $E_{\text{jet}} = 4$ GeV after 1 fm/c. Around $t = 5$ fm/c the jet energy is slightly below the final value for $\eta/s = 0.01$, but in principle on the same level. Finally, the jet energy in the case of $\eta/s = 0.5$ is just below $E_{\text{jet}} = 4$ GeV around $t = 5$ fm/c. This indicates that the jet has not yet thermalized at all.

8.3.3. Two-particle correlations
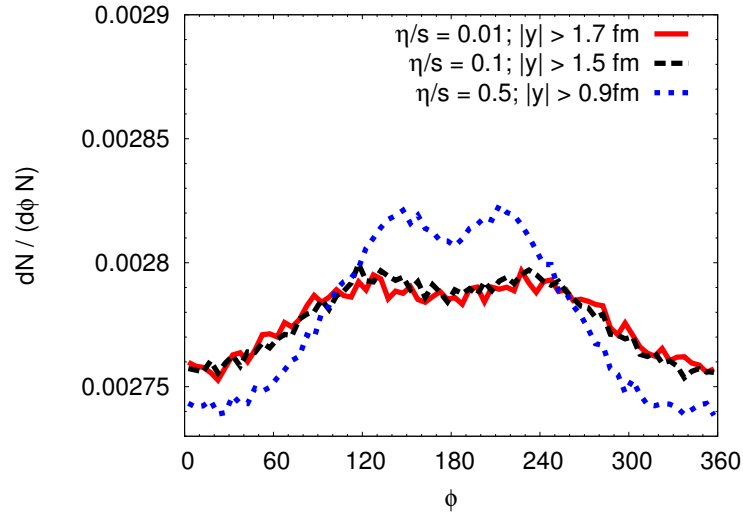
Figure 8.20.: Two-particle correlations, $\mathrm{d}N/(N\mathrm{d}\phi)$, with spatial cuts in the transverse y-direction extracted from BAMPS calculations for decelerating jets in a static box. The results are from the corresponding calculations in Fig. 8.17.

In the JET scenario discussed in Sec. 8.2.6 we have found that the double peak only appears when neglecting contributions originating from the head shock and the diffusion wake. In the following, we discuss the extracted two-particle correlations for the more realistic scenario including the natural deceleration of the jet. We address the question whether this scenario gives rise to a double-peak structure in the final distribution.

In Fig. 8.19, we show the normalized azimuthal particle distribution, $\mathrm{d}N/(N\mathrm{d}\phi)$, for several values of η/s and energy ranges. Figure 8.19a shows the distribution for the very low energy region, $E = 0$ to 1 GeV. In Figs. 8.19b, 8.19c, and 8.19d, we systematically neglect particles from the bulk medium and go to higher energy regions, since we know that the contribution for a double-peak structure originates more or less from highly energetic particles, as we have demonstrated in Sec. 8.1. Although the jet decelerates due to the natural interaction with the bulk medium, the contribution from the head shock and the diffusion wake are still too strong such that only a peak at $\phi = 0°$ builds

up. On the other hand, for the cases of larger values of η/s the diffusion wake vanishes, as discussed above and shown in Fig. 8.17, but a strongly shaped head shock in the x-direction still exists. Thus, the highly energetic particles mostly propagate in the x-direction and the double peak does not appear.

In order to obtain a double-peak structure, we have to perform spatial cuts in transverse y-direction, as shown in Fig. 8.20. As to be expected, if we apply those spatial cuts we observe a double-peak structure which originally is mainly overshadowed by the contribution of the head shock and/or the diffusion wake. Our findings are similar to those obtained in Fig. 8.15 where the JET scenario was considered.

The results in this section indicate that the scenario of a decelerating and quenched jet is not enough in order to obtain a double-peak structure. The origin of this failure is, similar to the JET scenario, the strong energy and momentum deposition of the jet, which induces the development of a head shock and diffusion wake. So far, our findings confirm previous studies in Refs. [50, 119, 124, 240, 248, 249, 250], where it was also claimed that the strong momentum deposition of a jet or projectile prevents the appearance of a double-peak structure.

8.4. Investigation of Mach cones in relativistic HIC

In this section we study the evolution of Mach cones induced by highly-energetic jets[32] in a fully $(3 + 1)$-dimensional system of relativistic HIC. The obvious difference compared to the previous sections is the longitudinal and transverse expansion. We address the question whether the longitudinal and transverse expansion of the system affects the final pattern of the jet-induced Mach cone as well as its corresponding particle distribution.

As discussed in Ref. [30], the flow-velocity profile created by jets in the transverse plane interacts with the radial flow of the background medium. This, for instance, changes the effective angle of a Mach cone. Motivated by the work in Ref. [30] the effect of transverse expansion to Mach cones has been also studied in Refs. [50, 51]. It was found that a double-peak structure can be created by averaging over different jet paths in the medium created in HIC. Some of these jets create Mach cones which propagate into the opposite direction to the radial flow. The interplay between radial flow and jets reduces the strong contribution of the diffusion wake and head shock and results in a double-peak structure. However, a much larger contribution to a double-peak structure originates from distorted jet-induced Mach cones which traverse the medium on different paths not in opposite direction to the radial flow. Those jets are then deflected by the radial flow and their superposition leads to the observation of a double-peak structure.

In the following, we investigate a similar setup as discussed in Refs. [50,51]. We focus on the investigation of the effect of the radial flow on the pattern of jet-induced Mach cones and the corresponding final particle distribution [37]. We neglect such effects as initial fluctuations which are relevant for heavy-ion collisions. We further study the influence of the shear viscosity over entropy density ratio, η/s, on the final results.

---

[32] as introduced in Sec. 8.3

8.4.1. Numerical setup

We use the framework of BAMPS in a fully $(3 + 1)$-dimensional setup designed for ultrarelativistic heavy-ion collisions introduced in Sec. 6.2. Similar to the previous sections we use a massless gas of gluon particles[33], with the degeneracy factor $g = 16$, and consider only binary collisions with an isotropic cross section, i.e., a cross section with an isotropic distribution of the collision angle. Furthermore, as introduced in Sec. 6.4 we perform the numerical calculations using a constant value of the shear viscosity over entropy density ratio, η/s.

In the following, we consider the mid-rapidity region [21] when extracting the hydrodynamic quantities as well as the azimuthal particle distribution. Thus, we introduce the space-time rapidity,

$$\eta_{\text{rap}} = \frac{1}{2} \ln \frac{t + z}{t - z} , \tag{8.15}$$

and momentum rapidity,

$$y_{\text{rap}} = \frac{1}{2} \ln \frac{E + p_z}{E - p_z} . \tag{8.16}$$

Here, t denotes the laboratory time of each particle, while E and p_z are the energy and longitudinal momentum, respectively. In the numerical analysis we consider only particles within a small space-time rapidity of $|\eta_{\text{rap}}| < 0.1$, i.e., the mid-rapidity region.

Since the parton cascade BAMPS has no effective hadronization process implemented yet, the final particle distribution is obtained by stopping the simulation at a certain time and extracting the hydrodynamic quantities as well as the two-particle correlations from the final gluon-momentum distribution.

Initial conditions

We use smoothed Glauber initial conditions for binary collisions only in the transverse direction [48, 49]. For this study we want to focus on the impact of the longitudinal and radial flow on the jet only and thus we neglect additional effects like local density fluctuations. The Gaussian momentum-rapidity distribution resembles the experimental observation at RHIC where it was found that the rapidity distribution of charged hadrons is nearly Gaussian [251]. On the other hand we use a simple estimate of the width of the nuclear overlap region at the point of the impact, based on the Lorentz-contracted nuclear thickness. In this case, it is simple to use a Gaussian distribution for the longitudinal z-direction as well[34]. For the high-p_T region we use a power law, which approximately fits the $p + p$ data [252, 253]. Thus, for the initial non-thermal single-particle distribution function we apply the following parametrization[35],

$$f(\vec{x}, \vec{p}) = K \frac{1}{E} \left(\frac{Q^n}{Q^n + p_T^n} \right)^m \exp\left(-\frac{y_{\text{rap}}^2}{\sigma_y^2} \right) \exp\left(-\frac{z^2}{\sigma_z^2} \right) T_{\text{A}} \left(x + \frac{b}{2}, y \right) T_{\text{B}} \left(x - \frac{b}{2}, y \right) . \tag{8.17}$$

_____

[33]We treat them as classical Boltzmann particles.

[34]Note that for a strictly boost-invariant system the width is zero at $t = 0$. Instead of forcing boost invariance onto the system, we initialize with a finite width. The system will behave after a certain time boost-invariant near $z = 0$, which has been checked.

[35]This parametrization has been provided by H. Niemi.

where $p_T = \sqrt{p_x^2 + p_y^2}$ denotes the transverse momentum and b is the impact parameter. We have introduced the nuclear thickness function [48],

$$T_A(x, y) = \int_{-\infty}^{+\infty} dz \rho_A(x, y, z), \tag{8.18}$$

which has to be integrated in z-direction, and $\rho_A(\vec{x})$ denotes the Woods-Saxon distribution for the nucleus A,

$$\rho_A(\vec{x}) = \frac{\rho_0}{1 + \exp\left(\frac{|\vec{x}| - R_A}{D}\right)}, \tag{8.19}$$

with

$$R_A = 1.12 A^{1/3} - 0.86 A^{-1/3} \tag{8.20}$$

and the mean density of the nucleus of $\rho_0 = 0.17\,\mathrm{fm}^{-3}$. For the thickness parameter we use $D = 0.54$ fm. We exclusively use a gold nucleus with a mass number of $A = B = 197$. Furthermore, we choose $Q = 1.3\,\mathrm{GeV}$, $n = 4$, $m = 1.5$, $\sigma_y = 1$, $\sigma_z = 0.13\,\mathrm{fm}$, and $K = 0.0135$. Moreover, we consider only central collisions, i.e., $b = 0$ fm, which results in neglecting effects originating from elliptic flow, v_2, or higher harmonics. The above parameters are chosen to approximate the energy densities of $\mathrm{Au} + \mathrm{Au}$ collisions at $\sqrt{s_{NN}} = 200$ GeV at RHIC [11, 48].

Jet initialization

In the following we investigate scenarios where the jet is set on top of the bulk medium. We restrict our studies and calculations to jets in the mid-rapidity region. We note that the jet interacts with the same cross section as the medium particles[36]. As introduced in Sec. 8.3.1 we use the test-particle method for the jet in order to preserve the correct jet-medium interaction[37].

Similar to the work of Refs. [50, 51] we initialize the starting points of the jet on a semi-circle displayed in Fig. 8.21 with a radius of $r = 4$ fm at mid-rapidity,

$$\vec{x}_{\mathrm{jet}} = r \begin{pmatrix} \cos \phi_{\mathrm{jet}} \\ \sin \phi_{\mathrm{jet}} \\ 0 \end{pmatrix}. \tag{8.21}$$

In the experiment back-to-back correlated jets are created due to momentum conservation. In this study we neglect the near-side jet contribution due to the assumption that the near-side jet escapes rapidly to the vacuum and thus only leads to a small contribution. In contrast, the away-side jet traverses the hot and dense medium of the collision and, depending on the value of η/s, it gets suppressed and deposits its energy to the medium.

Due to reasons of symmetry in central collisions the possible jet paths that need to be studied in the left panel of Fig. 8.21 reduces drastically, as shown in the right panel of

---

[36]When calculating the cross section we do not distinguish between jet and medium particles.
[37]The corresponding jet bundle is initialized in a small volume element.
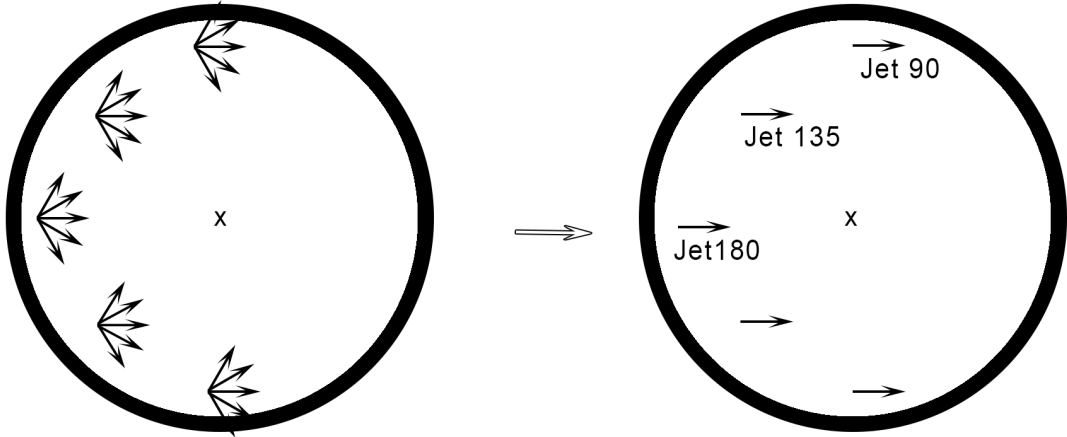
Figure 8.21.: Schematic representation of different jet paths on the semi circle, see also Refs. [50, 51]. The left panel shows all possible contributing paths, the right panel the reduced paths due to symmetry reasons, since we consider only central collisions, i.e., $b = 0$ fm.

Fig. 8.21. Initially, the jet has only momentum in the x-direction, i.e., $p_x = E_{\text{jet}} = 20$ GeV.

The extracted azimuthal particle distribution is equivalent to the two-particle correlation, since the propagation direction of the corresponding near-side jet is always the same. We note that the contribution of the background medium is a constant when considering central collisions only. Thus, contributions of the medium cancel out when inspecting the normalized particle distribution.

In the following we refer to three scenarios:

- **Scenario I**
  We consider a jet starting at a fixed-angle position of $\phi_{\text{jet}} = 180°$ on the semi circle. Here we investigate the contribution of the jet propagating in opposite direction to the radial flow.

- **Scenario II**
  We consider a jet starting at a fixed-angle position of $\phi_{\text{jet}} = 135°$ on the semi circle. Here we study the effects of deflection of the jet due to the radial flow.

- **Scenario III**
  We average over all possible angle positions, $\phi_{\text{jet}} = 90° - 270°$, of the jet on the semi circle.

8.4.2. Numerical results

Scenario I: Jet starting at a fixed-angle position of $\phi_{\text{jet}} = 180°$

In this particular case, the jet initially propagates in opposite direction to the radial flow generated in HIC. We perform calculations with different values of the shear viscosity

over entropy density ratio which reflect possible strengths for the medium interactions expected in HIC. In order to illustrate the results we show a time evolution of the LRF energy-density profile at mid-rapidity, $|\eta_{\mathrm{rap}}| < 0.1$, in Fig. 8.22. As an overlay we show the velocity profile as arrows with a scaled length arrow.

As to be expected, at early times, i.e., $t = 1$ fm/c, the energy density is very high in the central region of the transverse plane and decreases significantly at the edges. We also observe the jet on top of the bulk medium, which for any value of η/s has not built up any Mach cone yet. However, for these early times the energy density of the medium behind the jet is significantly lower for the smallest value of $\eta/s = 0.08$, indicating that matter is pushed in forward direction of the jet. This effect is reduced with increasing value of η/s.

For later times the energy density has drastically decreased due to the longitudinal and the transverse expansion. In addition, a conical structure induced by the jet has developed at $t = 5$ fm/c for $\eta/s = 0.08$. In contrast, such a structure has not built up for larger values of η/s. The differences in the shape of the Mach cone for various η/s becomes more evident at later times, $t = 9$ fm/c and $t = 12$ fm/c. In case of $\eta/s = 0.08$, the energy density in the region of the developed shock front is increased due to the fact that matter is pushed in forward direction and contributes to the shock-front region of the Mach cone, while this is not the case for $\eta/s = 0.2$. On the other hand, the maximum energy density in the head shock region for $\eta/s = 0.2$ is smaller than for $\eta/s = 0.5$. This is to be expected, since the interaction of the jet with the medium is weak for $\eta/s = 0.5$, i.e., the jet is almost not quenched. Similar to the discussion in Sec. 8.3 we observe that the propagation speed of the shock front is faster for a smaller value of η/s.

The results in Fig. 8.22 indicate that a Mach cone can develop for a single jet propagating through the middle of the medium considering moderate values of η/s and a sufficiently large simulation time[38]. However, the shock front is strongly curved, which is due to the strong jet quenching. This has already been found in Sec. 8.3.

In Fig. 8.22 the diffusion wake is not visible because it is superimposed by radial flow of the background medium. This indicates that the contribution of the diffusion wake and head shock in the final particle distribution is possibly reduced by the radial flow, since the jet initially propagates in opposite direction to the radial flow. In contrast, after passing the center of the collision the radial flow broadens the jet-induced shock front region.

We show the extracted normalized azimuthal particle distribution, $\mathrm{d}N/(N\mathrm{d}\phi)$, in Fig. 8.23. Using different cuts in p_T we demonstrate that a double-peak structure develops for several regions of p_T, and a rather small value for the shear viscosity over entropy density ratio, η/s. For $\eta/s = 0.08$ and $0.5 < p_T < 1$ GeV a double-peak structure is observable and we suggest that the contribution of head shock and diffusion wake is indeed compensated by the radial flow and the contribution from the Mach cone wings show up. The peaks are approximately at $\phi \approx \pm 70°$. However, for larger transverse momentum, i.e., $3 < p_T < 4$ GeV, and for $\eta/s = 0.08$ and 0.2 the double-peak structure appears but the peaks are approximately at $\phi \approx \pm 120°$. In this case we suggest that this contribution comes from the region of the diffusion wake,

---

[38]See also the discussion in Sec. 7.1.5.
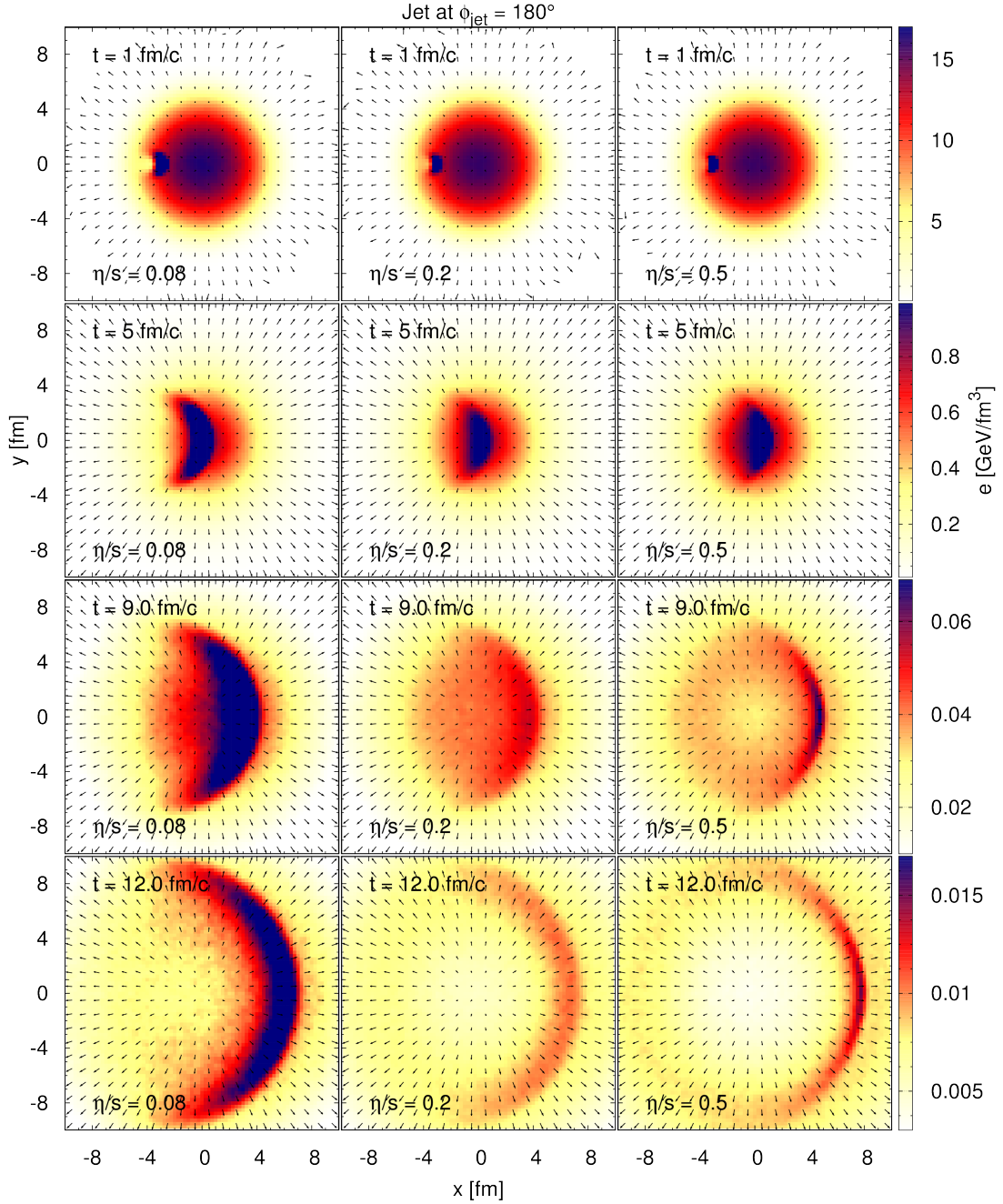
Figure 8.22.: Time evolution of a Mach cone in central HIC. We show the LRF energy density within a specific range at mid-rapidity, i.e., $|\eta_{\mathrm{rap}}| < 0.1$. As an overlay we show the velocity profile as arrows with a scaled length arrow. The results are depicted at different time steps and for different values of the shear viscosity over entropy density ratio, η/s. The jet is initialized at fixed-angle position of $\phi_{\mathrm{jet}} = 180°$ on the semi circle. The initial momentum is $p_x = E_{\mathrm{jet}} = 20$ GeV.

Figure 8.23.: Two-particle correlations, $\mathrm{d}N/(N\mathrm{d}\phi)$, extracted from BAMPS calculations using several values of η/s as shown in Fig. 8.22. The jet is initialized at fixed-angle position of $\phi_{\mathrm{jet}} = 180°$ on the semi circle. The results are shown for several regions of p_T and at fixed time $t = 12$ fm/c.

where matter flows into the region of lower pressure and energy density. Finally, the head-shock contribution for $\eta/s = 0.5$ is very strong and not reduced by the radial flow. The head-shock region contains particles which are mostly forward peaked and superimposes a possible double-peak structure.

A significantly stronger jet, i.e., a jet with initially much larger energy, would induce a stronger head shock and diffusion wake which cannot be reduced by the radial flow. This prevents the observation of a double-peak structure in this specific scenario. However, if the jet energy was too small no significant pattern of a Mach cone would develop due to the strong radial flow in opposite direction.

Scenario II: Jet starting at a fixed-angle position of $\phi_{\mathrm{jet}} = 135°$

In this scenario the jet starts at fixed-angle position of $\phi_{\mathrm{jet}} = 135°$ on the semi circle. The chosen value serves as an exemplary case for a possible jet deflection by radial flow. We perform calculations for different values of the shear viscosity over entropy density ratio, η/s, and show the corresponding time evolution in Fig. 8.24. We observe that due to the chosen position on the semi circle, the signal of a Mach cone is very weak for small values of η/s. A comparison to **scenario I** shows a significantly lower energy
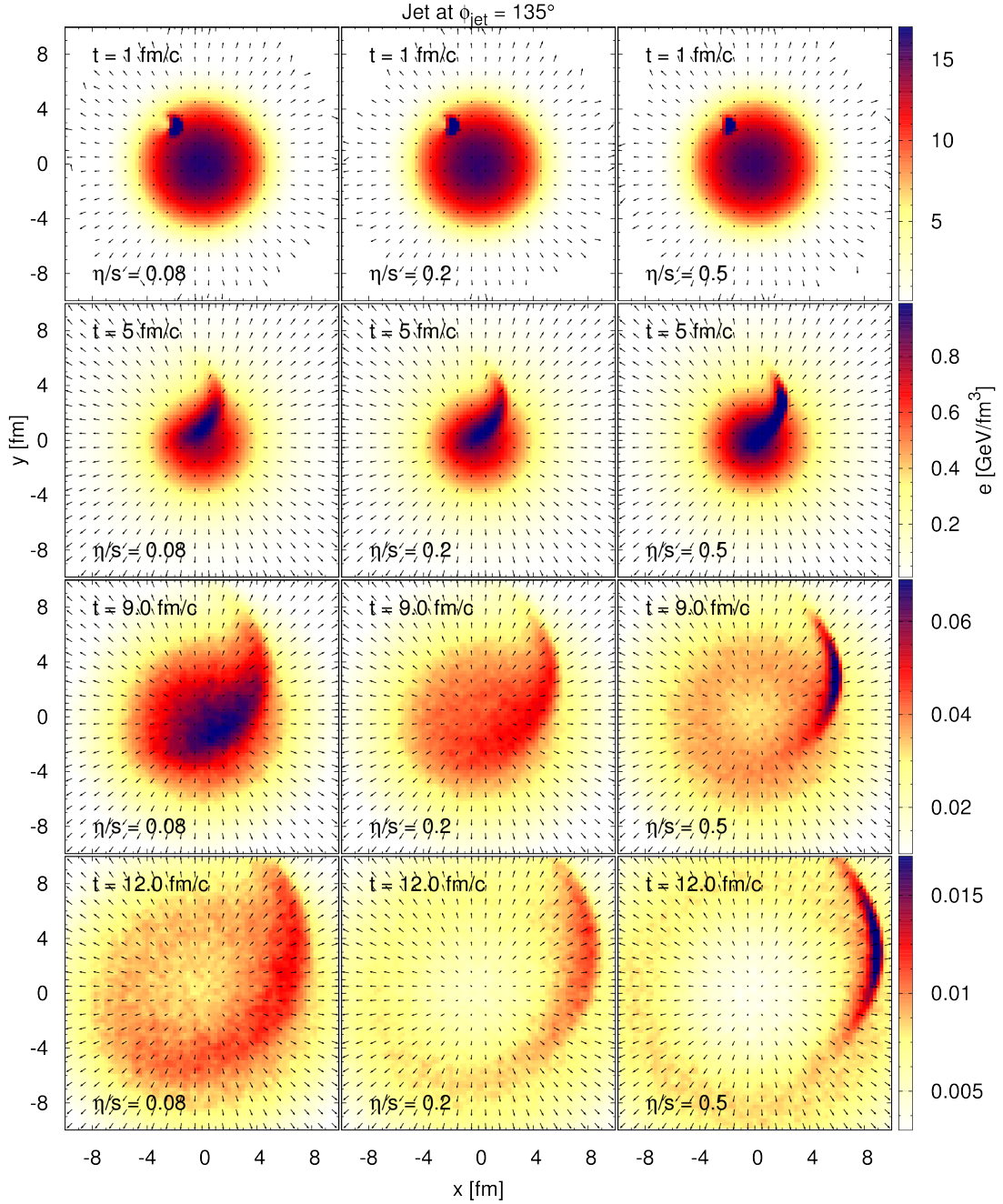
Figure 8.24.: Time evolution of a Mach cone in central HIC. We show the LRF energy density within a specific range at mid-rapidity, i.e., $|\eta_{rap}| < 0.1$. As an overlay we show the velocity profile as arrows with a scaled length arrow. The results are depicted at different time steps and for different values of the shear viscosity over entropy density ratio, η/s. The jet is initialized at fixed-angle position of $\phi_{jet} = 135°$ on the semi circle. The initial momentum is $p_x = E_{jet} = 20$ GeV.

density in the shock-front region for $\eta/s = 0.08$. Furthermore, due to the strong radial flow the jet is deflected and results in a distorted shock-front region. On the other hand, the deflection of the jet becomes weak for large η/s. This is to be expected, since the jet interacts weakly with the medium for $\eta/s = 0.5$ and keeps its initial propagation direction.

A direct comparison to **scenario I** indicates that the jet traverses a significantly lower energy-density region because of the different initial starting position. This implies that the mean free path of the jet in **scenario II** is larger than in **scenario I** which results in a reduced jet quenching. However, the value of $\eta/s = 0.08$ is still large enough to generate a collective behavior. The strong radial flow leads to a strongly distorted Mach cone pattern. In contrast, the shape of the jet-induced shock front is almost not affected for $\eta/s = 0.5$ and leads to only a large head-shock width.

Figure 8.25.: Two-particle correlations, $\mathrm{d}N/(N\mathrm{d}\phi)$, extracted from BAMPS calculations using several values of η/s as shown in Fig. 8.24. The jet is initialized at fixed-angle position of $\phi_\mathrm{jet} = 135°$ on the semi circle. The results are shown for several regions of p_T and at fixed time $t = 12$ fm/c.

Our observations indicate that, comparing **scenario I** and **scenario II**, the generated diffusion wake and head shock are less compensated by the radial flow in **scenario II** since the jet does not propagate in exactly opposite direction to the radial flow. The deflection of the jet for $\eta/s = 0.08$ leads to only one peak in the two-particle correlations, as displayed in Fig. 8.25. This peak originates from the head-shock region and

diffusion wake of the distorted Mach cone and becomes sharper and more obvious when going to higher p_T. Furthermore, we observe that the position of the peak changes with viscosity. The larger the value of η/s the smaller the angle, which reflects the fact that for larger η/s the jet is less deflected.

Although we observe only one peak in the two-particle correlations in this specific scenario, a double-peak structure is possible when considering in addition a second event with a jet starting at $\phi_{\text{jet}} = 225°$ on the semi circle. Summing up both contributions from the jets at initial positions $\phi_{\text{jet}} = 135°$ and $\phi_{\text{jet}} = 225°$, a double-peak structure resulting from those deflected jets is not unlikely [50, 51, 250, 254, 255]. Such a case occurs in the subsequent **scenario III** where we average over many jet events with different starting positions on the semi circle.

In order to understand this possible superposition of two jets in two events, we consider the simple model we derived in Sec. 8.1. Instead of two sources of the Mach-cone wings we now consider two deflected jet-induced Mach cones with the head shock and diffusion wake as the sources contributing to the final particle distribution. If the head shock and diffusion wake induced by the jets are sufficiently strong, i.e., the collective velocity of matter is sufficiently large, they may lead to a double-peak structure. However, the initial jet energy cannot be too large in order to observe a double-peak structure. Stronger jets punch through the medium resulting in less deflection. This finally leads to one peak in the two-particle correlations only. The jets cannot be too weak as well, since then the head-shock contribution cannot generate strong sufficient flow which is important to obtain a double-peak structure.

Scenario III: Jet at random-angle position, i.e., $\phi_{\text{jet}} = 90° - 270°$

In this scenario we average over all possible jets with randomly chosen starting positions on the semi circle, i.e., $\phi_{\text{jet}} = 90° - 270°$. **Scenario III** gets closest to the experimental situation as many different events are considered, in contrast to **scenario I** and **scenario II**. As shown in Fig. 8.26 we calculate the normalized azimuthal particle distribution for several p_T-cuts. The figure demonstrates that a double-peak structure appears for sufficiently high p_T and low η/s. The peaks are approximately at $\phi \approx 50°$. As shown in Fig. 8.26c, a double-peak structure appears for $\eta/s = 0.08$ but not for $\eta/s = 0.2$. Only for $p_T = 3 - 4$ GeV, as demonstrated in Fig. 8.26d, the double-peak structure also appears for the larger $\eta/s = 0.2$. However, for $\eta/s = 0.5$ there is no double-peak structure even for $p_T = 3 - 4$ GeV.

8.4.3. Further discussion and conclusion

The results obtained in this section provide evidence that Mach cones may form if the viscosity over entropy density ratio, η/s, is small enough. However, the pattern of the Mach cone is less conical but strongly curved resulting from jet quenching. In case the propagating jet is deflected due to radial flow, the shape of the induced Mach cone is distorted. The numerical calculations demonstrated that the radial flow occurring in HIC affects the final pattern of the Mach cone [30] and the final particle distribution as well. However, already the studies in a static medium reveal a lot information about the evolution of Mach cones. These studies are absolutely necessary in order to understand
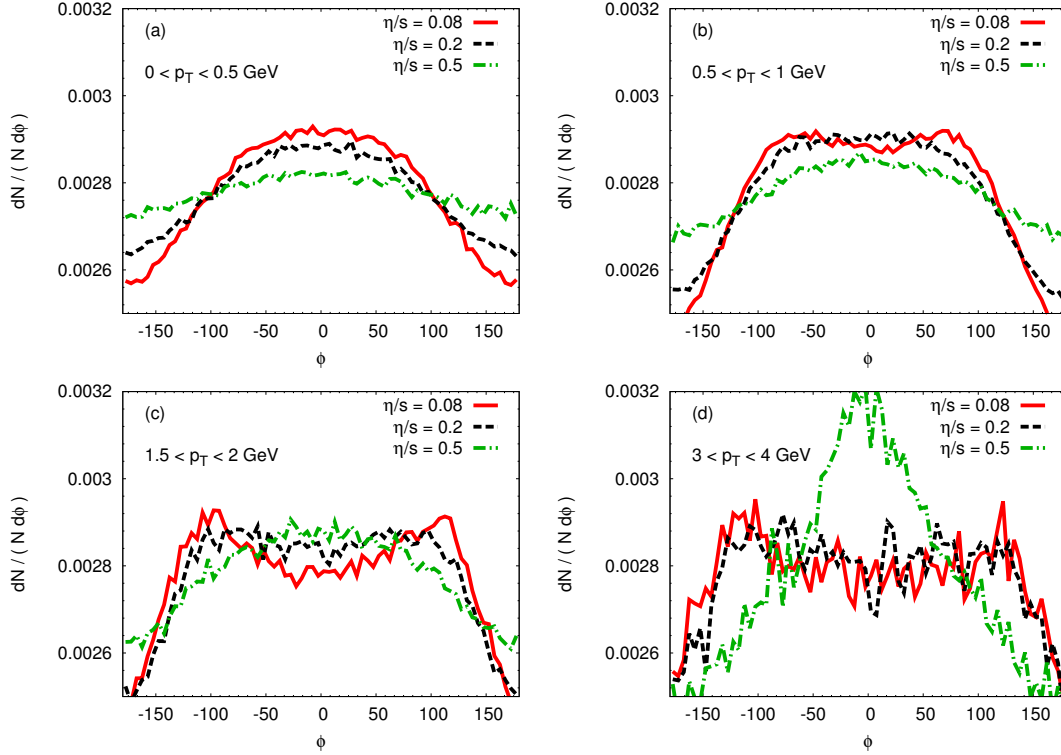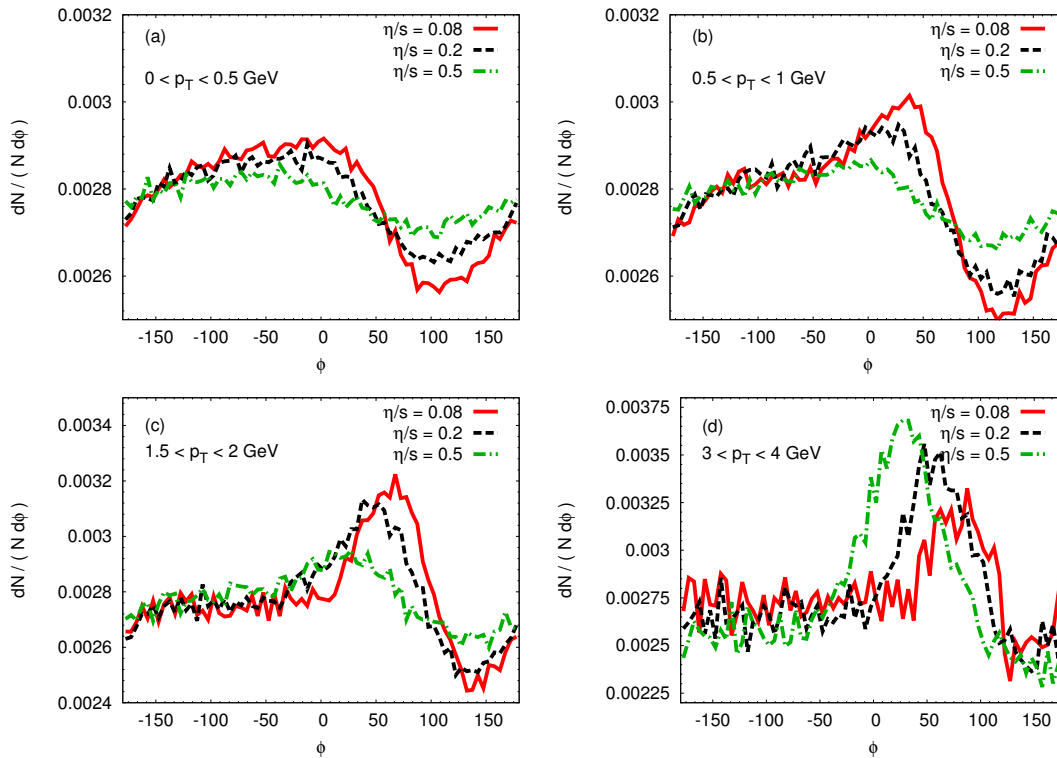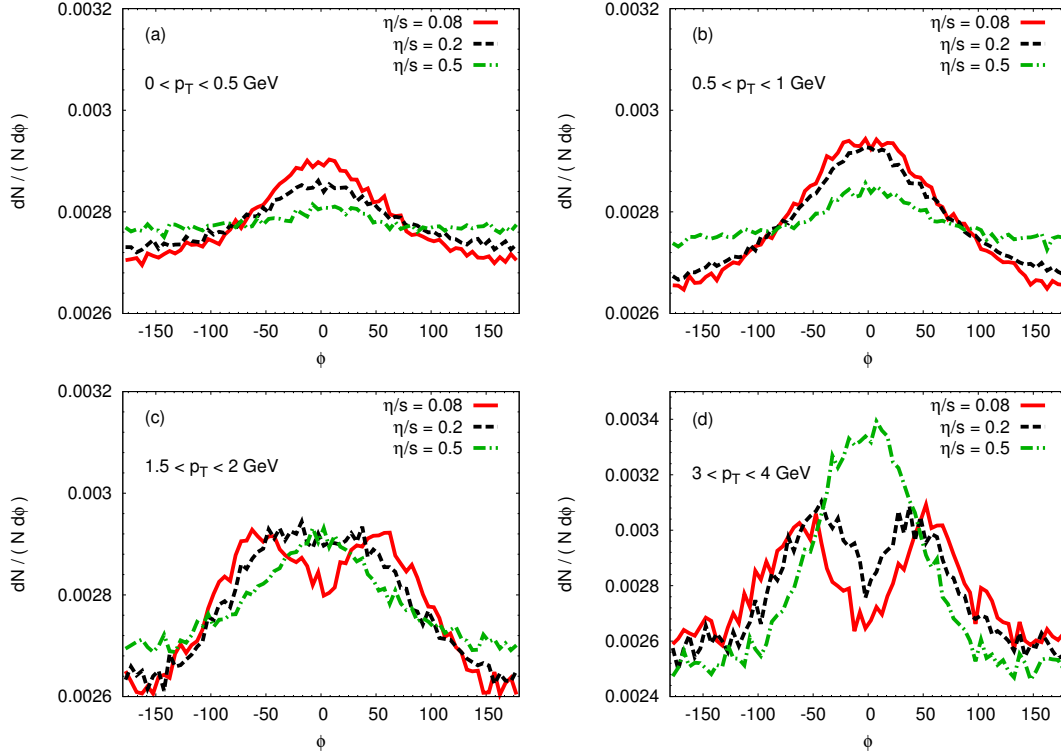
Figure 8.26.: Two-particle correlations, $dN/(Nd\phi)$, extracted from BAMPS calculations using several values of η/s. We consider all starting positions of the jet on the semi circle. The results are shown for several regions of p_T and at fixed time $t = 12$ fm/c.

the origin and properties of Mach cones itself.

Considering a single jet event for a sufficiently small value of $\eta/s = 0.08$ we have demonstrated that the interplay of jet-induced Mach cones and radial flow may lead to a double-peak structure, as shown in **scenario I**. In this scenario when considering only particles from the low-momentum region the contribution for the double-peak structure originates from the Mach-cone wings and appears only because the contribution of head shock and diffusion wake is superimposed by the radial flow. Additionally, a double-peak structure from a single jet event not traversing the medium in opposite direction to the radial flow shown in **scenario II** does not appear. In this scenario the jet is deflected by radial flow. This deflection leads to only one peak in the two-particle correlations. However, **scenario III** provides an average over many possible jet paths originating from different starting positions and is thus a superposition of many different cases of **scenario I+II**. In this scenario a double-peak structure appears and is generated mostly from the superposition of many deflected and distorted jet-induced Mach cones. The origin for the double-peak structure are not the wings of the Mach cone but the deflected head shock and diffusion wake of the distorted Mach cones [50, 51, 250].

We have demonstrated that a sufficiently large value of η/s tends to destroy the char-

acteristic shape of a Mach cone and a possible double-peak structure. The Mach cone eventually disappears in the single jet event in **scenario I** when increasing the shear viscosity over entropy density ratio to $\eta/s = 0.5$. This happens also for the double-peak structure. The reason is that the diffusion wake and head-shock contribution are not canceled anymore by the radial flow. The same is also true for **scenario III**, where the larger dissipation reduces the deflection of the jets and leads to the disappearance of the double-peak structure. However, not only the viscosity tends to destroy the double-peak structure, but also the strength of the jet. A jet with much larger initial energy punches through the medium and the effect of the radial flow weakens. In **scenario I** the diffusion wake and head-shock contribution would overshadow the double-peak structure, while in **scenario III** most of the jets would get less deflected. A jet with a too small initial energy would also not lead to a double-peak structure. In **scenario I** no Mach cone would develop since the jet is too weak to survive the radial flow, while in **scenario III** the head shock of the jet reaches not enough collective flow to provide a sufficiently strong signal for the double-peak structure.

Our findings imply that the influence of the radial flow is the most important requirement for the observation of a double-peak structure in the jet scenarios we have considered here because in a static system the double-peak structure was overshadowed by head shock and diffusion wake when considering jets with energy and momentum deposition. The importance of the radial flow is thus reflected in the effects of dissipation and initial jet energy. A large dissipation and/or large initial jet energy lead finally to a smaller influence of the radial flow.

The effect of longitudinal flow is studied here in a qualitative way, which was not considered in Refs. [50, 51]. We can conclude that the longitudinal flow does not affect the main results in a significant way.

The Mach-cone angle extracted from two-particle correlations is definitely not connected to the EoS [30]. **Scenario III** provides evidence that the contribution of this double-peak structure originates mostly from deflected jet-induced head shocks of Mach cones. In order to extract the Mach angle we would require a single jet event as shown in **scenario I**. However, this seems to be a difficult task experimentally.

In conclusion, the naive picture that only the Mach-cone wings only generate the double-peak structure is definitely not supported by our calculations. The diffusion wake and head-shock contribution originating from deflected jets inducing distorted Mach cones provide a much larger contribution to the double-peak structure. Although initial-state fluctuations should provide definitely a much larger contribution to the double-peak structure [15, 31, 32, 135, 239], the jet-medium interaction should not be neglected.

Although Mach cones should exist in HIC, we like to point out that the double-peak structure is definitely not the appropriate observable for the signal of Mach cones. This already became clear when studying the jet-medium interaction in static systems, since Mach cones were observed but a double-peak structure was not always visible. However, the studies obtained in this work revealed a lot information about the evolution and properties of a Mach cone. We investigated the effects of nonzero viscosity and different energy-deposition scenarios on the final pattern of the Mach cone.

In this study have neglected fluctuating initial conditions, the influence of a nonzero impact parameter and a reasonable hadronization process. It remains a future task to

include these effects in order to gain a better understanding of the experimental signal of the double-peak structure.

9. Summary and conclusions

9.1. Summary and conclusions

The purpose of this work was to study the formation and evolution of relativistic shock waves and Mach cones in viscous matter using a relativistic kinetic transport model. The microscopic transport model BAMPS (**B**oltzmann **A**pproach To **M**ulti-**P**arton **S**cattering) solves the relativistic Boltzmann equation (rBE), hence a complete transition from ideal to viscous shock-wave phenomena can be studied. We studied shock-wave formation in a simplified (1+1)-dimensional setup as well as Mach-cone formation induced by supersonic projectiles and/or jets in $(2+1)$- and $(3+1)$-dimensional static and expanding systems. We further addressed the question whether the jet-medium interaction resulting in Mach cones can contribute to a double-peak structure observed in two-particle correlations of heavy-ion collision experiments. Furthermore, BAMPS was used as a benchmark to compare with several hydrodynamic theories in order to verify their accuracy and find their limitations. This work is based on several publications [33, 34, 35, 36, 37, 38].

In Chapter 2 we gave a general introduction of the basic features and the phase diagram of Quantum Chromodynamics (QCD). Afterwards, we discussed the space-time evolution of matter in heavy-ion collisions (HIC) and discussed the possible existence of a new phase of matter, the quark-gluon plasma (QGP), created in recent HIC experiments. We then continued with the description of different probes and observables of the QGP which indicate that the QGP behaves as a nearly perfect fluid and that highly-energetic jets traversing the medium are suppressed. Both signalize the existence of shock waves in form of Mach cones. Furthermore, possible contributions to the double-peak structure observed in two-particle correlations were briefly introduced.

In Chapter 3 we have introduced the rBE in kinetic theory and subsequently reviewed the standard derivation of relativistic hydrodynamics. We started with the description of ideal hydrodynamics and continued with the framework of relativistic dissipative hydrodynamics. This chapter includes the discussion and interpretation of the fundamental dissipative quantities and reference frames in one- and multi-component systems used frequently in this work. Afterwards, the derivation of dissipative hydrodynamics from kinetic theory was briefly reviewed. We introduced the traditional first-order theory of Navier and Stokes, the second-order theory of Israel and Stewart (IS) and subsequently the recently derived theory named RTRFD (Resummed Transient Relativistic Fluid Dynamics).

Chapter 4 has provided an overview of the general definitions of sound waves and shock waves assuming a perfect fluid. We discussed the appearance of conical shock structures, such as Mach cones, caused by moving supersonic perturbations. We further discussed for larger perturbations, i.e., the perturbation emits shock waves, the Mach-angle dependence. Finally, we gave a short theoretical description of a shock

discontinuity.

In Chapter 5 we have introduced the relativistic Riemann problem (rRP) in the perfect-fluid limit. Its solution was used to test the accuracy of the microscopic transport model BAMPS and fluid-dynamical solver vSHASTA in the perfect-fluid limit. The rRP deals with the determination of the temporal evolution of a perfect fluid which initially has a sharp discontinuity in velocity or other thermodynamic variables. The initial discontinuity leads to the appearance of a shock wave and rarefaction wave. We discussed in detail the analytical solution of the shock-tube problem for a simple EoS and assuming that the velocities on both sides of the discontinuity are zero initially.

Chapter 6 provides a detailed overview of the microscopic transport model BAMPS, which is based on the stochastic interpretation of collision rates and used throughout this work when computing the solutions of shock waves based on kinetic modeling. We showed the details of this numerical model and discussed the differences to models based on the geometrical method. We also introduced the implementation of different cross sections and the extraction of the hydrodynamical quantities which are necessary for the proper understanding and discussion of the results.

The main results of this thesis are elaborated in two chapters. Chapter 7 deals with the investigation of shock-wave phenomena in various scenarios in a simplified $(1+1)$-dimensional setup, while in Chapter 8 we focused on the study and evolution of Mach cones in a $(2+1)$- and $(3+1)$-dimensional framework. The numerical solution of the rBE in kinetic theory were performed numerically by BAMPS while the different theories of relativistic dissipative fluid dynamics were solved numerically by the vSHASTA method introduced in Appendix D.

9.1.1. Investigation of shock-wave phenomena in kinetic theory and viscous hydrodynamics

In Chapter 7 we have started the investigation of relativistic shock waves in dissipative matter with non-zero shear viscosity and heat conductivity by solving the relativistic Riemann problem in the ultrarelativistic limit using isotropic and binary collisions only. We used BAMPS to solve the rBE, while the fluid-dynamical approach is based on IS theory and was solved numerically by the vSHASTA method. It was demonstrated that both approaches reproduce the analytic solutions of the rRP in the perfect-fluid limit and the numerical results converge when the numerical resolution is sufficiently high. This implies that further numerical solutions of BAMPS are trustworthy also for the viscous solutions of shock waves. By adjusting the shear viscosity over entropy density ratio, η/s, the transition from the ideal-fluid limit to free-streaming was demonstrated. Henceforth, instead of a discontinuous shock front, a contact discontinuity, and sharp rarefaction tails, we obtain continuously changing profiles, i.e., dissipation leads to the smoothening and broadening of these characteristic structures. For cases when the viscosity is small, the agreement between the rBE and IS theory is excellent. As the viscosity increases the agreement between the two different approaches starts to deteriorate. For even larger values of the η/s ratio, IS theory develops discontinuities which survive even after long times. We argued that part of this discrepancy can be understood to result from the inapplicability of IS theory for large Knudsen numbers. Furthermore, we also realized that the IS theory is unable to describe heat flow even

for very small Knudsen numbers, which shows the limits of this theory based on 14-dissipative fields. We also showed that a quantitative analysis in terms of an average Knudsen number is possible and it gives a good measure for the applicability of the IS theory. We found that for $Kn_e < 1/2$ the relative difference between kinetic theory and IS theory is less than ~ 10 %. In the following sections we further inspected the time evolution of shock waves in the weak and strong limits and discussed in detail the solutions. We found that shock waves need a certain time to develop. We also found a scaling behavior which can be expressed in terms of the Knudsen number. Furthermore, in a simplified study we also showed that the formation of shock waves in gluon matter with $\eta/s > 0.2$ probably takes longer than the lifetime of the QGP in HIC at RHIC energies.

The excellent performance of BAMPS motivated to study the evolution of the rRP using different properties of the matter. First we studied the effect of inelastic processes which turned out to affect the chemical equilibration in the system. Afterwards, we solved the rRP for a gas of massive particles which among others allowed the inspection of the bulk viscous pressure. Finally, multicomponent systems were investigated using two massless particles species with various cross sections.

In the following sections we modified the setup in order to investigate the heat-flow problem as encountered before when applying the IS theory to the solutions of the rRP. We compared the equations of motion of RTRFD at various levels of approximation with BAMPS for two different types of initial conditions. By a careful comparison with numerical solutions of the microscopic theory, we have demonstrated that this new formalism is able to handle problems with strong initial gradients in pressure or particle-number density. Furthermore, it provides not only the correct values for the shear-viscosity and heat-conduction coefficients, but also for the transport coefficients that couple the respective dissipative currents. The improvements are established by including higher moments and, thus, RTRFD resolved the previously observed differences between the solution of the IS theory and the rBE.

In order to inspect the shock-front region in more detail we studied the shock front in its rest frame using thermal reservoirs. This allowed a stationary solution and confirmed that the width of the shock front is proportional to a microscopic length scale of the system, like the mean free path of particles. This setup also enabled the detailed comparison of BAMPS to various approximations of RTRFD. The correct description of the shock-front region for large gradients by RTRFD failed when going to large velocities of the shock front. Hence, in contrast to our considerations on the heat flow, the inclusion of higher dynamical moments has no significant effect within this scenario, but we believe that the inclusion of higher-rank moments might improve RTRFD.

9.1.2. Investigation of Mach cones in a kinetic transport model

In Chapter 8 we turned to our studies of Mach cones. In order to understand the origin of the double-peak structure often connected with the naive picture of Mach-cone phenomena, we derived a simple model representing a Mach cone in a two-dimensional plane. We found that a double-peak structure does not always appear, but depends on the strength of the shock wave. Moreover, using special momentum cuts we also

found that the double-peak structure originates almost exclusively from the high-energy region of the distribution. Subsequently we investigated the structure of relativistic Mach cones by using the microscopic transport model BAMPS in a static $(2 + 1)$-dimensional system. The simulations were realized by using two different types of projectiles propagating through the matter, the PED and JET scenarios. The strength of the projectile-matter interaction was studied by varying the rate of energy dissipation from the projectile to the matter. Furthermore, the effect of viscosity of the matter was investigated by adjusting the shear viscosity over entropy density ratio, η/s.

We observed the formation of conical structures for both types of projectiles in the nearly perfect-fluid limit with the Mach-cone angle depending on the rate of energy dissipation. In the JET scenario we observed the development of a head shock and diffusion wake, while in the PED scenario an anti-diffusion wake but no head shock appeared. We also demonstrated that a non-vanishing viscosity tends to destroy the sharp conical structure. The larger the viscosity or equivalently the longer the time for development of the Mach cone, the more the structure depends on the details of the projectile-matter coupling. We also found a scaling behavior.

Although Mach cone-like structures are observed in BAMPS calculations for different energy- and momentum-deposition scenarios they are not necessarily associated with double-peak structures in the azimuthal particle distributions in $dN/(Nd\phi)$. We found that only the PED scenario together with a rather high rate of energy deposition leads to a double-peak structure, which otherwise cannot be observed because of the strong diffusion wake and head shock. However, the PED scenario has no equivalent in heavy-ion physics. On the other hand, the JET scenario is a simplified model but nevertheless demonstrates that a double-peak structure cannot be produced by jets with energy and momentum deposition, since the diffusion wake and head shock always overshadow the double-peak structure contribution of the Mach-cone wings.

In order to investigate the interplay between the jet and medium we used the same setup but replaced the projectiles with highly energetic jets, where the jet loses energy via scatterings within the medium. A Mach cone develops, but the shock front is strongly curved rather than conical due to jet quenching. We found that depending on the interaction strength between the medium and jet, the deceleration of the jet varies. We also inspected the azimuthal particle distributions in $dN/(Nd\phi)$ and found that the deceleration of the jet does not reduce the contribution of the head shock and diffusion wake. Similarly to the previously discussed JET scenario we argued that the contribution of head shock and diffusion wake overshadows the double-peak structure stemming from the Mach-cone wings.

Finally, we investigated the jet-induced Mach-cone formation and evolution in a $(3+1)$-dimensional expanding system in most central HIC, i.e., $b = 0$ fm, with smooth initial conditions. For small viscosities the formation of Mach cones is visible, while for large viscosities the initial sharp structures smear out and eventually vanish. The pattern of the Mach cone is less conical but strongly curved resulting from jet quenching. In case the propagating jet is deflected due to radial flow, the shape of the induced Mach cone is distorted.

The extracted azimuthal two-particle correlations shows a double-peak structure when the jet in a single event propagates in opposite direction to the radial flow. This suggests that in this specific scenario the contribution of the head shock and diffusion

wake is canceled by the radial flow. However, considering the superposition of many different jet paths, a double-peak structure appears. The double-peak structure in such cases originates mostly from a superposition of deflected jet-induced Mach cones with a contribution of head shock and diffusion wake. The observation of a double-peak structure in the single event as well as in the superposition of many jet paths is the strongest if the value for the shear viscosity over entropy density ratio is $\eta/s = 0.08$. Increasing the value of η/s tends to destroy the double-peak structure. For $\eta/s = 0.5$ the double-peak structure eventually vanishes.

Our results in more realistic scenarios indicate that the development of a double-peak structure induced by Mach cones requires an expanding system. However, the naive picture that the Mach-cone wings only generate the double-peak structure is definitely not supported by our calculations. The diffusion-wake and head-shock contribution originating from the superposition of deflected jets inducing distorted Mach cones has a much larger contribution to the double-peak structure. Although initial-state fluctuations should provide definitely a much larger contribution to the double-peak structure, the jet-medium interaction shown in this work should be not neglected. Mach cones might definitely exist in relativistic HIC, but we conclude that the double-peak structure is not the appropriate observable for the signal of Mach cones in heavy-ion collision experiments.

9.2. Outlook

The accurate solution of the rBE shown in this work allowed the detailed study of relativistic shock-wave phenomena in the fluid-dynamical regime and beyond starting from almost perfect-fluids to highly dissipative fluids. For the first time a complete transition from ideal to viscous shock waves was performed which enabled a detailed understanding of shock-wave phenomena.

This work made it possible to point out the limitations of current theories of relativistic dissipative hydrodynamics not only qualitatively but also served as a guide for quantitative advancements. The improvements of RTRFD in comparison to the standard IS theory are clearly visible. However, the applicability of RTRFD is still limited to systems close to local equilibrium with weak gradients. Furthermore, the propagation of shock waves is also an issue which requires a detailed investigation. Thus, a systematic study to improve this theory has to be done, and the framework of BAMPS is the best candidate to test these ideas.

In this work, the comparison of kinetic theory to dissipative hydrodynamics was restricted to the ultrarelativistic limit. BAMPS is also possible to follow the evolution of systems including inelastic processes, large masses, or systems consisting of more than one particle species. Relativistic hydrodynamics has not yet been completely established to answer these questions but remains a topic of intense investigation since, to properly understand these phenomena, more advanced theories of relativistic dissipative hydrodynamics are needed. However, as we have shown, viscous hydrodynamic theories can be also be compared and improved with respect to BAMPS when applied to different systems under different conditions. The work here can serve as a guideline for further studies.

To our knowledge, the complete transition from relativistic ideal to viscous Mach cones was performed for the first time within a kinetic transport model. The studies performed here revealed a lot about the development of Mach cones. Up to now we restricted our calculations to the ultrarelativistic limit. The influence of a nonzero mass or non-trivial EoS would further affect the final structure in the perfect-fluid and viscous regime. This is for example important in the hadronic phase of a heavy-ion collision, where large masses and small scattering rates occur. This implies also that a hadronization process is needed in BAMPS in order to improve the capability to compare with experimental data.

In this work, so far, we restricted our investigations of jet-induced Mach cones in HIC to a scenario with smooth initial conditions and vanishing impact parameter. Effects from fluctuating initial conditions definitely contribute to the final results, especially when addressing the question of the origin of the double-peak structure measured in two-particle correlations. As demonstrated by several works, the initial hot spots are good candidates in order to explain several observables occurring in HIC. The implementation of event-by-event fluctuations in BAMPS would lead to a better description of several flow observables and help to improve the capability of BAMPS to apply it to relativistic HIC.

Appendices

A. The Israel-Stewart equations for the $(1+1)$–dimensional expansion

For the sake of simplicity, we assume an ultrarelativistic massless Boltzmann gas with conserved particle number. In this case, the bulk viscosity vanishes, and the equation of state is simply $e = c_s^{-2}p$, where the speed of sound is $c_s = \sqrt{1/3}$. For massless particles, the energy density as a function of temperature is $e = 3nT$, where $n = \lambda\, gT^3/\pi^2$ is the number density, with g being the number of degrees of freedom. The entropy density is given by $s = (4 - \ln\lambda)n$.

In the following we choose the Landau frame. We shall briefly discuss and write the IS equations in (1+1)–dimensional Cartesian coordinates. We assume that the system is homogeneous in the transverse directions, y and z, and evolves along the longitudinal direction x such that the velocities as well as the derivatives in both transverse directions vanish identically. Thus the four-velocity is $u^\mu = \gamma_x(1, 0, 0, v_x)$ where $\gamma_x = (1 - v_x^2)^{-1/2}$, while the four-derivative is $\partial_\mu = (\partial_t, 0, 0, \partial_x)$. The following four-vector and tensor components vanish: $N^y = N^z = 0$ and $T^{0y} = T^{0z} = T^{yz} = T^{yx} = T^{zx} = 0$. This also implies that the heat-flow components $q^y = q^z = 0$ and shear-stress tensor components $\pi^{0y} = \pi^{0z} = \pi^{yz} = \pi^{yx} = \pi^{zx} = 0$ vanish identically.

Using the orthogonality of the heat-flow four-vector we obtain that $q^0 = q^x v_x$. We may also define the magnitude of the heat-flow four-vector by $q = \sqrt{-q^\mu q_\mu}$, thus $q^x = \gamma_x q$. Similarly, using the orthogonality property of the shear-stress tensor we get $\pi^{00} = \pi^{0x}v_x$ and $\pi^{0x} = \pi^{xx}v_x$. To satisfy the tracelessness condition we may choose $\pi^{yy} = \pi^{zz} = -\pi/2$ and $\pi^{xx} = \gamma_x^2\pi$.

Therefore, the non-vanishing components of the particle four-current and energy-momentum tensor are

$$N^0 \equiv n\gamma_x - \frac{q^x v_x}{h}\,, \tag{A.1}$$

$$N^x \equiv N^0 v_x - \frac{q^x}{\gamma_x^2 h}\,, \tag{A.2}$$

$$T^{00} \equiv (e + \mathcal{P}_x)\gamma_x^2 - \mathcal{P}_x\,, \tag{A.3}$$

$$T^{0x} \equiv v_x(T^{00} + \mathcal{P}_x)\,, \tag{A.4}$$

$$T^{yy} \equiv p - \frac{\pi}{2} = T^{zz}\,, \tag{A.5}$$

$$T^{xx} \equiv v_x T^{0x} + \mathcal{P}_x\,, \tag{A.6}$$

where the LRF effective pressure is,

$$\mathcal{P}_x = p(e, n) + \pi\,. \tag{A.7}$$

The LRF particle and energy densities expressed through the laboratory frame quan-

tities and the velocity are

$$n \;=\; N^0 \left[(1-v_x^2)^{-1/2} - \frac{q^x v_x}{e+p} \right]^{-1} , \tag{A.8}$$

$$e \;=\; T^{00} - v_x T^{0x} = T^{00} - \frac{(T^{0x})^2}{T^{00} + \mathcal{P}_x} , \tag{A.9}$$

$$v_x \;=\; \frac{T^{0x}}{T^{00} + \mathcal{P}_x} . \tag{A.10}$$

The conservation equations are

$$\partial_t N^0 + \partial_x (v_x N^0) \;=\; \partial_x \left[\frac{q^x n}{\gamma^2 (e+p)} \right] , \tag{A.11}$$

$$\partial_t T^{00} + \partial_x (v_x T^{00}) \;=\; -\partial_x (v_x \mathcal{P}_x) , \tag{A.12}$$

$$\partial_t T^{0x} + \partial_x (v_x T^{0x}) \;=\; -\partial_x \mathcal{P}_x . \tag{A.13}$$

The relaxation equations for the heat conductivity are calculated from Eqs. (3.73) and (3.74). In the (1+1)–dimensional case the terms containing the vorticity vanish; therefore the relaxation equations can be formally written as

$$D q^x \;=\; \frac{1}{\tau_q} (q_{NS}^x - q^x) - I_{q1}^x - I_{q2}^x - I_{q3}^x , \tag{A.14}$$

$$D \pi \;=\; \frac{1}{\tau_\pi} (\pi_{NS} - \pi) - I_{\pi 1} - I_{\pi 2} - I_{\pi 3} , \tag{A.15}$$

where the Navier-Stokes values for the heat conductivity and shear stress are,

$$\pi_{NS} \;=\; -\frac{4}{3} \left(\frac{\eta}{s} \right) s\, \theta_x , \tag{A.16}$$

$$q_{NS}^x \;=\; \left(\frac{\kappa_q T}{s} \right) \frac{(Ts)n}{e+p} \gamma_x^2 \left(v_x \frac{\partial_t \lambda}{\lambda} + \frac{\partial_x \lambda}{\lambda} \right) . \tag{A.17}$$

The expansion rate is denoted by $\theta_x = \partial_t \gamma_x + \partial_x (\gamma_x v_x)$. In the ultrarelativistic limit, the coefficients introduced in Sec. 3.4.3 are $\alpha_1 = -1/(4p)$, $\beta_1 = 5/(4p)$, $\beta_2 = 3/(4p)$, $a_1 = 0$, and $a_1' = 5\alpha_1$. The terms in the relaxation equations are given explicitly as

$$I_{q1}^x \;=\; \frac{1}{2} q^x \left(\theta_x + D \ln \frac{\beta_1}{T} \right) , \tag{A.18}$$

$$I_{q2}^x \;=\; -q^x v_x \gamma_x^3 \left(\partial_t v_x + v_x \partial_x v_x \right) , \tag{A.19}$$

$$I_{q3}^x \;=\; \frac{1}{5} \left[\gamma_x^2 \left(v_x \partial_t \pi + \partial_x \pi \right) + \gamma_x \pi \left(v_x \theta_x + \gamma_x \partial_t v_x \right) \right] , \tag{A.20}$$

and

$$I_{\pi 1} \;=\; \frac{1}{2} \pi \left(\theta_x + D \ln \frac{\beta_2}{T} \right) , \tag{A.21}$$

$$I_{\pi 2} \;=\; \frac{10}{9} (q^x \gamma_x^2) \left(\partial_t v_x + v_x \partial_x v_x \right) , \tag{A.22}$$

$$I_{\pi 3} \;=\; \frac{2}{9} \left(v_x \partial_t q^x + \partial_x q^x - \frac{q^x v_x}{\gamma_x} \theta_x \right) . \tag{A.23}$$

The terms I_{q3}^x, $I_{\pi 2}$, and $I_{\pi 3}$ represent a coupling between the heat-flow four-vector and shear-stress tensor.

In this work the term I_{q3}^x is neglected in most cases unless otherwise stated. The reason is that the agreement with kinetic theory is better without it, but results with and without this coupling term will be shown when we discuss in Chapter 7 the viscous solutions to the relativistic Riemann problem.

B. Resummed Transient Relativistic Fluid Dynamics

We briefly introduce the new derivation of viscous hydrodynamics, which is an approximation to the relativistic Boltzmann equations and is named RTRFD (Resummed Transient Relativistic Fluid Dynamics). For more details we refer to the original works [35, 46, 47]. Note that in this section we use a different notation for the particle diffusion current, $n^\mu \equiv V^\mu$, and the particle four-momentum, $k^\mu \equiv p^\mu$.

In RTRFD [47], $f_\mathbf{k}$ is expanded in terms of an orthonormal and complete basis in momentum space. The expansion basis contains two basic ingredients: The first are the *irreducible* tensors, 1, $k^{\langle \mu \rangle}$, $k^{\langle \mu_1} k^{\mu_2 \rangle}, \ldots, k^{\langle \mu_1} \cdots k^{\mu_m \rangle}$, which form a *complete and orthogonal* set, analogously to the spherical harmonics [39, 47]. Here, we use the notation $A^{\langle \mu_1 \cdots \mu_\ell \rangle} \equiv \Delta^{\mu_1 \cdots \mu_\ell}_{\nu_1 \cdots \nu_\ell} A^{\nu_1 \cdots \nu_\ell}$, with $\Delta^{\mu_1 \cdots \mu_m}_{\nu_1 \cdots \nu_m}$. The latter quantities are projectors onto the subspaces orthogonal to u^μ. Their definition is explicitly given in Refs. [39, 47]. Except for $m = 1$, where $\Delta^\mu_\nu = g^\mu_\nu - u^\mu u_\nu$, they are traceless. E.g., for $m = 2$, $\Delta^{\mu\nu}_{\alpha\beta} = (\Delta^\mu_\alpha \Delta^\nu_\beta + \Delta^\mu_\beta \Delta^\nu_\alpha)/2 - \Delta^{\mu\nu} \Delta_{\alpha\beta}/3$. Note that the expansion of $f_\mathbf{k}$ in IS theory is not in terms of the irreducible tensors $k^{\langle \mu_1} \cdots k^{\mu_m \rangle}$, but in terms of the tensors $k^{\mu_1} \cdots k^{\mu_m}$ which are complete but neither irreducible nor orthogonal.

The second ingredient are orthogonal polynomials in $E_\mathbf{k} = u^\mu k_\mu$, $P^{(\ell)}_{n\mathbf{k}} = \sum^n_{r=0} a^{(\ell)}_{nr} E^r_\mathbf{k}$. For details in constructing the polynomials, see Ref. [47]. Then, $f_\mathbf{k}$ is expanded as

$$f_\mathbf{k} = f_{0\mathbf{k}} + f_{0\mathbf{k}} \sum_{\ell=0}^{\infty} \sum_{n=0}^{N_\ell} \mathcal{H}^{(\ell)}_{n\mathbf{k}} \, \rho^{\mu_1 \cdots \mu_\ell}_n \, k_{\langle \mu_1} \cdots k_{\mu_\ell \rangle} \, , \tag{B.1}$$

where $f_{0\mathbf{k}} = \exp\left(\alpha_0 - \beta_0 E_\mathbf{k}\right)$ is the local equilibrium distribution function, with $\alpha_0 = \mu/T$ being the ratio of chemical potential to temperature and $\beta_0 = 1/T$ the inverse temperature. We further introduced the energy-dependent coefficients $\mathcal{H}^{(\ell)}_{n\mathbf{k}} \equiv \left(W^{(\ell)}/\ell!\right) \sum^{N_\ell}_{m=n} a^{(\ell)}_{mn} P^{(\ell)}_{m\mathbf{k}}$, with a normalization constant $W^{(\ell)}$, and the irreducible moments of $\delta f_\mathbf{k} = f_\mathbf{k} - f_{0\mathbf{k}}$,

$$\rho^{\mu_1 \cdots \mu_\ell}_r \equiv \int \mathrm{d}K \, E^r_\mathbf{k} \, k^{\langle \mu_1} \cdots k^{\mu_\ell \rangle} \, \delta f_\mathbf{k}. \tag{B.2}$$

Here, $\mathrm{d}K \equiv g \mathrm{d}\vec{k}/[(2\pi)^3 k^0]$ is the Lorentz-invariant momentum-space volume. Some of the irreducible moments are related to the fields in Eqs. (3.40) and (3.41): $n^\mu = \rho^\mu_0$ and $\pi^{\mu\nu} = \rho^{\mu\nu}_0$. The values of α_0 and β_0 are defined by the matching conditions $n \equiv \langle E_\mathbf{k} \rangle_0$ and $\varepsilon \equiv \langle E^2_\mathbf{k} \rangle_0$, where $\langle \cdots \rangle_0 \equiv \int \mathrm{d}K \, (\cdots) f_{0\mathbf{k}}$. The matching conditions and the definition of u^μ according with the Landau picture imply that the following moments should vanish: $\rho_1 = \rho_2 = \rho^\mu_1 = 0$.

The equations of motion for ρ^μ_r and $\rho^{\mu\nu}_r$ together with their respective transport coefficients were derived in Ref. [47]. Since we are investigating the massless limit,

the scalar moments ρ_r will not play a dominant role[1] and we set them to zero. We also neglect all irreducible moments with tensor rank higher than 2, since they are traditionally not considered in fluid dynamics. Then, the equations for the first- and second-rank tensors ρ_r^μ and $\rho_r^{\mu\nu}$ read

$$
\dot\rho_r^{\langle\mu\rangle} + \sum_{n=0,\neq 1}^{N_\ell} \mathcal{A}_{rn}^{(1)} \rho_n^\mu = \alpha_r^{(1)} I^\mu + \rho_r^\nu \omega_\nu^\mu - \frac{r+3}{3}\rho_r^\mu \theta - \Delta_\lambda^\mu \nabla_\nu \rho_{r-1}^{\lambda\nu} + r\rho_{r-1}^{\mu\nu}\dot u_\nu
$$
$$
- \frac{2r+3}{5}\rho_r^\nu \sigma_\nu^\mu + \frac{\beta_0 I_{r+2,1}}{\varepsilon_0 + P_0}\Delta_\nu^\mu \partial_\lambda \pi^{\lambda\nu},
$$
$$
\dot\rho_r^{\langle\mu\nu\rangle} + \sum_{n=0}^{N_\ell} \mathcal{A}_{rn}^{(2)} \rho_n^{\mu\nu} = 2\alpha_r^{(2)}\sigma^{\mu\nu} - \frac{2}{7}(2r+5)\rho_r^{\lambda\langle\mu}\sigma_\lambda^{\nu\rangle} + 2\rho_r^{\lambda\langle\mu}\omega_\lambda^{\nu\rangle} + \frac{2}{5}\nabla^{\langle\mu}\rho_{r+1}^{\nu\rangle}
$$
$$
- \frac{2}{5}(r+5)\rho_{r+1}^{\langle\mu}\dot u^{\nu\rangle} - \frac{r+4}{3}\rho_r^{\mu\nu}\theta, \tag{B.3}
$$

where $\dot\rho_r^{\langle\mu_1\cdots\mu_\ell\rangle} \equiv \Delta_{\nu_1\cdots\nu_\ell}^{\mu_1\cdots\mu_\ell} u^\mu \partial_\mu \rho_r^{\nu_1\cdots\nu_\ell}$, $I^\mu = \nabla^\mu \alpha_0$, $\sigma^{\mu\nu} = \partial^{\langle\mu}u^{\nu\rangle}$, and $\nabla^\mu = \partial^{\langle\mu\rangle}$ [47]. We also defined the thermodynamic integrals

$$
I_{nq}(\alpha_0,\beta_0) = \frac{1}{(2q+1)!!}\int dK\, E_{\mathbf{k}}^{n-2q}\left(-\Delta^{\alpha\beta}k_\alpha k_\beta\right)^q f_{0\mathbf{k}}. \tag{B.4}
$$

The coefficients

$$
\mathcal{A}_{rn}^{(\ell)} = \frac{1}{4\ell+2}\int dK dK' dP dP'\, W_{\mathbf{kk'}\to\mathbf{pp'}} f_{0\mathbf{k}} f_{0\mathbf{k'}} \tilde f_{0\mathbf{p}} \tilde f_{0\mathbf{p'}} E_{\mathbf{k}}^{r-1} k^{\langle\nu_1}\cdots k^{\nu_\ell\rangle}
$$
$$
\times \left(\mathcal{H}_{\mathbf{k}n}^{(\ell)} k_{\langle\nu_1}\cdots k_{\nu_\ell\rangle} + \mathcal{H}_{\mathbf{k'}n}^{(\ell)} k'_{\langle\nu_1}\cdots k'_{\nu_\ell\rangle} - \mathcal{H}_{\mathbf{p}n}^{(\ell)} p_{\langle\nu_1}\cdots p_{\nu_\ell\rangle} - \mathcal{H}_{\mathbf{p'}n}^{(\ell)} p'_{\langle\nu_1}\cdots p'_{\nu_\ell\rangle}\right) \tag{B.5}
$$

contain all the information of the microscopic theory, while $\alpha_r^{(\ell)}$ are complicated functions of β_0 and α_0 [47].

The equations of motion for 13 dynamical variables or moments[2] can be obtained from Eqs. (B.3) for $\rho_0^\mu = n^\mu$ and $\rho_0^{\mu\nu} = \pi^{\mu\nu}$ where $\rho_1^\mu \equiv W^\mu = 0$ by definition. Similarly, the equations of motion for the additional fields ρ_2^μ and $\rho_1^{\mu\nu}$ follow from Eqs. (B.3). In this approximation, RTRFD becomes a theory with 21 moments as dynamical variables[3]. For completeness we recall these equations.

$$
\hat\tau_n \Delta_\alpha^\mu \frac{d\vec n^\alpha}{d\tau} + \vec n^\mu = \vec\kappa I^\mu - \hat\tau_n \vec n_\nu \omega^{\nu\mu} - \hat\delta_{nn}\vec n^\mu \theta + \hat\ell_{n\pi}\Delta^{\mu\nu}\partial_\lambda \vec\pi_\nu^\lambda - \hat\tau_{n\pi}\vec\pi^{\mu\nu} F_\nu
$$
$$
- \hat\lambda_{nn}\vec n_\nu \sigma^{\mu\nu} - \hat\lambda_{n\pi}\vec\pi^{\mu\nu} I_\nu,
$$
$$
\hat\tau_\pi \Delta_{\alpha\beta}^{\mu\nu} \frac{d\vec\pi^{\alpha\beta}}{d\tau} + \vec\pi^{\mu\nu} = 2\vec\eta\sigma^{\mu\nu} + 2\hat\tau_\pi \vec\pi_\lambda^{\langle\mu}\omega^{\nu\rangle\lambda} - \hat\delta_{\pi\pi}\vec\pi^{\mu\nu}\theta - \hat\tau_{\pi\pi}\vec\pi^{\lambda\langle\mu}\sigma_\lambda^{\nu\rangle}
$$
$$
- \hat\tau_{\pi n}\vec n^{\langle\mu} F^{\nu\rangle} + \hat\ell_{\pi n}\nabla^{\langle\mu}\vec n^{\nu\rangle} + \hat\lambda_{\pi n}\vec n^{\langle\mu} I^{\nu\rangle}, \tag{B.6}
$$

---

[1] They contribute mainly to the bulk viscous pressure.

[2] Had we included the scalar moments, there would have been 14 moments.

[3] Had we included the scalar moments, there would have been 23 moments.

where we define the vectors,

$$\vec{n}^{\mu} = \begin{pmatrix} n^{\mu} \\ \rho_2^{\mu} \end{pmatrix}, \quad \vec{\pi}^{\mu\nu} = \begin{pmatrix} \pi^{\mu\nu} \\ \rho_1^{\mu\nu} \end{pmatrix}. \tag{B.7}$$

Here $\hat{\tau}_n$, $\hat{\tau}_{\pi}$, $\hat{\ell}_{n\pi}$, $\hat{\ell}_{\pi n}$, $\hat{\delta}_{nn}$, $\hat{\delta}_{\pi\pi}$, $\hat{\tau}_{n\pi}$, $\hat{\tau}_{\pi\pi}$, $\hat{\tau}_{\pi n}$, $\hat{\lambda}_{nn}$, $\hat{\lambda}_{n\pi}$, and $\hat{\lambda}_{\pi n}$ are 2×2 matrices, while $\vec{\kappa}$ and $\vec{\eta}$ are two-component vectors. The microscopic formulas for these transport coefficients are computed for a gas of massless classical particles with a constant cross section, σ, in Ref. [35].

C. The speed of sound

The speed of sound is defined as [139, 140]

$$c_s = \sqrt{\left(\frac{\partial p}{\partial e}\right)_{s/n}}.$$ (C.1)

In the following we calculate the speed of sound for a massive Boltzmann gas and vanishing chemical potential, i.e., for $\mu = 0$. We can write

$$c_s^2 = \left.\left(\frac{\partial p/\partial T}{\partial e/\partial T}\right)\right|_{\mu=0}.$$ (C.2)

The equilibrium pressure, p, and energy density, e, with $\mu = 0$ read

$$
\begin{aligned}
p(T) &= \frac{g}{2\pi^2} m^2 T K_2\left(\frac{m}{T}\right) T, \\
e(T) &= 3p(T) + \frac{g}{2\pi^2} m^3 T K_1\left(\frac{m}{T}\right),
\end{aligned}
$$ (C.3)

where $K_n(x)$ is the modified Bessel function of the second kind, m is the mass, T is the temperature and g is the degeneracy factor. In order to calculate the derivatives of the pressure and energy density we have to know the derivative of the modified Bessel function, $K_n(x)$, which in general reads

$$\frac{\mathrm{dK_n(x)}}{\mathrm{d}x} = -\frac{K_{n-1}(x) + K_{n+1}(x)}{2}.$$ (C.4)

However, since the argument x of the Bessel function in our case is not linear, we have to use the chain rule. Hence, we get with $x = m/T$,

$$\frac{\mathrm{d}K_n\left(\frac{m}{T}\right)}{\mathrm{d}T} = \frac{m}{T^2}\left(\frac{K_{n-1}\left(\frac{m}{T}\right) + K_{n+1}\left(\frac{m}{T}\right)}{2}\right),$$ (C.5)

which we use to obtain the derivatives

$$
\begin{aligned}
\frac{\mathrm{d}p}{\mathrm{d}T} &= \frac{gm^2}{2\pi^2}\left[2TK_2 + \frac{m}{2}\left(K_1 + K_3\right)\right], \\
\frac{\mathrm{d}e}{\mathrm{d}T} &= 3\frac{\mathrm{d}p}{\mathrm{d}t} + \frac{gm^2}{2\pi^2}\left[mK_1 + \frac{m^2}{2T}\left(K_0 + K_2\right)\right].
\end{aligned}
$$ (C.6)

We have replaced $K_n = K_n(m/T)$ to enhance the readability. Finally, the speed of sound for a massive Boltzmann gas with a constant mass m reads

$$c_s(T) = \left.\sqrt{\frac{2TK_2 - \frac{m}{2}\left(K_1 + K_3\right)}{6TK_2 - \frac{3m}{2}\left(K_1 + K_3\right) + mK_1 + \frac{m^2}{2T}\left(K_2 + K_0\right)}}\right|_{\mu=0}.$$ (C.7)

The final expression depends on the temperature. In the case of vanishing mass, or in the limit $m/T \to 0$, we obtain the speed of sound for an ultrarelativistic gas of massless particles, which reads

$$\lim_{\frac{m}{T} \to 0} c_s = \frac{1}{\sqrt{3}} \, .$$

<div align="right">(C.8)</div>

D. The viscous hydro solver vSHASTA

In order to solve the IS equations of causal relativistic fluid dynamics and the recently derived equations of RTRFD we use a version of the sharp and smooth transport algorithm (SHASTA) [256]. This numerical method is widely used in modeling relativistic heavy-ion collisions, and has hence been extensively tested in the perfect-fluid approximation [168, 257]. We apply SHASTA to solve both the conservation equations and the relaxation equations rearranged in conservation form and call this numerical method vSHASTA[1] [258].

This algorithm requires the Courant-Friedrichs-Lewy (CFL) condition

$$\lambda_{\mathrm{CFL}} = \Delta t / \Delta x \leq 0.5 \,, \tag{D.1}$$

where Δt is the time step and Δx is the cell size. In all our numerical calculations we take $\lambda_{\mathrm{CFL}} = 0.4$. In a first-order finite-difference approach this means that causal transport of matter covers only a distance $\lambda_{\mathrm{CFL}} \Delta x$, while the remaining part of the matter is acausally diffused over a distance $(1 - \lambda_{\mathrm{CFL}}) \Delta x$. The remaining low-order numerical diffusion represents the so-called numerical viscosity of the algorithm. This purely numerical effect called prediffusion is partially removed by non-linear corrections in SHASTA. In a strict sense numerical viscosity does not fully correspond to real physical viscosity which is independent of the numerical method and resolution. However, its presence is inevitable and at the same time compulsory to keep the computations stable and to smoothen out dispersion errors. By increasing the numerical resolution this numerical diffusion can always be reduced to smaller values than the physical one.

We also mention another rather trivial numerical artifact which is present in the numerical solutions at early times. The numerical solutions at early times[2] do not represent the correct and accurate physical behavior, not even in the perfect-fluid limit. However, this will change in time as the solution spreads over a larger number of cells while the structures are resolved on a finer grid. Therefore, the numerical solutions approach the correct solution only after some amount of time.

---

[1] We thank H. Niemi and E. Molnar for running the code and delivering the results.
[2] In case of very strong gradients.

E. Numerical sampling in BAMPS

In the numerical transport model BAMPS as well as in other Monte Carlo-based models, it is often required to sample values of a given distribution function. Such a procedure, if frequently used throughout a numerical simulation, consumes a lot of numerical time. Therefore, it is desirable to implement a method which is as fast as possible. The sampling methods used in BAMPS are mostly performed using the inverse-transform and rejection sampling which we will introduce briefly in the following. For a more detailed discussion on such implementations and their mathematical description, we refer to Refs. [259, 260, 261] and other textbooks. The following sections are based on the discussion in the PhD thesis of O. Fochler [182].

E.1. Inverse-transform sampling

We define a continuous univariate probability density, $f(u)$, such that we obtain a probability, $P[a \leq X \leq b] = \int_a^b f(u)\mathrm{d}u$, of the random variable, X, to be in the interval, $[a, b]$. We have to make sure that $f(u)$ is normalized, i.e., $\int_{-\infty}^{\infty} f(u)\mathrm{d}u = 1$. Then the cumulative distribution function

$$F(x) = \int_{-\infty}^{x} f(u)\mathrm{d}u \tag{E.1}$$

gives the probability for X to be smaller than x, i.e., $P[X \leq x]$.

The next step is to randomly choose values, x, that are distributed according to the density f or, equivalently, the distribution, F. Using a Monte-Carlo generator, we obtain a uniformly distributed random number, y, from the interval $[0, 1)$ in order to compute

$$x = F^{-1}(y) \tag{E.2}$$

from the inverse of the cumulative distribution function.

This method is very fast and simple if indeed the following conditions are fulfilled:

1. there is only one random number which we have to sample according to the univariate distribution,

2. the inverse of the distribution function, F^{-1}, can easily be obtained.

In general, the distribution function used in the numerical framework in BAMPS does not obey these conditions. The distribution function is often too complicated and depends on more than one random number. Therefore, the rejection-sampling method has to be applied.

E.2. Rejection sampling

As mentioned above, the inverse-transform sampling can only be used if we have a uni-variate distribution function and, in addition, we know the inverse of the cumulative distribution. If these conditions are not fulfilled, we are able to use rejection sampling. The univariate case will be discussed first and then generalized to multivariate distributions.

We start with the same notation as above and define $f(u)$ as a continuous univariate probability density with cumulative distribution $F(x) = \int_{-\infty}^{x} f(u)\mathrm{d}u$. Now, we have to find the Lebesgue-integrable envelope function, $g(u)$, such that $f(u) \leq g(u)\,\forall u$. The function $g(u)$ should be sufficiently simple in order to be able to perform, for example, the inverse-transform sampling as discussed before. The rejection method can then be summarized as follows:

1. Sample x according to g (for example using the inverse-transform method).

2. Sample y uniformly from $[0, 1)$.

3. Accept x if $y < \frac{f(x)}{g(x)}$, otherwise reject x and start again.

The rejection sampling samples points $(x, v = yg(x))$ uniformly distributed under the curve of g. Now, we have to check whether $v = yg(x)$ is below $f(x)$ or not. If $yg(x) < f(x)$, the value x is accepted. Otherwise it is rejected. If the latter is the case, the procedure has to be repeated until the condition $yg(x) < f(x)$ is fulfilled. The method here ensures that the area under $f(x)$ is sampled uniformly and thus x is sampled according to f.

The method introduced here can be extended to distributions of multiple random variables, if the envelope function g is still sufficiently simple to apply the inverse-transform method. Choosing $g(x_1, \cdots, x_n) = A = const.$ with $A \leq \sup\{f(x) : x \in \mathbb{R}\}$, step no. 1 of the algorithm above becomes trivial since all points $(x_1, \cdots, x_n)$ are equally probable.

The rejection method introduced has a big advantage, since it can be extended easily to multivariate distributions. Insofar the envelope function, g, is well-chosen, the method is also very fast. If latter is not the case, it may happen that step no. 3 has to be repeated many times, which therefore increases the computational time.

F. Momentum sampling

F.1. Sampling of the thermal distribution

In the following, we introduce the numerical method to sample the thermal distribution of a Boltzmann gas

$$\frac{(2\pi)^3 \mathrm{d}N}{\mathrm{d}^3 p} = f(x, p) = g\, e^{-\frac{u^\mu p_\mu - \mu}{T}}\,, \tag{F.1}$$

using the accept/rejection method[1]. We split our discussion into two parts, one for a thermal distribution at rest, i.e., $\vec{v} = 0$, and one for a boosted thermal distribution, i.e., $\vec{v} \neq 0$. We neglect the chemical potential, μ, the degeneracy factor, g, and the factor $(2\pi)^3$ in the following discussion, because they do not count in the sampling method.

For the following discussion, we repeat some definitions as introduced in Chapter 3. The four-velocity is $u^\mu = \gamma(1, \vec{v})$ and the four-momentum vector is $p^\mu = (E, \vec{p})$. The relativistic energy-momentum relation reads $E^2 = p^2 + m^2$. T is the temperature and $\vec{v}$ denotes the collective velocity or boost of the system. Without loss of generality, we restrict the direction of the velocity to the x-direction. Therefore, we use a modified spherical coordinate system for the momentum vector,

$$\vec{p} = \begin{pmatrix} p_x \\ p_y \\ p_z \end{pmatrix} = \begin{pmatrix} p \cos\theta \\ p \sin\theta \cos\phi \\ p \sin\theta \sin\phi\,. \end{pmatrix} \tag{F.2}$$

For more details we refer to Ref. [262]. We use the integration measure

$$\mathrm{d}^3 p = p^2\, \mathrm{d}\phi\, \mathrm{d}\cos\theta\, \mathrm{d}p\,. \tag{F.3}$$

The number of particles[2], N, in a specified volume, V, is obtained using Eq. (3.26) for massive particles and Eq. (3.30) for massless particles,

$$N = \gamma n_{\mathrm{eq}}(T, \lambda)\, V\,. \tag{F.4}$$

In the following, we use a Monte Carlo generator, as to generate uniformly distributed random numbers, ω, in the interval $[0, 1)$.

F.1.1. Thermal distribution at rest

The thermal distribution for a Boltzmann gas at rest, i.e., $\vec{v} = 0$, reads

$$\frac{\mathrm{d}N}{\mathrm{d}^3 p} = f(x, p) = e^{-\frac{E}{T}}\,. \tag{F.5}$$

---

[1]See appendix E for more details.
[2]In BAMPS N has to be multiplied with N_{test} in order to get the number of particles used in the simulation.

We have to calculate the momentum distribution, $\mathrm{d}N/\mathrm{d}p$. Using the expression (F.3) we write

$$\frac{\mathrm{d}N}{\mathrm{d}p} = \int_0^{2\pi} \mathrm{d}\phi \int_{-1}^1 \mathrm{d}\cos\theta\, p^2 e^{-\frac{E}{T}} \,. \tag{F.6}$$

We integrate over $\mathrm{d}\phi$ and $\mathrm{d}\cos\theta$, leading to

$$f(p) = \frac{\mathrm{d}N}{\mathrm{d}p} = 4\pi p^2 e^{-\frac{E}{T}} \,, \tag{F.7}$$

which is our probability density. However, the integral of the equation above is analytically not invertible, so we have to find a function which is larger, $g(p) \geq f(p)$, and the integral $G(p)$ is analytically invertible. This is

$$g(p) = 4T^2 e^{-\frac{p}{2T}} \,. \tag{F.8}$$

The momentum, p, is obtained via

$$p = -2T\log\omega \,, \tag{F.9}$$

where ω is a random number. In order to accept the sampled momentum, p, the condition

$$\frac{f(p)}{g(p)} \leq \omega \tag{F.10}$$

has to be fulfilled. The angular distribution is calculated via

$$\begin{aligned}
\phi &= 2\pi\omega_1 \,, \\
\cos\theta &= \cos(\omega_2\pi) \,, \\
\sin\theta &= \sqrt{1 - \cos^2\theta} \,,
\end{aligned} \tag{F.11}$$

where ω_1 and ω_2 are independent random numbers.

Now, performing the procedure above for a given number of particles, N, in some volume element, V, we are able to calculate the energy and momenta of particles using the expressions (F.2).

F.1.2. Thermal distribution for non-vanishing velocities

The thermal distribution for a Boltzmann gas with non-vanishing velocity, v_x, reads

$$\frac{\mathrm{d}N}{\mathrm{d}^3p} = f(x, p) = e^{-\gamma\frac{E - v_x p_x}{T}} \,, \tag{F.12}$$

Similarly to the previous discussion, we have to find the momentum distribution, $\mathrm{d}N/\mathrm{d}p$. Using the expression (F.3) we write

$$\frac{\mathrm{d}N}{\mathrm{d}p} = \int_0^{2\pi} \mathrm{d}\phi \int_{-1}^1 \mathrm{d}\cos\theta\, p^2 e^{-\gamma\frac{E - v_x p_x}{T}} \,. \tag{F.13}$$

The integration over ϕ gives 2π. Moreover, we use $p_x = p\cos\theta$ to rewrite

$$\frac{\mathrm{d}N}{\mathrm{d}p} = 2\pi p^2 e^{-\frac{\gamma E}{T}} \int_{-1}^1 \mathrm{d}\cos\theta\, e^{-\frac{\gamma p v_x \cos\theta}{T}} \,. \tag{F.14}$$

After integration over $\cos\theta$ we obtain

$$f(p) = \frac{\mathrm{d}N}{\mathrm{d}p} = 4\pi \frac{pT}{\gamma v_x} e^{-\frac{\gamma E}{T}} \sinh\frac{\gamma v_x p}{T}\,, \tag{F.15}$$

which is our probability density. A corresponding enveloping function, $g(p)$, can be of the form

$$g(p) = \frac{4\pi T^2}{(1-v_x)\gamma^2 v_x} e^{\gamma p \frac{1-v_x}{2T}}\,. \tag{F.16}$$

The momentum, p, is obtained via

$$p = -\frac{2T}{\gamma(1-v_x)}\log(\omega)\,. \tag{F.17}$$

In order to accept the sampled momentum, p, the condition

$$\frac{f(p)}{g(p)} \le \omega \tag{F.18}$$

has to be fulfilled.

In contrast to the previous case, where we have used a thermal distribution, the angular distribution has to be calculated with the rejection sampling. Using a Monte-Carlo random generator we sample the angles

$$\begin{aligned}\phi &= 2\pi\omega_1\,,\\ \cos\theta &= \cos(\omega_2\pi)\,,\\ \sin\theta &= \sqrt{1-\cos^2\theta}\,.\end{aligned} \tag{F.19}$$

Using the chosen p, the angular distribution, $f'(\theta)$, we like to sample reads

$$f'(\theta) = Cp^2 \sin\theta\, e^{\gamma p \frac{1+v_x \cos\theta}{T}}\,, \tag{F.20}$$

with C being an arbitrary constant. The enveloping function we choose is a constant,

$$g'(\theta) = Cp^2 e^{\gamma p \frac{1+v_x}{T}}\,. \tag{F.21}$$

In order to accept the sampled angle distribution, the condition

$$\frac{f'(\theta)}{g'(\theta)} \le \omega \tag{F.22}$$

has to be fulfilled.

In analogy to the previous case for the distribution function in rest, we perform the procedure above for a given number of particles, N, in some volume element, V. The obtained results determine the momenta as given in Eq. (F.2).

F.2. Sampling of thermal reservoirs

At some point in this work, we consider the numerical realization of reservoirs within the static-box scenario. The reservoirs are characterized by a thermal distribution function with a given temperature, T, chemical potential, μ, and velocity, $\vec{v}$, which emit massless particles at a given rate. In the following, we introduce the numerical method in BAMPS. This method has already been introduced in Refs. [184, 187, 263] for similar setups.

We consider the x-direction, whereas the y- and z-directions are assumed to be homogeneous. The left reservoir is at position $x \leq x_{\mathrm{min}}$, the right one at $x \geq x_{\mathrm{max}}$. The area A is spanned by the y- and z-plane. If not otherwise stated, particles in the box touching the borders of the reservoirs are removed from the simulation. Independently of the removal, particles are inserted by at given rate and probability, as discussed in the following.

We now discuss the calculation of the rate for a massless gas which admits an analytical expression for the rate[3]. The probability that a particle is emitted by the reservoir at a time, t, reads

$$P(t) = \frac{1}{\tau} e^{-\frac{t}{\tau}} \,, \tag{F.23}$$

where τ is the inverse rate. The relation above is normalized,

$$\int_0^\infty P(t)\mathrm{d}t = 1 \,. \tag{F.24}$$

Using a random number, ω, in the interval $[0, 1)$, we write

$$\int_t^\infty P(t')\mathrm{d}t' = \omega \,. \tag{F.25}$$

In a time interval, Δt, the number of particles emitted by the reservoir is $\Delta t/\tau$. We calculate the rate by integrating over all momenta and positions of the particles in the reservoir, i.e.,

$$\frac{\mathrm{d}N}{A\,\mathrm{d}t} = \frac{g}{(2\pi)^3} \frac{1}{A\,\mathrm{d}t} \int \mathrm{d}^3p \int \mathrm{d}^3x \, e^{-\frac{u^\mu p_\mu - \mu}{T}} \,. \tag{F.26}$$

$A = \Delta y \Delta z$ is the area of reservoir walls. For the integration over d^3x we obtain $A\mathrm{d}t p_x/E$ and we can write

$$\frac{\mathrm{d}N}{A\,\mathrm{d}t} = \frac{g}{(2\pi)^3} \int \frac{\mathrm{d}^3p}{E} p_x \, e^{-\frac{u^\mu p_\mu - \mu}{T}} \,. \tag{F.27}$$

In order to perform the integration over momentum space, we apply the following

---

[3]In this work, we only use a massless gas of particles when considering the reservoirs.

relations[4]

$$E = p_T \cosh y, \tag{F.28}$$

$$p_x = p_T \sinh y, \tag{F.29}$$

$$\mathrm{d}^3 p = p_T \cosh y \, \mathrm{d}^2 p_T \, \mathrm{d}y, \tag{F.30}$$

$$\mathrm{d}^2 p_T = p_T \, \mathrm{d}p_T \, \mathrm{d}\phi, \tag{F.31}$$

$$p_T = \sqrt{p_y^2 + p_z^2}, \tag{F.32}$$

Thus, we can write

$$\frac{\mathrm{d}N}{A \, \mathrm{d}t} = \frac{g}{(2\pi)^3} e^{\frac{\mu}{T}} \int_0^{2\pi} \mathrm{d}\phi \int_{-\infty}^{+\infty} \mathrm{d}p_T \int \mathrm{d}y \, p_T^2 \sinh y \, e^{-\frac{p_T \cosh(y-\beta)}{T}}, \tag{F.33}$$

where we have introduced $\beta = \operatorname{Artanh} b$, where b is the boost. In the following, we have to integrate over momentum space. The integration over $\mathrm{d}\phi$ and $\mathrm{d}p_T$ is straightforward, but, considering the integration over $\mathrm{d}y$, we have to distinguish between the left and right reservoir,

$$
\begin{aligned}
\tau_L^{-1} &= \frac{\mathrm{d}N}{\mathrm{d}t} = \frac{g}{(2\pi)^3} 4\pi A T_L^3 \lambda_L \int_0^\infty \mathrm{d}y \frac{\sinh y}{\cosh^3 (y - \beta_L)}, \\
\tau_R^{-1} &= \frac{\mathrm{d}N}{\mathrm{d}t} = \frac{g}{(2\pi)^3} 4\pi A T_R^3 \lambda_R \int_{-\infty}^0 \mathrm{d}y \frac{\sinh y}{\cosh^3 (y - \beta_R)}.
\end{aligned}
\tag{F.34}
$$

For the left reservoir, we integrate only from 0 to ∞ because only particles with positive momentum p_x pass the border. For the right reservoir only particles with negative momentum $-p_x$ pass the border such that the integration runs from $-\infty$ to 0. We replaced the expression for the fugacity, $e^{\frac{\mu}{T}}$, by λ. After integrating over $\mathrm{d}y$, we obtain the following expressions for the rates:

$$
\begin{aligned}
\tau_L^{-1} &= \frac{g}{(2\pi)^3} 4\pi A T_L^3 \lambda_L \left(\sinh \beta_L + \cosh \beta_L - \frac{1}{2\cosh \beta_L} \right), \\
\tau_R^{-1} &= \frac{g}{(2\pi)^3} 4\pi A T_R^3 \lambda_R \left(-\sinh \beta_R + \cosh \beta_R - \frac{1}{2\cosh \beta_R} \right).
\end{aligned}
\tag{F.35}
$$

Using the rates derived here, we are able to compute the timesteps when particles are emitted by the reservoirs. The corresponding momentum sampling of the particles is performed as introduced in Sec. F.1.

---

[4]We note that we have used a different coordinate system.

G. The energy density and velocity in the Landau frame

In this thesis, the velocity in the Eckart and the Landau frame is extracted using the numerical transport model BAMPS. While the calculation of the Eckart velocity is straightforward, the calculation of the Landau velocity and the corresponding LRF energy density is rather complicated. In this section we discuss the method how to obtain the Landau velocity and energy density analytically, as long as the full energy-momentum tensor $T^{\mu\nu}$ is known[1].

We split this discussion into two parts. In Sec. G.1, we obtain a fourth-order polynomial which has to be solved in order to get the energy density. As soon as the energy density is known, the components of the velocities can be obtained. In Sec. G.2, we discuss how to solve the previously derived fourth-order polynomial analytically.

G.1. The energy density and velocity in the Landau frame

We repeat the definition of the four-velocity in the Landau frame introduced in Sec. 3.3.3. It reads

$$u^\mu = \frac{T^{\mu\nu}u_\nu}{e}, \tag{G.1}$$

where e is the LRF energy density and $u^\mu = \gamma v^\mu$. Using the latter expression, we can cancel out the Lorentz factor, γ, and write for the velocity in the laboratory frame

$$v^\mu = \frac{T^{\mu\nu}v_\nu}{e}. \tag{G.2}$$

We have an inhomogeneous system of four equations. Writing

$$
\begin{aligned}
ev^0 &= T^{00}v^0 - T^{01}v^1 - T^{02}v^2 - T^{03}v^3, \\
ev^i &= T^{i0}v^0 - T^{i1}v^1 - T^{i2}v^2 - T^{i3}v^3,
\end{aligned}
\tag{G.3}
$$

and using $v^0 = 1$ we obtain

$$
\begin{aligned}
T^{01}v^1 + T^{02}v^2 + T^{03}v^3 &= T^{00} - e, \\
(T^{11} + e)v^1 + T^{12}v^2 - T^{13}v^3 &= T^{10}, \\
T^{21}v^1 + (T^{22} + e)v^2 - T^{23}v^3 &= T^{20}, \\
T^{31}v^1 + T^{32}v^2 - (T^{33} + e)v^3 &= T^{30}.
\end{aligned}
\tag{G.4}
$$

---

[1]The extraction of the energy-momentum tensor using BAMPS is discussed in Chapter 6.

From these relations, we obtain

$$
v^1 = \frac{\begin{vmatrix} T^{10} & T^{12} & T^{13} \\ T^{20} & T^{22}+e & T^{23} \\ T^{30} & T^{23} & T^{33}+e \end{vmatrix}}{\begin{vmatrix} T^{11}+e & T^{12} & T^{13} \\ T^{12} & T^{22}+e & T^{23} \\ T^{13} & T^{23} & T^{33}+e \end{vmatrix}}, \tag{G.5}
$$

$$
v^2 = \frac{\begin{vmatrix} T^{11}+e & T^{10} & T^{13} \\ T^{12} & T^{20} & T^{23} \\ T^{13} & T^{30} & T^{33}+e \end{vmatrix}}{\begin{vmatrix} T^{11}+e & T^{12} & T^{13} \\ T^{12} & T^{22}+e & T^{23} \\ T^{13} & T^{23} & T^{33}+e \end{vmatrix}}, \tag{G.6}
$$

$$
v^3 = \frac{\begin{vmatrix} T^{11}+e & T^{12} & T^{10} \\ T^{12} & T^{22}+e & T^{20} \\ T^{13} & T^{23} & T^{33} \end{vmatrix}}{\begin{vmatrix} T^{11}+e & T^{12} & T^{13} \\ T^{12} & T^{22}+e & T^{23} \\ T^{13} & T^{23} & T^{33}+e \end{vmatrix}}. \tag{G.7}
$$

As the next step, we have to calculate the determinants. After that, the expressions v^1, v^2, und v^3 are inserted into the first equation of (G.4). After some algebraic transformations, we obtain the following fourth-order polynomial

$$
\boxed{e^4 + be^3 + ce^2 + de + f = 0}. \tag{G.8}
$$

The corresponding coefficients read

$$
b = \frac{b_1}{a_1}, \quad c = \frac{c_1 - c_2}{a_1}, \quad d = \frac{d_1 - d_2}{a_1}, \quad f = \frac{f_1 - f_2}{a_1}, \tag{G.9}
$$

with

$$
a_1 = -1, \tag{G.10}
$$

$$
b_1 = T^{00} - T^{11} - T^{22} - T^{33}, \tag{G.11}
$$

$$
\begin{aligned} c_1 = & \left[T^{11} + T^{22} + T^{33}\right] T^{00} \\ & - \left[T^{11}T^{22} + T^{11}T^{33} + T^{22}T^{33} - (T^{13})^2 - (T^{23})^2 - (T^{12})^2\right] \end{aligned}, \tag{G.12}
$$

$$
c_2 = (T^{10})^2 + (T^{20})^2 + (T^{30})^2, \tag{G.13}
$$

$$
\begin{aligned} d_1 = & \left[T^{11}T^{22} + T^{11}T^{33} + T^{22}T^{33} - (T^{13})^2 - (T^{23})^2 - (T^{12})^2\right] T^{00} \\ & - \left[T^{11}T^{22}T^{33} + 2\, T^{12}T^{13}T^{23} - (T^{13})^2 T^{22} - (T^{23})^2 T^{11} - (T^{12})^2 T^{33}\right] \end{aligned}, \tag{G.14}
$$

$$
\begin{aligned} d_2 = & \left[(T^{10})^2 + (T^{30})^2\right] T^{22} + \left[(T^{10})^2 + (T^{20})^2\right] T^{33} + \left[(T^{20})^2 + (T^{30})^2\right] T^{11} \\ & - 2\, T^{10}T^{30}T^{13} - 2\, T^{10}T^{20}T^{12} - 2\, T^{20}T^{30}T^{23} \end{aligned}, \tag{G.15}
$$

$$f_1 = \left[T^{11}T^{22}T^{33} + 2\,T^{12}T^{13}T^{23} - (T^{13})^2 T^{22} - (T^{23})^2 T^{11} - (T^{12})^2 T^{33} \right] T^{00}, \quad \text{(G.16)}$$

$$\begin{aligned}
f_2 =&\, (T^{10})^2 T^{22}T^{33} + (T^{20})^2 T^{11}T^{33} + (T^{30})^2 T^{11}T^{22} + 2\,T^{01}T^{12}T^{23}T^{03} \\
&+ 2\,T^{01}T^{13}T^{23}T^{02} + 2\,T^{13}T^{03}T^{02}T^{12} - 2\,T^{01}T^{03}T^{13}T^{22} \\
&- 2\,T^{01}T^{02}T^{12}T^{33} - 2\,T^{02}T^{03}T^{23}T^{11} - (T^{10})^2 (T^{23})^2 \\
&- (T^{13})^2 (T^{02})^2 - (T^{03})^2 (T^{12})^2
\end{aligned} \qquad \text{(G.17)}$$

In general, the fourth-order polynomial (G.8) has four solutions. One of them is positive, the other three are negative. Hence, only the positive one is the exact physical solution of the LRF energy density. The method to solve Eq. (G.8) is discussed in Sec. G.2. If the LRF energy density is known in the Landau frame, the velocities can be calculated easily via Eqs. (G.5), (G.6), and (G.7).

G.2. The solution of a fourth-order polynomial

Solving a fourth-order polynomial, also named as quartic equation, can be realized via numerical root finding, or even better, by finding an exact analytical solution [264]. The determination using an analytical expression is more accurate and much faster than the numerical root finding. Therefore, we can save a lot of computational time. We introduce the general solution of a quartic equation, which is numerically implemented in BAMPS used to obtain the energy density as discussed in the previous section.

Hence, we introduce the method solving an equation of the form:

$$x^4 + ax^3 + bx^2 + cx + d = 0, \qquad \text{(G.18)}$$

with a, b, c, and d being the coefficients. If the coefficients do not vanish, we obtain four solutions for x. In order to solve the above equation, we make the substitution

$$x = y - \frac{a}{4}, \qquad \text{(G.19)}$$

as to eliminate the cubic part. This leads to

$$y^4 + py^2 + qy + r = 0. \qquad \text{(G.20)}$$

The new coefficients are

$$\begin{aligned}
p &= b - \frac{3}{8}a^2, \\
q &= \frac{1}{8}a^3 - \frac{1}{2}ab + c, \\
r &= -\frac{3a^4 - 16a^2b + 64ac - 256d}{256}.
\end{aligned} \qquad \text{(G.21)}$$

Equation (G.20) can be solved via its resolvent cubic [265],

$$z^3 - 2pz^2 + (p^2 - 4r)z + q^2. \qquad \text{(G.22)}$$

Now we have to solve the cubic equation

$$z^3 - Rz^2 + Sz + T, \qquad \text{(G.23)}$$

with

$$R = 2p \,,$$
$$S = p^2 - 4r \,,$$
$$T = q^2 \,.$$

(G.24)

We make another substitution,

$$z = \tilde{z} - \frac{R}{3} \,,$$

(G.25)

and obtain the equation in a reduced form

$$\tilde{z}^3 + P\tilde{z} + Q = 0 \,,$$

(G.26)

where

$$P = S - \frac{1}{3}R^2 \,,$$
$$Q = \frac{2}{27}R^3 - \frac{1}{3}RS + T \,,$$

(G.27)

are the corresponding coefficients. Now, using the expression

$$\Theta = \left(\frac{Q}{2}\right)^2 + \left(\frac{P}{3}\right)^3 \,,$$

(G.28)

we have to distinguish between three different cases.

- For $\Theta > 0$ we obtain one real and two complex solutions. We solve the equation via *Cardano's method* [266]. Here,

$$u = \left(-Q/2 + \sqrt{\Theta}\right)^{\frac{1}{3}} \,,$$
$$v = \left(-Q/2 - \sqrt{\Theta}\right)^{\frac{1}{3}} \,,$$

(G.29)

and thus the three solutions are

$$\tilde{z}_1 = u + v \,,$$
$$\tilde{z}_2 = -\frac{1}{2}(u+v) - i\frac{1}{2}(u+v)\sqrt{3} \,,$$
$$\tilde{z}_3 = -\frac{1}{2}(u+v) + i\frac{1}{2}(u+v)\sqrt{3} \,.$$

(G.30)

We note that i is the imaginary unit.

- For $\Theta = 0$ we can solve the equation via *Cardano's method*, too. The difference is that we get three real solutions, where two of them collapse. Here,

$$u = v = \left(-\frac{Q}{2}\right)^{\frac{1}{3}} \,,$$

(G.31)

and the three solutions are

$$\tilde{z}_1 = 2u \,,$$
$$\tilde{z}_{2,3} = -u \,,$$

(G.32)

- For $\Theta < 0$ we have the *casus irreducibilis* [266]. The solutions are obtained using

$$u = \sqrt{-\left(\frac{P}{3}\right)^3}\,,$$

$$\cos w = -\frac{Q}{2u}\,,$$

(G.33)

and v, which is either $0°$, $120°$, or $240°$. We obtain three solutions

$$\tilde{z}_1 = 2u^{\frac{1}{3}}\cos\frac{w}{3}\,,$$

$$\tilde{z}_2 = 2u^{\frac{1}{3}}\cos\frac{w}{3} + 120°\,,$$

$$\tilde{z}_3 = 2u^{\frac{1}{3}}\cos\frac{w}{3} + 240°\,.$$

(G.34)

After obtaining the three solutions of $\tilde{z}$, we have to undo the substitution, i.e.,

$$z_1 = \tilde{z}_1 - \frac{R}{3}\,,$$

$$z_2 = \tilde{z}_2 - \frac{R}{3}\,,$$

$$z_3 = \tilde{z}_3 - \frac{R}{3}\,.$$

(G.35)

Then, Vieta's formula [267] predicts that the product of the three solutions z_1, z_2, and z_3 has to be equal to the linear part of the equation, that is $q^2 = z_1 z_2 z_3$. The solutions are

$$y_1 = \sqrt{-z_1} + \sqrt{-z_2} + \sqrt{-z_3}\,,$$

$$y_2 = \sqrt{-z_1} - \sqrt{-z_2} - \sqrt{-z_3}\,,$$

$$y_3 = -\sqrt{-z_1} + \sqrt{-z_2} - \sqrt{-z_3}\,,$$

$$y_4 = -\sqrt{-z_1} - \sqrt{-z_2} + \sqrt{-z_3}\,,$$

(G.36)

while the sign in front of the square roots has to be chosen such that $-q = \sqrt{z_1}\sqrt{z_2}\sqrt{z_3}$. Finally, we have to substitute back to get the final solutions of Eq. (G.18), which accordingly read

$$x_1 = y_1 - \frac{a}{4}\,,$$

$$x_2 = y_2 - \frac{a}{4}\,,$$

$$x_3 = y_3 - \frac{a}{4}\,,$$

$$x_4 = y_4 - \frac{a}{4}\,.$$

(G.37)

H. Extraction of the temperature and fugacity

In this appendix we discuss the extraction of the temperature, T, and fugacity, λ, both for a massless and massive gas, as well as for a multicomponent system. For most definitions we refer to the general introduction of the hydrodynamic quantities as discussed in details in Chapter 3.

H.1. One-component system

H.1.1. Massless particles

The extraction of the temperature, T, and fugacity, λ, of a system of massless particles is obtained in a few steps without any difficulty.

The relation $p = nT$ for a relativistic Boltzmann gas connects the temperature with the particle density, n, and equilibrium pressure, p, of the system. When the system contains only one species of massless particles, the bulk viscous pressure vanishes, i.e., $\Pi = 0$. This implies that the equilibrium pressure is equal to the isotropic pressure, i.e., $P = p$. Since the isotropic pressure, P, as well as the particle density, n, are easily extracted from the numerical simulation, the temperature is obtained via

$$T = \frac{P}{n} \, . \tag{H.1}$$

With the knowledge of the temperature, we know the equilibrium particle density assuming vanishing chemical potential, $n_{\text{eq}(T,\mu=0)}$. Using this, we can calculate the fugacity directly via

$$\lambda = \exp\left(\frac{\mu}{T}\right) = \frac{n}{n_{\text{eq}(T,\mu=0)}} \, . \tag{H.2}$$

H.1.2. Massive particles

The calculation for a one-component system of massive particles with a constant mass, m, is a little bit more complicated and requires the *secant method*.

In contrast to the massless case, the bulk viscous pressure, Π, is not always zero. Therefore, we cannot use the relation $p = nT$ directly in order to extract the temperature, because we have two unknowns T and p. For that reason, we use the energy density, e, instead of the equilibrium pressure, p, in order to achieve our goal.

Using Eqs. (3.26) and (3.28), the ratio of energy density and particle density reads

$$\frac{e}{n} = \frac{e_{\text{eq}}(T,\mu)}{n_{\text{eq}}(T,\mu)} = \frac{3p_{\text{eq}}(T,\mu) + \frac{g}{2\pi^2}m^3 T e^{\mu/T} K_1(m/T)}{\frac{g}{2\pi^2}m^2 T e^{\mu/T} K_2(m/T)} \, , \tag{H.3}$$

The left part is given numerically. Although the fugacity, $\lambda = \exp\left(\mu/T\right)$, is canceled out, we cannot extract the temperature directly because of the non-invertible Bessel functions, $K_n(x)$. Therefore, we transform the right part

$$\frac{e}{n} = 3\frac{p_{\text{eq}}(T,\mu)}{n_{\text{eq}}(T,\mu)} + \frac{mK_1(m/T)}{K_2(m/T)} \,, \tag{H.4}$$

and move everything to the left side

$$3T + \frac{mK_1(m/T)}{K_2(m/T)} - \frac{e}{n} = 0 \,. \tag{H.5}$$

The temperature can be extracted from the above expression via iteration it using the secant method. In order to achieve this we need an upper and lower limit, $T_{\max}$ and $T_{\min}$, respectively. They read

$$
\begin{aligned}
\lim_{\frac{m}{T}\to 0} \frac{e_{\text{eq}}(T,\mu)}{n_{\text{eq}}(T,\mu)} &\to T_{\max} = \frac{e}{3n} \,, \\
\lim_{\frac{m}{T}\to\infty} \frac{e_{\text{eq}}(T,\mu)}{n_{\text{eq}}(T,\mu)} &\to T_{\min} = \frac{1}{3}\left(\frac{e}{n} - m\right) \,.
\end{aligned}
\tag{H.6}
$$

The upper one is the limit we know for an ultrarelativistic massless gas. The lower limit is the case when the masses are huge compared to the kinetic energy.

H.2. Multicomponent system

In Sec. 3.3.5 we have discussed the problem of finding a definition of the temperature and the fugacity for a system containing more than one particle species. Although we are able to obtain a temperature and fugacity for each species, its physical meaning is questionable. However, calculating these quantities which we refer to as pseudo-temperatures and fugacites for each species separately is important to obtain a temperature, T, and fugacity, λ, for the whole system. This is discussed in the following.

   The determination of the temperature for the whole system, independent of whether it is in local equilibrium or not, is realized via

$$T = \frac{p}{n} = \frac{\sum n_i T_i}{\sum n_i} \,, \tag{H.7}$$

where i denotes each particle species. Hence, we have to calculate the temperature as well as the particle density for each particle species in order to determine the temperature for the whole system. Furthermore, using the obtained temperature, T, a similar procedure is realized to determine the fugacity for the whole system:

$$\lambda = \frac{n}{n_{\text{eq}}(T,\mu=0)} = \frac{\sum n_i}{\sum n_{\text{eq,i}}(T,\mu=0)} \,. \tag{H.8}$$

At first glance, however, we obtain strange results when determining the hydrodynamic quantities according the procedure introduced. For instance, we assume two massless

particle species, each of them in equilibrium, but each with different temperatures, T_A and T_B. The average temperature, T, of the system lies in between T_A and T_B, and there is no bulk pressure for the whole system, i.e., $\Pi = \Pi_A + \Pi_B = 0$. However, for each particle species separately, the bulk pressure does not vanish, i.e., $\Pi_A \neq \Pi_B \neq 0$. We make this observation in Sec. 7.2.3.

I. The solution of the relativistic Vlasov equation

In Chapter 5, we have discussed in particular solutions of the relativistic Riemann problem. In a more detailed discussion in Sec. 5.1 and 5.2, we have introduced an analytical solution of the shock-tube problem for a perfect fluid. This deals with the propagation of a shock wave and rarefaction wave starting from a sharp discontinuity in velocity and/or several thermodynamic quantities.

In this section, we introduce the shock-tube problem with exactly the same initial conditions as in Sec. 5.1. The only difference is that we assume a non-interacting gas instead of a perfect fluid. Furthermore, we fix the equation of state to $e = 3p$, hence we consider an ultrarelativistic gas of massless particles. In the following, we refer to the derived analytical solution as the *free-streaming* solution which has been discussed also in Refs. [143, 268]. We use $\mathrm{d}\tilde{p} \equiv g\,\mathrm{d}^3 p/[(2\pi)^3 E]$.

We construct a solution of the particle four-flow (3.8),

$$N^\mu(x^\mu) = \int \mathrm{d}\tilde{p}\, p^\mu f(\vec{x}, \vec{p}, t)\,, \tag{I.1}$$

and the energy-momentum tensor (3.9),

$$T^{\mu\nu}(x^\mu) = \int \mathrm{d}\tilde{p}\, p^\mu p^\nu f(\vec{x}, \vec{p}, t)\,, \tag{I.2}$$

for a given distribution function, $f(\vec{x}, \vec{p}, t)$, which solves the relativistic Vlasov equation

$$p^\mu \partial_\mu f(\vec{x}, \vec{p}, t) = 0\,. \tag{I.3}$$

The Vlasov equation is the special limit of the Boltzmann equation (3.2), where the collision term vanishes on the right-hand side. The initial conditions are the same as in the shock-tube problem discussed in Sec. 5.1. We assume matter to be in thermal equilibrium and, for the sake of simplicity, to be homogeneous in the transverse $y - z$ plane, such that the problem becomes $(1+1)$-dimensional. We have matter in thermodynamical equilibrium separated by a membrane at $x_N = 0$. The temperatures on the left ($x < 0$) and right ($x \geq 0$) sides of the membrane are denoted by T_L and T_R, respectively. The chemical potentials and velocities vanish on both sides.

First, we calculate the quantities which do not vanish due to symmetry. These quantities are N^0, N^1, T^{00}, T^{11}, T^{22}, T^{33}, and T^{10}. Then we are able to calculate the velocity, the LRF thermodynamic quantities, and the dissipative quantities. This will be discussed in the end of this section. We separate the problem into two parts, i.e., left and right of the discontinuity. The final solution is the sum of them

$$
\begin{aligned}
N^\mu(x^\mu) &= N_L^\mu(x^\mu) + N_R^\mu(x^\mu)\,,\\
T^{\mu\nu}(x^\mu) &= T_L^{\mu\nu}(x^\mu) + T_R^{\mu\nu}(x^\mu)\,.
\end{aligned}
\tag{I.4}
$$

We discuss the solution of one quantity, T^{00}, where the other quantities are calculated analogously. They are provided in the end of this section.

The left part of the energy density in the laboratory frame reads

$$T_L^{00}(x^\mu) = \frac{g}{(2\pi)^3} \int f_L(\vec{x_0}, \vec{p}, t_0) \, E \, \delta(x - x_0 - \frac{p_x}{E}\Delta t) \, \Theta(x_N - x_0) \, \mathrm{d}^3 p \, \mathrm{d}x_0. \qquad (I.5)$$

The subindex 0 denotes the inital time or position of quantities. We denote $\Delta t = t - t_0$ as the timestep. The δ-function is constructed such that we consider only particles starting at position x_0, and reaching the final position x at final time t within the distance $\frac{p_x}{E}\Delta t$. Furthermore, we introduce the Θ-function, which considers only particles from the left or the right part of the discontinuity, respectively. The Θ-function is defined such that it is one when its argument is positive, otherwise it is zero. Analogously, we define the right part of the energy density in the laboratory frame, i.e.,

$$T_R^{00}(x^\mu) = \frac{g}{(2\pi)^3} \int f_R(\vec{x_0}, \vec{p}, t_0) \, E \, \delta(x - x_0 - \frac{p_x}{E}\Delta t) \, \Theta(x_N + x_0) \, \mathrm{d}^3 p \, \mathrm{d}x_0. \qquad (I.6)$$

In the following, we calculate the solution of Eq. (I.5) in a detailed way.

The initial distribution function $f(\vec{x_0}, \vec{p}, t_0)$ is the thermal distribution (3.25) of a massless Boltzmann gas,

$$f(\vec{x_0}, \vec{p}, t_0) = e^{-\frac{E}{T}} . \qquad (I.7)$$

As mentioned above, the chemical potential and velocity vanish initially. We obtain

$$T_L^{00}(x^\mu) = \frac{g}{(2\pi)^3} \int e^{-\frac{E}{T_L}} \, E \, \delta(x - x_0 - \frac{p_x}{E}\Delta t) \, \Theta(x_N - x_0) \, \mathrm{d}^3 p \, \mathrm{d}x_0. \qquad (I.8)$$

We integrate over x_0, where the δ-function contributes only for $x_0 = x - \frac{p_x}{E}\Delta t$. With $x_N = 0$, we obtain $\Theta(-x + \frac{p_x}{E}\Delta t)$. We introduce a common transformation of variables[1]

$$E = p_T \cosh y, \qquad (I.9)$$

$$p_x = p_T \sinh y, \qquad (I.10)$$

$$\mathrm{d}^3 p = p_T \cosh y \, \mathrm{d}^2 p_T \, \mathrm{d}y, \qquad (I.11)$$

$$p_T = \sqrt{p_y^2 + p_z^2}, \qquad (I.12)$$

as to simplify our further calculations. Here, p_T is the transverse momentum and y is the momentum rapidity. Using $\tanh y = p_x/E$ we obtain the following expression:

$$T_L^{00}(x^\mu) = \frac{g}{(2\pi)^3} \int e^{-\frac{p_T \cosh y}{T_L}} \, \Theta(-x + \tanh y \Delta t) \, p_T^2 \cosh^2 y \, \mathrm{d}^2 p_T \, \mathrm{d}y. \qquad (I.13)$$

Next, we use the relation

$$\mathrm{d}^2 p_T = p_T \, \mathrm{d}p_T \, \mathrm{d}\phi , \qquad (I.14)$$

which allows us to rewrite

$$T_L^{00}(x^\mu) = \frac{g}{(2\pi)^3} \int \Theta(-x + \tanh y \, \Delta t) \cosh^2 y \, \mathrm{d}y \left(\int_0^\infty \int_0^{2\pi} p_T^3 e^{-\frac{p_T \cosh y}{T_L}} \, \mathrm{d}p_T \, \mathrm{d}\phi \right) . \qquad (I.15)$$

---

[1] We note that we used a different coordinate system.

Carrying out the integrations leads to

$$T_L^{00}(x^\mu) = \frac{12gT_L^4}{8\pi^2} \int\limits_{-\infty}^{\infty} \Theta(-x + \tanh y\,\Delta t)\, \frac{1}{\cosh^2 y}\mathrm{d}y\,. \tag{I.16}$$

Furthermore, we make use of the relation

$$\frac{\mathrm{d}y}{\cosh^2 y} = \mathrm{d}\tanh y\,, \tag{I.17}$$

by which Eq. (I.16) turns into

$$T_L^{00}(x^\mu) = \frac{12gT_L^4}{8\pi^2} \int\limits_{-1}^{1} \Theta(-x + \tanh y\,\Delta t)\, \mathrm{d}\tanh y\,. \tag{I.18}$$

We remember that the Θ-function is non-zero for positive arguments only. This requires that $x/\Delta t < \tanh y$. We can hence replace the lower limit -1 by $x/\Delta t$ and obtain for T^{00} on the left side of the discontinuity

$$T_L^{00}(x^\mu) = \frac{12gT_L^4}{8\pi^2}\left(1 - \frac{x}{\Delta t}\right). \tag{I.19}$$

Analogously, we obtain for T^{00} on the right side of the discontinuity

$$T_R^{00}(x^\mu) = \frac{12gT_R^4}{8\pi^2}\left(1 + \frac{x}{\Delta t}\right). \tag{I.20}$$

We summarize the final quantities for the energy-momentum tensor

$$T^{00}(x^\mu) = \frac{12g}{8\pi^2}\left[T_L^4 + T_R^4 + \frac{x}{\Delta t}\left(T_R^4 - T_L^4\right)\right], \tag{I.21}$$

$$T^{11}(x^\mu) = \frac{4g}{8\pi^2}\left[T_L^4 + T_R^4 + \left(\frac{x}{\Delta t}\right)^3\left(T_R^4 - T_L^4\right)\right], \tag{I.22}$$

$$T^{22}(x^\mu) = \frac{6g}{8\pi^2}T_L^4\left[\frac{2}{3} - \frac{x}{\Delta t} + \frac{1}{3}\left(\frac{x}{\Delta t}\right)^3\right]$$
$$+ \frac{6g}{8\pi^2}T_R^4\left[\frac{2}{3} + \frac{x}{\Delta t} - \frac{1}{3}\left(\frac{x}{\Delta t}\right)^3\right], \tag{I.23}$$

$$T^{33}(x^\mu) = \frac{6g}{8\pi^2}T_L^4\left[\frac{2}{3} - \frac{x}{\Delta t} + \frac{1}{3}\left(\frac{x}{\Delta t}\right)^3\right]$$
$$+ \frac{6g}{8\pi^2}T_R^4\left[\frac{2}{3} + \frac{x}{\Delta t} - \frac{1}{3}\left(\frac{x}{\Delta t}\right)^3\right], \tag{I.24}$$

$$T^{10}(x^\mu) = \frac{6g}{8\pi^2}\left[T_L^4 - T_R^4 + \left(\frac{x}{\Delta t}\right)^2\left(T_R^4 - T_L^4\right)\right], \tag{I.25}$$

and the particle-four flow

$$N^0(x^\mu) = \frac{4g}{8\pi^2}\left[T_L^3 + T_R^3 + \frac{x}{\Delta t}\left(T_R^3 - T_L^3\right)\right], \tag{I.26}$$

$$N^1(x^\mu) = \frac{2g}{8\pi^2}\left[T_L^3 - T_R^3 + \left(\frac{x}{\Delta t}\right)^2\left(T_R^3 - T_L^3\right)\right]. \tag{I.27}$$

With the energy-momentum tensor and particle four-flow we are able to calculate all further hydrodynamic quantities, as discussed in Chapter 3.

Bibliography

[1] E. Schrödinger, *Was ist Leben?: Die lebende Zelle mit den Augen des Physikers betrachtet.* Sammlung Dalp. Francke, 1951.

[2] C. Darwin, *The Origin of Species.* No. Bd. 11 in The Harvard Classics. P. F. Collier & Son, 1909.

[3] R. Dawkins, *The Selfish Gene.* Oxford paperbacks. Oxford University Press, 1989.

[4] B. Povh, K. Rith, C. Scholz and F. Zetsche, *Teilchen und Kerne: eine Einführung in die physikalischen Konzepte.* Springer Berlin Heidelberg New York, 2006.

[5] S. Glashow, *Partial Symmetries of Weak Interactions*, *Nucl.Phys.* **22** (1961) 579–588.

[6] S. Weinberg, *A Model of Leptons*, *Phys.Rev.Lett.* **19** (1967) 1264–1266.

[7] J. Letessier and J. Rafelski, *Quark-Gluon Plasma.* No. 18 in Cambridge Monographs on Particle Physics, Nuclear Physics and Cosmology. Cambridge University Press, 2005.

[8] E. V. Shuryak, *Theory of Hadronic Plasma*, *Sov.Phys.JETP* **47** (1978) 212–219.

[9] B. A. Freedman and L. D. McLerran, *Fermions and Gauge Vector Mesons at Finite Temperature and Density. 3. The Ground State Energy of a Relativistic Quark Gas*, *Phys.Rev.* **D16** (1977) 1169.

[10] P. Romatschke and U. Romatschke, *Viscosity Information from Relativistic Nuclear Collisions: How Perfect is the Fluid Observed at RHIC?*, *Phys.Rev.Lett.* **99** (2007) 172301 [0706.1522].

[11] M. Luzum and P. Romatschke, *Conformal Relativistic Viscous Hydrodynamics: Applications to RHIC results at $\sqrt{s_{NN}} = 200$ GeV*, *Phys.Rev.* **C78** (2008) 034915 [0804.4015].

[12] H. Song, S. A. Bass and U. Heinz, *Viscous QCD matter in a hybrid hydrodynamic+Boltzmann approach*, *Phys.Rev.* **C83** (2011) 024912 [1012.0555].

[13] B. Schenke, S. Jeon and C. Gale, *Anisotropic flow in $\sqrt{s} = 2.76$ TeV Pb+Pb collisions at the LHC*, *Phys.Lett.* **B702** (2011) 59–63 [1102.0575].

[14] H. Song, S. A. Bass and U. Heinz, *Elliptic flow in 200 A GeV Au+Au collisions and 2.76 A TeV Pb+Pb collisions: insights from viscous hydrodynamics + hadron cascade hybrid model*, Phys.Rev. **C83** (2011) 054912 [`1103.2380`].

[15] B. Schenke, S. Jeon and C. Gale, *Elliptic and triangular flow in event-by-event (3+1)D viscous hydrodynamics*, Phys.Rev.Lett. **106** (2011) 042301 [`1009.3244`].

[16] H. Song and U. W. Heinz, *Extracting the QGP viscosity from RHIC data - A Status report from viscous hydrodynamics*, J.Phys. **G36** (2009) 064033 [`0812.4274`].

[17] H. Niemi, G. S. Denicol, P. Huovinen, E. Molnar and D. H. Rischke, *Influence of the shear viscosity of the quark-gluon plasma on elliptic flow in ultrarelativistic heavy-ion collisions*, Phys.Rev.Lett. **106** (2011) 212302 [`1101.2442`].

[18] P. Danielewicz and M. Gyulassy, *Dissipative Phenomena in Quark Gluon Plasmas*, Phys.Rev. **D31** (1985) 53–62.

[19] P. Kovtun, D. Son and A. Starinets, *Viscosity in strongly interacting quantum field theories from black hole physics*, Phys.Rev.Lett. **94** (2005) 111601 [`hep-th/0405231`].

[20] L. P. Csernai, J. Kapusta and L. D. McLerran, *On the Strongly-Interacting Low-Viscosity Matter Created in Relativistic Nuclear Collisions*, Phys.Rev.Lett. **97** (2006) 152303 [`nucl-th/0604032`].

[21] J. D. Bjorken, *Highly relativistic nucleus-nucleus collisions: The central rapidity region*, Phys. Rev. D **27** (Jan, 1983) 140–151.

[22] M. Gyulassy and M. Plumer, *Jet quenching in lepton nucleus scattering*, Nucl.Phys. **B346** (1990) 1–16.

[23] X.-N. Wang and M. Gyulassy, *Gluon shadowing and jet quenching in $A + A$ collisions at $\sqrt{s} = 200$ GeV*, Phys.Rev.Lett. **68** (1992) 1480–1483.

[24] X.-N. Wang and M. Gyulassy, *Gluon shadowing and jet quenching in relativistic heavy ion collisions*, Nucl.Phys. **A544** (1992) 559–564.

[25] **STAR** Collaboration, J. Adams *et. al.*, *Experimental and theoretical challenges in the search for the quark gluon plasma: The STAR Collaboration's critical assessment of the evidence from RHIC collisions*, Nucl.Phys. **A757** (2005) 102–183 [`nucl-ex/0501009`].

[26] **BRAHMS** Collaboration, I. Arsene *et. al.*, *Quark gluon plasma and color glass condensate at RHIC? The Perspective from the BRAHMS experiment*, Nucl.Phys. **A757** (2005) 1–27 [`nucl-ex/0410020`].

[27] **PHENIX** Collaboration, K. Adcox *et. al.*, *Formation of dense partonic matter in relativistic nucleus-nucleus collisions at RHIC: Experimental evaluation by the PHENIX collaboration*, Nucl.Phys. **A757** (2005) 184–283 [`nucl-ex/0410003`].

[28] **PHOBOS** Collaboration, B. Back, M. Baker, M. Ballintijn, D. Barton, B. Becker *et. al.*, *The PHOBOS perspective on discoveries at RHIC, Nucl.Phys.* **A757** (2005) 28–101 [`nucl-ex/0410022`].

[29] H. Stöcker, *Collective flow signals the quark gluon plasma, Nucl.Phys.* **A750** (2005) 121–147 [`nucl-th/0406018`].

[30] L. Satarov, H. Stöcker and I. Mishustin, *Mach shocks induced by partonic jets in expanding quark-gluon plasma, Phys.Lett.* **B627** (2005) 64–70 [`hep-ph/0505245`].

[31] R. S. Bhalerao, M. Luzum and J.-Y. Ollitrault, *Understanding anisotropy generated by fluctuations in heavy-ion collisions, Phys.Rev.* **C84** (2011) 054901 [`1107.5485`].

[32] G.-L. Ma and X.-N. Wang, *Jets, Mach cone, hot spots, ridges, harmonic flow, dihadron and γ-hadron correlation in high-energy heavy-ion collisions, Phys.Rev.Lett.* **106** (2011) 162301 [`1011.5249`].

[33] I. Bouras, E. Molnar, H. Niemi, Z. Xu, A. El *et. al.*, *Relativistic shock waves in viscous gluon matter, Phys.Rev.Lett.* **103** (2009) 032301 [`0902.1927`].

[34] I. Bouras, E. Molnar, H. Niemi, Z. Xu, A. El *et. al.*, *Investigation of shock waves in the relativistic Riemann problem: A Comparison of viscous fluid dynamics to kinetic theory, Phys.Rev.* **C82** (2010) 024910 [`1006.0387`].

[35] G. Denicol, H. Niemi, I. Bouras, E. Molnar, Z. Xu *et. al.*, *Solving the heat-flow problem with transient relativistic fluid dynamics*, `1207.6811`.

[36] I. Bouras, A. El, O. Fochler, H. Niemi, Z. Xu *et. al.*, *Transition From Ideal To Viscous Mach Cones In A Kinetic Transport Approach, Phys.Lett.* **B710** (2012) 641–646 [`1201.5005`].

[37] I. Bouras, B. Betz, Z. Xu and C. Greiner, *Investigation of Mach cones in relativistic HIC,* in preparation, .

[38] G. Denicol, H. Niemi, I. Bouras, E. Molnar, Z. Xu and C. Greiner, *Solving the problem of finite propagation speed in transient relativistic fluid-dynamics,* in preparation, .

[39] S. Groot, W. Leeuwen and C. van Weert, *Relativistic kinetic theory: principles and applications.* North-Holland Pub. Co., 1980.

[40] C. Cercignani and G. M. Kremer, *The Relativisitic Boltzmann Equation: Theory and Applications.* Birkhaeuser Verlag, 2002.

[41] Z. Xu and C. Greiner, *Thermalization of gluons in ultrarelativistic heavy ion collisions by including three-body interactions in a parton cascade, Phys.Rev.* **C71** (2005) 064901 [`hep-ph/0406278`].

[42] H. Grad, *On the kinetic theory of rarefied gases*, *Comm. Pure Appl. Math* **2** (1949) 331–407.

[43] W. Israel, *Nonstationary irreversible thermodynamics: A Causal relativistic theory*, *Annals Phys.* **100** (1976) 310–331.

[44] W. Israel and J. Stewart, *Transient relativistic thermodynamics and kinetic theory*, *Annals Phys.* **118** (1979) 341–372.

[45] P. Huovinen and D. Molnar, *The Applicability of causal dissipative hydrodynamics to relativistic heavy ion collisions*, *Phys.Rev.* **C79** (2009) 014906 [`0808.0953`].

[46] G. S. Denicol, *Microscopic Foundations of Relativistic Dissipative Fluid Dynamics*. PhD thesis, University of Frankfurt, 2012.

[47] G. Denicol, H. Niemi, E. Molnar and D. Rischke, *Derivation of transient relativistic fluid dynamics from the Boltzmann equation*, *Phys.Rev.* **D85** (2012) 114047 [`1202.4551`].

[48] P. Kolb, U. W. Heinz, P. Huovinen, K. Eskola and K. Tuominen, *Centrality dependence of multiplicity, transverse energy, and elliptic flow from hydrodynamics*, *Nucl.Phys.* **A696** (2001) 197–215 [`hep-ph/0103234`].

[49] M. L. Miller, K. Reygers, S. J. Sanders and P. Steinberg, *Glauber modeling in high energy nuclear collisions*, *Ann.Rev.Nucl.Part.Sci.* **57** (2007) 205–243 [`nucl-ex/0701025`].

[50] B. Betz, *Jet Propagation and Mach-Cone Formation in (3+1)-dimensional Ideal Hydrodynamics*. PhD thesis, 2009. `0910.4114`.

[51] B. Betz, J. Noronha, G. Torrieri, M. Gyulassy and D. H. Rischke, *Universal Flow-Driven Conical Emission in Ultrarelativistic Heavy-Ion Collisions*, *Phys.Rev.Lett.* **105** (2010) 222301 [`1005.5461`].

[52] R. U. Sexl and H. Urbantke, *Gravitation und Kosmologie: Eine Einführung in die allgemeine Relativitätstheorie*. Spektrum Akademischer Verlag, 5. edition ed., 2002.

[53] M. E. Peskin and D. V. Schroeder, *An introduction to quantum field theory*. Westview Press, 1995.

[54] L. H. Ryder, *Quantum Field Theory*. Cambridge University Press, second ed., 1996.

[55] M. Gell-Mann, *A Schematic Model of Baryons and Mesons*, *Phys.Lett.* **8** (1964) 214–215.

[56] **BESIII** Collaboration, M. Ablikim *et. al.*, *Observation of a charged charmoniumlike structure in e+e- to pi+pi-J/psi at $\sqrt{s} = 4.26$ GeV*, *Phys.Rev.Lett.* **110** (2013) 252001 [`1303.5949`].

[57] S. Janowski, D. Parganlija, F. Giacosa and D. H. Rischke, *The Glueball in a Chiral Linear Sigma Model with Vector Mesons*, Phys.Rev. **D84** (2011) 054007 [`1103.3238`].

[58] W. I. Eshraim, S. Janowski, F. Giacosa and D. H. Rischke, *Decay of the pseudoscalar glueball into scalar and pseudoscalar mesons*, Phys.Rev. **D87** (2013) 054036 [`1208.6474`].

[59] G. Bali and K. Schilling, *Static quark - anti-quark potential: Scaling behavior and finite size effects in SU(3) lattice gauge theory*, Phys.Rev. **D46** (1992) 2636–2646.

[60] D. Gross and F. Wilczek, *Ultraviolet Behavior of Nonabelian Gauge Theories*, Phys.Rev.Lett. **30** (1973) 1343–1346.

[61] H. D. Politzer, *Reliable Perturbative Results for Strong Interactions?*, Phys.Rev.Lett. **30** (1973) 1346–1349.

[62] S. Bethke, *Determination of the QCD coupling α_s*, J.Phys. **G26** (2000) R27 [`hep-ex/0004021`].

[63] R. Stock, *Relativistic nucleus-nucleus collisions: From the BEVALAC to RHIC*, J.Phys. **G30** (2004) S633–S648 [`nucl-ex/0405007`].

[64] M. Gazdzicki, R. Stock and P. Seyboth, "Has the deconfinement phase transition been seen?." `http://cerncourier.com/cws/article/cern/28914`, 2003.

[65] **NA49** Collaboration, C. Alt *et. al.*, *Strangeness from 20-A-GeV to 158-A-GeV*, J.Phys. **G30** (2004) S119–S128 [`nucl-ex/0305017`].

[66] D. H. Rischke, *The Quark gluon plasma in equilibrium*, Prog.Part.Nucl.Phys. **52** (2004) 197–296 [`nucl-th/0305030`].

[67] M. Tannenbaum, *Recent results in relativistic heavy ion collisions: From 'a new state of matter' to 'the perfect fluid'*, Rept.Prog.Phys. **69** (2006) 2005–2060 [`nucl-ex/0603003`].

[68] M. Gyulassy, I. Vitev, X.-N. Wang and B.-W. Zhang, *Jet quenching and radiative energy loss in dense nuclear matter*, `nucl-th/0302077`.

[69] P. F. Kolb and U. W. Heinz, *Hydrodynamic description of ultrarelativistic heavy ion collisions*, `nucl-th/0305084`.

[70] U. W. Heinz and M. Jacob, *Evidence for a new state of matter: An Assessment of the results from the CERN lead beam program*, `nucl-th/0002042`.

[71] E. Shuryak, *Why does the quark gluon plasma at RHIC behave as a nearly ideal fluid?*, Prog.Part.Nucl.Phys. **53** (2004) 273–303 [`hep-ph/0312227`].

[72] M. Gyulassy and L. McLerran, *New forms of QCD matter discovered at RHIC*, Nucl.Phys. **A750** (2005) 30–63 [`nucl-th/0405013`].

[73] E. V. Shuryak, *What RHIC experiments and theory tell us about properties of quark-gluon plasma?*, Nucl.Phys. **A750** (2005) 64–83 [`hep-ph/0405066`].

[74] P. W. Higgs, *Broken Symmetries and the Masses of Gauge Bosons*, Phys.Rev.Lett. **13** (1964) 508–509.

[75] **ALICE** Collaboration, *Charged-particle multiplicity density at midrapidity in central pb-pb collisions at $\sqrt{s_{NN}} = 2.76$ TeV*, Phys. Rev. Lett. **105** (Dec, 2010) 252301.

[76] **ALICE** Collaboration, *Elliptic flow of charged particles in pb-pb collisions at $\sqrt{s_{NN}} = 2.76$ TeV*, Phys. Rev. Lett. **105** (Dec, 2010) 252302.

[77] **ALICE** Collaboration, *Centrality dependence of the charged-particle multiplicity density at midrapidity in pb-pb collisions at $\sqrt{s_{\mathrm{NN}}} = 2.76$ TeV*, Phys. Rev. Lett. **106** (Jan, 2011) 032301.

[78] **ALICE** Collaboration, *Higher harmonic anisotropic flow measurements of charged particles in pb-pb collisions at $\sqrt{s_{NN}} = 2.76$ TeV*, Phys. Rev. Lett. **107** (Jul, 2011) 032301.

[79] M. Stephanov, *QCD phase diagram: An Overview*, PoS **LAT2006** (2006) 024 [`hep-lat/0701002`].

[80] C. Schmidt, *Lattice QCD at finite density*, PoS **LAT2006** (2006) 021 [`hep-lat/0610116`].

[81] D. Bailin and A. Love, *Superfluidity and Superconductivity in Relativistic Fermion Systems*, Phys.Rept. **107** (1984) 325.

[82] S. B. Rüster, V. Werth, M. Buballa, I. A. Shovkovy and D. H. Rischke, *The Phase diagram of neutral quark matter: Self-consistent treatment of quark masses*, Phys.Rev. **D72** (2005) 034004 [`hep-ph/0503184`].

[83] G. Münster and M. Walzl, *Lattice gauge theory: A Short primer*, `hep-lat/0012005`.

[84] O. Philipsen, *Lattice QCD at non-zero temperature and baryon density*, `1009.4089`.

[85] F. Karsch, *Lattice QCD at high temperature and density*, Lect.Notes Phys. **583** (2002) 209–249 [`hep-lat/0106019`].

[86] F. Karsch, E. Laermann and A. Peikert, *The Pressure in two flavor, (2+1)-flavor and three flavor QCD*, Phys.Lett. **B478** (2000) 447–455 [`hep-lat/0002003`].

[87] M. Cheng, N. Christ, S. Datta, J. van der Heide, C. Jung *et. al.*, *The QCD equation of state with almost physical quark masses*, Phys.Rev. **D77** (2008) 014511 [`0710.0354`].

[88] A. Bazavov, T. Bhattacharya, M. Cheng, N. Christ, C. DeTar *et. al.*, *Equation of state and QCD transition at finite temperature*, *Phys.Rev.* **D80** (2009) 014504 [`0903.4379`].

[89] Y. Aoki, G. Endrodi, Z. Fodor, S. Katz and K. Szabo, *The Order of the quantum chromodynamics transition predicted by the standard model of particle physics*, *Nature* **443** (2006) 675–678 [`hep-lat/0611014`].

[90] Y. Aoki, S. Borsanyi, S. Durr, Z. Fodor, S. D. Katz *et. al.*, *The QCD transition temperature: results with physical masses in the continuum limit II.*, *JHEP* **0906** (2009) 088 [`0903.4155`].

[91] Z. Fodor and S. Katz, *A New method to study lattice QCD at finite temperature and chemical potential*, *Phys.Lett.* **B534** (2002) 87–92 [`hep-lat/0104001`].

[92] Z. Fodor and S. Katz, *Lattice determination of the critical point of QCD at finite T and μ*, *JHEP* **0203** (2002) 014 [`hep-lat/0106002`].

[93] Z. Fodor and S. Katz, *Critical point of QCD at finite T and μ, lattice results for physical quark masses*, *JHEP* **0404** (2004) 050 [`hep-lat/0402006`].

[94] C. Allton, S. Ejiri, S. Hands, O. Kaczmarek, F. Karsch *et. al.*, *The Equation of state for two flavor QCD at nonzero chemical potential*, *Phys.Rev.* **D68** (2003) 014507 [`hep-lat/0305007`].

[95] P. de Forcrand and O. Philipsen, *The QCD phase diagram for three degenerate flavors and small baryon density*, *Nucl.Phys.* **B673** (2003) 170–186 [`hep-lat/0307020`].

[96] B. Müller and J. L. Nagle, *Results from the relativistic heavy ion collider*, *Ann.Rev.Nucl.Part.Sci.* **56** (2006) 93–135 [`nucl-th/0602029`].

[97] **PHENIX** Collaboration, S. Afanasiev *et. al.*, *Elliptic flow for phi mesons and (anti)deuterons in Au + Au collisions at $\sqrt{s_{NN}} = 200$ GeV*, *Phys.Rev.Lett.* **99** (2007) 052301 [`nucl-ex/0703024`].

[98] **STAR** Collaboration, B. Abelev *et. al.*, *Mass, quark-number, and $\sqrt{s_{NN}}$ dependence of the second and fourth flow harmonics in ultra-relativistic nucleus-nucleus collisions*, *Phys.Rev.* **C75** (2007) 054906 [`nucl-ex/0701010`].

[99] J.-Y. Ollitrault, *Anisotropy as a signature of transverse collective flow*, *Phys.Rev.* **D46** (1992) 229–245.

[100] A. M. Poskanzer and S. Voloshin, *Methods for analyzing anisotropic flow in relativistic nuclear collisions*, *Phys.Rev.* **C58** (1998) 1671–1678 [`nucl-ex/9805001`].

[101] R. Feynman, *The behavior of hadron collisions at extreme energies*, *Conf.Proc.* **C690905** (1969) 237–258.

[102] R. Fries, B. Müller, C. Nonaka and S. Bass, *Hadronization in heavy ion collisions: Recombination and fragmentation of partons*, Phys.Rev.Lett. **90** (2003) 202303 [`nucl-th/0301087`].

[103] R. Fries, B. Müller, C. Nonaka and S. Bass, *Hadron production in heavy ion collisions: Fragmentation and recombination from a dense parton phase*, Phys.Rev. **C68** (2003) 044902 [`nucl-th/0306027`].

[104] P. Huovinen, P. Kolb, U. W. Heinz, P. Ruuskanen and S. Voloshin, *Radial and elliptic flow at RHIC: Further predictions*, Phys.Lett. **B503** (2001) 58–64 [`hep-ph/0101136`].

[105] Z. Xu, C. Greiner and H. Stöcker, *PQCD calculations of elliptic flow and shear viscosity at RHIC*, Phys.Rev.Lett. **101** (2008) 082302 [`0711.0961`].

[106] Z. Xu and C. Greiner, *Shear viscosity in a gluon gas*, Phys.Rev.Lett. **100** (2008) 172301 [`0710.5719`].

[107] A. El, Z. Xu and C. Greiner, *Third-order relativistic dissipative hydrodynamics*, Phys.Rev. **C81** (2010) 041901 [`0907.4500`].

[108] **ATLAS** Collaboration, G. e. a. Aad, *Observation of a centrality-dependent dijet asymmetry in lead-lead collisions at $\sqrt{s_{NN}} = 2.76$ TeV with the atlas detector at the lhc*, Phys. Rev. Lett. **105** (Dec, 2010) 252303.

[109] **CMS** Collaboration, S. e. a. Chatrchyan, *Observation and studies of jet quenching in pbpb collisions at $\sqrt{s_{NN}} = 2.76$ tev*, Phys. Rev. C **84** (Aug, 2011) 024906.

[110] M. Spousta, *Jet Quenching at LHC*, `1305.6400`.

[111] M. J. Tannenbaum, *Critical examination of RHIC paradigms: Mostly high p_T*, PoS **CERP2010** (2010) 019 [`1008.1536`].

[112] **STAR** Collaboration, F. Wang, *Soft physics from STAR*, Nucl.Phys. **A774** (2006) 129–138 [`nucl-ex/0510068`].

[113] **PHENIX** Collaboration, A. Adare *et. al.*, *Dihadron azimuthal correlations in Au+Au collisions at $\sqrt{s_{NN}} = 200$ GeV*, Phys.Rev. **C78** (2008) 014901 [`0801.4545`].

[114] V. Koch, A. Majumder and X.-N. Wang, *Cerenkov radiation from jets in heavy-ion collisions*, Phys.Rev.Lett. **96** (2006) 172302 [`nucl-th/0507063`].

[115] B. Alver and G. Roland, *Collision geometry fluctuations and triangular flow in heavy-ion collisions*, Phys.Rev. **C81** (2010) 054905 [`1003.0194`].

[116] **STAR** Collaboration, J. G. Ulery, *Are there Mach cones in heavy ion collisions? Three-particle correlations from STAR*, Int.J.Mod.Phys. **E16** (2007) 2005–2010 [`0704.0224`].

[117] J. Ruppert and B. Müller, *Waking the colored plasma*, *Phys.Lett.* **B618** (2005) 123–130 [`hep-ph/0503158`].

[118] R. Neufeld and I. Vitev, *Parton showers as sources of energy-momentum deposition in the QGP and their implication for shockwave formation at RHIC and at the LHC*, *Phys.Rev.* **C86** (2012) 024905 [`1105.2067`].

[119] T. Renk and J. Ruppert, *Mach cones in an evolving medium*, *Phys.Rev.* **C73** (2006) 011901 [`hep-ph/0509036`].

[120] R. Neufeld and T. Renk, *The Mach cone signal and energy deposition scenarios in linearized hydrodynamics*, *Phys.Rev.* **C82** (2010) 044903 [`1001.5068`].

[121] S. S. Gubser, S. S. Pufu and A. Yarom, *Sonic booms and diffusion wakes generated by a heavy quark in thermal AdS/CFT*, *Phys.Rev.Lett.* **100** (2008) 012301 [`0706.4307`].

[122] J. Noronha, M. Gyulassy and G. Torrieri, *Di-Jet Conical Correlations Associated with Heavey Quark Jets in anti-de Sitter Space/Conformal Field Theory Correspondence*, *Phys.Rev.Lett.* **102** (2009) 102301 [`0807.1038`].

[123] G. Ma, S. Zhang, Y. Ma, H. Huang, X. Cai *et. al.*, *Di-hadron azimuthal correlation and mach-like cone structure in parton/hadron transport model*, *Phys.Lett.* **B641** (2006) 362–367 [`nucl-th/0601012`].

[124] J. Casalderrey-Solana, E. Shuryak and D. Teaney, *Conical flow induced by quenched QCD jets*, *J.Phys.Conf.Ser.* **27** (2005) 22–31 [`hep-ph/0411315`].

[125] S. Zhang, G. Ma, Y. Ma, X. Cai, J. Chen *et. al.*, *Transverse momentum and pseudorapidity dependences of 'Mach-like' correlations for central Au + Au collisions at $\sqrt{s_{NN}} = 200$ GeV*, *Phys.Rev.* **C76** (2007) 014904 [`0706.3820`].

[126] W. Li, S. Zhang, Y. Ma, X. Cai, J. Chen *et. al.*, *Reaction plane angle dependence of dihadron azimuthal correlations from a multiphase transport model calculation*, *Phys.Rev.* **C80** (2009) 064913.

[127] P. Rau, J. Steinheimer, B. Betz, H. Petersen, M. Bleicher *et. al.*, *Conical Emission from Shock Waves in Ne(1-20 AGeV)+U Collisions*, `1003.1232`.

[128] J. Casalderrey-Solana, *Mach Cones in Quark Gluon Plasma*, *J.Phys.* **G34** (2007) S345–352 [`hep-ph/0701257`].

[129] W. Scheid, H. Müller and W. Greiner, *Nuclear Shock Waves in Heavy-Ion Collisions*, *Phys.Rev.Lett.* **32** (1974) 741–745.

[130] J. Hofmann, H. Stöcker, U. W. Heinz, W. Scheid and W. Greiner, *Possibility of Detecting Density Isomers in High Density Nuclear MACH Shock Waves*, *Phys.Rev.Lett.* **36** (1976) 88–91.

[131] H. Baumgardt, J. Schott, Y. Sakamoto, E. Schopper, H. Stöcker *et. al.*, *Shock Waves and MACH Cones in Fast Nucleus-Nucleus Collisions*, *Z.Phys.* **A273** (1975) 359–371.

[132] H. Gutbrod, K. Kampert, B. Kolb, A. M. Poskanzer, H. Ritter *et. al.*, *SQUEEZEOUT OF NUCLEAR MATTER AS A FUNCTION OF PROJECTILE ENERGY AND MASS*, *Phys.Rev.* **C42** (1990) 640–651.

[133] H. H. Gutbrod, A. M. Poskanzer and H. G. Ritter, *PLASTIC BALL EXPERIMENTS*, *Rept.Prog.Phys.* **52** (1989) 1267.

[134] M. Gyulassy, D. H. Rischke and B. Zhang, *Hot spots and turbulent initial conditions of quark - gluon plasmas in nuclear collisions*, *Nucl.Phys.* **A613** (1997) 397–434 [`nucl-th/9609030`].

[135] J. Takahashi, B. Tavares, W. Qian, R. Andrade, F. Grassi *et. al.*, *Topology studies of hydrodynamics using two particle correlation analysis*, *Phys.Rev.Lett.* **103** (2009) 242301 [`0902.4870`].

[136] R. Andrade, F. Grassi, Y. Hama and W.-L. Qian, *A Closer look at the influence of tubular initial conditions on two-particle correlations*, *J.Phys.* **G37** (2010) 094043 [`0912.0703`].

[137] **STAR** Collaboration, B. Abelev *et. al.*, *Indications of Conical Emission of Charged Hadrons at RHIC*, *Phys.Rev.Lett.* **102** (2009) 052302 [`0805.0622`].

[138] C. A. Pruneau, *Methods for jet studies with three-particle correlations*, *Phys.Rev.* **C74** (2006) 064910 [`nucl-ex/0608002`].

[139] L. D. Landau and E. M. Lifschitz, *Lehrbuch der theoretischen Physik - Band 6; Hydrodynamik.* Akademie-Verlag Berlin, 4th ed., 1981.

[140] W. Greiner and H. Stock, *Hydrodynamik.* Harri Deutsch, 4th ed., 1991.

[141] L. Saint-Raymond, *Hydrodynamic Limits of the Boltzmann Equation.* Springer, 2009.

[142] W. Greiner, H. Stöcker and H. Neise, *Thermodynamik und Statistische Mechanik.* Harri Deutsch, 2nd ed., 1993.

[143] C. Greiner and D. H. Rischke, *Shell - like structures in an expanding quark - anti-quark plasma*, *Phys.Rev.* **C54** (1996) 1360–1365 [`nucl-th/9604044`].

[144] E. W. Weisstein, "Modified bessel function of the second kind." Visited on 05/01/13.

[145] D. H. Rischke, *Ultrarelativistische Schwerionenphysik - Untersuchungen zur Zustandsgleichung heißer und dichter Kernmaterie.* PhD thesis, University of Frankfurt, 1992.

[146] A. Muronga, *Relativistic dynamics of non-ideal fluids: Viscous and heat-conducting fluids. ii. transport properties and microscopic description of relativistic nuclear matter*, *Physical Review C (Nuclear Physics)* **76** (2007), no. 1 014910.

[147] D. H. Rischke, *Fluid dynamics for relativistic nuclear collisions*, `nucl-th/9809044`.

[148] C. Eckart, *The Thermodynamics of irreversible processes. 3.. Relativistic theory of the simple fluid*, Phys.Rev. **58** (1940) 919–924.

[149] A. Monnai and T. Hirano, *Relativistic Dissipative Hydrodynamic Equations at the Second Order for Multi-Component Systems with Multiple Conserved Currents*, Nucl.Phys. **A847** (2010) 283–314 [`1003.3087`].

[150] A. El, I. Bouras, C. Wesp, Z. Xu and C. Greiner, *Dissipative hydrodynamics for multi-component systems*, Eur.Phys.J. **A48** (2012) 166 [`1206.3465`].

[151] A. El, I. Bouras, F. Lauciello, Z. Xu and C. Greiner, *Dissipative Hydrodynamics for Relativistic Multi-Component Systems*, `1103.4038`.

[152] W. Hiscock and L. Lindblom, *Stability and causality in dissipative relativistic fluids*, Annals Phys. **151** (1983) 466–496.

[153] W. A. Hiscock and L. Lindblom, *Generic instabilities in first-order dissipative relativistic fluid theories*, Phys.Rev. **D31** (1985) 725–733.

[154] S. Pu, T. Koide and D. H. Rischke, *Does stability of relativistic dissipative fluid dynamics imply causality?*, Phys.Rev. **D81** (2010) 114039 [`0907.3906`].

[155] G. Denicol, T. Koide and D. Rischke, *Dissipative relativistic fluid dynamics: a new way to derive the equations of motion from kinetic theory*, Phys.Rev.Lett. **105** (2010) 162501 [`1004.5013`].

[156] J. Stewart, *Non-equilibrium relativistic kinetic theory*, .

[157] A. Muronga, *Causal theories of dissipative relativistic fluid dynamics for nuclear collisions*, Phys.Rev. **C69** (2004) 034903 [`nucl-th/0309055`].

[158] W. A. Hiscock and L. Lindblom, *Linear plane waves in dissipative relativistic fluids*, Phys. Rev. **D35** (1987) 3723–3732.

[159] E. Molnar, H. Niemi and D. Rischke, *Numerical tests of causal relativistic dissipative fluid dynamics*, Eur.Phys.J. **C65** (2010) 615–635 [`0907.2583`].

[160] S. Chapman and T. Cowling, *The Mathematical Theory of Non-uniform Gases: An Account of the Kinetic Theory of Viscosity, Thermal Conduction and Diffusion in Gases*. Cambridge Mathematical Library. Cambridge University Press, 1970.

[161] A. Chorin and J. Marsden, *A Mathematical Introduction to Fluid Mechanics*. Texts in Applied Mathematics. Springer, 1993.

[162] R. Courant and K. Friedrichs, *Supersonic flow and shock waves*. Applied Mathematical Sciences Series. Springer-Verlag GmbH, 1976.

[163] D. H. Rischke, H. Stöcker and W. Greiner, *Flow in conical shock waves: a signal for the deconfinement transition?*, Phys.Rev. **D42** (1990) 2283–2292.

[164] G. I. Taylor and J. W. Maccoll, *The air pressure on a cone moving at high speeds. i*, Proc. R. Soc. A **139** (1933) 278–297.

[165] G. I. Taylor and J. W. Maccoll, *The air pressure on a cone moving at high speeds. ii*, Proc. R. Soc. A **139** (1933) 298–311.

[166] A. Taub, *Relativistic Rankine-Hugoniot Equations*, Phys.Rev. **74** (1948) 328–334.

[167] R. D. Reitz, *One-dimensional compressible gas dynamics calculations using the boltzmann equation*, Journal of Computational Physics **42** (1981), no. 1 108 – 123.

[168] V. Schneider, U. Katscher, D. Rischke, B. Waldhauser, J. Maruhn *et. al.*, *New algorithms for ultrarelativistic numerical hydrodynamics*, J.Comput.Phys. **105** (1993) 92–107.

[169] J. Centrella and J. R. Wilson, *Planar numerical cosmology. ii - the difference equations and numerical tests*, apjs **54** (Feb., 1984) 229–249.

[170] P. Mach, *Analytic solutions of the Riemann problem in relativistic hydrodynamics and their numerical applications*, ArXiv e-prints (July, 2010) [`1007.1650`].

[171] D. H. Rischke, Y. Pürsün and J. A. Maruhn, *Relativistic hydrodynamics for heavy ion collisions. 2. Compression of nuclear matter and the phase transition to the quark - gluon plasma*, Nucl.Phys. **A595** (1995) 383–408 [`nucl-th/9504021`].

[172] R. Romero, J. M. Marti, J. A. Pons, J. M. Ibanez and J. A. Miralles, *The Exact solution of the Riemann problem in relativistic MHD with tangential magnetic fields*, J.Fluid Mech. **544** (2005) 323 [`astro-ph/0506527`].

[173] B. Giacomazzo and L. Rezzolla, *The Exact solution of the Riemann problem in relativistic MHD*, `gr-qc/0507102`.

[174] G. Denicol, T. Kodama, T. Koide and P. Mota, *Shock propagation and stability in causal dissipative hydrodynamics*, Phys.Rev. **C78** (2008) 034901 [`0805.1719`].

[175] A. Lang, H. Babovsky, W. Cassing, U. Mosel, H.-G. Reusch and K. Weber, *A new treatment of boltzmann-like collision integrals in nuclear kinetic equations*, Journal of Computational Physics **106** (1993), no. 2 391 – 396.

[176] P. Danielewicz and G. F. Bertsch, *Production of deuterons and pions in a transport model of energetic heavy ion reactions*, Nucl. Phys. **A533** (1991) 712–748.

[177] G. Ferini, M. Colonna, M. Di Toro and V. Greco, *Scalings of Elliptic Flow for a Fluid at Finite Shear Viscosity*, *Phys.Lett.* **B670** (2009) 325–329 [`0805.4814`].

[178] W. Cassing, *Anti-baryon production in hot and dense nuclear matter*, *Nucl.Phys.* **A700** (2002) 618–646 [`nucl-th/0105069`].

[179] B. Zhang, *ZPC 1.0.1: A Parton cascade for ultrarelativistic heavy ion collisions*, *Comput.Phys.Commun.* **109** (1998) 193–206 [`nucl-th/9709009`].

[180] L.-W. Chen, V. Greco, C. M. Ko and P. F. Kolb, *Pseudorapidity dependence of anisotropic flows in relativistic heavy-ion collisions*, *Phys.Lett.* **B605** (2005) 95–100 [`nucl-th/0408021`].

[181] D. Molnar and M. Gyulassy, *New solutions to covariant nonequilibrium dynamics*, *Phys.Rev.* **C62** (2000) 054907 [`nucl-th/0005051`].

[182] O. Fochler, *Investigation of high-p_T phenomena within a partonic transport model*. PhD thesis, University of Frankfurt, 2011.

[183] C. Wesp, A. El, F. Reining, Z. Xu, I. Bouras *et. al.*, *Calculation of shear viscosity using Green-Kubo relations within a parton cascade*, *Phys.Rev.* **C84** (2011) 054911 [`1106.4306`].

[184] F. Reining, I. Bouras, A. El, C. Wesp, Z. Xu *et. al.*, *Extraction of shear viscosity in stationary states of relativistic particle systems*, *Phys.Rev.* **E85** (2012) 026302 [`1106.4210`].

[185] A. El, F. Lauciello, C. Wesp, Z. Xu and C. Greiner, *Shear viscosity of an ultrarelativistic Boltzmann gas with isotropic inelastic scattering processes*, `1207.5331`.

[186] D. Molnar, *Differential elliptic flow prediction at the LHC from parton transport*, `0707.1251`.

[187] M. Greif, F. Reining, I. Bouras, G. Denicol, Z. Xu *et. al.*, *Investigation of Heat Conductivity in Relativistic Systems using a Partonic Cascade*, *Phys. Rev. E 87*, **033019** (2013) [`1301.1190`].

[188] G. Baym, *THERMAL EQUILIBRATION IN ULTRARELATIVISTIC HEAVY ION COLLISIONS*, *Phys. Lett.* **B138** (1984) 18–22.

[189] K. Geiger and B. Müller, *Dynamics of parton cascades in highly relativistic nuclear collisions*, *Nuclear Physics B* **369** (1992), no. 3 600 – 654.

[190] E. V. Shuryak, *Two stage equilibration in high-energy heavy ion collisions*, *Phys.Rev.Lett.* **68** (1992) 3270–3272.

[191] S. Wong, *Thermal and chemical equilibration in a gluon plasma*, *Nucl.Phys.* **A607** (1996) 442–456 [`hep-ph/9606305`].

[192] H. Heiselberg and X.-N. Wang, *Thermal equilibration in an expanding parton plasma*, *Nucl.Phys.* **B462** (1996) 389–414 [`hep-ph/9601247`].

[193] R. Baier, A. H. Mueller, D. Schiff and D. Son, *'Bottom up' thermalization in heavy ion collisions*, *Phys.Lett.* **B502** (2001) 51–58 [`hep-ph/0009237`].

[194] A. El, *Untersuchung des 'Bottom-Up' Szenarios der Thermalisierung im Rahmen einer pQCD basierten partonischen Kaskadesimulation*, Master's thesis, University of Frankfurt, 2006.

[195] A. El, Z. Xu and C. Greiner, *Thermalization of a color glass condensate and review of the 'Bottom-Up' scenario*, *Nucl.Phys.* **A806** (2008) 287–304 [`0712.3734`].

[196] O. Fochler, *Energy loss of high-p_T partons in transport simulations of heavy ion collisions*, Diplomarbeit, Goethe-Universität Frankfurt, 2006.

[197] D. Teaney, *The Effects of viscosity on spectra, elliptic flow, and HBT radii*, *Phys.Rev.* **C68** (2003) 034913 [`nucl-th/0301099`].

[198] H. Song and U. W. Heinz, *Causal viscous hydrodynamics in 2+1 dimensions for relativistic heavy-ion collisions*, *Phys.Rev.* **C77** (2008) 064901 [`0712.3715`].

[199] K. Dusling and D. Teaney, *Simulating elliptic flow with viscous hydrodynamics*, *Phys.Rev.* **C77** (2008) 034905 [`0710.5932`].

[200] Z. Xu and C. Greiner, *Transport rates and momentum isotropization of gluon matter in ultrarelativistic heavy-ion collisions*, *Phys.Rev.* **C76** (2007) 024911 [`hep-ph/0703233`].

[201] Z. Xu and C. Greiner, *Elliptic flow of gluon matter in ultrarelativistic heavy-ion collisions*, *Phys.Rev.* **C79** (2009) 014904 [`0811.2940`].

[202] A. El, A. Muronga, Z. Xu and C. Greiner, *Shear viscosity and out of equilibrium dissipative hydrodynamics*, *Phys.Rev.* **C79** (2009) 044914 [`0812.2762`].

[203] O. Fochler, J. Uphoff, Z. Xu and C. Greiner, *Radiative parton processes in perturbative QCD - an improved version of the Gunion and Bertsch cross section from comparisons to the exact result*, `1302.5250`.

[204] J. Uphoff, O. Fochler, Z. Xu and C. Greiner, *Heavy quark production at RHIC and LHC within a partonic transport model*, *Phys.Rev.* **C82** (2010) 044906 [`1003.4200`].

[205] **PHENIX** Collaboration, A. Adare *et. al.*, *Heavy Quark Production in $p + p$ and Energy Loss and Flow of Heavy Quarks in Au+Au Collisions at $\sqrt{s_{NN}} = 200$ GeV*, *Phys.Rev.* **C84** (2011) 044905 [`1005.1627`].

[206] J. Uphoff, O. Fochler, Z. Xu and C. Greiner, *Open Heavy Flavor in Pb+Pb Collisions at $\sqrt{s} = 2.76$ TeV within a Transport Model*, *Phys.Lett.* **B717** (2012) 430–435 [`1205.4945`].

[207] A. El, Z. Xu and C. Greiner, *Third-order dissipative hydrodynamics from the entropy principle*, *J.Phys.Conf.Ser.* **230** (2010) 012046 [`1004.4452`].

[208] A. El, I. Bouras, Z. Xu and C. Greiner, *Dissipative hydrodynamics for multi-component systems*, To appear in the proceedings of Quark Matter 2012.

[209] I. Bouras, E. Molnar, H. Niemi, Z. Xu, A. El *et. al.*, *Development of relativistic shock waves in viscous gluon matter*, Nucl.Phys. **A830** (2009) 741C–744C [0907.4519].

[210] I. Bouras, A. El, O. Fochler, C. Greiner, E. Molnar *et. al.*, *Comparisons between transport and hydrodynamic calculations*, Acta Phys.Polon. **B40** (2009) 973–978.

[211] M. Mendoza, B. M. Boghosian, H. J. Herrmann and S. Succi, *Fast Lattice Boltzmann Solver for Relativistic Hydrodynamics*, Physical Review Letters **105** (July, 2010) 014502 [0912.2913].

[212] D. Hupp, M. Mendoza, I. Bouras, S. Succi and H. Herrmann, *On the relativistic Lattice Boltzmann method for quark-gluon plasma simulations*, Phys.Rev. **D84** (2011) 125015 [1109.0640].

[213] M. Mendoza, I. Karlin, S. Succi and H. J. Herrmann, *Relativistic Lattice Boltzmann Model with Improved Dissipation*, ArXiv e-prints (Jan., 2013) [1301.3423].

[214] F. Mohseni, M. Mendoza, S. Succi and H. Herrmann, *Lattice Boltzmann model for ultra-relativistic flows*, 1302.1125.

[215] L. P. Csernai, *Introduction to relativistic heavy ion collisions*. Wiley, 1994.

[216] J. A. S. Lima, A. Kandus and R. Opher, *Thickness of a mildly relativistic collisional shock wave*, Phys. Rev. D **67** (Jan, 2003) 023002.

[217] C. Cercignani and A. Majorana, *Structure of shock waves in relativistic simple gases*, Physics of Fluids **31** (1988), no. 5 1064–1068.

[218] M. Torrilhon, *Characteristic waves and dissipation in the 13-moment-case*, vol. 12. Springer-Verlag, 2000.

[219] H. Freistühler and G. Warnecke, *Hyperbolic Problems: Theory, Numerics, Applications : Eighth International Conference in Magdeburg, February/March 2000*. No. Bd. 1 in International Series of Numerical Mathematics Series. Birkhäuser, 2001.

[220] M. T. J. D. Au and W. Weiss, *The shock tube problem in extended thermodynamics*, Phys. Fluids **13** (2001).

[221] H. Struchtrup and M. Torrilhon, *Regularization of grad's 13 moment equations: Derivation and linear analysis*, Fluids **15** (2003) 2668–2680.

[222] H. Struchtrup and M. Torrilhon, *Regularized 13-moment equations: shock structure calculations and comparison to burnett models*, Journal of Fluid Mechanics **513** (2004) 171.

[223] R. Bhalerao, J.-P. Blaizot, N. Borghini and J.-Y. Ollitrault, *Elliptic flow and incomplete equilibration at RHIC*, *Phys.Lett.* **B627** (2005) 49–54 [`nucl-th/0508009`].

[224] A. El, A. Muronga, Z. Xu and C. Greiner, *A Relativistic dissipative hydrodynamic description for systems including particle number changing processes*, *Nucl.Phys.* **A848** (2010) 428–442 [`1007.0705`].

[225] T. Biro, E. van Doorn, B. Müller, M. Thoma and X. Wang, *Parton equilibration in relativistic heavy ion collisions*, *Phys.Rev.* **C48** (1993) 1275–1284 [`nucl-th/9303004`].

[226] D. K. Srivastava, M. G. Mustafa and B. Müller, *Expanding quark - gluon plasmas: Transverse flow, chemical equilibration and electromagnetic radiation*, *Phys.Rev.* **C56** (1997) 1064–1074 [`nucl-th/9611041`].

[227] D. M. Elliott and D. H. Rischke, *Chemical equilibration of quarks and gluons at rhic and lhc energies*, *Nuclear Physics A* **671** (2000), no. 1-4 583 – 608.

[228] F. Gelis, K. Kajantie and T. Lappi, *Chemical thermalization in relativistic heavy ion collisions*, *Phys.Rev.Lett.* **96** (2006) 032304 [`hep-ph/0508229`].

[229] W. Israel and J. Stewart, *Thermodynamics of nonstationary and transient effects in a relativistic gas*, *Physics Letters A* **58** (1976), no. 4 213 – 215.

[230] W. Israel and J. M. Stewart, *On transient relativistic thermodynamics and kinetic theory. ii*, *Proceedings of the Royal Society of London. A. Mathematical and Physical Sciences* **365** (1979), no. 1720 43–52.

[231] B. Betz, D. Henkel and D. Rischke, *From kinetic theory to dissipative fluid dynamics*, *Prog.Part.Nucl.Phys.* **62** (2009) 556–561 [`0812.1440`].

[232] B. Betz, D. Henkel and D. Rischke, *Complete second-order dissipative fluid dynamics*, *J.Phys.* **G36** (2009) 064029.

[233] B. Betz, G. Denicol, T. Koide, E. Molnar, H. Niemi *et. al.*, *Second order dissipative fluid dynamics from kinetic theory*, *EPJ Web Conf.* **13** (2011) 07005 [`1012.5772`].

[234] **STAR** Collaboration, F. Wang, *Measurement of jet modification at RHIC*, *J.Phys.* **G30** (2004) S1299–S1304 [`nucl-ex/0404010`].

[235] **STAR** Collaboration, J. Adams *et. al.*, *Distributions of charged hadrons associated with high transverse momentum particles in pp and Au + Au collisions at $\sqrt{s_{NN}} = 200$ GeV*, *Phys.Rev.Lett.* **95** (2005) 152301 [`nucl-ex/0501016`].

[236] **PHENIX** Collaboration, S. Adler *et. al.*, *Dense-Medium Modifications to Jet-Induced Hadron Pair Distributions in Au+Au Collisions at $\sqrt{s_{NN}} = 200$ GeV*, *Phys.Rev.Lett.* **97** (2006) 052301 [`nucl-ex/0507004`].

[237] **STAR** Collaboration, J. G. Ulery, *Two- and three-particle jet correlations from STAR*, *Nucl.Phys.* **A774** (2006) 581–584 [`nucl-ex/0510055`].

[238] **PHENIX** Collaboration, N. Ajitanand, *Extraction of jet topology using three particle correlations*, *Nucl.Phys.* **A783** (2007) 519–522 [`nucl-ex/0609038`].

[239] A. Ayala, I. Dominguez and M. E. Tejeda-Yeomans, *Head shock vs Mach cone: azimuthal correlations from 2 to 3 parton processes in relativistic heavy-ion collisions*, `1212.1127`.

[240] B. Betz, J. Noronha, G. Torrieri, M. Gyulassy, I. Mishustin *et. al.*, *Universality of the Diffusion Wake from Stopped and Punch-Through Jets in Heavy-Ion Collisions*, *Phys.Rev.* **C79** (2009) 034902 [`0812.4401`].

[241] D. Molnar, *Fate of the Mach cone in covariant transport theory*, *AIP Conf.Proc.* **1182** (2009) 791–794 [`0908.0299`].

[242] B. Betz, M. Gyulassy and G. Torrieri, *Polarization probes of vorticity in heavy ion collisions*, *Phys.Rev.* **C76** (2007) 044901 [`0708.0035`].

[243] I. Bouras, E. Molnar, H. Niemi, Z. Xu, A. El *et. al.*, *Relativistic Shock Waves and Mach Cones in Viscous Gluon Matter*, *J.Phys.Conf.Ser.* **230** (2010) 012045 [`1004.4615`].

[244] O. Fochler, Z. Xu and C. Greiner, *Energy loss in a partonic transport model including bremsstrahlung processes*, *Phys.Rev.* **C82** (2010) 024907 [`1003.4380`].

[245] **PHENIX** Collaboration, K. Adcox *et. al.*, *Suppression of hadrons with large transverse momentum in central Au+Au collisions at $\sqrt{s_{NN}} = 130$ GeV*, *Phys.Rev.Lett.* **88** (2002) 022301 [`nucl-ex/0109003`].

[246] **STAR** Collaboration, J. Adams *et. al.*, *Transverse momentum and collision energy dependence of high $p(T)$ hadron suppression in Au+Au collisions at ultrarelativistic energies*, *Phys.Rev.Lett.* **91** (2003) 172302 [`nucl-ex/0305015`].

[247] **PHENIX** Collaboration, A. Adare *et. al.*, *Suppression pattern of neutral pions at high transverse momentum in Au + Au collisions at $\sqrt{s_{NN}} = 200$ GeV and constraints on medium transport coefficients*, *Phys.Rev.Lett.* **101** (2008) 232301 [`0801.4020`].

[248] A. Chaudhuri and U. Heinz, *Effect of jet quenching on the hydrodynamical evolution of QGP*, *Phys.Rev.Lett.* **97** (2006) 062301 [`nucl-th/0503028`].

[249] J. Casalderrey-Solana, E. Shuryak and D. Teaney, *Hydrodynamic flow from fast particles*, `hep-ph/0602183`.

[250] T. Renk and J. Ruppert, *The Rapidity structure of Mach cones and other large angle correlations in heavy-ion collisions*, *Phys.Lett.* **B646** (2007) 19–23 [`hep-ph/0605330`].

[251] I. Bearden *et. al.*, *Charged meson rapidity distributions in central Au+Au collisions at $\sqrt{s_{NN}} = 200$ GeV,* .

[252] **PHENIX** Collaboration, S. Adler *et. al.*, *Mid-rapidity neutral pion production in proton proton collisions at $\sqrt{s} = 200$ GeV, Phys.Rev.Lett.* **91** (2003) 241803 [`hep-ex/0304038`].

[253] **STAR** Collaboration, J. Adams *et. al.*, *The Multiplicity dependence of inclusive p_t spectra from pp collisions at $\sqrt{s} = 200$ GeV, Phys.Rev.* **D74** (2006) 032006 [`nucl-ex/0606028`].

[254] A. Chaudhuri, *Conical flow due to partonic jets in central Au + Au collisions, Phys.Rev.* **C75** (2007) 057902 [`nucl-th/0610121`].

[255] A. Chaudhuri, *Di-jet hadron pair correlation in a hydrodynamical model with a quenching jet, Phys.Rev.* **C77** (2008) 027901 [`0706.3958`].

[256] J. P. Boris and D. L. Book, *Flux-corrected transport i. shasta, a fluid transport algorithm that works, J. Comput. Phys.* **11** (1972) 38–69.

[257] D. H. Rischke, S. Bernard and J. A. Maruhn, *Relativistic hydrodynamics for heavy ion collisions. 1. General aspects and expansion into vacuum, Nucl.Phys.* **A595** (1995) 346–382 [`nucl-th/9504018`].

[258] E. Molnar, *Comparing the first and second order theories of relativistic dissipative fluid dynamics using the 1+1 dimensional relativistic flux corrected transport algorithm, Eur.Phys.J.* **C60** (2009) 413–429 [`0807.0544`].

[259] W. H. Press, S. A. Teukolsky, W. T. Vetterling and B. P. Flannery, *Numerical Recipes 3rd Edition: The art of scientific computing.* Cambridge University Press, 3 ed., Sept., 2007.

[260] M. Newman and G. T. Barkema, *Monte Carlo methods in statistical physics.* Oxford Univ Pr, Apr., 1999.

[261] C. P. Robert and G. Casella, *Monte Carlo statistical methods.* Springer, Berlin, 2. a. ed., Sept., 2004.

[262] W. Greiner, *Theoretische Physik 1. Klassische Mechanik 1: Kinematik und Dynamik der Punktteilchen - Relativität.* Klassische Mechanik. Deutsch Harri GmbH, 2007.

[263] F. Reining, *Untersuchung von Scherfluss und -viskosität in einer partonischen Kaskade*, 2009.

[264] E. W. Weisstein, "Quartic equation." Visited on 24/12/12.

[265] E. W. Weisstein, "Resolvent cubic." Visited on 24/12/12.

[266] E. W. Weisstein, "Cubic formula." Visited on 24/12/12.

[267] E. W. Weisstein, "Vieta's formulas." Visited on 24/12/12.

[268] I. Bouras, *Untersuchung von Stosswellenphaenomenen in einer partonischen Kaskade*, Master's thesis, University of Frankfurt, 2008.

Danksagung

Ich möchte an dieser Stelle die Gelegenheit nutzen, meinen tiefen Dank an all jene Menschen zum Ausdruck bringen, die es mir ermöglicht haben, diese Doktorarbeit zu schreiben und mich während der Fertigstellung unterstützt haben.

Einen herzlicher Dank richtet sich an Prof. Dr. Carsten Greiner und Prof. Dr. Zhe Xu für die Betreuung und große Unterstützung bei der Durchführung meiner Arbeit. Sie haben mir ermöglicht, die Arbeit nach meinen Wünschen, Ideen und Interessen zu gestalten. Ein ganz besonderer Dank gilt auch Prof. Dr. Dirk H. Rischke, welcher mir eine sehr große Hilfestellung bei vielen Problemen war.

Ein großer Dank gilt meinem externen Betreuer Prof. Dr. Christoph Blume für die Unterstützung während der gesamten Arbeit. Auch möchte ich mich bei meinem Mentor Prof. Dr. Horst Stöcker für seine Unterstützung bedanken.

Einen besonderen Dank richte ich ebenfalls an die Mitglieder meiner Arbeitsgruppe, mit denen ich in all den Jahren zusammenarbeiten durfte und auch außerhalb der Forschung sehr viel Spaß hatte. Ich danke Dr. Andrej El und Dr. Oliver Fochler für ihre intensive Unterstützung bei meiner Arbeit. Gleichwohl richtet sich mein Dank an Dr. Frank Michler, Felix Reining, Christian Wesp und Jan Uphoff für viele hilfreiche Diskussionen.

Ein großer Dank gilt Dr. Etele Molnar, Dr. Harri Niemi und Dr. Gabriel S. Denicol für die großartige Zusammenarbeit, zahlreiche Diskussionen und den großen Spaß über die vielen Jahre. Ich danke auch Dr. Etele Molnar ganz herzlich für seine Gastfreundschaft bei meinen Aufenthalten in Budapest. Ein großer Dank gilt auch Prof. Dr. Marcus Bleicher, Dr. Pasi Huovinen, Dr. Hannah Petersen, Dr. Barbara Betz, Dr. Giorgio Torrieri, Dr. Jorge Noronha, Dr. Jason Ulery, Dr. Hendrik van Hees, Dr. Francesco Giacosa, Philip Rau, Dr. Hannu Holopainen, Dr. Björn Bäuchle für hilfreiche Diskussionen. Ganz herzlich bedanken möchte ich mich auch Prof. Dr. Pedro Bicudo für seine Gastfreundschaft während der Aufenthalte in Lissabon. Ein großer Dank gilt auch Denise Meixler und Daniela Radulescu für die Unterstützung in einer Vielzahl administrativer Angelegenheiten.

Ich möchte hier noch Dr. Etele Molnar, Dr. Frank Michler, Dr. Oliver Fochler, Dr. Barbara Betz, Dr. Harri Niemi, Dr. Gabriel S. Denicol und Dr. Pasi Huovinen für das Korrekturlesen von Teilen meiner Arbeit danken.

Ich möchte mich hier ganz herzlich bei der Helmholtz Graduate School for Hadron and Ion Research (HGS-HIRe) für die finanzielle Unterstützung und für die ausgezeichnete Organisation zahlreicher Veranstaltungen bedanken. Ganz besonderer Dank gilt Prof. Dr. Henner Büsching, Dr. Gerhard Burau und Dr. Sascha Vogel. Ein großer Dank gilt auch den Rechenclustern des Center for Scientific (CSC) der Goethe-Universität für die Bereitstellung der für die Arbeit notwendigen Kapazitäten.

Nicht vergessen möchte ich die Menschen, die ich auf zahlreichen Konferenzen, Workshops, Lecture Weeks und Soft Skill Seminaren treffen durfte und mich für den aktuellen

und menschlichen Austausch bedanken.

Zu guter Letzt möchte ich mich bei meinen Eltern Eleni und Konstantinos Bouras, meinem Bruder Alexandros Bouras, meinem Freund Marko Markovic und meiner Freundin Brunhilde Dörr für ihre uneingeschränkte Unterstützung bedanken.

Erklärung

Ich versichere hiermit, die vorliegende Arbeit selbstständig verfasst und keine anderen als die angegebenen Hilfsmittel verwendet zu haben. Des weiteren sind sämtliche Stellen, die benutzten Werken im Wortlaut oder dem Sinn nach entnommen sind, mit Quellen- beziehungsweise Herkunftsangaben kenntlich gemacht.

_____   _____
Ort, Datum   Ioannis Bouras

Lebenslauf

Persönliche Informationen

Name:	BOURAS, Ioannis
Anschrift:	Dresdner Str. 27 63165 Mühlheim am Main
Geburtsdatum:	26.08.1983 in Offenbach am Main
Nationalität:	Griechisch
Familienstand:	Ledig, keine Kinder

Universitäre und schulische Bildung

01/2010	**Philipp-Siedler-Preis** Auszeichnung für die beste Diplomarbeit im Fach Physik 2010
2009 – 2012	**Stipendium für PhD** vom Helmholtz International Center for Facility for Antiproton and Ion Research (HIC for FAIR)
Seit 03/2009	Mitglied beim Helmholtz International Center for Facility for Antiproton and Ion Research (HIC for FAIR)
Seit 12/2008	**Beginn der Dissertation im Fach Physik** an der Johann Wolfgang Goethe-Universität Frankfurt am Main Forschungsgebiet: *Investigation of relativistic shock waves and Mach cones in a partonic cascade* Betreuer: Prof. Dr. C. Greiner
13.10.2008	Abschluss als **Diplom-Physiker**, *Abschlussnote: 1,0 (summa cum laude)*
23.09.2008	Diplomarbeit, *Note: 1,0* Titel der Arbeit: *Untersuchung von Stoßwellenphänomenen in einer partonischen Kaskade* Betreuer: Prof. Dr. C. Greiner
2003 – 2008	**Studium der Physik** an der Johann Wolfgang Goethe-Universität Frankfurt am Main
1994 – 2003	Leibniz-Gymnasium Offenbach am Main Leistungskurse: Mathematik, Physik
1990 – 1994	Anne-Frank Schule in Offenbach am Main

Berufliche Erfahrungen

Seit 10/2012	Wissenschaftlicher Angestellter der Goethe-Universität Frankfurt Betreuung von Übungsgruppen in der Theoretischen Physik
2008 - 2012	Wissenschaftlicher Angestellter der Goethe-Universität Frankfurt von 12/2008 bis 07/2009; danach Stipendiat am Helmholtz International Center for Facility for Antiproton and Ion Research (HIC for FAIR) bis 09/2012
2006 - 2009	Betreuung von Übungsgruppen in der Theoretischen Physik Von 10/2006 bis 07/2009 als Studentische Hilfskraft

Publikationen

I. Bouras, E. Molnar, H. Niemi, Z. Xu, A. El *et. al.*, *Relativistic shock waves in viscous gluon matter*, Phys.Rev.Lett. **103** (2009) 032301 [`0902.1927`].

I. Bouras, E. Molnar, H. Niemi, Z. Xu, A. El *et. al.*, *Development of relativistic shock waves in viscous gluon matter*, Nucl.Phys. **A830** (2009) 741C–744C [`0907.4519`].

I. Bouras, E. Molnar, H. Niemi, Z. Xu, A. El *et. al.*, *Investigation of shock waves in the relativistic Riemann problem: A Comparison of viscous fluid dynamics to kinetic theory*, Phys.Rev. **C82** (2010) 024910 [`1006.0387`].

D. Hupp, M. Mendoza, I. Bouras, S. Succi and H. Herrmann, *On the relativistic Lattice Boltzmann method for quark-gluon plasma simulations*, Phys.Rev. **D84** (2011) 125015 [`1109.0640`].

C. Wesp, A. El, F. Reining, Z. Xu, I. Bouras *et. al.*, *Calculation of shear viscosity using Green-Kubo relations within a parton cascade*, Phys.Rev. **C84** (2011) 054911 [`1106.4306`].

F. Reining, I. Bouras, A. El, C. Wesp, Z. Xu *et. al.*, *Extraction of shear viscosity in stationary states of relativistic particle systems*, Phys.Rev. **E85** (2012) 026302 [`1106.4210`].

I. Bouras, A. El, O. Fochler, H. Niemi, Z. Xu *et. al.*, *Transition From Ideal To Viscous Mach Cones In A Kinetic Transport Approach*, Phys.Lett. **B710** (2012) 641–646 [`1201.5005`].

G. Denicol, H. Niemi, I. Bouras, E. Molnar, Z. Xu *et. al.*, *Solving the heat-flow problem with transient relativistic fluid dynamics*, `1207.6811`.

A. El, I. Bouras, C. Wesp, Z. Xu and C. Greiner, *Dissipative hydrodynamics for multi-component systems*, Eur.Phys.J. **A48** (2012) 166 [`1206.3465`].

M. Greif, F. Reining, I. Bouras, G. Denicol, Z. Xu *et. al.*, *Investigation of Heat Conductivity in Relativistic Systems using a Partonic Cascade*, Phys. Rev. E 87, **033019** (2013) [`1301.1190`].

Vorgestellte Arbeiten

2013

22.07. - 27.07.	*Strangeness in Quark Matter 2013*, Birmingham (United Kingdom)
04.03. - 08.03.	*77. Jahrestagung der DPG*, Dresden (Germany)

2012

14.10. - 20.10.	*Hot Quarks 2012*, Copamarina, (Puerto Rico)
12.08. - 19.08.	*Quark Matter 2012*, Washington D.C. (USA)
25.06. - 30.06.	*Non-equilibrium Dynamics & Turic Network Workshop*, Hersonissos, Crete (Greece)
06.05. - 12.05.	*Excited QCD 2012*, Peniche (Portugal)

2011

05.09. - 08.09.	*Toric Workshop 2011*, Heraklion (Greece)
30.03. - 04.04.	*Quark Matter 2011 - The 22nd International Conference on Ultra-relativistic Nucleus-Nucleus Collisions*, Annecy (France)
21.03. - 25.03.	*75. Jahrestagung der DPG*, Münster (Germany)
24.01. - 28.01.	*XLIX International Winter Meeting on Nuclear Physics*, Bormio (Italy)

2010

26.09. - 30.09.	*Toric Workshop 2010*, Sardinia (Italy), 2010
21.06. - 26.06.	*Hot Quarks 2010*, La Londe Les Maures (France), 2010
15.03. - 19.03.	*74. Jahrestagung der DPG*, Bonn (Germany), 2010
25.01. - 29.01.	*XLVIII International Winter Meeting on Nuclear Physics*, Bormio (Italy), 2010
02.01. - 09.01.	*26th Winter Workshop on Nuclear Dynamics*, Ocho Rios (Jamaica), 2010

2009

28.10.	*PAC of HIC for Fair*, Frankfurt (Germany), 2009
11.10. - 13.10.	*HIC for FAIR Workshop on Dense QCD Phases in Heavy Ion Collisions and Supernovae*, Prerow (Germany), 2009
14.09. - 18.09.	*Flow and dissipation in ultrarelativistic Heavy Ion Collisions*, Trento (Italy), 2009
06.04. - 08.04.	*Nearly Perfect Liquids - From Quark-Gluon Plasma to Ultra-Cold Atoms*, Durham (USA), 2009

30.03. - 04.04.   *Quark Matter 2009 - The 21st International Conference on Ultra-relativistic Nucleus-Nucleus Collisions*, Knoxville (USA), 2009

16.03. - 20.03.   *73. Jahrestagung der DPG*, Bochum (Germany), 2009

Frankfurt am Main, 4. Dezember 2013

Akademische Lehrer

Prof. Dr. Wolf Aßmus
Prof. Dr. Johann Baumeister
Prof. Dr. Marcus Bleicher
Prof. Dr. Christoph Blume
Prof. Dr. Thomas Boller
Prof. Dr. George Bruls
Prof. Dr. Bruno Martin Deiss
Prof. Dr. Hermann Dinges
Prof. Dr. Reinhard Dörner
Prof. Dr. Carsten Greiner
Prof. Dr. Walter Greiner
Prof. Dr. Michael Huth
Prof. Dr. Joachim Jacoby
Prof. Dr. Joachim Maruhn
Prof. Dr. Udo Müller-Nehler
Prof. Dr. Ulrich Ratzinger
Prof. Dr. Dirk-Hermann Rischke
Prof. Dr. Hartmut Roskos
Prof. Dr. Jürgen Schaffner-Bielich
Prof. Dr. Horst Stöcker
Prof. Dr. Herbert Ströbele
Prof. Dr. Joachim Weidmann
Prof. Dr. Alfred Ziegler